POLITECNICO DI TORINO
Repository ISTITUZIONALE

Joining of Dissimilar Materials

Original
Joining of Dissimilar Materials / BANGASH, MUHAMMAD KASHIF. - (2018 Jul 17).

Availability:
This version is available at: 11583/2711296 since: 2018-07-25T12:35:59Z

Publisher:
Politecnico di Torino

Published
DOI:

Terms of use:
openAccess

This article is made available under terms and conditions as specified in the corresponding bibliographic description in the repository

Publisher copyright

(Article begins on next page)

04 August 2020

Doctoral Dissertation
Doctoral Program in Materials Science and Technology (30th Cycle)

Joining of Dissimilar Materials

Muhammad Kashif Bangash

* * * * * *

Supervisors
Prof. Monica Ferraris
Prof. Graziano Ubertalli
Dr. Valentina Casalegno

Doctoral Examination Committee:
Prof. Conor McCarthy, University of Limerick, Ireland
Prof. Andrea Lazzeri, University of Pisa, Italy
Prof. Milena Salvo, Politecnico di Torino, Italy
Prof. Federico Smeacetto, Politecnico di Torino, Italy
Prof. Alberto Ortona, University of Applied Sciences and Arts of Southern Switzerland, Switzerland.

Politecnico di Torino
June 20, 2018

Declaration

I hereby declare that, the contents and organisation of this dissertation constitute my own original work and does not compromise in any way the rights of third parties, including those relating to the security of personal data.

Muhammad Kashif Bangash
Turin, June 20, 2018

* This dissertation is presented in partial fulfilment of the requirements for a **Ph.D. degree** in the Graduate School of Politecnico di Torino (ScuDo).

I dedicate this thesis to my late parents:

Zahida Bangash
and
Dr. Gul Hussain Bangash

With love and eternal appreciation.

Acknowledgement

I would like to extend thanks to the many people, in many countries, who so generously contributed to the work presented in this thesis.

First of all, I am extremely grateful to my research supervisor, Dr. Monica Ferraris, Professor, DISAT, Politecnico di Torino, for her valuable guidance, scholarly inputs, consistent encouragement and unconditional support I received throughout the research work. She is a person with an amicable and positive disposition and has always made herself available to clarify my doubts despite her busy schedules. It was a great privilege and honour to work and study under her guidance. I gratefully acknowledge the additional funding I received towards my over-stay in Politecnico di Torino from Professor Monica Ferraris.

My special and heartily thanks to my co-supervisor, Dr. Graziano Ubertalli, Associate Professor, DISAT, Politecnico di Torino, whose support and guidance made my thesis work possible. He has been actively interested in my work and has always been available to advise me. I am thankful to him for his patience, motivation, enthusiasm, and immense knowledge in metallurgy and composites.

I have been extremely lucky to have Dr. Valentina Casalegno, Asst. Professor, DISAT, Politecnico di Torino, as my co-tutor, who cared so much about my work, and responded to my questions and queries so promptly. I would also like to thank her for her support, empathy, and a great sense of humour.

I express my gratitude to Dr. Milena Salvo, Associate Professor, DISAT, Politecnico di Torino for encouraging my research and for allowing me to grow as a research scientist. Your advice on both research as well as on my career have been invaluable.

I am grateful to Dr. Hans-Juergen Grande and Alaitz Ruiz, IK4-CIDETEC, Spain and Dr. Omer Berek, Professor, Head of Textile and Fashion Department, Istanbul Technical University, for the guidance and supervising my mobility research activities and for inviting me to work with them in their respective institutes. I would like to extend my deepest gratitude to the KMM-VIN (European Virtual Institute on Knowledge-based Multifunctional Materials AISBL) their generous grant for research mobility in IK4-CIDETEC, Spain.

I am also so thankful to my fellow researcher especially Pardeep Kumar, Shahrukh, Yasir Akram, Alok Kumar Das, Usman Zubair and Stefano De la Pierre, whose challenges and productive critics, have provided new ideas for the work.

I want to thank present and past lab-assistants, accountants and technicians in the DISAT, Politecnico di Torino: Stefano Jamali, Domenico Di Fonte and Rosaria Lo Bue, Antonio Favero and Mauro Raimondo, for arranging the experimental materials, characterisation equipments and for sharing their knowledge.

Words cannot express how grateful I am to my family: Dr. Yasir Bangash, Dr. Shumaila Bangash and Roya Farooq for all the sacrifices that you've made on my behalf. Your prayer for me was what sustained me thus far. I would also like to thank all of my friends who supported me in writing and pushed me to strive towards my goal.

My experience at Politecnico di Torino has been nothing short of amazing. I have been given unique opportunities... and taken advantage of them. I am so grateful to the Higher Education Commission Pakistan for the 5 years continuous funding and making it possible for me to study here.

May the Almighty God bless all of you.

Thesis Abstract

Material manufacturers and engineering structure designers are currently focusing new ways to exploit the benefits of light-weight, hybrid materials with improved properties at a low cost. The ability to join dissimilar materials is enabling the design engineers to develop light-weight and efficient automobiles, aircraft and space vehicles.

The objective of this PhD research study was to produce alternative and efficient joining solutions for automotive and aerospace applications. The joining of dissimilar material was experimented to obtain light-weight Fibre Reinforced Polymer (FRP) sandwich composites, Al-foam sandwich (AFS) composites, hybrid dynamic FRP epoxy/polyurethane composites and the joining of Ti6Al4V alloy with and without surface modification to Ceramic Matrix Composite (CMC) and itself.

The joining of Al-foam and Al-honeycomb to FRP skins was performed. The experimental results show that higher flexural properties can be achieved by replacing Al-honeycomb with low-cost Al-foam as a core material in the sandwich structures. Compared to FRP-honeycomb sandwich panels, FRP-Al foam sandwich panels display ~25 % and ~65 % higher flexural strength in a long and short span three-point bending tests respectively.

AFS composites with complete metallic character, to withstand high-temperature application conditions, were produced by soldering/brazing techniques using Zn-based and Al-based joining alloys. A post-brazing thermal treatment was designed to recover the mechanical properties of AFS composites, lost during the soldering/brazing process. The microstructural analysis of the Al-skin/Al-foam interface revealed that the diffusion of joining materials into the joining substrates (Al-sheet and Al-foam) was achieved. Around 80% higher bending load before

failure was observed when the AFS specimens produced with Zn-based joining alloys were subjected to flexural load compared to those produced with Al-based joining alloys.

Hybrid dynamic Carbon Fibre Reinforced Polymer (CFRP) composites with enhanced impact properties were produced by exploiting the reversible cross-linking functionalities of dynamic epoxy and dynamic PU resin systems. By joining dynamic CFRP-epoxy and dynamic CFR-PU laminates, hybrid dynamic composite in three different configurations and a non-hybrid composite were obtained. The four dynamic composites were characterised for structural, thermal, flexural and impact properties. The damage initiation upon impact was observed at around 95% higher energy level in the hybrid configuration (CFRP-4), compared to the non-hybrid configuration. The hybrid configuration CFRP-3 responded with around 55% higher perforation threshold energy compared the non-hybrid configuration.

Preliminary work on ***Adhesive joining of the Ti6Al4V alloy to itself*** was performed to analyse the effect micro-machining on adhesion and the effect of shape/design of micro-slots on an adhesive joint strength. Three types of micro-slots: V, semi-circle and U-shaped micro-slots were produced on Ti6Al4V sheet surface by using an in-house developed Micro-Electro-Discharge Machining (Micro-EDM) setup. Ti6Al4V alloy specimens with and without micro-machined surfaces were bonded together using a commercial epoxy adhesive. The Single Lap Offset (SLO) shear test results revealed that the micro-slot oriented perpendicular to the applied load displayed ~23 % higher joining strength compared to when the micro-slots were oriented parallel to the applied load. U-shaped micro-slots configuration displayed ~30 % improvement in the joint shear strength compared to the specimens with un-modified surfaces. The fractured surfaces analysis revealed mix (adhesive-cohesive) with cohesive dominated failure in bonded specimens with micro-machined surfaces compared to the as-received where pure adhesive failure was observed.

The joining of CMCs (C/SiC and SiC/SiC) to Ti6Al4V alloy was experimented using active brazing alloy (Cusil-ABA) and Zr-based brazing alloy (TiB590) in a pressure-less argon atmosphere. The CMC-Ti6Al4V joint strength was further improved by modifying the surface of Ti6Al4V alloy using an in-house built Micro-EDM setup. Around 40% higher joining strength was recorded when the Zr-based brazing alloy was used as a joining material compared to the conventional active brazing alloy, Cusil-ABA. Improvement in the joining strength was noticed when the Ti6Al4V surface was modified prior to joining.

Contents

List of Tables

List of Figures

XXI

Annexes

Annex 1

List of Publications

List of Conferences

List of External Research Activities

Annex 2

Preparation and Investigation of AFS from Al-6013 And Al6Si Foams by Brazing Method

Annex 3

Adhesive Joining and Disassembling of Alumina (Al2O3) – Steel

Thesis Outline

The overview of the research area and the introduction of the joining methods and materials and their applications are discussed in **Chapter 1.** The experimental work is discussed in the following five sections based on the category of joined substrates and joining methods.

Chapter 2 discusses the joining Al-foam and Al-honeycomb core materials to Glass and Carbon Fibre Reinforced Polymer (FRP) facing skins by in-situ fabrication of sandwich panels method. The strengthening of the CFRP facing skins with the addition of Multi-Wall Carbon Nano Tubes (MWCNTs), the flexural behaviour of sandwich panels and the comparison of properties among the different configurations of FRP-sandwich panels is discussed in this chapter.

Chapter 3 describes the introduction to Al-foam Sandwich (AFS) composites, the experimental procedures adopted to join Al-sheets to Al-foams and the post-brazing thermal to recover the mechanical properties of AFS base components. The microstructural analysis of the AFS base components (Al-foam and Al-skin), Al-foam/Al-skin joint interface and the flexural characterisation of AFS specimens are discussed in detail.

Chapter 4 discusses the reversible/dynamic cross-linking properties of polymer systems, the development, hybridization and characterisation of new hybrid dynamic Carbon Fibre Reinforced (CFR) epoxy/PU (Polyurethane) composites.

Chapter 5 discusses the experimental work carried out to improve the adhesion by the surface modification of Ti-6Al-4V alloy. The effect of U, V and semi-circle micro-slots on the adhesion and the adhesive joint strength is reported in comparison to, as-received bonded specimens having un-modified surfaces.

Chapter 6 discusses some of the recent findings in the joining of ceramic matrix composites (CMC) to Ti6Al4V alloy and the alternative joining solutions experimented in this study. Furthermore, in this chapter, the working of in-house built Micro-Electro-Discharge Machining (Micro-EDM) and the effect of surface modification of Ti6Al4V on the joint shear strength is described in detail.

Chapter 1

1. Background

1.1 Objectives

The objective of this research study was to review the currently available joining techniques and to introduce new solutions to join dissimilar material for automotive and aerospace applications. Several new joining methods and joining materials were experimented successfully and proposed as cost-effective and efficient joining solutions.

The specific objectives of this PhD study will follow:

- Joining of Al-foam and Al-honeycomb to Fibre Reinforced Polymer (FRP) Skins to obtain FRP-Sandwich composites.
- Joining of Al-foam to Al-Skins to obtain Aluminium Foam Sandwich (AFS) Composites.
- Development and characterisation of hybrid epoxy/PU dynamic thermoset composites.
- Joining of Ceramic Matrix Composites (CMC) to Ti6Al4V Alloy
- Adhesion improvement of Ti6Al4V bonded joints by surface modification.

1.2 Overview of the Joining of Dissimilar Materials

Joining is a complex phenomenon and involves a variety of materials and techniques. Technically it is defined as "*The process used to bring separate parts of components together to produce a unified whole assembly or structural entity*'' [1]. Campbell et.al [2] defined the joining as: "*A large number of processes used to assemble individual parts into a larger, more complex component or assembly*''.

According to the European joining technology platform a joining process is: ‘‘*Creating a bond of some description between materials or components to achieve a specific physical performance*’’ [3]. Joining is therefore can be concluded as an activity of putting or attaching components together to create an assembly or a single unit with or without using a third party joining material.

Joining and assembling processes are essential for a product manufacturing and its functionality. In the early stages of production, designers consider the efficient joining and coupling of the components into a single functional unit. An appropriate joining technique offers a cost effective, a structurally sound and an aesthetically satisfying design solution. The ability to join similar and dissimilar materials enables the design engineers to develop light-weight and efficient automobiles, aircrafts, space vehicles and the development of advance generations of medical equipment and consumer appliances.

In automotive and aerospace industries, structural components are produced and assembled into a single structure. Generally, these structural components are made of different materials to satisfy and withstand the service requirement such as high-temperature resistance, corrosion resistance, toughness, wear resistance and the strength [4]. Recent emerging trends in structural engineering, such as the use of light weight and multi-functional materials have been increased. The multi-material hybrid structures are becoming essential part of a structure for its improved properties. Thus, the need for advance joining solutions for dissimilar materials is highly focused by the research community.

The joining of similar materials with high processing and production speed has already been established. Furthermore, the improvement in material properties, improved traditional joining techniques for similar materials and the extended use of the advance additive manufacturing processes has reduced the need and the number joints in the product [5]. However, the “joint-free” manufacturing concept, when dissimilar materials are involved, is currently somehow unrealistic. It is now not possible to produce a hybrid product without a joint, due to functional needs and technological limitations [6,7].

The joining of dissimilar materials is comparatively more challenging than the joining of similar materials due to the difference in intrinsic properties which decreases the number of joining possibilities. The ability to join dissimilar materials enables the design engineers to develop light-weight and efficient automobiles, aircraft and space vehicles [5,8].

A joint in an engineering structure or assembly is a region of heterogeneity, where the properties of the bulk material change and become discontinuous. In order to evaluate the assembled system and for the quality control, careful attention is paid to the fracture strength of the joint, the composition of filler material and surface properties of the components. The mechanical requirements for an engineering assembly include the homogeneity and continuity in strength, toughness and stiffness properties across the structure.

Dissimilar joining requires the engineering compatibility of the joining components, especially in terms of mechanical, physical and chemical properties. Poor chemical compatibility causes the formation of brittle intermetallic compounds during the joining process [9]. The elastic constants mismatch leads to the shear stresses parallel to the interface in normal conditions while the thermal expansion (CTE) mismatch results in the development of localised thermal stresses and reduce its load-carrying capacity of the components [9,10].

Currently, the realization of concept engineering structure design possibilities is highly restricted due to the lack of joining and assembling techniques. The knowledge of joining technologies is a key factor for progress in manufacturing sector and a continuous development of novel joining materials and techniques is hence required [9].

The joining and assembling processes of engineering components is carried out in two fundamental ways: mechanically or chemically, with and without the formation of chemical bonds respectively.

1.2.1 Joining techniques

Reliable joining technologies are necessary to integrate dissimilar materials into an engineering structure [11]. In past, several joining solutions such as brazing/soldering, adhesive bonding, welding, mechanical joining etc. were introduced for multi-material systems [12–15]. The techniques used for the joining of dissimilar materials in this work can be summarized as follows:

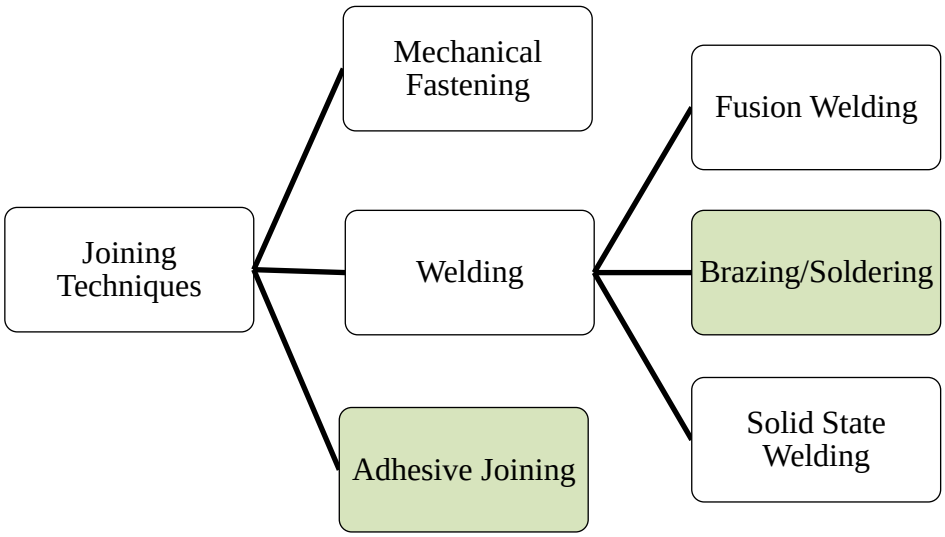

Figure 1-1 Classification of Joining Techniques: highlighted, those used in this work.

In this study, the joining of dissimilar materials was carried out mainly using brazing, soldering and adhesive joining techniques. The joining techniques were selected on the basis of simplicity of operations, available lab facilities and most

importantly the possibility to join dissimilar materials (metal/metal, metal/non-metal, polymer/metals) preferably in a pressure less environment.

1.2.1.1 Mechanical Fastening

Mechanical fastening is a technique to join components using additional clamping components, such as screws and rivets without fusing the joining surfaces. Special operations are required for mechanical fastening prior to joining process like drilling of holes into the joining components, making screw thread etc. [11,16]. Mechanical joints utilise fasteners or integral devices, which help the structural components to mate together and to interfere on the macroscopic scale [17]. It is a simple, save operational time and additional efforts like surface preparations or surface treatments before joining and most importantly it is a cold process which significantly decreases the energy cost during production [17].

In mechanical fastening, the joint configuration depends on end use of the component and the properties of dissimilar joining components. For example, some joints are made to tolerate thermal strain mismatch, while some are designed to allow complete freedom of movement. The joining of dissimilar materials such as metal to polymers or ceramics using integral mechanical attachments and/or mechanical fastening is possible. The integral attachment requires grooves and dovetails while mechanical fastening require rivets and bolts to provide interlocking [18].

However, mechanical fastening does have limitations. It increases the weight of the component, making holes in the joining components which affects the mechanical properties of the structure, induce localised stresses and corrosion related problems [19].

1.2.1.2 Fusion Welding

Fusion welding is a joining process in which the metal coalescence is created by melting a substrate and filler metal together, or by melting the base metal alone [20]. Arc Welding, Resistance welding, laser beam welding and electron beam welding are the principal fusion welding techniques currently adopted in the industry.

Electric arc is used as a heat source which is struck between the workpieces and the tip of an electrode (consumable or non-consumable) to melt and join the components in an arc welding process [21].

In a resistance welding process, heat is generated by the resistance of the overlapping joining substrates, under pressure, to the flow of a heavy electric current for a short period of time [22].

Laser beam welding is used to join metal or thermoplastic components where a concentrated beam from a solid state or gas laser provides heat for coalescence [23].

Electron beam welding utilises a beam of high-velocity electrons to generate heat across the joining substrates. The kinetic energy of electrons transforms into heat upon impact with the joining pieces [24].

Fusion welding techniques rely on the melting of joining substrates therefore are relatively restricted to the joining of materials with similar composition and thermal properties. Another disadvantage of fusion welding processes is the heat affected zone around the joined area due to the high-temperature phase transitions inherited to these processes however, the improved techniques such as electron beam welding or laser beam welding, often minimize this effect by introducing comparatively little heat into the work piece [25].

1.2.1.3 Solid State Welding

In principle, Solid state welding is a joining process, in which two work pieces are welded under a pressure providing coalescence at a temperature essentially below the melting point of the parent material. In this process melting of materials is not involved. The bonding of the materials is a result of diffusion of atoms at the interface. Ultrasonic and friction welding is the most famous forms of solid-state welding [26].

Solid state welding techniques are simple, cost effective and can produce strong joints with fine microstructure. In general, these joining techniques do not require filler materials, fluxes and shielding gases. It is also capable of joining dissimilar metals such as steel - aluminium alloy steel - copper alloy etc. [27].

However, the solid-state welding techniques are not suitable to join brittle non-metallic or porous metallic materials such as ceramics and metal foams due to high pressure process involved.

1.2.1.4 Brazing

According to the American Welding Society (AWS) definition; "*Brazing is a group of joining processes that produce the coalescence of materials by heating them to the brazing temperature in the presence of a brazing filler metal that has a liquidus temperature above 450ºC and below the solidus temperature of the base materials. The brazing filler metal is distributed between the closely fitted faying surfaces of the joint by capillary action*" [28].

Brazing is a joining technique where atomic-level bonding joins two similar or dissimilar components. It relies on the melting, spreading and solidification of brazing material. The joining materials are generally metals or metal alloys with relatively low melting point compared to the joining substrates and it serves as an intermediate material [28]. At the brazing temperature, the joining material melts only and forms metallurgical bonds while the joining substrates do not undergo melting [29].

Brazing processes used to join metals to ceramics can be further divided into following three main types.

- Active Metal Brazing
- Noble Metal Brazing
- Refractory Metal Brazing

Highly reactive metal such as titanium or zirconium-based alloys are used as joining materials in active metal brazing to form bonds by reacting with the non-metallic constituents of the ceramics. The active metal brazing operation is usually performed in an inert or vacuum environment to avoid oxidation because excessive oxygen reacts with the active elements in the braze filler and can compromise the joint strength [30].

Under special oxidizing conditions, noble metals such as platinum, palladium, or gold layer, 0.25–1.0 μm thick, is produced on joining substrates to avoid the underlying layer from oxidation which can prevent the wetting and flow of brazing filler during the noble metal brazing process [31].

Refractory metal brazing involves oxidation reaction between molybdenum salt and manganese to bond with ceramics [32].

Brazing can be carried out in the air or in a controlled atmosphere. Furnace brazing is suitable for brazing of dissimilar materials where controlled environment is generally a requirement. The brazing filler metal powder or foils are placed at the joint and then the assembly is placed in the furnace and heated to achieve a brazed joint.

1.2.1.5 Soldering

Soldering is a kind of brazing and can be differentiated by the fact that soldering fillers melt and flow at or below 450 ^{o}C. Like brazing, during soldering, the solder materials melt at a lower temperature compared to base materials to be joined. At soldering temperature, the diffusion of solder filler alloying elements into the base material takes place.

The performance of soldering depends on the cleanliness of the surfaces to be joined, the compatibility of the solder with both interfaces, differences in the CTE of the two materials and the differences in melting points [33]. A thin oxide layer immediately forms on most of the metal surface after cleaning. The oxide layer impedes the wetting by solder. The cleaned metal surfaces are usually covered with fluxes to avoid the formation of oxidation layer.

The selection of solder filler depends on the composition and properties of base materials to be joined. However, lead and tin-based alloy solders are usually used to join similar and dissimilar metals [34]. For the soldering of ceramics to metals, indium-based solders are very common because it wets virtually all ceramics and metals [35].

Sometimes ceramic composites are metallised using processes such as physical vapour deposition or sputtering to improve wetting and bonding. The ceramic materials that are not provided with metallic solderable coatings can be soldered only with active solders. The detailed studies of metal-ceramic soldering are reported in the literature [36,37].

1.2.1.6 Adhesive Joining

Adhesive joining is by far the universal joining technique offering high performance with a great design flexibility which can be easily integrated into industrial/mass production processes. The adhesive material is a non-metallic substance having an internal strength and capable of joining similar or dissimilar materials by surface bonding [38].

According to the American Welding Society (AWS) definition, the adhesive is "*A polymeric material having chemical and physical properties differing from those of the base materials, placed at their faying surfaces, to join the materials together as a result of the attractive forces of this polymeric material*" [39].

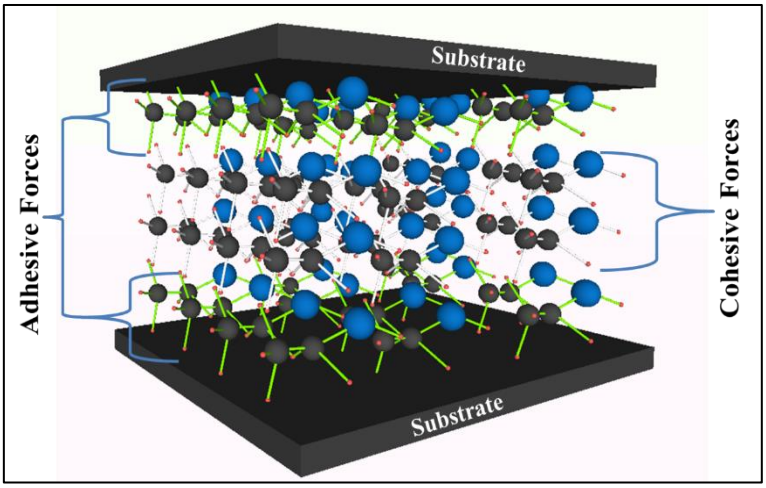

Figure 1-2 Distribution of forces in an adhesively bonded joint.

Adhesive materials adhere to the surfaces of the two joining substrates and develop a surface-to-surface bonding by transferring the forces from one adherent to another. The adherence of substrates to the adhesive is mainly due to adhesive forces while the adherence of adhesive molecules to its self is due to the cohesive forces, shown in Figure 1-2.

In general, substrates of different geometries, sizes and composition are bonded using adhesives. Following are main the three steps involved in adhesive joining process of dissimilar materials.

- Surface preparation of adherents
- Application of Adhesive to the surfaces
- Curing

The performance of an adhesive joint greatly depends on the nature of adhesive, joint configuration and joint thickness.

The performance of an adhesive joint greatly depends on the nature of adhesive, joint configuration and joint thickness. Adhesive bonding relies on the formation of intermolecular forces at the interface between the joining substrate and adhesive itself for a reliable joint formation. The surface contamination such as oil and grease significantly lower the surface energy of the adherents. The adhesives do not wet the surface, if the surface energy adhesive is higher than that of the adherents.

The use of adhesives enhances the resistance to impact and fatigue, reduces noise and vibration and eliminates the additional components such as screws, nuts and rivets etc. Adhesive joints display uniform distribution of stresses and avoid stress concentrations that can lead to joint fracture. It also reduces the galvanic corrosion potential associated with dissimilar metals joining.

Adhesive materials can be classified as natural and synthetic.

The natural adhesives are low cost and are generally used for low-stress applications. Natural adhesives can be of organic or inorganic nature. The organic adhesives are derived from natural organic sources such as tree gums, starch, collagen, soya flour etc. The inorganic adhesives are principally based on sodium silicate and magnesium oxychloride [40,41]. Most of the natural adhesive materials are now been replaced by synthetically made adhesives.

The synthetic adhesives started with the discovery of phenolic resins in 1920 which was followed by epoxide resins and polyurethanes in 1940’s. Synthetic adhesives gradually replaced the natural adhesives. With the advancements in the field of polymer chemistry, adhesives are now designed according to the specifications of the joining surfaces to achieve the specific and/or improved joining properties [42].

The recent developments in this field have also been resolved the longstanding problems of extended curing times, lower joint strengths and the long-term durability of adhesive joints exposed to adverse environments [43]. Thermoplastic and thermoset are the two important subgroups of synthetic adhesives.

1.2.1.6.1 Thermoplastic Adhesives

Thermoplastic materials are composed of linear or branched polymer molecules structures linked by intermolecular interactions or Van Der Waals forces. If the polymer chains are packed in an orderly manner, it will give a crystalline structure which gives high strength otherwise amorphous structure is achieved which shows poor strength properties. Thermoplastic adhesives are recyclable because once they cross-link can be reversed by applying heat or pressure.

Polyamides, Acrylates, Cyanoacrylates, vinyl and non-vulcanizing neoprene rubbers based thermoplastic adhesives are generally used to bond metals, glasses and porous materials [44].

1.2.1.6.2 Thermoset Adhesives

Thermoset materials are composed of highly cross-linked and chemically bonded polymer chains and display higher mechanical properties compared to thermoplastic materials. Unlike thermoplastics, thermosetting adhesives once cured cannot be reversed and are generally used for higher temperature service [45].

Some of the most important adhesives currently used in industries are thermosetting resins. During curing they harden by polymerization, condensation or vulcanization. Thermosetting adhesives can be further classified as the phenolic-resin base and the epoxy-resin based adhesives.

1.2.1.6.2.1 Phenolic Adhesives

Phenolic adhesives are produced by the condensation of phenol and formaldehyde. These adhesives maintain structural integrity and dimensional stability when subjected to mechanical load and withstand high temperatures. Phenolic resins readily adhere to organic and inorganic surfaces. It has exceptional compatibility with cellulose fillers and is used as a binder for particle board, hardboard and plywood panels.

The major drawback of phenolic adhesives is that during curing (>100 ^{o}C) water is released which stays as vapour in the joint and is removed by applying pressure. The curing is, therefore, must be assisted by pressure to avoid moisture [46].

1.2.1.6.2.2 Epoxy Adhesives

The epoxy-based adhesives are the most versatile structural adhesives. They bond well to a variety of plastics, metals and glass surfaces. Epoxies can be easily modified to achieve desired mechanical properties. When cured, they display higher chemical and thermal stability and minimal shrinkage. Epoxy based adhesives are extensively used in automotive, marine and aerospace industries [42]

Epoxy adhesives are brittle in nature and are toughened when required by the addition of tougheners such as nitrile rubbers or urethane oligomers [47,48].

1.3 Joined Materials

1.3.1 Sandwich structures

Sandwich structures are composed of two thin, stiff and strong facing skins separated by a relatively thick and light core material. The facing skins are bonded to core material using adhesive, brazing/soldering or mechanical fastenings to allow the load transfer mechanism among the components [49].

Wood and cork are common natural cellular materials used as a core material in the past which are now replaced by the synthetic core materials such as synthetic honeycombs and porous foams. The unique properties of the cellular structure are exploited to absorb energy upon impact and maximise the stiffness per unit density of the composite structure [50].

1.3.2 Al-Foam

Al-foams are a cellular structure consisting of pores/cells with solid aluminium walls. Foams can be divided into open and closed cell foams. The Al-foams with sealed pores is termed as closed cell foams while those with open pore walls are termed as open-cell foams.

Al-foam can be produced either by foaming molten aluminium by introducing gasses or by foaming solid precursors containing a blowing agent [51]. Following are two most common production routes currently in practice to produce Al-foams by foaming Al-melt [52]:

- Foaming melts with blowing agents
- Foaming melts by gas injection

Production of Al-foams by foaming precursors involves an additional step to the process chain. The advantage of this process is that complex shapes can be achieved easily. Following are the three established production routes to make Al-foams by foaming precursor [53].

- Foaming of powder compacts
- Foaming thixo-cast precursor material
- Foaming of ingots containing blowing agents

The Al-foams offer high stiffness in conjunction with low weight and due to its high energy absorbance capacity, they can go under large deformations at a constant stress. Al-foams are very effective in terms of electromagnetic shielding and

structural damping and absorb impacts regardless of direction. Al-foams are non-flammable and 100 % recyclable materials [54].

1.3.3 Al-Honeycomb

Honeycombs are lightweight materials and have the geometry of natural honeycomb. They are composed of regular and periodically repeated arrays of hexagonal hollow cells formed between thin vertical walls. Al-honeycombs are generally used as core materials in sandwich structural composites and display relatively higher out-of-plane compression and out-of-plane shear properties [55].

The manufacturing of Al-honeycomb core material is carried out using following two methods [55]:

- Expansion method
- Corrugation method

The bonding can be carried out using brazing, resistance welding, diffusion bonding and thermal fusion if the cores are supposed to be used at higher temperatures. The unique properties of honeycomb cores such as high stiffness to weight ratio, fire retardancy, superior insulation and design flexibility make these materials a preferred choice for applications in the fields of aerospace, shipbuilding, automobiles, construction, energy absorber, thermal isolators and packaging etc. [55,56].

1.3.4 Fibre Reinforced Polymers (FRP)

Fibre reinforced polymer (FRP) is composed of a polymer matrix reinforced with natural or synthetic fibres. The combination of polymer with a reinforcement results in a composite material with unique properties that are unattainable with the monolithic component.

Epoxy, polyester or vinyl ester and phenol formaldehyde resins are the most common polymers used as a matrix in FRPs. Natural fibres such as jute or sisal etc. [57] are used as reinforcements for low-cost applications, however, for high-end commercial applications such as aerospace and automotive industries, the synthetic fibres such as glass, aramid or carbon are employed as reinforcements [58]. There are three main steps involved in the production of FRP's:

- Reinforcement layup in the desired shape
- Matrix infiltration
- Curing

Several techniques are currently used to produce FRP. In the hand lay-up technique, the matrix is applied manually using rollers or by using spray guns. In the Vacuum Infusion Process (VIP), the preform is bagged in an air-tight sheet

while the resin is infiltrated using vacuum across the preform [59]. In the Resin Transfer Moulding (RTM) or Vacuum Assisted Resin Transfer Moulding (VARTM) technique, the reinforcement is placed in a single or two-piece mould where the resin is injected under pressure. Pultrusion is a technique which enables a continuous production of FRP's. The fibres are pulled through a pool of resin and are then passed through a closed heated die for curing [60].

1.3.4.1 Carbon Fibre Reinforced Polymers (CFRP)

CFRP having carbon fibres as a reinforced are commonly referred as Carbon Fibre reinforced polymer composites (CFRP).

Carbon fibres are extensively used in form of continuous fibres, roving, woven fabrics and chopped fibres in CFRP composites for their excellent mechanical properties, low density, high thermal and chemical stability, excellent creep and high electrical conductivity [61,62].

1.3.4.2 Glass Fibre Reinforced Polymers (GFRP)

The FRP containing glass fibres as reinforcement is generally termed as Glass Fibre Reinforced Polymer composites (GFRP). The types of glass fibres commonly used in GFRP are based on its properties such as E-Glass fibres displays improved electrical insolation, C-Glass fibres show high chemical resistance and S-glass fibres are used when high mechanical strength is required [63].

Glass fibres are lightweight, strong and robust reinforcement materials and are obtained starting from quartz sand, sodium sulphate, potassium oxide, soda and several refining and dying agents. Glass fibres are less stiff and much less expensive compared to carbon fibres.

1.3.5 Ceramic Matrix Composites (CMC)

Ceramics are non-metallic and inorganic materials made up of metal and non-metal or metalloid atoms typically held in ionic and covalent bonds. They show high modulus and hardness, high melting point and high corrosion resistance properties. However, ceramics are usually brittle in nature and display poor fracture toughness. Therefore, the ceramic matrix is reinforced with fibres (mostly SiC or C fibres) to improve toughness and are termed as ceramic matrix composites (CMC).

1.3.5.1 SiC Based CMC

The SiC/SiC composites are composed of SiC matrix reinforced with SiC fibres while the C/SiC composites have a SiC matrix reinforced with carbon fibres.

In general, the production of CMC involves three steps. In the first step, the reinforcement material is laid in a mould of the desired shape of a component. In the second step, the matrix is infiltrated. The third step mainly involves the final

machining (grinding, drilling, lapping or milling) and coatings to cover the porosities if required [64]. Several manufacturing routes are available to make CMC's which can be differentiated based on the method adopted for matrix infiltration. The three major routes currently in practice to produce CMC are listed below [65]:

- Gas phase route
- Liquid phase route
- Ceramic route

SiC-based ceramic composites have the potential to withstand about 1500 ^{o}C service temperature [64].

1.3.6 Metals

The Ti6Al4V, Al-6016 and Al-7046 alloys used in this study are the most commonly used metal alloys in automotive and aerospace industries.

1.3.6.1 Titanium alloy (Ti6Al4V)

Titanium is a light-weight, high strength metal with outstanding corrosion resistance properties. Titanium is mostly used in its alloy form. Ti6Al4V is one of the most used titanium alloys due to its machinability and excellent mechanical properties [66].

Ti6Al4V is an alpha-beta ($\alpha + \beta$) alloy. The aluminium in Ti6Al4V acts as α phase stabilizer while the vanadium stabilizes the β phase. The microstructure of Ti-6Al-4V alloy is composed of a low-temperature hexagonal close-packed (hcp) α phase, and a high-temperature body-centred cubic (bcc) β phase [67,68].

1.3.6.2 Aluminium alloys

Aluminium is the third most plentiful element on our planet. It is 100 % recyclable, lightweight, strong, nonmagnetic, and nontoxic material. Pure aluminium is relatively soft and is therefore alloyed with one or more elements such as boron, copper, zinc, manganese, magnesium, tin, silicon or lithium for improved properties. Alloying elements are added to aluminium mainly for two reasons: the precipitation hardening and the control of matrix microstructure [69].

Aluminium is highly corrosion resistant due to its natural ability to generate a protective oxide layer on the surface. It is ductile and can be deep drawn into complex shapes with ease.

1.4 Applications

The applications of Al-foam sandwich composites with FRP skins or Al-skins are widespread. They are used in car crash boxes, car engine compartment insulation, aeroplanes and cruise ships floorings, trains compartments and floorings, insulated fuel storage tanks, refrigerated truck and railroad containers, tunnels and building insulation, cover boxes of electronic devices emitting electromagnetic waves, lightweight transport and aerospace vehicle structures, impact resistant and shockproof military vehicles etc. [70–72].

CFRPs offers weight reduction, strength improvement and superior styling to the automotive industry. CFRP is also a currently preferred material for lightweight drones and aircrafts structures, windmills, turbine blades, light pressure vessels, satellites, offshore platforms, drilling risers and sports goods etc. [73]. GFRP have found applications in aerospace, marine, automotive, oil and gas pipelines, pressure vessels, military armours and civil industries [72].

Ceramic matrix composites materials have found extensive applications such as thermo-structural materials for heat exchangers in rocket and jet engines [74] gas turbines in power plants, heat shields in space vehicles and inner walls of the plasma chamber of nuclear fusion reaction [75] brake disks for high-end cars [76] etc.

Ti6Al4V has found extensive applications in aircraft, automotive and aerospace industries such as aircraft turbine engine and structural components, aerospace fasteners; high-performance automobile parts, medical devices and sports gears etc [77,78].

Chapter 2

2. Joining of Fibre Reinforced Polymer (FRP) Skins to Al-foam and Al-honeycomb

2.1 Abstract

Material manufacturers and engineering structure designers are currently focusing new ways to exploit the benefits of hybrid materials with improved properties at a low cost. In this study, using two different core materials (Al-foam or Al-Honeycomb) and three types of fibre reinforced polymer facing skins, sandwich composites were produced in 6 different configurations. The response of both core materials to compression load was compared independently. The flexural behaviour of Al-foam Sandwich (AFS) panels was compared with Al-Honey comb sandwich (HCS) panels.

Improvement in bending strength was observed when MWCNTs were added to CFRP-facing skins. Compared to FRP-honeycomb sandwich panels, FRP-Al-foam sandwich panels displayed around 25 % and around 65 % higher flexural properties in a long and short span three-point bending tests respectively.

Key Words: CFRP, GFRP, Sandwich composites, Al-foam, Al-Honeycomb, Flexural properties.

2.2 Graphical Abstract

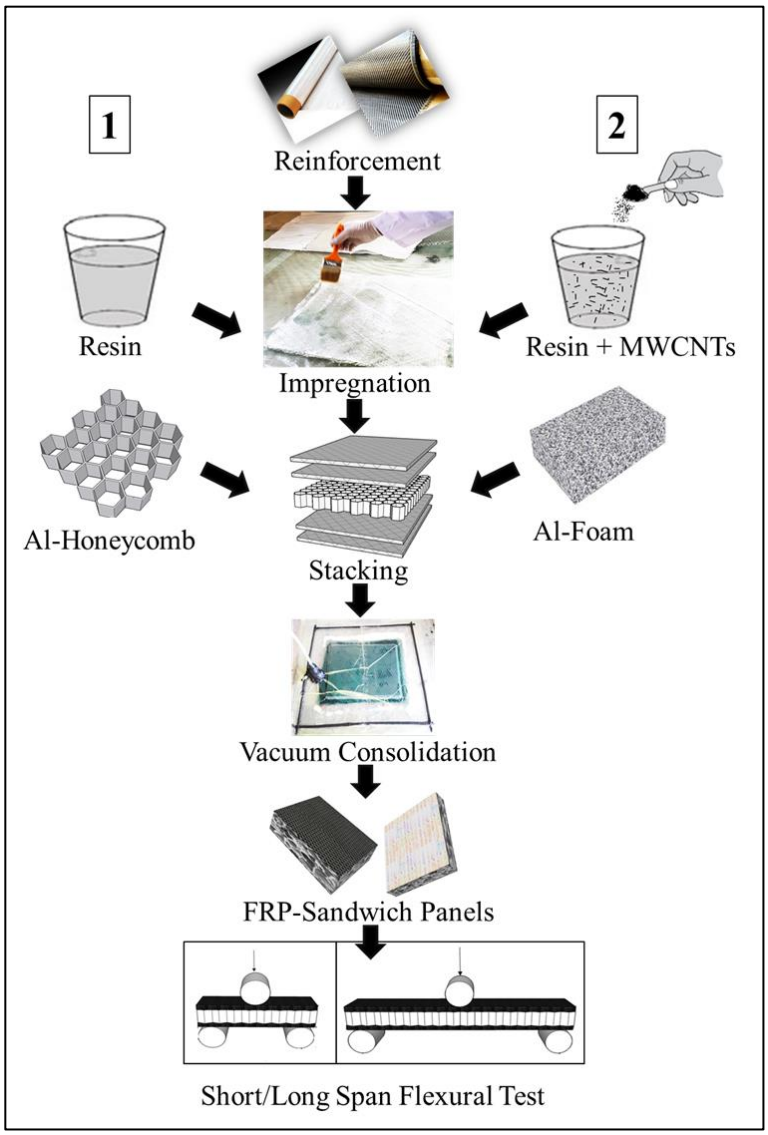

Abbreviations	**Meaning**
FRP	Fibre Reinforced Polymer
CFRP	Carbon Fibre Reinforced Polymer
CFRE	Carbon Fibre Reinforced Epoxy
GFRP	Glass Fibre Reinforced Polymer
GFRE	Glass Fibre Reinforced Epoxy
AFS	Aluminium foam sandwich
HCS	Aluminium honeycomb sandwich
MWCNTs	Multiwall carbon Nano-tubes
LS	Long span
SS	Short span
Symbols	Meaning
m	Mass [g]
v	Volume [cm^3]
l	Length [mm]

b	Width [mm]
t	Thickness [mm]
t_s	Sandwich panel thickness
t_c	Core material thickness
t_f	Facing skin thickness
σ	Stress [MPa]
σ_c	Compression stress [MPa]
ε	Strain [%]
$\boldsymbol{\sigma_c^{2\%}}$	Stress at 2% deflection [MPa]
E_c	Compressive modulus [MPa]
W	Energy [J]
eff	Efficiency [%]
FVF	Fibre volume fraction [%]
ρ	Density [g/cm^3]
L	Cross head displacement / Deformation [mm]
F	Load / Force [N]

E_f	Flexural elastic modulus
d	Sandwich thickness [mm]
c	Core material thickness [mm]

2.3 Introduction

Composite sandwich panels are currently in demand due to their lightweight, low cost and excellent mechanical properties for applications in construction, marine, automotive and aerospace industries. Unlike metals high-performance Fibre Reinforced Polymers (FRPs) have displayed great potential in eliminating the corrosion concerns. These materials offer low maintenance and a longer life-span in construction, automotive, marine and aerospace applications [79–83].

Most of the previous work regarding sandwich panel is concerned with polymeric foams or wood as a core material [84,85]. The increasing demand for sandwich composites in engineering structures has led the researchers to produce novel sandwich composite structures with lightweight metallic materials in the core [49]. Gibson et al [86] reported a thorough overview of the literature on metallic cellular materials. Polymeric foam sandwich structures are indicated to be inferior to honeycomb and other core concepts such as metal-foams and corrugated structures [87]. Yet the honeycomb materials are quite expensive with respect to alternative polymeric foams or balsa wood core materials [88].

2.3.1 Al-foam vs Al-honeycomb

Al-foam is a low cost, lightweight, non-flammable porous metallic material with high energy absorption, excellent sound absorptivity, electromagnetic pulse shielding and lower conductivity than bulk aluminium [89–91]. It can potentially replace the Al-honeycomb as a core material which is focused in this chapter. Furthermore, Al-foam has higher potential surface area available for joining compared to honeycomb and show higher load bearing and energy absorbance capability which makes it a suitable for heavy duty applications. Sandwich structure with Al-foam as a core material can be easily incorporated into the curved or complex shapes and can sustain hot [49] and humid [92] working conditions compared to the Al-honeycomb core.

2.3.2 Effect of MWCNTs on FRP laminates

Carbon Nanotubes (CNTs) are widely acknowledged for strengthening the mechanical properties of the fibre reinforced laminates [93]. Qian et al [94] reported that addition of only 1% of CNTs by weight in a matrix material can increase the

stiffness of CFRPs by ~40% and the tensile strength by ~25%. Improved results can be achieved using Single Wall Carbon Nano Tubes (SWCNTs), however, MWCNTs are preferred in this study for its low cost (~100 times less than the SWCNTs [95]), easy production and easy dispersion [96] into the polymer matrix. Moreover, MWCNTs and MWCNTs-g-carbon precursors using COOH functionalized MWCNTs with PAN display higher thermal stability (up to 850 ^{o}C) and improved UV absorption [97].

2.3.3 Sandwich Composites flexural collapse behaviour

In the recent past, several researchers performed theoretical and practical analysis regarding the collapse mechanisms of AFS and HCS panels under static three-point bending [98,99]. Petras et al. [100] studied the failure modes of GFRP/Nomex honeycomb core sandwich panels in a three-point bending configuration and reported that the maximum failure load is influenced by the thickness and density of skin and core materials while span length was observed as the main test parameter which influences the flexural behaviour.

Mohr et al. [101] studied the deformation induced in monolithic honeycomb structures and observed that under a large deformation, Al-honeycombs also exhibit microstructural heterogeneity such as Al-foam. In a three-point bending test configuration, Sandwich beams with metal foam core fail due to face yield, core shear, indentation and face wrinkling [98]. The failure and collapse behaviour of AFS beams depends on the core thickness, loading velocity and the span length [102–104].

Abbadi et al. [105] studied the effect of core material density and type of Al-foam on the mechanical properties of sandwich composites. They suggested that increase in the density of the core material induces an increase in the stiffness of the sandwich structure while the architecture of the core material influences the collapse behaviour. Gupta et al. [106] found that the microstructure of core material influences the flexural properties of the sandwich structure.

To the best of our knowledge, the comparative study of the flexural behaviour of Al-honeycomb and Al-foam sandwich composites having similar thickness and facing skins has not yet established which is focused in this research activity.

In this study, the development and flexural characterization of Al-foam and Al-honey comb sandwich panels with glass and carbon fabric reinforced polymeric skins was carried out. The effect of MWCNTs on the flexural behaviour of CFRP facing skins in sandwich panels was experimented. All the sandwich panels were produced by in-situ fabrication of sandwich panels technique. The facing skins, the core materials and the sandwich panels were characterised by flexural properties using three-point bending test adopting short and long span three-point bending

assemblies. The results were analysed and a comparison between the flexural behaviour of different types of sandwich panels was established.

2.4 Experimental Work

2.4.1 Materials

DURATEK 1000 resin system, supplied by Duratek, Turkey, suitable for open mould lamination processes, small parts and quick production cycles was used as a matrix material. DTE 1000 + DTS 1100 resin system shows 1.10 ± 0.05 g/cm^3 density, 950 ± 100 cP viscosity and 40 ± 5 minutes pot life at room temperature [107].

MWCNTs were supplied by Cheap Tubes Inc., USA. MWCNTs had the outer diameter of 30÷50 nm and an average length ranging from 10÷20 μm.

Al-foam and Al-Honeycomb panels were used as core materials in sandwich composites. Closed cell, Al-foam plates were supplied by Vaber, Italy in the form of 900 mm x 600 mm x 9 mm foam panels. The average density of the Al-foam was 0.28 g/cm^3 (measured as mass/volume). The distribution of cells in the Al-foam was non-homogenous. Macrographs of 25 Al-foam samples of dimension 30 mm x 20 mm x 9 mm were analysed using the free digital image analysis software (Image-J) to figure out a reasonable average pore size and distribution of the as-received Al-foam.

Figure 2-1 (a) and (b) represents the surface and cross-sectional views of the as-received Al-foam. Figure 2-1 (c) shows a representative Al-foam specimen englobed in resin and Figure 2-1 (d) represents the analysed image of the same specimen after using the Image-J software.

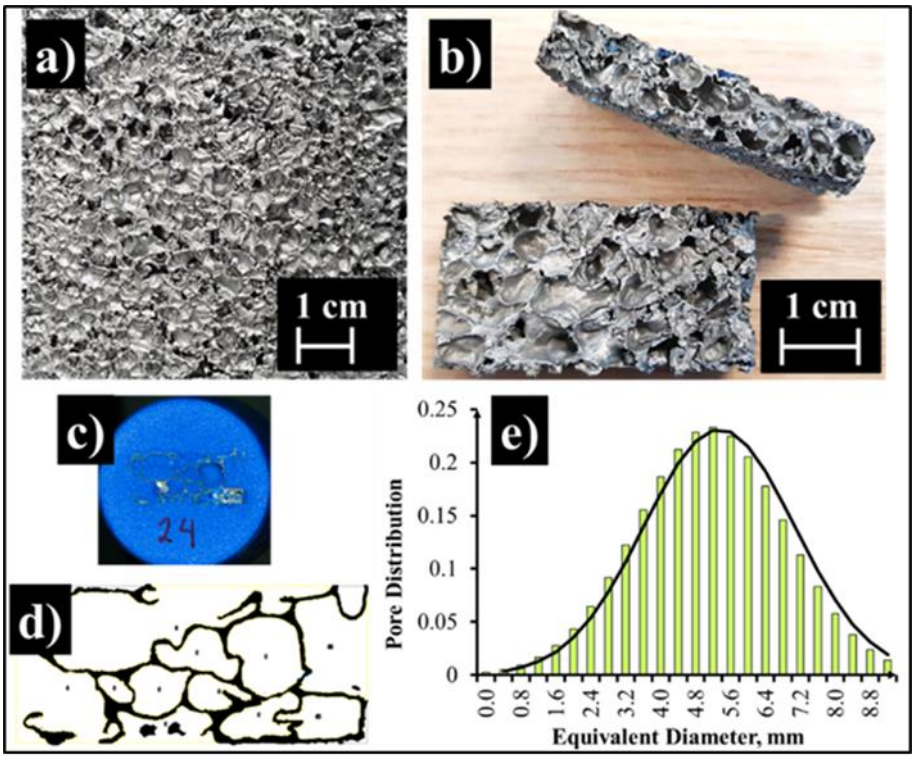

Figure 2-1 (a) Al-foam surface morphology, (b) Al-Foam front and cross-section views, (c) Al-foam specimen cross-section, englobed for analysis, (d) Image analysed using Image-J software, (e) Al-foam pore size distribution-Bell curve.

The equivalent pore diameter calculated was 5.2 mm ± 1.5 mm and the pores distribution of the Al-foam samples fits into a bell shape curve, Figure 2-1 (e). The surface Al-foam cell walls, which constitute the potential joining area, was around 12.8 % of the total theoretical surface area. In the sandwich structure, the numbers of cell walls at the surface of Al-foam are directly proportional to the available area for joining to the facing skins.

Al-Honeycomb (density = 0.018 g/cm^3 (m/v)) was supplied by Thales Alenia Space, France. Figure 2-2 (a) shows the as received Al-honeycomb surface and Figure 2-2 (b) represents the scheme of its dimensional specifications. The area of the hexagonally shaped honeycomb pore was calculated 93.53 mm^2 and its perimeter was found 36 mm.

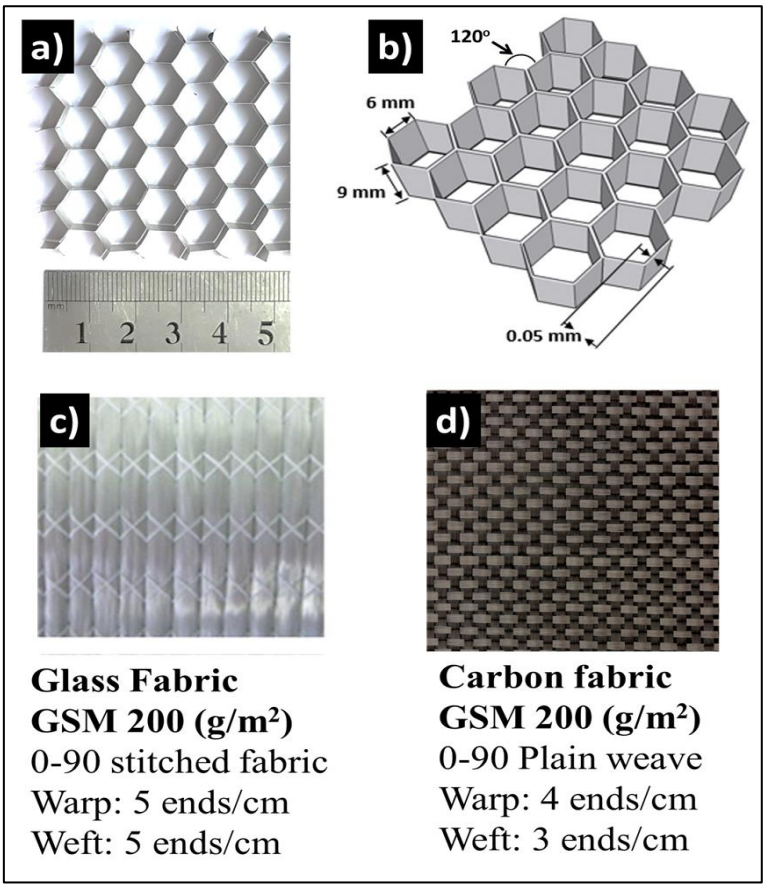

Figure 2-2. (a) Al-Honeycomb Surface, (b) Al-Honeycomb specifications, (c) Glass fabric (d) Carbon fabric.

Carbon and Glass fibre fabrics are the most common reinforcement materials which are currently used in composites manufacturing industries. Carbon fibre fabric 0-90° with plain weave architecture (GSM-200) supplied by Spintex, Turkey and 0-90° stitched Glass fabric (GSM-200), supplied by Resintex, Italy, were used as reinforcements in the facing (sheet) skins of sandwich panels. Both the fabrics had a weight of 200 g/m^2. The front images and specifications of the reinforcement materials used in this study to produce FRP-sandwich panels are reported in Figure 2-2 (c) and (d).

2.4.2 FRP-Sandwich Composites Preparation

100 parts of DTE 1000 resin by weight were mixed with 35 parts of fast hardener DTS 1100 (100:39 parts by volume) to impregnate the fabric reinforcement. Figure 2-3 shows, the two resin preparation processes adopted to produce the FRP sandwich panels in this study.

To improve the flexural properties of the CFRP-skins, 0.1 wt.% of COOH functionalized Multi-Walled Carbon Nano Tubes (MWCNTs) were added to the epoxy resin. MWCNTs were dispersed in epoxy resin using Hielscher UP 400S 400W sonicator equipped with H3 sonotrode (tip diameter = 3 mm) in a soundproof box. Sonication was carried out for 1 hour at 0.5 Hz frequency and 60 % amplitude.

MWCNT's were added to the epoxy resin prior to resin/hardener addition, as shown in Figure 2-3 (Process 2).

The epoxy resins with and without MWCNTs were degassed for 30 minutes to remove the air bubbles produced during mixing prior to use.

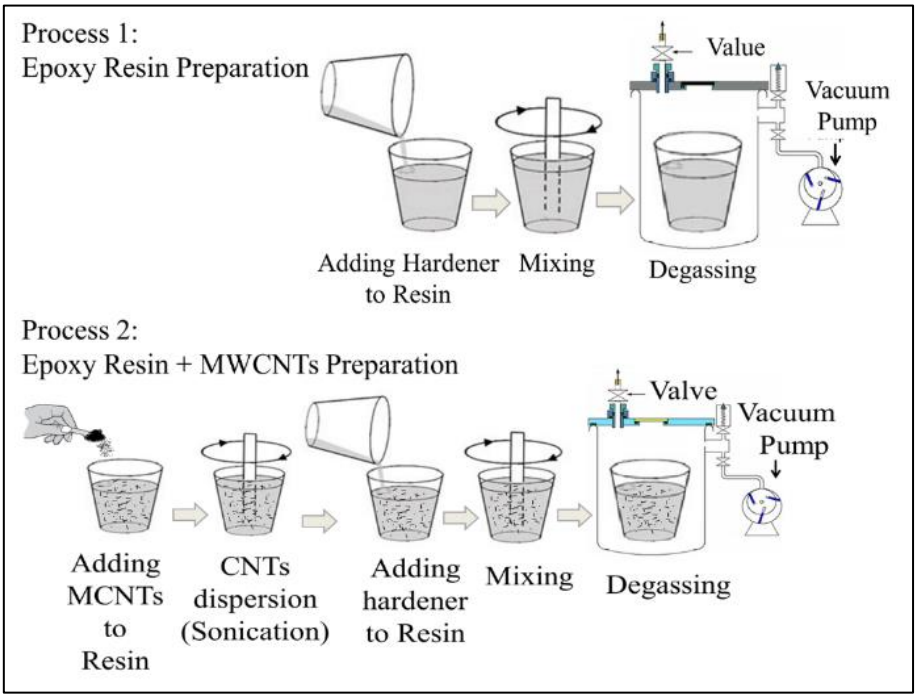

Figure 2-3. (Process 1) Epoxy resin preparation process, (Process 2) Addition of MWCNTs to epoxy resin.

Figure 2-4 shows the step by step process of the FRP sandwich fabrication adopted in this study. The base materials (reinforcements and the core materials) were first cut off in the dimensions, 350 mm x 250 mm from the larger sheets.

The reinforcement layers were impregnated with resin using hand layup method. Facing skins were produced in the following three configurations:

- 2-layered Glass Fabric Reinforced Epoxy (GFRP) face sheets.
- 2-layered Carbon Fabric Reinforced Epoxy (CFRP) face sheet.
- 2-layered Carbon Fabric Reinforced Epoxy + MWCNTs (CFRP+MWCNTs) face sheets.

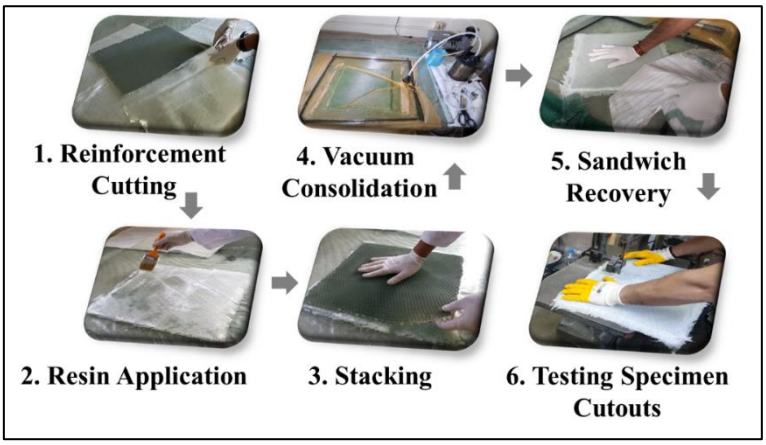

Figure 2-4. Steps followed during the in-situ fabrication of FRP sandwich panels.

The impregnated reinforcement layers and the core materials were stacked in six different sandwich configurations, as shown in Figure 2-5. Each stacking was then covered with peel ply, flow mesh, breather fabric and was sealed in a polyurethane bag for vacuum consolidation to avoid bubbles in the facing skins and to achieve improved compaction.

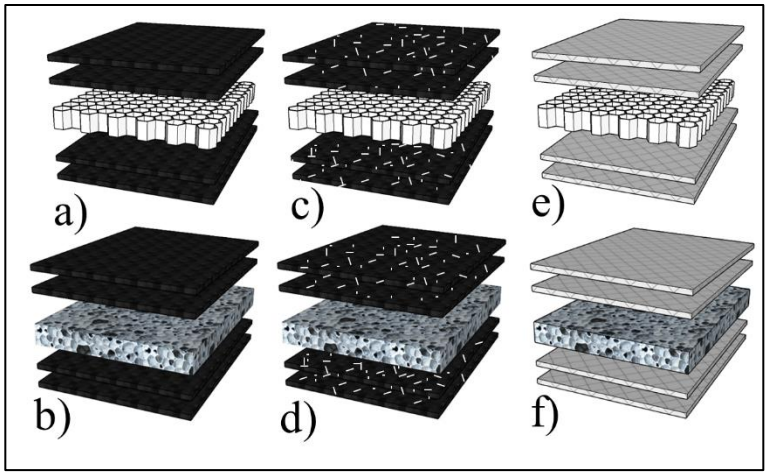

Figure 2-5. Sandwich panels stacking configurations. (a) 2CFRP/HC/2CFRP, (b) 2CFRP+MWCNTs/HC/2CFRP+MWCNTs, (c) 2GFRP/HC/2GFRP, (d) 2CFRP/AF/2CFRP, (e) 2CFRP+MWCNTs/AF/2CFRP+MWCNTs, (f) 2GFRP/AF/2GFRP.

The peel ply was used to remove the bagging with ease from the cured composite panels, flow mesh helps in the even distribution of resin across the composite surface under vacuum and the breather fabric helps in absorbing the excess resin. The sandwich panels were recovered after a curing cycle of 4 hrs consolidation (at room temperature) under vacuum and 24 hrs without vacuum (at room temperature). By combining 3 types of facing skins and 2 types of core material in the configuration shown in Figure 2-5, in total six sandwich panels, each of dimension 350 mm x 250 mm, were produced.

The GFRP-AFS and GFRP-honeycomb sandwich composites were produced and characterized in *Politecnico di Torino, Italy* and the CFRP-AFS and CFRP-honeycomb sandwich composites were produced and characterized in *Istanbul Technical University, Turkey*.

2.4.3 Characterisation

2.4.3.1 Core materials compression

Three specimens of dimension 50 mm x 50 mm x 9 mm, of each core material (Al-foam and the Al-Honeycomb) were subjected to a flatwise compression load to analyse their energy absorbance capacity and ASTM C365/365M [108] standard procedure was followed. The loading was carried out at a rate of 4 mm/min. Compression tests were conducted using Shimadzu universal testing machine equipped with a 50 kN load cell at room temperature (25 ^{o}C) and 65% humidity.

The stress-strain curve (σ_c - ε_c) was obtained from the recorded load and punch displacement values using Eq. 1 and Eq.2 [109].

- stress σ_c [MPa]

$$\sigma_c = \frac{F}{A} \text{ [MPa]} \qquad \text{Eq. 1}$$

- strain ε_c [%]

$$\in = \frac{\Delta t}{t} 100 \text{ [\%]} \qquad \text{Eq.2}$$

- Collapse stress σ_{cs} [MPa]

$$\sigma_{cs} = \frac{F_{\max elastic}}{A} \text{ [MPa]} \qquad \text{Eq. 3}$$

- core flatwise compressive chord modulus, E_c [MPa]

$$E_c = \frac{(P_{0.003} - P_{0.001}).t}{(\delta_{0.003} - \delta_{0.001}).A} \text{ [MPa]} \qquad \text{Eq. 4}$$

- Energy W [J]

$$W = \int_0^L F(L)dL \qquad \text{Eq. 5}$$

The stress value at which the deformation initiates in the core material under compression is defined as collapse stress and was calculated using Eq. 3. Core flatwise compressive chord modulus was determined using Eq. 4, which is also the slope of the linear elastic region. The energy absorbance capacity of the core materials is the area below the curve and was determined using Eq. 5. The average energy absorbed in the elastic regime is defined as elastic energy and the average

energy absorbed by the core material when the strain value reaches around 2% of the yield energy.

2.4.3.2 Flexural Analysis

Flexural properties of the sandwich composites were determined using both long and short span (specimen dimensions are reported in Table 2-1) three-point bending tests. ASTM C-393 [109] was followed to analyse the flexural properties of the sandwich composites using long and short span three-point bending assembly, as demonstrated by Ubertalli et al [49].

Three specimens of each of the facing skins were subjected to three-point bending test to analyse the flexural behaviour of FRP facing skins and the effect of MWCNTs addition on the flexural properties of the CFRP skins.

Three specimens of each FRP-Sandwich composite were subjected to three-point bending tests to analyse their flexural behaviour at different span lengths. Figure 2-6 shows the three-point bending assembly configurations and the test parameters. The dimension of the flexural test specimens is reported in Table 2-1.

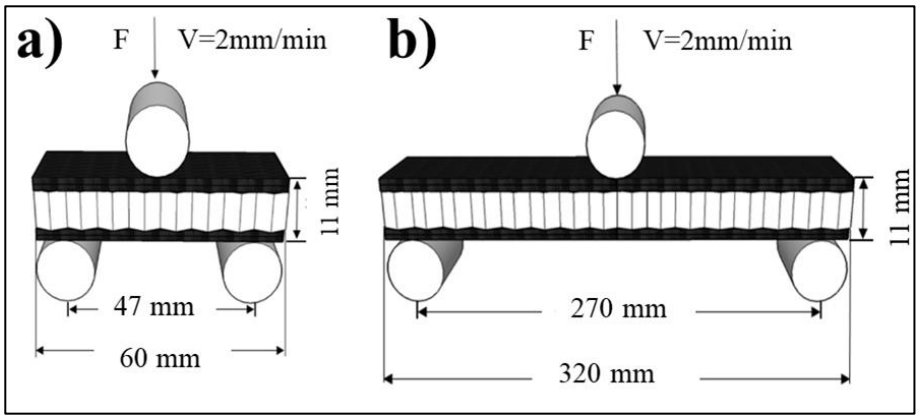

Figure 2-6. Three-point test assemblies and geometrical parameters, (a) Short span three-point bending assembly, (b) Long span three-point bending assembly.

The flexural tests were conducted using Shimadzu universal testing machine equipped with a 50 kN load cell at room temperature and 65% humidity. The bending and collapse behaviour of the sandwich panels at different span lengths as well as the fracture initiation and propagation during loading were recorded using a digital video and a still images camera to evidence the failure modes.

Table 2-1 Average three-point bending test specimen dimensions.

Test Specimen	Short Span		Long Span		$t_{s,}$ [mm]	$t_{c,}$ [mm]	$t_{f,}$ [mm]	ρ, [g/cm^3]
	l, [mm]	b, [mm]	l, [mm]	b, [mm]				
GFRP Skin	62.3	21.8	-	-	0.99	-	0.99	1.08

CFRP Skin	61.13	20.23	-	-	0.63	-	0.63	0.99
CFRP-MWCNTs-Skin	60.2	20.08	-	-	0.68	-	0.68	-
GFRP-AFS	61.84	21.53	315.7	41.61	10.05	9	0.95	0.58
CFRP-AFS	59.96	20.13	319.67	40.26	9.61	9	0.61	0.35
CFRP-MWCNTs-AFS	60.76	20.83	319.5	40.95	9.76	9	0.76	0.33
GFRP-HCS	61.23	21.81	323.73	41.25	10.97	9	1.97	0.28
CFRP-HCS	62.55	23.2	322.33	42.03	10.53	9	1.53	0.27
CFRP-MWCNTs-HCS	62.77	23.01	324.17	41.6	10.4	9	1.4	0.26

Flexural elastic modulus, core shear stress and facing bending stress were determined using the load-cross head displacement values recorded during the short and long span three-point bending tests using the following Eq. 6, Eq. 7 and Eq. 8 respectively (ASTM C-393 [109]).

Flexural elastic modulus, E_f = Slope of the elastic region Eq. 6

Core shear stress, $\sigma = \frac{PL}{2t(d+c)b}$ [MPa] Eq. 7

Facing bending stress, $\tau = \frac{P}{(d+c)b}$ [MPa] Eq. 8

where t is the facing thickness, d sandwich thickness, c core thickness, b sandwich width, P load, and L is the span length.

2.5 Results and Discussion

2.5.1 Compression Test (Core Materials)

Figure 2-7 shows the compression test assembly and the core materials specimens before and after the compression test. Figure 2-8 represents the behaviour of Al-foam and Al-Honeycomb subjected to a compression load. The average analysed values determined for both the core materials are reported in Table 2-2.

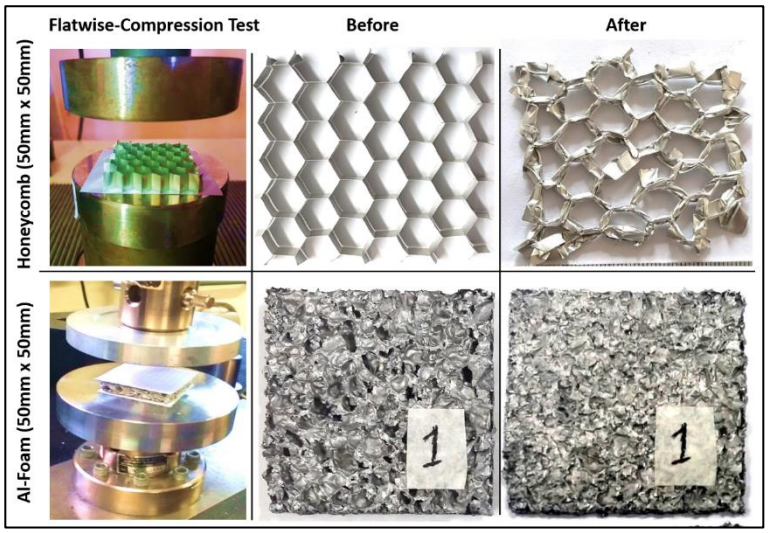

Figure 2-7. Compression test assembly and representative core material specimens before and after the compression test.

Both the core materials showed elastic behaviour in the first part of the curves where there is a linear relationship between stress and strain values. After the initial elastic behaviour, the Al-foam started plastic deformation followed by progressive crushing. A so-called plateau region was evidenced where the deformation rate is higher compared to increase in load. A bulking effect was observed after the so-called plateau region where most of the bigger cells collapsed, and upon further increase in the cross-head displacement, the Al-foam display behaviour like a massive/bulk metal sheet.

Scattering was observed in the curves in Figure 2-8 for Al-foam due to the non-homogeneity in the pore size and distribution compared to those in the Al-honeycomb.

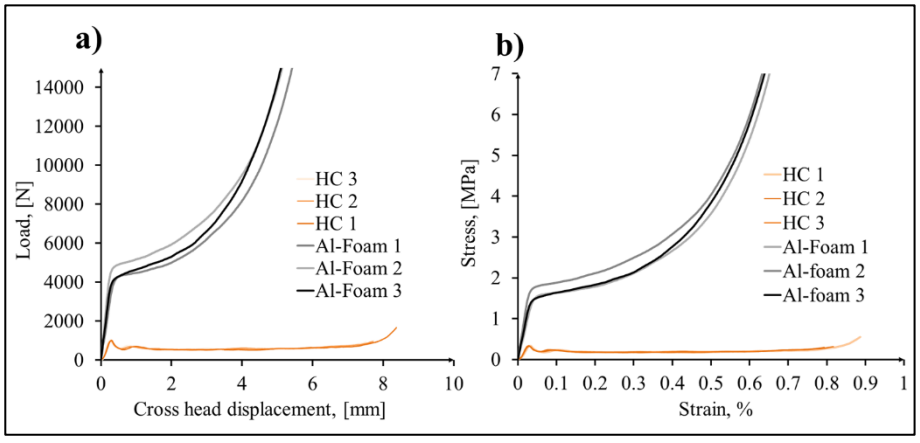

Figure 2-8. Compression test results for core materials. (a) Load vs Cross head displacement plot, (b) Stress vs Strain plot.

Deformation in the Al-honeycomb structure started when the load reached around 1000 N followed by a sharp drop of around 50% in the load. With further

increase in crosshead displacement, the sudden drop in the compression load was followed by a series of stress oscillations due to the bending of honeycomb cell walls where the load fluctuation was observed in the range 480 N to 550 N. The plateau continued as the crushing progressed till the cross-head displacement reached around 8 mm where the bulking behaviour of Al-honeycomb started.

In the elastic regime and till 2 % strain, the Al-foam structure showed around 6 times higher energy absorption capacity compared to Al-honeycomb. The density of Al-foam was around 15 times higher than Al-honeycomb, therefore during the flatwise compression loading, deformation in Al-foam started late and bulking effect was observed earlier compared to Al-honeycomb core of similar thickness.

Table 2-2. Average results for core materials subjected to flatwise compression test.

Specimen	Stress at 2% deflection [MPa]	Stress at 2%/ Yield [MPa]	Ultimate Stress [MPa]	Compression modulus [MPa]	Elastic energy [J]	Yield Energy [J]
Honeycomb	0.18	0.178	0.33	120.45	0.5	0.18
Al Foam	1.07	1.07	1.55	423.61	2.67	1.15

The plateau region mainly corresponds to the energy absorbing capacity of the core materials. Al-honeycomb displayed longer plateau at lower stress values while Al-foam displayed shorter plateau at higher stress values. The higher energy absorption properties, as observed, makes Al-foam more suitable core material compared to Al-honeycomb for heavy duty applications such as train compartments, buildings and tunnel insulation and car crash box etc.

2.5.2 Flexural Behaviour of FRP facing skins

In the long span bending configuration, the maximum bending load for both the GFRP and CFRP-skins subjected to transverse load was observed less than 2 N and produced highly scattered data, therefore, the results were not taken into consideration. While, the facing skins displayed noticeable bending strength when subjected to a transverse load in short span bending test configuration.

Figure 2-9 represents the flexural behaviour of facing skins subjected to a transverse load in short span three-point bending configuration. The CFRP facing skins showed improved elasticity and displayed failure at around 2 times higher bending load compared to GFRP facing skins. While CFRP-MWCNTs skins displayed around 12% higher bending load at failure in comparison to the CFRP skins, Figure 2-9.

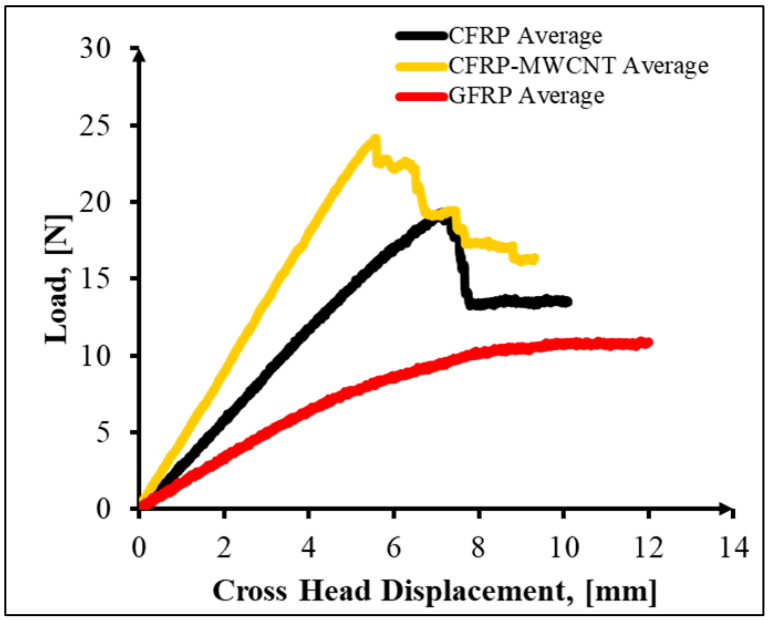

Figure 2-9. Flexural behaviour of facing skins subjected to short span three-point bending test.

After the maximum bending load value, the CFRP and the CFRP+MWCNTs facing skins responded with brittle failure at a relatively lower cross-head displacement compared to the GFRP skins. The sharp drop in the CFRP and CFRP-MWCNTs curves, in Figure 2-9, was mainly due to cracks in the matrix which appeared first at a point of loading followed by the fractures in the underlying fibres. No apparent cracks were observed in the GFRP skins during loading even when the cross-head displacement reached around 12 mm, where all the bending tests were stopped.

The increased stiffness of the CFRP-MWCNTs facing skins was due to the strengthening effect of nanoparticles dispersed in the matrix material. The MWCNTs increases the stiffness of the facing skin and hinders the propagation of cracks in the matrix [110]. The higher flexural strength of carbon reinforcement based facing skins with respect to GFRP ones is mainly due to the intrinsic properties of the respective reinforcement materials [111].

2.5.3 Flexural Behaviour of FRP-Sandwich Panels

Short Span Three Point Bending Test

Figure 2-10 shows the average behaviour of six types of sandwich panels specimens subjected to a flexural load in a short span three-point bending configuration. It was observed that the Sandwich panels with Al-foam in the core, in general, responded with higher flexural strength before failure and displayed improved energy absorbing capacity at higher stress levels compared to sandwich panels with Al-honeycomb core.

During the short span three-point bending test, FRP-HCS composite specimens responded initially with an elastic behaviour until the peak load reached. With further increase in crosshead displacement, immediately after the maximum load point, a noticeable drop (30 % - 40 %) in the bending load was observed mainly due to the cracks in the facing skins followed by the collapse of underlying honeycomb cell walls at a point of loading. The drop was followed by a so-called plateau corresponding to the crushing of cell walls and the shear across the core which was maintained at a load with slightly decreasing/increasing trend for an extended displacement till the core material fail.

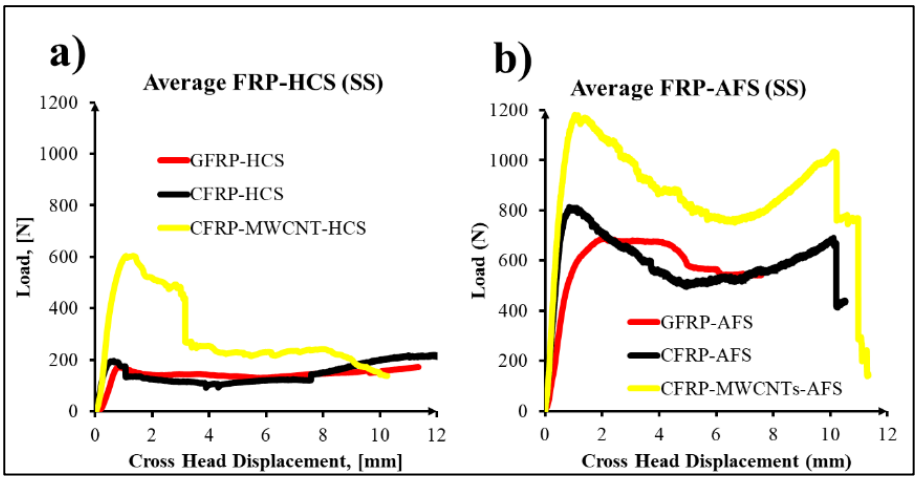

Figure 2-10. Flexural behaviour of FRP sandwich panel specimens subjected to short span three-point bending test.

Figure 2-11 shows the macro images of tested FRP-sandwich specimens in short span three-point bending configuration. After the maximum bending load, the CFRP+MWCNTs- and CFRP-HCS responded with core shear failure and the cracks are visible at the approximate midline of the core material. While a failure due to the collapse of the honeycomb cells at a point of loading was evident in the GFRP-HCS composite specimens, Figure 2-11. The GFRP-HCS specimens did not display evident shear in the core compared to CFRP-HCS specimens due to the relatively ductile nature of glass fibric reinforcements which resulted in a hinge formation at a point of loading. No delamination of composite laminates was observed.

CFRP- and CFRP+MWCNTs-AFS composite specimens after the initial elastic behaviour displayed a gradual decrease (~35 %) in load mainly due to cracks in the facing skins followed by the deformation of foam cells at the loading point and shear and shear across the core material. At around 5 mm cross head displacement the foam cells collapse reached the bulking point at a point of loading, which is evident by an increasing trend in the curves, Figure 2-10 (b). However, the shear deformation across the core continued with increasing load until a sharp drop appeared due the cracks in the Al-foam.

Unlike the sandwich composites with CFRP facing skins, the GFRP-AFS composite specimens did not show a sharp drop or decreasing trend in bending load after the elastic behaviour and maintained the maximum bending load for around 5 mm cross head displacement till the cracks appeared in the core material, evidenced by multiple peak drops, Figure 2-10 (f).

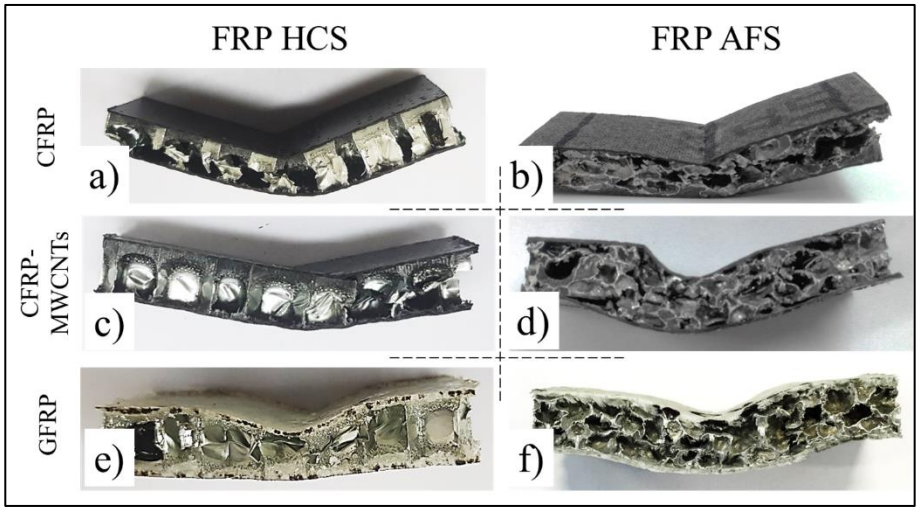

Figure 2-11. A cross-sectional view of the post short span three-point bending test sandwich panels specimens, (a), (c), (e) FRP-HCS and (b), (d), (f) FRP-AFS sandwich panels.

Figure 2-11, failure analysis reveals that CFRP-AFS specimens failed mainly due to excessive core stress and the GFRP-AFS due to deformation of facing skin and underlying foam cells at a point of loading. The failure in CFRP+MWCNTs-AFS was observed as a mix of excessive core shear failure and deformation in the facing skin and underlying foam cells at a point of loading. The relatively ductile behaviour of the GFRP facing skins of the sandwich composites resulted in hinge formation compared to the CFRP facing skins. The addition of MWCNTs to the CFRP facing, however, improved the ductility which resulted in failure with a mix hinge and cracks formation at a point of loading, Figure 2-11 (c) and (d).

Comparison of FRP-Sandwich Panels based on Short Span Three Point Bending Test

Figure 2-12 represents the comparison of the average flexural behaviour of the FRP-HCS and the FRP-AFS composite panels subjected to a transverse load in short span three-point bending configuration. Comparing the sandwich panels with similar core material but different facing skins, it was observed that, the CFRP-MWCNTs HSC specimens displayed around 70% higher bending load compared to CFRP- and GFRP-HCS specimens. The addition of MWCNTs to the CFRP skins in CFRP-MWCNTs-AFS resulted in around 31% improvement in the maximum bending load of the CFRP AFS sandwich specimens. The CFRP-AFS specimens showed around 16 % higher bending load at failure compare to GFRP-AFS.

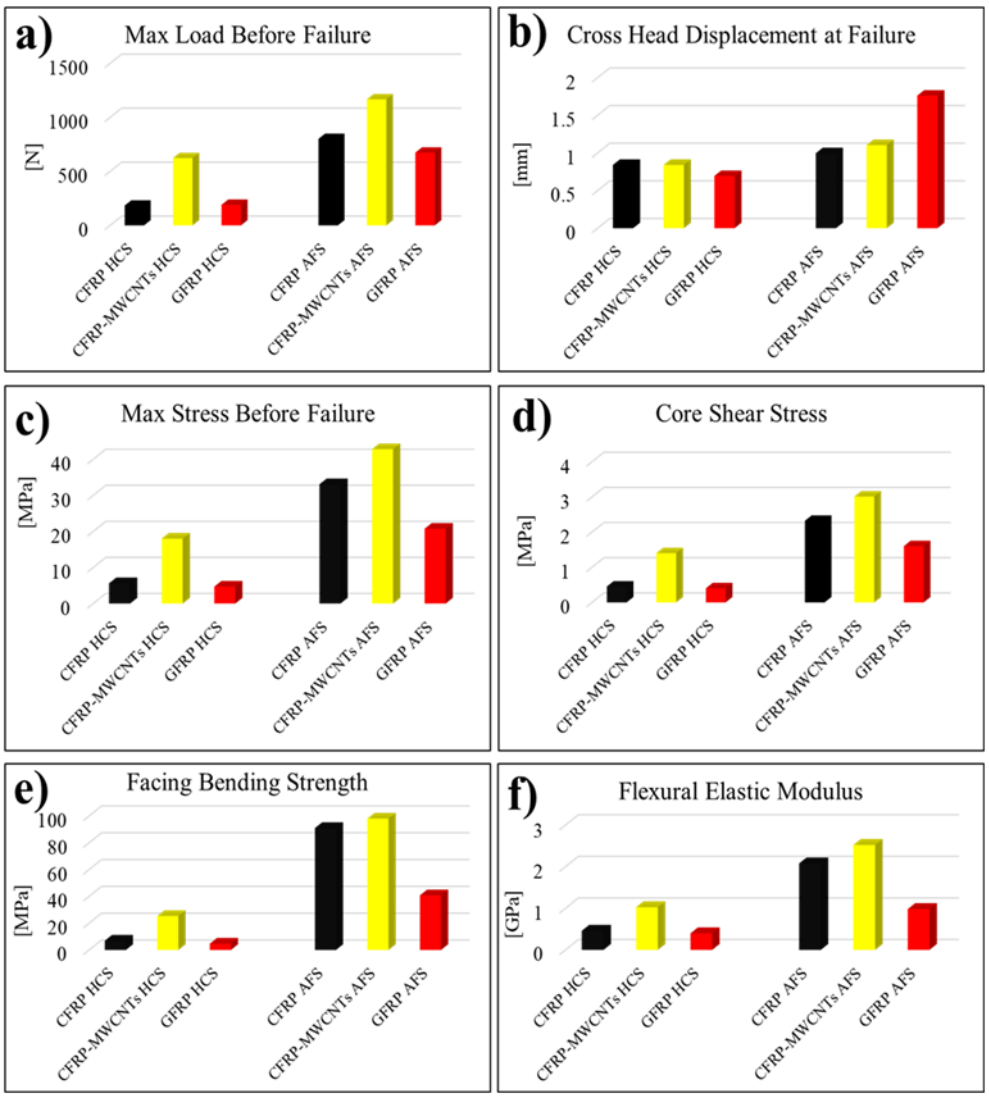

Figure 2-12. Analysis of FRP sandwich panels Flexural test data (Short span three-point bending).

Comparing sandwich panels with similar facing skins and dissimilar core material, the GFRP-AFS specimens displayed around 73 %, CFRP-AFS around 76 % and CFRP-MWCNTs-AFS around 48 % higher maximum bending load compared to sandwich panels with similar facing skins but honeycomb as a core material.

The average values determined using Eq.6, Eq.7 and Eq.8 for FRP-sandwich panels subjected to short span three-point bending test are compared in Figure 2-12 (d), (e) and (f) which shows that the FRP-sandwich specimens having Al-foam in the core responded with higher flexural performance compared to the ones with Al-honeycomb core.

The addition of MWCNTs to the CFRP facing skins improved the flexural behaviour of the sandwich specimens and its effect was more prominent when

coupled with Al-Foam core compared to the Al-honeycomb core. The plateau regimes evidence the progressive deformation of core material mainly due to shear stresses under a transverse load after the maximum bending load at around constant load (slightly increasing/decreasing) for an extended cross-head displacement.

2.5.4 Long Span Three Point Bending Test

Figure 2-13 represents the behaviour of FRP-Sandwich panels subjected to a transverse load in long span three-point bending test configuration. Figure 2-14 represents the macro images of the FRP-Sandwich panels after the three-point bending test in long span configuration.

Unlike the CFRP- and GFRP-HCS specimens, the CFRP+MWCNTs-HCS specimens responded with relatively higher bending load before failure with a rather brittle failure to a transverse load. The properties of facing skins were observed dominating the flexural behaviour of CFRP+MWCNTs-HCS specimens compared CFRP- and GFRP-HCS specimens.

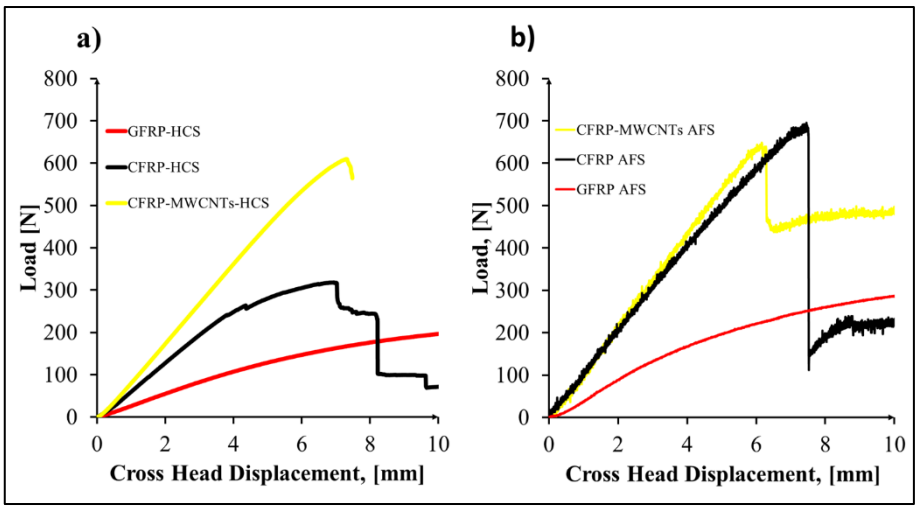

Figure 2-13. Flexural behaviour of FRP sandwich panel specimens subjected to long span three-point bending test.

The CFRP-MWCNTs HCS specimens did not display failure at the point of loading when subjected to a transverse load in long span configuration. After the maximum bending load, the cracks appeared in the honeycomb core and bottom facing skin, which triggered a brittle failure at the point where the specimen was supported during the bending test as can be seen in Figure 2-14 (b).

In a long span configuration, the GFRP- and CFRP-HCS specimens displayed a relatively ductile behaviour. The failure in the CFRP-HCS specimens was observed due to the excessive shear deformation in the core along the length of the specimen while the GFRP-AFS the progressive deformation of facing skin was followed by the collapse of honeycomb cells at a point of loading Figure 2-14 (c). The hinge formation at a point of loading in the GFRP- and CFRP-HCS specimens

was due to the compressive yielding of the facing skin adjacent to the loading bar and the underlying core, Figure 2-14 (a) and (c).

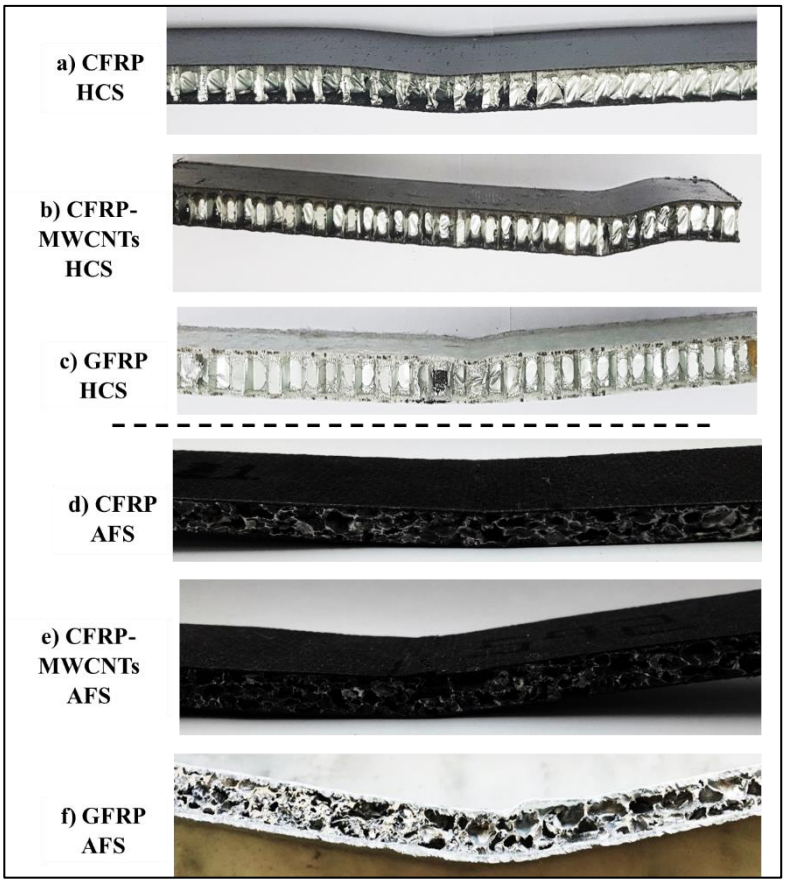

Figure 2-14. Post long span three-point bending test, cross-sectional view of sandwich panels specimens. (a), (b), (c) FRP-Al foam and (d), (e), (f) shows FRP-honeycomb sandwich panel representative specimens.

The CFRP+MWCNTs- and CFRP-AFS specimens displayed brittle failure due to the cracks in facing skin and underlying core material at a loading point. GFRP-AFS specimens did not respond with brittle fracture, but a rather ductile failure response was observed due to the progressive deformation of underlying foam core at a point of loading while no hinge formation was observed.

During the bending test in long span configuration, no delamination of facing skins was observed, however, a partial delamination was observed in one out of three specimens of GFRP-AFS specimens when the crosshead displacement reached around 15 mm due to the excessive shear stresses at the GFRP/Al-foam interface.

Figure 2-15 (a), (b) and (c) represents the average bending load, displacement and bending strength values recorded during flexural tests in long span configuration. The properties of the core materials predominantly influenced the flexural behaviour of FRP-sandwich panels during the long-span flexural test. The CFRP-AFS displayed failure at around 54 % higher bending load compared to the CFRP-HCS specimens. While the GFRP-AFS showed around 32 % improved bending load at with respect to GFRP-HCS composite panel specimens, Figure 2-15 (a).

Average values determined using Eq.6, Eq.7 and Eq.8 for FRP-sandwich panels are presented in Figure 2-15 (d), (e) and (f). The CFRP-MWCNTs-AFS and CFRP-MWCNTs-HCS composite specimens displayed around similar maximum bending strength values due to the higher stiffness of the skin which dominated the flexural behaviour in the long span bending and apparently overshadowed the effect of core material, Figure 2-15 (d).

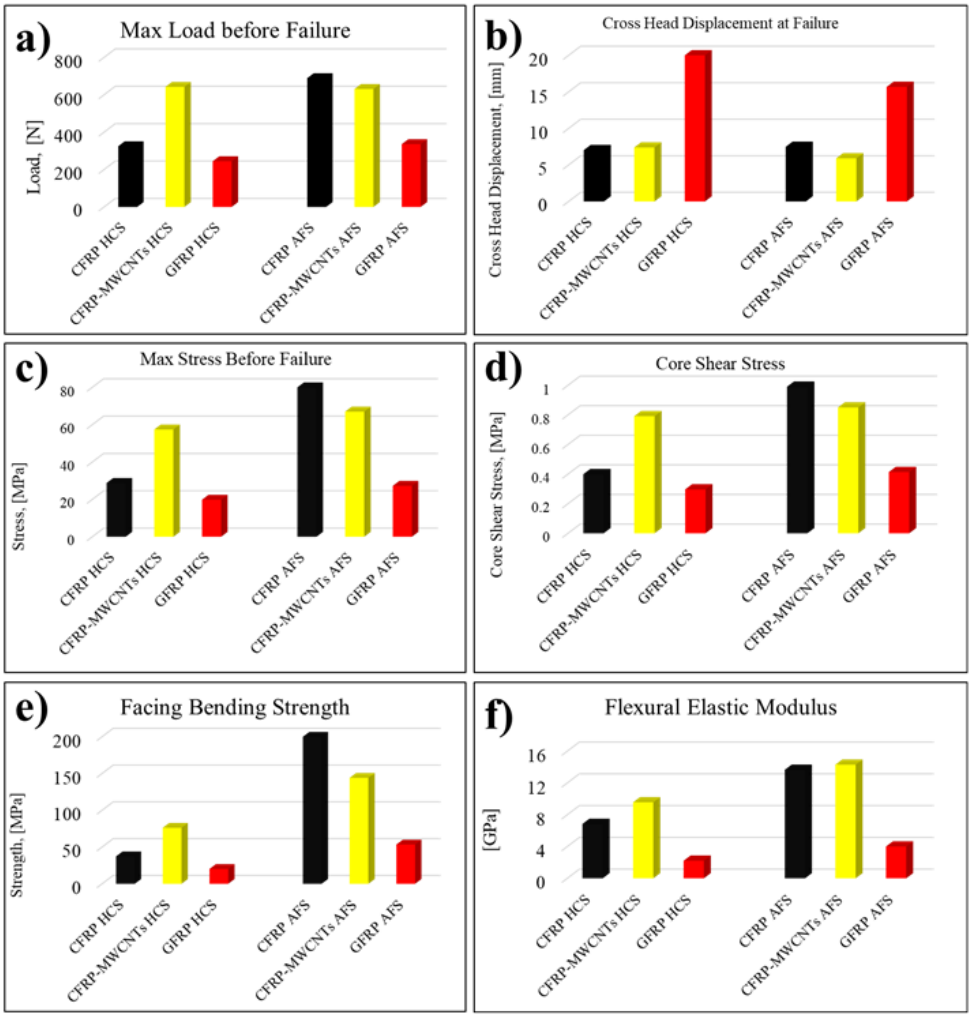

Figure 2-15. Analysis of FRP sandwich panels Flexural test data (Long span three-point bending).

The properties of facing skins also influenced the flexural behaviour of FRP sandwich panels. The sandwich panels with CFRP skins showed ~47 % higher bending strength compared to the specimens with GFRP facing skin. The CFRP-MWCNTs-AFS failed at around 8% lower bending load with respect CFRP-AFS specimens but CFRP-MWCNTs skins having honeycomb in the core showed around 46 % higher bending load at failure compared to CFRP-HCS specimens.

Unlike the short span flexural test, the load-displacement curves of the long span flexural test, presented in Figure 2-13, evidence that the addition of MWCNTs to CFRP skins are more effective when coupled with Al-honeycomb core compared to Al-foam core.

Comparison of AFS-Sandwich based on variation in Span Length

The results presented in Figure 2-16, evidence that the FRP sandwich panels subjected to a transverse load in three-point bending configuration but different span lengths respond with a relatively different flexural behaviour.

It was observed that the FRP sandwich panels having Al-honeycomb responded with higher flexural load values when subjected to three-point bending test in long span configuration. CFRP-HCS, CFRP+MWCNTs-HCS and GFRP-HCS failed at around 55 %, 3 % and 22 % higher bending load respectively in long span configuration compared to short span. While the FRP sandwich panels with Al-foam in the core displayed higher flexural properties during the short span three-point bending test where CFRP-AFS, CFRP+MWCNTs-AFS and GFRP-AFS failed at around 13 %, 45 % and 50 % higher bending strength.

Moreover, the behaviour of the FRP sandwich panels was observed dominated by the face skins properties when were subjected to a transverse load in long span configuration. Whereas, the core material properties dominated the flexural behaviour of the FRP sandwich panels when a short span three-point bending assembly was adopted.

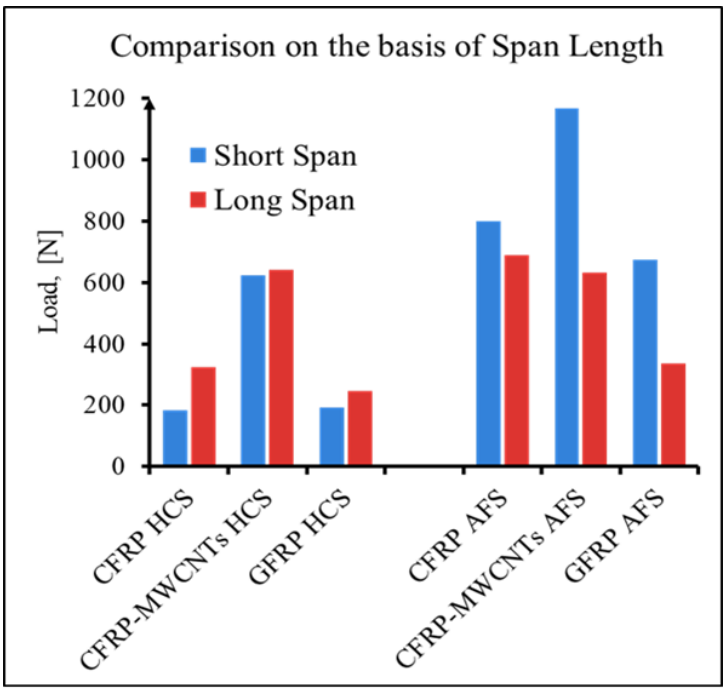

Figure 2-16. Comparison of Load at failure values of FRP sandwich panels subjected to long and short span three-point bending test.

The prominent plateau region observed in the load-displacement curves, presented in Figure 2-12, and during the shorter span length flexural tests shows the dominant role of core material in a sandwich structure. Such plateau regions were not evident when the sandwich panels were subjected to a transverse load in long span configuration.

The test method and adopted parameters, specimens shape and dimensions, type of facing and core materials highly influence the behaviour and response of a sandwich composite. Therefore, a direct comparison of sandwich specimen with variable dimension and type of materials tested on different parameters is not suitable. However for an approximation the results published in the recent past related to Al-foam and honeycomb compression analysis [112,113], flexural behaviour analysis of GFRP-honeycomb sandwich composites [114], flexural response of adhesively bonded CFRP-Al foam sandwich panels [115], flexural behaviour study of natural fibre reinforced honeycomb and cork sandwich composites [116] the strength evaluation of CFRP sandwich composites with honeycomb and foam in the core [117] can be compared to the results presented in this study for the compression analysis of Al-foam and honeycomb core and the flexural response of GFRP-AFS, GFRP-HCS, CFRP-AFS and CFRP-HCS composites.

2.6 Conclusion

Using two different core materials, and three different types of facing skins, FRP-Sandwich panels were produced in six different configurations.

It was observed that the flexural behaviour and the collapse mode of the sandwich panels with same structural configuration are influenced by the type of core material, type of facing skins and the span length adopted during the flexural test.

Experimental results showed that higher flexural properties can be achieved by replacing Al-honeycomb with Al-foam as a core material in the sandwich structures having similar facing skins.

Compared to HCS sandwich panels, the AFS sandwich panels displayed ~25 % and ~65 % higher flexural properties in a long and short span three-point bending test respectively.

The flexural behaviour of the FRP-sandwich panels was observed dominated by the face skins properties when the specimens were subjected to a transverse load in long span configuration compared to the short span, where the core material properties were dominating the flexural behaviour of the FRP sandwich panels.

The addition of MWCNTs to the CFRP skins improved the stiffness properties of the facing skins. The addition of MWCNTs to CFRP facing skins was found more effective when coupled with Al-Foam core compare to the Al-honeycomb core during the short span three-point bending tests, while during the long span based flexural tests, the addition of MWCNTs to CFRP skins was found effective when coupled with Al-honeycomb core compared to Al-foam core.

The results obtained in this research activity will be helpful in the designing of an engineering sandwich composite structure for marine, automotive and construction applications.

3. Joining of Aluminium Foam to Aluminium Skins to obtain Sandwich Composites

3.1 Abstract

Al-Foam is a lightweight, a non-flammable porous material with improved energy absorption, electromagnetic pulse shielding with lower conductivities than bulk metal materials and excellent sound absorptivity. It is used in civil, automotive, aerospace applications for noise and weight reduction.

The aim of the research activity was to develop soldering and brazing techniques for joining Al-metal sheets to Al-Foams to obtain Aluminium Foam Sandwich (AFS) composite panels for automotive and aerospace applications where higher thermal working conditions are requirement.

Al-6016 and Al-7046 aluminium metal sheets were successfully soldered/brazed to Al-foam using Zn-based alloys and Al-based amorphous alloys at temperature ranging from 400 °C - 590 °C in an argon atmosphere. The Al-7046 sheets and the sandwich panels were further subjected to a carefully designed post-brazing solution heat treatment to recover the mechanical properties of AFS components lost during the brazing process.

A three-point bending test was conducted to evaluate the flexural properties of the AFS composites. The effect of heat treatments on the microstructure of base materials and the cross-sectional morphology of the Al-Sheet/Al-Foam brazed joints was analysed using Scanning Electron Microscope (SEM) equipped with Electron Dispersion X-Ray Spectroscopy (EDS). The experimental work was focused on the optimization and comparison of the joining processes and joining materials.

Key Words: Al-Foam Sandwich (AFS); Soldering; Brazing; Micro Hardness; Flexural Properties; Automotive; Aerospace.

3.2 Graphical Abstract

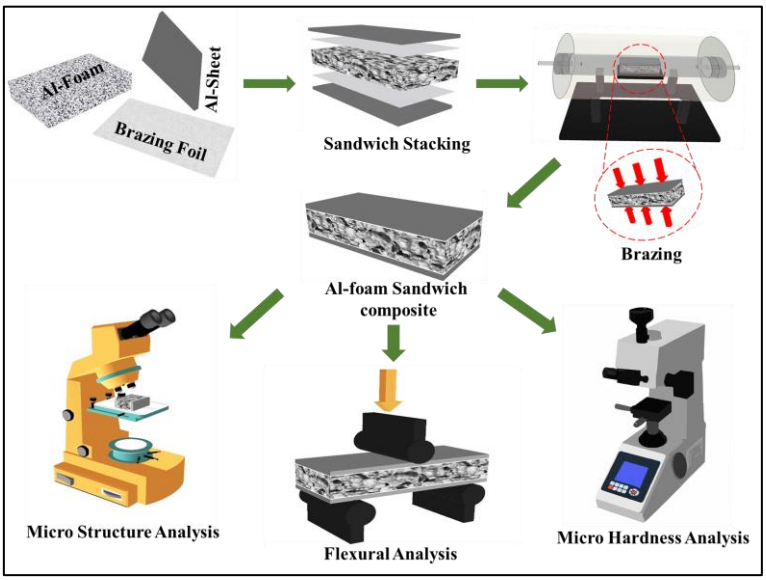

3.3 Introduction

Currently, the growing demand for higher fuel-efficient vehicles to reduce the energy consumptions and the CO_2 emissions to overcome the air pollution is a challenge for the automotive and aerospace industry. The design engineers are responding to this challenge by introducing alternate energy sources, making more efficient powertrains such as hybrid systems and using lightweight body structures [118]. Reduction in vehicle body weight is particularly important because ~10% weight reduction improves around a 5.5% fuel economy [119].

Presently, to decrease the body-weight of an engineering structure, the design engineers are coming up with new types of hybrid material sandwich panels. Among them, Aluminium Foam Sandwich (AFS) panel is an emerging class of hybrid sandwich composite materials. Al-foam is a 100% recyclable, low cost and non-flammable, lightweight porous material. It displays high energy absorption, excellent sound absorptivity, electromagnetic pulse shielding and lower conductivity in comparison to bulk Aluminium [120].

3.3.1 AFS Sandwich Panels

AFS is fabricated by sandwiching a thick, but light Al-foam core between two thin, stiff and massive skins of Al sheets. The outer skins bear the tensile loads while the core material contributes to impact energies absorption and, most importantly, weight reduction [121]. AFS panels compared to Al bulk components are multifunctional, low-density and economically viable for many applications including automotive, marine, aerospace, construction and railway industries [51]. AFS panels provides good dimensional stability, high specific strength, improved

damping and acoustic insulation properties [122,123] and is now finding widespread use in automobile and aerospace industry due to their multi-functionality and unique performances [124,125].

To produce an AFS composite panel, the facing skins are joined with the core material. The facing skins bonded to Al-foam using commercial adhesives restricts the applications of AFS panels to the lower temperature conditions, i.e. below 220°C [126,127]. For aerospace and high-end automotive applications, the thermal expansion, moisture absorption and low elastic modulus of adhesives are also a concern [128]. The AFS composite panels with complete metallic character can meet the heat resistance, stability at elevated temperatures and non-flammability requirements, which are not satisfied by the sandwich composite panels produced by gluing face sheets to the core material [129].

3.3.2 AFS Sandwich Panels with Metallic Facing Skins Production

The recent trend, to exploit the applications of AFS panels in high-temperature environments, has led to the development of various Al-foam/Al-sheet joining and AFS manufacturing techniques such as casting [130], brazing [131] and soldering [132,133] etc. Some modified joining methods are also proposed to produce AFS panels, such as flux-less soldering with surface abrasion [134], laser foaming to produce Al-foam cores inside a hollow profile [135], friction stir incremental forming technique to transform a surface layer into a massive skin [132], pressing-bonding, rolling bonding, powder metallurgy foaming process and Self-propagating High-temperature Synthesis (SHS) [136]. The in-situ formation of Al-foam in a hollow Al-piece to produce AFS structures is also largely studied [51].

Soldering/Brazing is a joining method well-known to an industry where a relatively low melting temperature filler material is used to bond two similar or dissimilar metals by heating. The success of soldering/brazing depends on careful optimization of fundamental parameters such as time, temperature and provided atmosphere (inert/vacuum). The formation of an oxide layer on Al surface is very swift which hinders the surface wettability by soldering/brazing alloy.

The removal of or to avoid the Al oxide layer during brazing/soldering process is not easy and requires strong fluxes such as an organic amine-based flux (up to 285°C), inorganic fluxes (chloride or fluoride up to 400°C), and complex fluoroaluminate salts (above 550°C). Besides fluxes, mechanical rubbing, ultrasonic cleaning, abrading or blasting away the Al oxide layer to allow the aluminium subsurface wetting is also needed. If the brittle intermetallic formation and low-temperature eutectics constituents are avoided during the brazing/soldering process, reliable joining properties can be achieved [30].

The above mentioned, joining techniques have made AFS composites interesting for certain practical applications, such as the realization of low-cost light-weight structures with high mechanical strength and enhanced capacity of

energy dissipation under impacts [136,137]. However, the AFS fabrication techniques currently in practice are very complex, costly and mostly restricted to batch production where a much-needed improvement is required.

The research work discussed in this chapter is focused on the optimization of joining methods for continuous production and the selection of joining materials to produce AFS composite panels for higher temperature applications in automotive and aerospace industries.

3.3.3 Joining Materials

3.3.3.1 Zn-Based soldering/brazing alloys

Zinc-based solders (zinc as alloyed with Pb, Cd, Sn, Cu, and/or Al) are generally used in assistance with fluxes for activation and the residues of the soft soldering fluxes are removed after soldering of Al parts. However, the presence of Tin in a joining material causes an electrochemical corrosion problem because of its galvanic potential. The anticipated worldwide ban on lead has pushed the joining industry towards lead-free joining materials while the Cd-containing joining alloys have been recently banned due to operator's health concerns. These restrictions have removed some of the most suitable and ductile and/or higher-temperature soft solders from the available list of joining alloys [138].

Zn is a distinctive alloying element for Al-alloys and shows the highest solubility among the other most used alloying elements [139]. The eutectic point of Al-Zn system is at about 380°C. When the Al percentage in Al-Zn system is higher than 30% at eutectic temperature, the α solid solution is the stable phase. Moreover, Due to weak interaction between Al and Zn atoms, Al and Zn do not form intermetallic phases. The small difference between the electrode potential of Al and Zn reduces the possibility of galvanic corrosion [140,141].

3.3.3.2 Al-Based soldering/brazing alloys

Al-Si alloys are sometimes used as filler materials, for sandwich composites with Al face sheet of 6xxx series, which usually contain 7-12 wt.% silicon as a melting point depressant [142]. The addition of Mg, Si, and Cu to Al, if added up to their respective solubility limits, increases the mechanical strength of the aluminium alloy [143].

In general, a configuration comprising two massive face sheets or a hollow metal piece with a foamable material in the core layer is adapted to produce in-situ bonded AFS. The central foam-able Al-based material melts at a lower temperature with respect to face sheets. This difference in the melting temperatures is exploited to produce AFS composite panel by expanding the foamable material and prevent the face sheets from liquefying [70]. It is suggested that an optimum foam

expansion can be achieved when the Si content is in the range 6-7wt.% [144], which results in ≈50% eutectic melt at the eutectic temperature of 577 °C.

The in-situ production of AFS involves the melting of the central foam-able Al-based material at a lower temperature with respect to face sheets. Al-Si alloy powder having Si content up to 12% was used initially as a precursor in powder metallurgy applications to obtain Al-foam [145]. However, a satisfactory pore structure was not achieved using only binary Al-Si system and the research progressed towards the addition of alloying elements that further lowers the melting point of the precursor.

The solubility of Mg, Cu and Ti in solid Al, by weight, is 17.4 % at 460 °C, 5.65 % at 548 °C and 1.3 % at 665 °C respectively [146] and their addition can suppress the melting point of Al-based alloy and/or precursor. The addition of Ti traces to Al-Si-Mg system is suggested to be further beneficial as the diffusion of Ti atoms towards Al is more pronounced than Al atoms towards Ti [147]. To exploit their foamable character of the precursor composition, two Al-based (Al-Cu-Mg and Al-Si-Mg-Ti) amorphous alloys produced by Niu et al. [148] were used as a joining material to braze Al-foam to Al-skin in this research activity.

The melting temperature of the most common foam-able precursor alloy ($AlSi_6Cu_4$ or $AlSi_6Cu_6$) is 524 °C and it can be coupled with 1xxx, 3xxx, 5xxx and 6xxx series Al-alloys face sheets to produce AFS composite panels in an in-situ bonding process [129]. Nannan et al [131] successfully experimented high-temperature brazing of Al-foam to Al-foam in vacuum at 590 °C using Al_8Si_6Mg alloy as the brazing material.

Soldering and brazing joining are so far found the superior solution to join AFS components, however, at higher joining temperatures, the microstructure of Al-facing sheets is affected and its mechanical properties are deteriorated [49]. To the best of authors knowledge, rare studies [149] are reported regarding the mechanical strength recovery of the of AFS composite panels by age hardening. The age hardening of Al sheets is an almost established concept and is simpler [150,151] if the facing skin is age hardenable. Age hardening of AFS is still a challenge due to its composite nature and complicated cooling mechanism due to low thermal conductive Al-foam during quenching.

In this chapter, two Zn-based fillers and two Al-based (Al-Cu-Mg and Al-Si-Mg-Ti), amorphous alloys are introduced to join Al-foam to Al-facing skins and to satisfy the requirements such as high thermal stability and corrosion resistance. The Al-sheets and the AFS sandwich panels were subjected to a carefully designed post-brazing heat treatment to recover the strength properties of AFS components.

Microstructure analysis of Al-sheet/Al-foam joints is carried out using Optical Microscopy (OM), Scanning Electron Microscopy (SEM) and Electron Dispersion Spectroscopy (EDS). Microhardness profiles of base materials after thermal

treatment were determined. Three-point bending test is conducted to analyses the flexural properties and determine the bending strength of the AFS composite panels. A comprehensive comparison is established among the proposed joining processes and joining materials and those reported in the literature.

The effects of post-brazing thermal treatments on the microstructure, microhardness and flexural properties of Al-sheet, Al-foam and Al-sheet/Al-foam interface are analysed and the results are discussed in detail.

The experimental activity was designed based on the detailed literature study. Several combinations of Al-alloys (such as 3xxx, 5xxx, 6xxx and 7xxx Al alloys), forms of joining materials (powders, foils and strips) and joining processes were shortlisted and investigated initially to limit the number of test events. Based on the analysis of the trial experiments, the best practices were selected, studied in detail and modified to experiment new joining materials, which are discussed in this chapter.

3.4 Materials and Methods

Two most common aluminium alloys used in automotive, sports and aerospace industries, A.A (Aluminium Alloy)-6016 and A.A-7046 were selected and used as a facing skin to produce Aluminium Foam Sandwich (AFS) composite panels. The specifications of both Al alloy sheets used in this study are reported in Table 3-1.

Table 3-1. Properties of Al alloys selected as facing skin for AFS sandwich panels.

Al-Alloy	Composition	Density, g/cm^3	Thickness, mm
AA 6016	Al 98.8 %+Mg 0.25%+Si 1%	2.7	1.2
AA 7046	Al 91%+Zn 6.5%+Mg 1%+Cu 0.15+Zr 0.12+Fe 0.2%+Si 0.13%+Mn 0.05%+Cr 0.1%+Ti 0.05%	2.82	1.3

An ultralight, 100 % non-flammable, 9 mm thick Al-foam produced by Foamtech, Korea was supplied by Vaber, Italy. Figure 3-1 represents the porous surface and cross-section of Al-foam plate used in the current study. The average variation of cell size and its distribution was carefully evaluated using a free software, Image-J, discussed in Chapter 2 Section 2.4. The equivalent pore diameter of the Al-foam cells was found 5.2 mm ± 1.5 mm and the pores distribution of the Al-foam samples fit into a bell shape curve. The pore cell walls, which offers the

potential joining area, accounts for around 12.8 % of the total Al-foam plate surface area.

Pore density and the pore size of Al-foam cells highly influence the Al-sheet to Al-foam joining process and the mechanical performance of AFS composite panels. A higher number of pores in a unit surface area of Al-foam offers a higher number of cell walls which altogether makes the potential surface available for joining. Higher pore density leads to a higher density of Al-foam and is used to produce AFS panels where higher mechanical strength is a priority. Bigger pore size corresponds to the low density of aluminium foam and results in lighter weight AFS components with relatively lower mechanical properties.

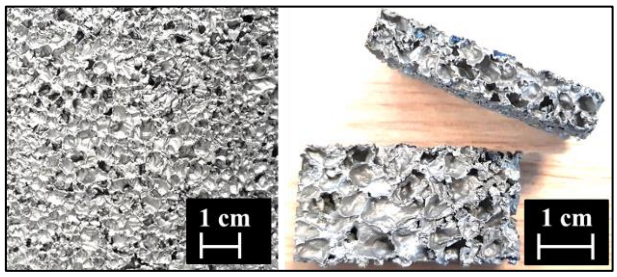

Figure 3-1. Surface and cross section of Al-foam used as a core material in AFS panels production in this study.

Four types of joining alloys were used to join Al-sheets to Al-foam core to produce AFS composite panels. Two Zn based joining materials, Pure-Zn foil and Zn-2Al strips (Supplied by Lucas Milhaupt, USA) were selected as joining materials due to the high solubility of Zn in Al and two Al-based amorphous brazing alloys, Al-4Mg-14Cu alloy and AL-7Si-.5Mg-1Ti (provided by Harbin Institute of Technology, China) were selected to produce AFS for higher temperature applications. The composition of Al-based brazing alloys was selected on the basis of the composition of precursor materials used to produce Al-foams [70,120,152]. The specifications of the selected joining alloys are reported in Table 3-2.

Table 3-2. Specifications of Joining alloys adopted to produce AFS composite panels.

Joining Material	**Thickness, mm**	**Melting Point, °C**
Pure Zn Foil	0.35	420
Zn+2Al Strips	0.25	405
Al-4Mg-14Cu Foil	0.06	~550
Al-7Si-.5Mg-1Ti foil	0.08	~550

Al-6 flux supplied by Stella srl, Italy was used for thorough wetting of the joining surfaces and to prevent the entrapment of aluminium oxide inclusions in the joints. Nitric acid (12%) was used to remove the oxide layer from Al-foams used in this experimental work.

Aluminium skin and Al-foam substrates of required dimensions were cut from aluminium alloy sheets and Al-foam plates using ATM Brilliant® cutting machine equipped with a ceramic blade.

3.4.1 Preparation of AFS specimens

The joining faces of Al-sheet and Al-foam were first abraded with 120-360 grid SiC paper to remove the surface oxide layer. Al-foam surface was further activated by using 12% nitric acid solution for 30 minutes as suggested in [136]. The abraded surfaces were cleaned with alcohol in Sonica® ultrasonic bath at 60 ºC for 10 minutes. Al-flux was applied to the joining surfaces before stacking in a sandwich configuration. Figure 3-2 represents the stacking configuration adopted for AFS sandwich composite in this study.

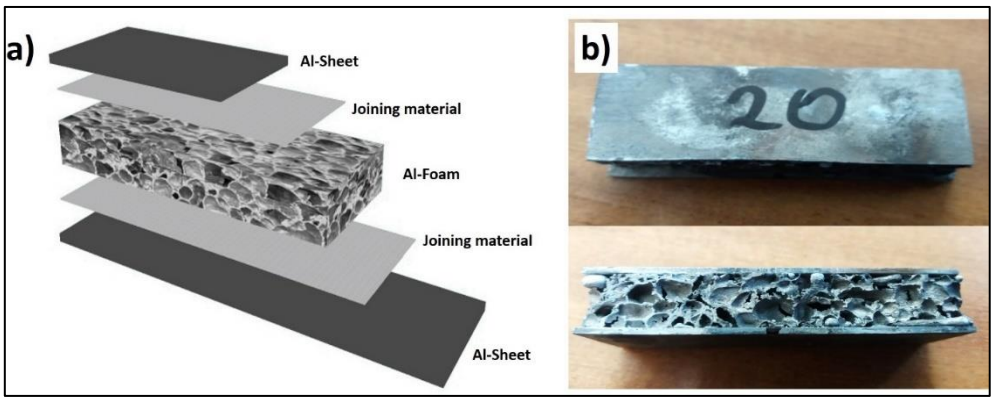

Figure 3-2.(a) AFS components stacking configuration, (b) Produced AFS panel specimen (60mm x 60mm x11 mm).

The initial soldering/brazing parameter adopted were decided based on relative phase diagrams and past studies. To optimise the joining parameters, for each joining alloy several sets of time/temperature conditions were experimented to achieve good joints in AFS composite specimens. The optimized joining parameters observed during joining experiments are reported in Table 3-3.

All the soldering/brazing experiments were carried out in a ceramic tube Carbolite® Gero tube furnace in an argon atmosphere to avoid oxidation. The specimens were then slow cooled (at a cooling rate of 100 °C/h) in flowing argon to avoid residual stresses and achieve phases closer to the stable equilibrium state, as suggested in [140].

Table 3-3. The optimised soldering/brazing parameters adopted to join Al-foam to Al-skins to produce AFS composite panels.

AFS #	Joint	Temperature, ºC	Dwell Time, minutes	Heating rate, º C/hr.

A	Al6016/Pure Zn/Al-Foam	400	5	1000
B	Al6016/ Zn+2%Al/Al-Foam	405	1-2	1000
C	Al6016/Al-4Mg-14Cu/Al-Foam	590	15	800
D	Al6016/AL-7Si-0.5Mg-1Ti /Al-Foam	580	15	800
E	Al7046/PureZnAl-7046	490	5	1000
F	Al7046/Zn2Al/Al-7046	510	5	1000

At the optimized conditions, three AFS composite specimens were produced (using each pair of joining substrates) for flexural properties characterization. The bonded AFS samples produced for a mechanical test were 60 mm long, 20 mm wide with a total thickness of about 11 and/or 11.6 mm. MTS®-810 testing machine equipped with 5kN load cell was used with a three-point bending assembly to evaluate the flexural behaviour of AFS specimens.

Figure 3-3 represents the three-point bending test assembly and the parameters adopted during the three-point bending test. All the flexural tests were conducted at room temperature, 25 ºC, and 65% Humidity. When 10 mm cross head displacement was reached, loading was stopped. The collapse behaviour of Al-foam and the failure modes of AFS components were analysed using still images and the videos recorded for each test event.

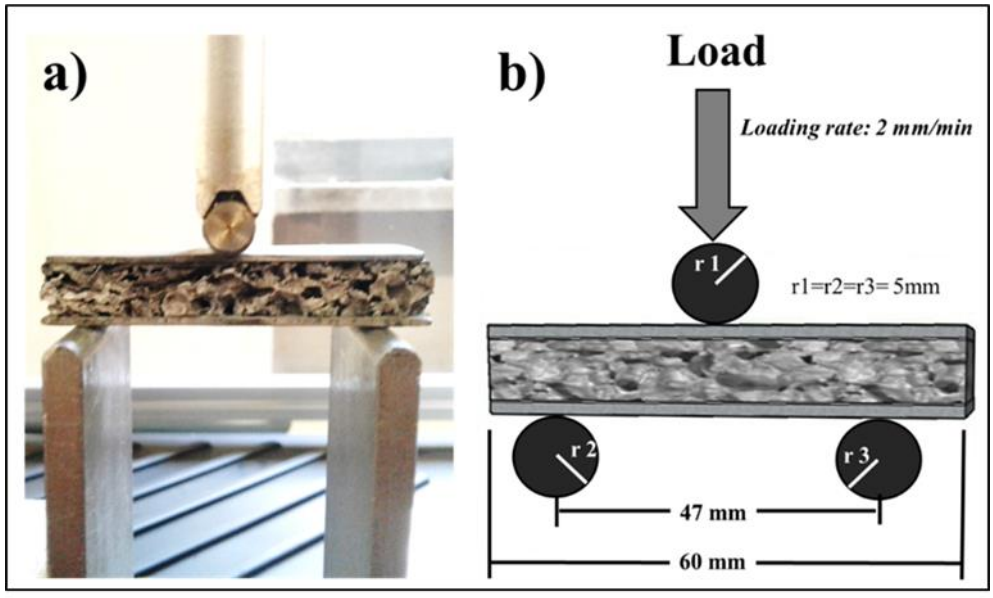

Figure 3-3. (a) Three-point bending test assembly, (b) Three-point bending test parameter.

The metallographic cross-section analysis of the polished Al-sheet/Al-foam interface cross sections was carried out using Optical Microscope (OM), and ZEISS SUPRA™ 40 Field Emission Scanning Electron Microscope (FE-SEM). The chemical composition of the phases in the diffusion zones and the joining seams were analysed using Energy Dispersive X-rays detector (EDS) synced with ZEISS SUPRA™ 40 FESEM. The microhardness profiles were determined using Hermet HX-1000 microhardness testing machine using 25-gram force with 15 seconds of dwell.

3.4.2 Post brazing heat treatment to recover the mechanical properties

To optimize the mechanical properties of Al alloys, the understanding and controlling of recrystallization through careful utilization of thermomechanical processes is important. Three separate experiments were conducted in this study to recover the mechanical properties of Al-7046 alloy and subsequent AFS components after brazing thermal treatment.

In experiment 1, Al-7046 alloy sheets were subjected to thermal treatment in a furnace to simulate the brazing conditions adopted for AFS A and B, while in experiment 2, Al-7046 alloy sheets were subjected to thermal treatment in a furnace to simulate the brazing conditions adopted for AFS E and F.

The flow chart of the steps followed during the experiment 1 is shown in Figure 3-4. The simulated Soldering/Brazing Heat Treatment (BHT) was then followed by Solution Heat Treatment (SHT) process designed to recover the mechanical strength of the Al-alloy by the redistribution of agglomerated alloying elements. Following parameters of BHT and SHT were adopted during the experiment 1 and experiment 2:

- BHT-1: 10 minutes @ 450 ^{o}C followed by cooling at a rate of 10 ^{o}C/min.
- SHT-1: BHT + 600 minutes @ 370 ^{o}C followed by water quenching.
- BHT-2: 5 minutes @ 500 ^{o}C followed by cooling at a rate of 10 ^{o}C/min.
- SHT-2: BHT-2 + 180 minutes @ 370 ^{o}C followed by water quenching.

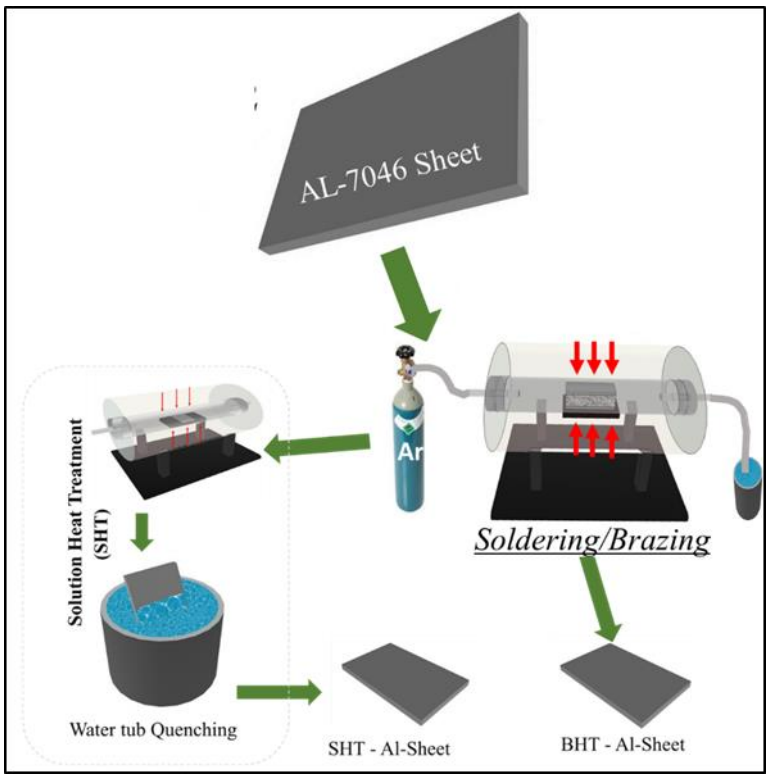

Figure 3-4 Flow chart of the step followed by the experiment 1 and experiment 2.

In experiment 3, the AFS-E and AFS-F composite specimens were subjected to SHT-2 type thermal heat treatment to recover the mechanical properties of the base components of the brazed AFS composite panels affected during the brazing (similar to BHT-2) cycle. Figure 3-5 represents the flow chart of the steps followed during the AFS composite panels production and the solution heat treatment adopted in experiment 3.

In experiment 3, the AFS sandwich panels were not dipped directly into the water for quenching because of the porous Al-foam in the core. Dipping of AFS sandwich can produce a vapour pressure inside the pores which will exert a pressure on the facing skins at joining interface. Such pressure may cause the delamination of still hot specimens. Therefore, a shower quenching apparatus, as shown in Figure 3-5, was developed in-house to put only the Al-7046 skins in direct contact with water during quenching.

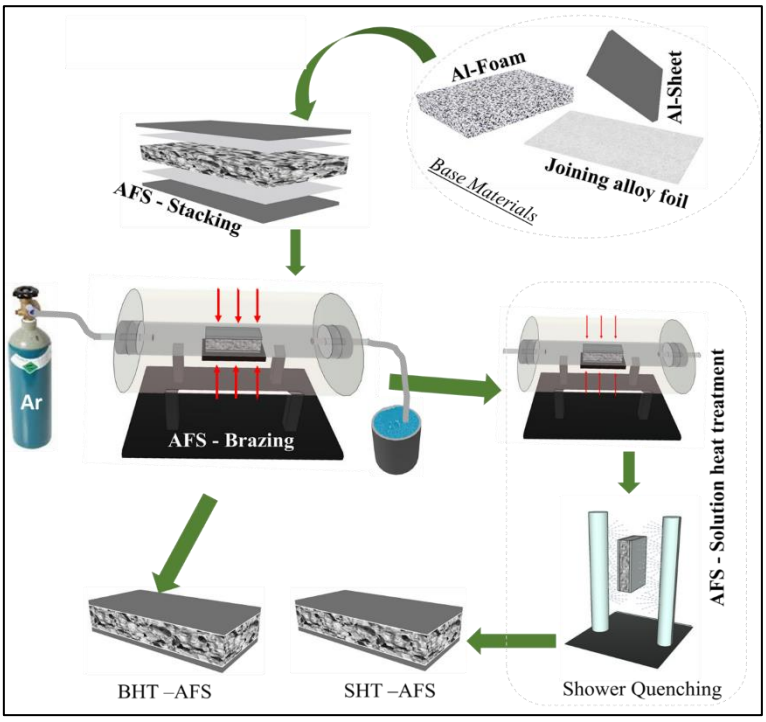

Figure 3-5. Flowchart of the step followed in the development of AFS panels E and F followed by the experiment 3 solution heat treatment.

The effect of thermal treatments on the microstructure of the Al-7046 alloy sheets and the AFS panels was investigated for microstructure and microhardness using SEM equipped EDS analyser and Remet HX-1000 microhardness testing machine. For each specimen, at least 10 micro hardness events were performed using 25-gram force with 15 seconds of dwell time.

A set of three specimens of dimension, 60 mm (length) x 20 mm (width) x 1.2 mm (thickness), of as received, post-brazing and post-brazing thermally treated AFS base components (Al-sheet and Al-foam) and AFS panel specimens were subjected to a static three-point bending flexural test, to analyses the effect of thermal treatments on the flexural behaviour.

3.5 Results and Discussion

3.5.1 Microstructural analysis

3.5.1.1 Al-6016/Zn-based alloys/Al-foam joints (AFS-A and AFS-B)

Figure 3-6 shows the sound AFS specimen obtained by soldering Al-6016 facing skins to Al-foam using Zn-based joining alloys. The Al-skin/Al-foam joining interface in AFS-A and AFS-B, Figure 3-6, was not continuous and the connecting points were developed during soldering process where the Al-foam cell

walls were touching the Al-skin. The amount of such connecting points at Al foam/Al Skin interface is directly related to the pore size of Al-foam [49].

According to Al-Zn binary phase diagram [139], at the soldering temperature, reported in Table 3-3, Zn melts first due to lower melting point and reacts with Al producing a liquid solution (joining melt) at the Al-foam/Al-skin interface. The melting temperature of the joining melt increases as it enriches in aluminium until β' solid solution.

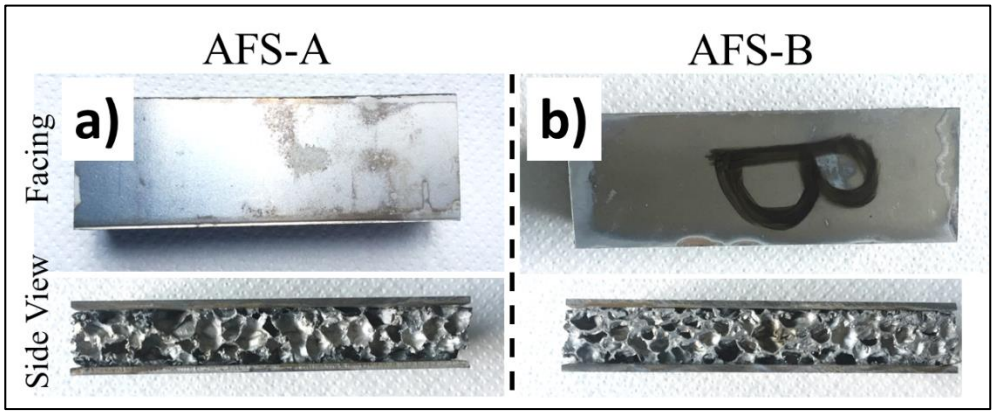

Figure 3-6. Facing and cross-sectional view of (a) AFS-A produced using pure Zn as a joining alloy, and (b) AFS-B produced using Zn2Al as a joining alloy.

Figure 3-7 represents the SEM images of the Al-6016/Al-foam interface of the AFS-A and AFS-B specimens. The diffusion effect starts when the foils start melting producing a joining melt at the Al-foam/Al-sheet interface. During cooling, the joining melt left a porous construction like Al-foam in the melted zones due to contraction upon solidification. Typically, the porosity in the joining seams is not desired as it affects the mechanical strength of the joint itself. However, in this case, it is acceptable, because one of joining substrate (Al-foam) itself is a porous material.

The solidified melted zones along the joining seams showed a dendritic and eutectic morphology, Figure 3-7 (a) and (d) with precipitated particles in the melted zone. The reaction of the liquid (Zn+Al) with α Al phase produces a certain amount of Zn-rich β (fcc) phase. This last one during solidification becomes unstable supersaturated Zn-rich β's (fcc) and decomposes into Al-rich α phase (fcc) and Zn-rich η phases (hcp).

The amount and type of soldering material affect the volume quantity of liquid phase, and therefore, the joining seam thickness. In fact, the diffusion effect was more evident when soldering was carried out using Zn2Al joining alloy than with pure Zn, at same soldering temperature. This is due to lower the melting point of Zn2Al alloy than pure Zn.

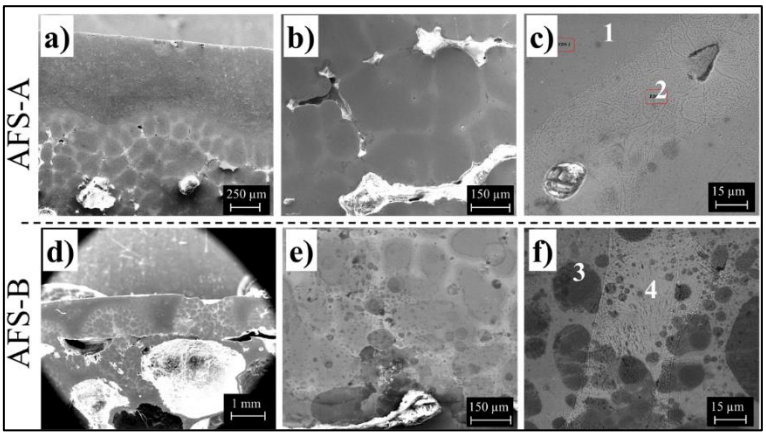

Figure 3-7 SEM micro-images (a), (b) and (c) AFS-A, Al-6016/Pure Zn/Al-foam interface, (d), (e) and (f) AFS-B, Al-6016/Zn2Al/Al-foam interface.

The localized melted pool observed in Figure 3-7 (a) and (d) along the Al sheet and Al foam interface sometimes melt the Al-skin through thickness. The soldering parameters were carefully optimized to avoid the localized melting of Al sheet and to allow uniform distribution of joining melt at the Al-foam/Al-skin interface.

At higher magnification, a dendritic segregation is evident in the diffusion zone, Figure 3-7 (b) and (e), sometimes with a primary arm columnar growth starting from the wall pool and a reduced amount of interdendritic morphologies together with shrinkage porosities. Moreover, some polygonal or rounded Si particles, always bigger than those observed in sheet and foam, are evident in the joint interface, Figure 3-7 (c). At the soldering temperature, the silicon solves in liquids, but it's very low solubility in Al-rich and Zn rich phases respectively, induces a sudden crystalline Si nucleation and growth.

The interdendritic microstructure evidences a physical mixture of two phases (α and η) with a relative distribution sometime lamellar, Figure 3-7 (c) and (f). The EDS analysis, reported in Table 3-4, effected on dendrite and interdendritic areas respectively, evidence higher amount of Zn in the interdendritic zone, also confirmed by the η phase precipitation observed in the metallographic microstructure.

Table 3-4. Electron Dispersion X-Ray (EDS) spectroscopy analysis of the phases formed at the joining interfaces of the AFS-A and AFS-B composite panels during the soldering process.

EDS point	**Composition (wt.%)**	
	Al	**Zn**
1	23	77

2	60	40
3	22	78
4	62	38

The depth of diffusion along of the aluminium sheets was non-homogeneous in the entire surface and is thicker at the areas where the foam cell walls touch the Al sheets. In these zones, the joining depth ranges from around 200 µm, in case of pure Zn soldering alloy and 800 µm in case of Zn2Alsoldering alloy.

3.5.1.2 Al-6016/Al-based alloys/Al-foam joints (AFS-C and AFS-D)

In another attempt, brazing technique was adopted to join Al-6016 to Al-foam to produce AFS composite panel using two Al-based amorphous brazing alloys (provided by Harbin Institute of Technology, China) as joining material for the applications where even higher service temperature tolerance is a requirement. Figure 3-8 shows the macrographs of AFS-C and AFS-D cross section after the brazing cycle. The optimized brazing parameters at which the AFS-C and AFS-D composites were produced are reported in Table 3-3.

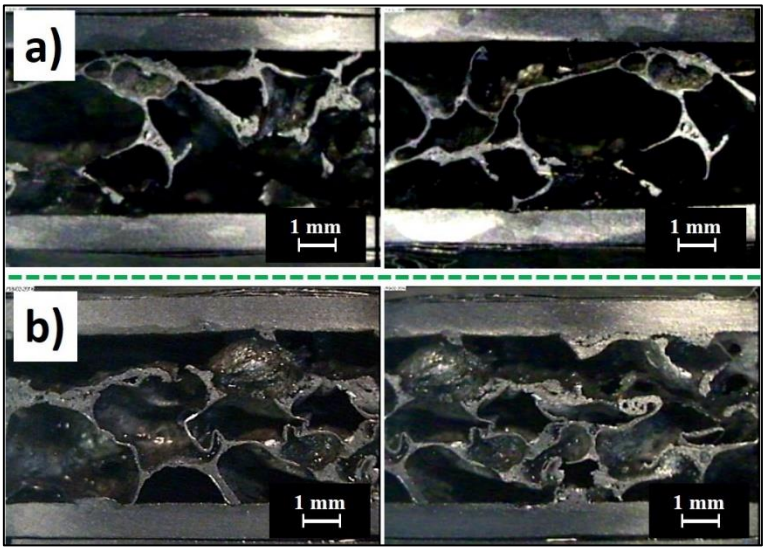

Figure 3-8 Macrograph of a polished cross-section of (a) AFS-C produced using AL-Cu-Mg amorphous alloy, and (b) AFS-D produced using AL-Si-Mg-Ti amorphous alloy.

SEM analysis of AFS-C and AFS-D joining seams, shown in Figure 3-9, display sound connections achieved between the Al-sheet and Al-foam by a brazing process. To analyse the chemical composition of the phases appeared in the diffusion zones, point EDS examination was performed at the points indicated in Figure 3-9 (b) and (d).

The effect of diffusion of joining alloy at the brazing temperature melted almost the through the thickness of Al-skin and the porous cross-sectional morphology, as can be seen in Figure 3-9 (b) and (d) is due to the contraction of joining melt during the cooling process. In the diffusion zones towards the Al-sheet along the joining seam, the precipitation of Si alloying element is evident.

Since the aluminium foam was produced from liquid aluminium at T >700 ^{o}C, the dendritic microstructure in the cross-section of Al-foam was present even before the brazing. However, localized small pores appeared in the aluminium foam cell walls during the solidification of joining melt in the diffusion zone near the joining seam.

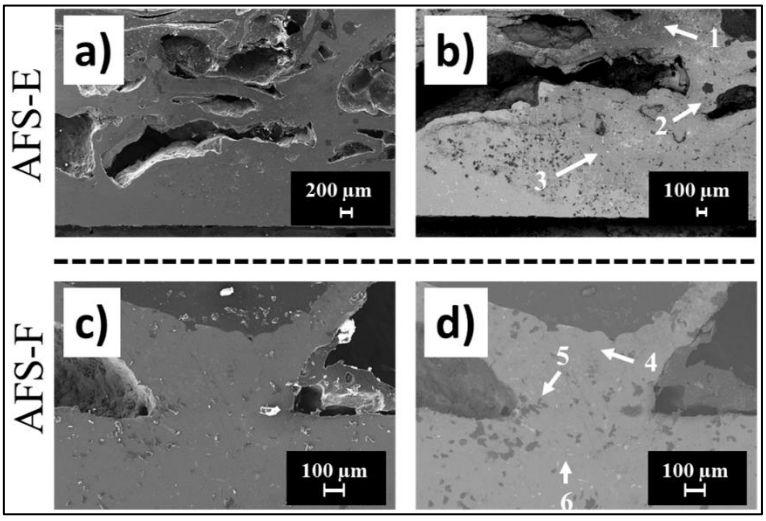

Figure 3-9 SEM micro-images (a) and (b) Al-6016/Al-Cu-Mg/Al-foam interface, (d), (e) and (f) Al-6016/Al-Si-Mg-Ti/Al-foam interface

The EDS examination results are reported in Table 3-5. The maximum solubility of Cu in Al is 5.65% at a eutectic temperature (548 ^{o}C) which decreases with the decrease in temperature (Figure 3-9 (b), EDS 1 and 2). At brazing temperature (580 ^{o}C), alloy with 14% Cu exists in L+ α (liquid + alpha) phase. α-phase rejects excess Cu as a relatively coarse in size precipitate particles of θ. At room temperature, α contains less than 0.5% Cu while an inter-metallic compound, $CuAl_2$ (θ) contains 52% Cu. The θ particles have a moderate strengthening effect on alloy properties [153].

A noticeable amount of oxides was observed in the results reported in Table 3-5 which shows the brittle character to the joints. The possible reasons for the oxidation are the entrapped air inside the foam cells or a possible imperfect argon environment inside the tube furnace.

In the case of brazing processes, especially when Al-alloy is supposed to be brazed to another Al-alloy, the role of the surface oxides is very important particularly when Mg containing joining alloys are involved. It is an accepted fact

that Mg favours the formations of oxides and a reliable joint with low oxides in it can be achieved only if the Mg content is restricted to or below 0.3% along with the use of standard brazing flux [154].

Higher levels of Mg content lead to brazing failure due to the formation of higher melting point compounds, which reduce the fluidity of molten cladding alloy. At the temperature above 570°C, Mg vaporizes and produces a “mag burst” which works as an oxygen getter. The loss of filler metal to vaporization reduces the quantity of joining material and compromised the joint strength and sealing ability [155]. It is evident from the EDS results, reported in Table 3-5, that MgO has formed. Similar observations are reported in the previous studies [156].

Table 3-5. EDS Analysis of AFS-C and AFS-D joining interfaces.

EDS	**Composition (wt.%)**					
	Al	**Cu**	**Mg**	**Ti**	**O**	**Si**
1	90.51	0.65	2.84	-	6	-
2	67.81	1.24	5.95	-	25	-
3	96.24	-	3.76	-	-	-
4	86.5	-	4.57	8.28	-	0.65
5	87.2	-	-	-	-	12.8
6	72.66	-	7.28	14.93	5.13	-

Besides oxidation, Mg also reacts with Al (Figure 3-9 (b), EDS-3 and Figure 3-9 (d), EDS 1, 4 and 5). At equilibrium, Al-Mg forms stable intermetallic compounds, β-Al_3Mg_2, with a large unit cell containing 1168 atoms [157] and the ɤ-$Al_{12}Mg_{17}$ phase, which has a cubic structure but with a much smaller unit cell containing 58 atoms [158]. Both of these intermetallic compounds are brittle in nature and affect the mechanical properties of resultant alloy [159,160]. The overall effect of Cu content in joining alloy is assumed as positive on the properties of the brazed joint.

At the eutectic temperature (577 ^{o}C), the solubility of Si in Al reaches around 1.6% giving α+Si eutectic. When the system is slowly cooled to a room temperature, Si precipitates and the undesired coarse and brittle flakes of Si appears (Figure 3-9 b, EDS 2 and 3) [161].

Aluminium is referred as an alpha stabilizer for Al-Ti alloys which stabilizes alpha to higher temperatures. In Al-Ti system, at higher temperatures, apart from α and β phases, develop α_2 (Ti_3Al phase) and ɤ (TiAl) intermetallic phases. Both of these phases have higher melting temperature [162] (Figure 3-9 (b), EDS 1 and 4) which are not desired for brazing processes.

3.5.1.3 Al-7046/Zn-based alloys/Al-foam joints (AFS-E and AFS-F)

AFS panels (E and F) with Al-7046 facing skins and Al-foam as a core material were produced using Zn based joining alloys. Al-alloys of 7000 series contains Zn, Mg and Cu alloying elements. Al-alloys of 7000 series shows high strength, good machinability and corrosion resistant. However, these alloys display poor weldability due to poor solidification microstructure, porosity infusion zone and they lose their mechanical strength when are welded by fusion welding techniques [163]. Figure 3-10 shows the macro images of AFS-E and AFS-F panels produced using Zn based joining alloys.

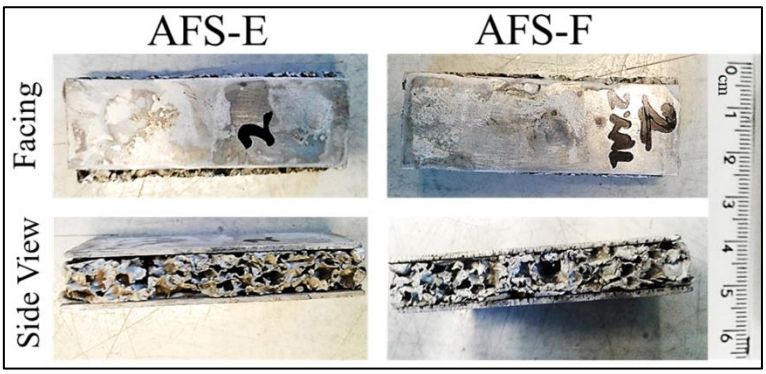

Figure 3-10. Facing and cross-sectional view of (a) AFS-E produced using pure Zn as a joining alloy, and (b) AFS-F produced using Zn2Al as a joining alloy.

Figure 3-11 represents the SEM images of the Al-7046/Al-foam joints produced with Zn based joining materials. Figure 3-11 (a), (b), (d) and (e) shows the diffusion affected zones of the joining substrates along the Al-7046 sheet/Al-foam interface. The dendritic microstructure visible in the diffusion zone was similar to that observed when Al-6016 were soldered to Al-foam using the same joining alloy.

The phenomenon of Zn diffusion into the aluminium substrates is discussed in detail in Section 3.5.1.1. As observed and discussed in section 3.5.1.1 and Section 3.5.1.2, the porous morphology appeared due to the fact that during brazing Al-Zn joining melt is produced at the Al-7046/Al-foam interface. During cooling the joining melt contracts leaving porous morphology in the diffusion zone, as can be seen in Figure 3-11.

Tomoshi et al. [164], experimented quaternary and ternary inter-diffusions to investigate the concentration profiles in 7000 series aluminium alloys and reported that at T > 481 ^{o}C the diffusion distance of Zn is higher with respect to other elements such as Mg and Cu, due to its higher inter-diffusion coefficient. This reasoning also supports the diffusion of Zn through Al-7046 facing thickness at some points. However, a careful optimization of brazing conditions can control the extent of diffusion into the joining substrates (Al-foam and Al-Skin).

At the optimized brazing conditions, the diffusion of Zn into AFS (E and F) joining substrates (Al-7046 sheet and Al-foam) was observed to the distance in the range of 200 µm – 600 µm from the Al-7046/Al-foam interface. Bigger diffusion zones were observed in the areas where the Al-foam cell walls were touching the Al-sheet and are representing the connecting points at the Al-sheet/Al-foam interface.

The chemical composition of the phases in dendritic segregation, identified in Figure 3-11 (c) and (f) analysed by EDS, are reported in Table 3-6.

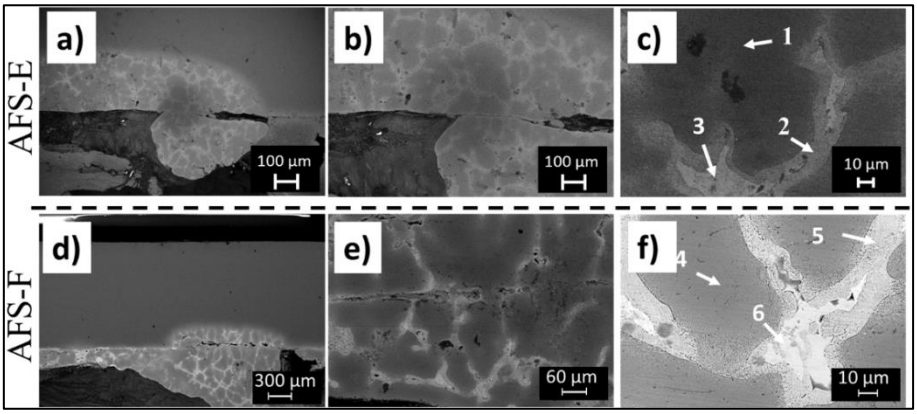

Figure 3-11 SEM micro-images (a) and (b) Al-7046/Pure Zn/Al-foam interface, (d), (e) and (f) Al-7046/Zn2Al/Al-foam interface.

The EDS analysis of the interdendritic segregations in the diffusion zones mainly exhibits Al and Zn rich phases. The major part of the dendritic segregation was observed as Al-rich phase (Al-Zn system) which is darker in colour and almost rounded in shape. The Zn rich phase is lighter in colour, surrounds the darker Al-rich zones and looks like grain boundary in the diffusion zone. A third phase in the lighter zone of the dendritic region was observed; mainly composed of Zn and Mg.

The dendritic segregation in Al-foam at the diffusion zone was found almost similar to that of Al-sheet. However, a certain amount of oxides was observed and the possible reason for that is the presence of Mg in the facing skins which has possibly reacted with oxygen from air trapped within the foam cells.

Table 3-6. EDS Analysis of AFS-E and AFS-F joining interfaces.

EDS point	**Composition (wt.%)**

	Al	Zn	Mg	Ti	O	Zr
1	53.13	46.4	-	0.48	-	-
2	1.22	92.74	6.04	-	-	-
3	43.98	55.84	-	-	-	0.18
4	67.49	32.51	-	-	-	-
5	24.34	75.66	-	-	-	-
6	1.22	80.72	14.52	-	3.2	-

The traces of Ti in Al-7000 series activates grain refining. The Al_3Ti particles act as nucleation sites and moreover lead to smaller Precipitate Free Zones (PFZ) and finer grain boundary precipitation [165]. The Zr content in Al-7000 series (Al-7046) reacts with Al_3Ti compounds to make it a less effective nucleation site [44]. During the SEM and EDS analysis, hard insoluble brittle particles of the $FeAl_3/FeAl_6$ type were observed along grain boundaries together with $MgZn_2$ or $Mg_3Zn_3Al_3$ along and grain boundaries and inside the grains.

3.5.1.4 Effect of Post Brazing Thermal Heat Treatment on the microstructure

3.5.1.4.1 Al-7046 Alloy sheet

Figure 3-12 represents the SEM images of the as received and thermally treated Al-7046 alloys. The alloying element in as received Al-7046 alloy were found well-dispersed Figure 3-12 (a) and (b), and a small number of isolated regions, were observed at a higher magnification, with a high percentage of Ti and Fe, almost round in shape and of average dimension around 1 µm in diameter. These areas are spread all over the microstructure with continuity.

A.A 7046 contains Mg, Cu, Zn with additives such as Cr, Mn, Zr and the ever-present Fe and Si traces. In the cast form, it forms one or more types of $(Fe, Cr)_3SiAI1_2$, Mg_2Si, and a pseudo-binary eutectic phase of Al and $MgZn_2$, EDS 1 and 2 (Figure 3-12 (c)). During the heat treatments (BHT-1/BHT-2), the iron-rich phases transform into AI_7Cu_2Fe [166]. The grain boundaries, hexagonal and octagonal in shape, were observed in specimens after subjecting to simulated BHT-1 thermal treatment. The grain boundaries were composed of 1-2 µm thick and 5-10 µm long crystal compounds in BHT-1 specimen and around 1 µm thick and 3-4 µm long precipitate crystals in BHT-2 specimens. The higher amount of such precipitates was observed along the grain boundaries in BHT-2 specimen morphology, Figure 3-12 (d), (e), compared to BHT-1 specimens Figure 3-12 (j), (k). The EDS analysis of the points indicated in Figure 3-12 are reported in Table 3-7.

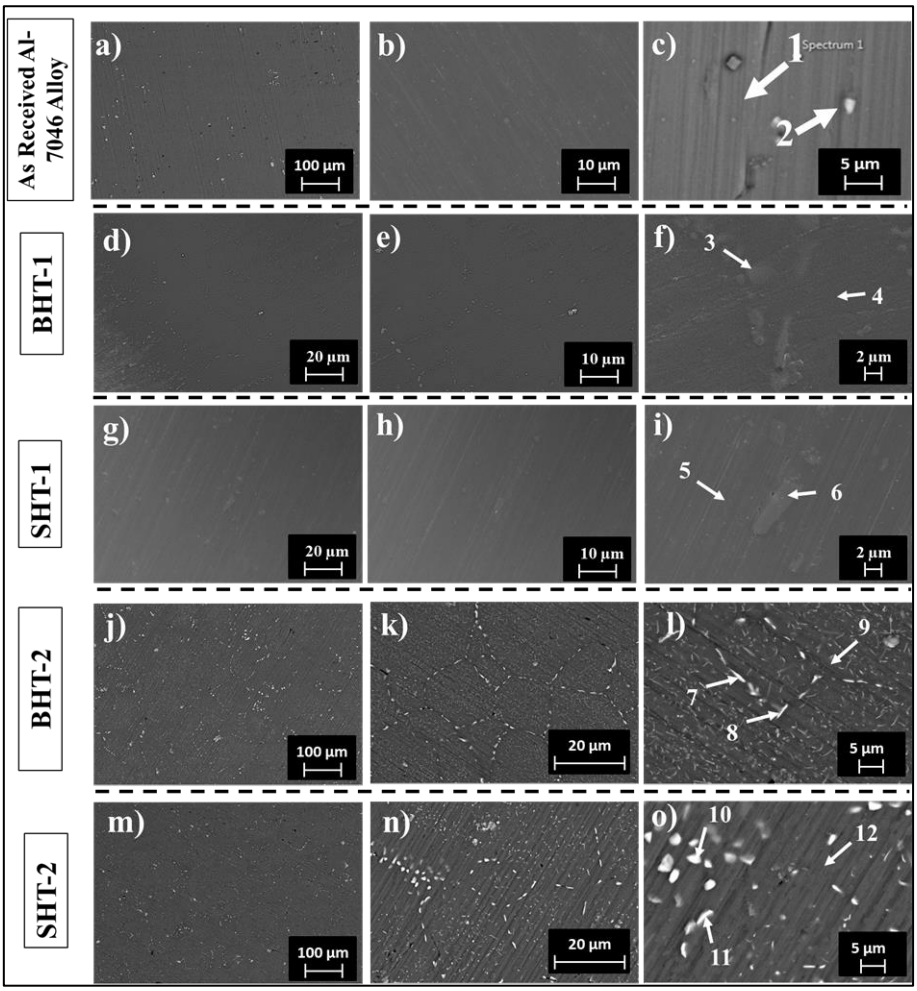

Figure 3-12. SEM (a), (b) and (c) As received Al-7046 surface, (d), (e) and (f) BHT-1 Al-7046 surface, (g), (h) and (i) SHT-1 Al-7046 surface, (j), (k) and (l) BHT-2 Al-7046 surface, (m), (n) and (o) SHT-2 Al-7046 surface.

The SHT specimens, which were solutionised after the brazing heat treatment, displayed a redistribution of precipitates along the grain boundaries into the Al matrix. The SHT process decreased the number of precipitates by dissolving them back into Al matrix but not to the level of the as-received specimen. The crystal-shaped precipitates in the grain boundaries of BHT specimens now became almost rounded in shape with 1-2 µm diameter in SHT-2 specimens which is close to the precipitate size observed in as received specimens. Unlike BHT-2 specimens, the apparent grain boundary did not disappear completely in SHT-2 specimens, but less number of the precipitated crystals were observed.

During the artificial ageing of the A.A 7xxx-series, the α solid solution transforms into GP zones which is followed by metastable phase, η'[167]. The hardened state of A.A 7xxx-series is due to the fine distribution of metastable hexagonal or pseudo-hexagonal phase η' precipitates into the Al matrix [168]. During the brazing/soldering process, these precipitates agglomerate along the grain boundaries while the solution heat treatment adopted in this activity helped the redistribution of precipitates.

Table 3-7 Electron Dispersion X-Ray (EDX) spectroscopy analysis of Al-7046 alloy sheet microstructure before and after the thermal treatments.

EDS	Composition, wt. %					
	Al	**Zn**	**Mg**	**Fe**	**Ti**	**Mn**
1	90.16	7.07	1.53	0.44	-	0.8
2	66.43	6.33	1.1	4.86	21.27	-
3	91.54	6.75	1.72	-	-	-
4	39.94	45.77	14.29	-	-	-
5	91.54	6.75	1.72	-	-	-
6	65.31	-	-	34.69		
7	87.88	10.18	1.94	-	-	-
8	89.63	8.57	1.8	-	-	-
9	91.74	6.75	1.51	-	-	-
10	86.31	11.64	2.05	-	-	-
11	80.05	16.51	3.44	-	-	-
12	80.05	16.51	3.44	-	-	-

During the solution heat treatment, Mg (Zn, Cu, AI)$_2$ rapidly begins to dissolve while Al_2CuMg precipitates at the same time. These precipitates need high temperatures with lengthy dwells to become completely dissolved. In a well-solutionised wrought alloy contains AI_7Cu_2Fe, $(Fe, Cr)_3$ $SiAI_{12}$, and Mg_2Si phases along with the dispersoid. Recrystallized grains are extremely elongated but sometimes appear flattened due to the dispersoid banding. The un-recrystallized regions hold very fine sub-grains in which the boundaries are ornamented by hardening precipitate. It is the dispersoids that inhibit recrystallization and the formation of the fine sub-grain structures [166].

3.5.1.4.2 Effect of Post brazing heat treatment on AFS-E and AFS-F joining seam

Figure 3-13 and Figure 3-14 represents the SEM images of the AFS-E and AFS-F cross section after the solution heat treatment.

It was observed that during the solution heat treatment, most probably during the quenching step, the joining seam was affected. As the thermal conductivity of the Al-foam is very low with respect to massive Al-skin, this difference can create several defects mostly at the joining seam. The water entering the Al-foam cells during quenching of AFS specimens produce water vapours and the consequent pressure exerting on the facing skin. This pressure can even delaminate the facing skins if too much water enters the foam cells at once. However, the shower quenching adopted in this experiment reduced this effect by allowing only a few drops to enter hot Al-foam cells compared water tub quenching (by dipping).

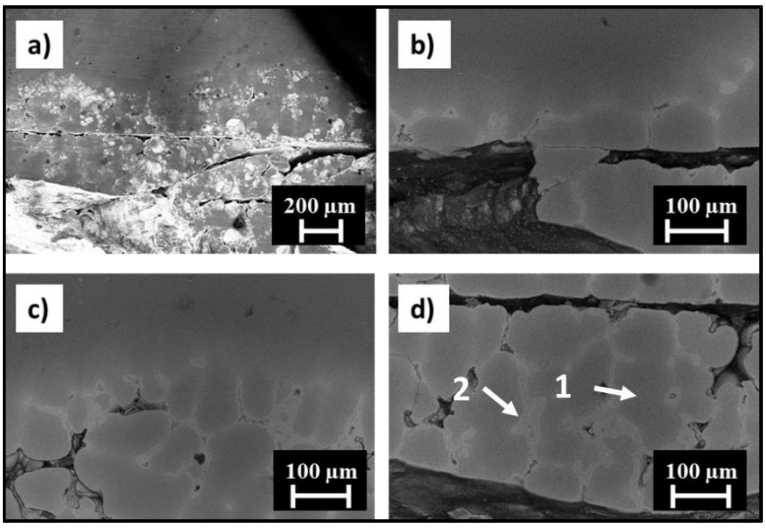

Figure 3-13. SEM micro images SHT-2 Al-7046/Al-foam joint interface using Pure Zn as joining material.

After the solution heat treatment, along with dendritic segregation in the diffusion zone, large precipitates of alloying elements were observed agglomerated in the Al-foam, Figure 3-14 (d). In the past studies, Al-foam was observed unaffected when the joining processes were below < 450 ^{o}C [49,133,169]. The micro-structure of Al-foam, however, was observed affected when subjected to prolonged thermal treatment (experiment 3) after brazing process in the range 490-510 ^{o}C. Although the quenching step for AFS was optimised, the Al-7046/Al-foam interface was observed affected when the facing skins were rapidly cooled compared to the Al-foam.

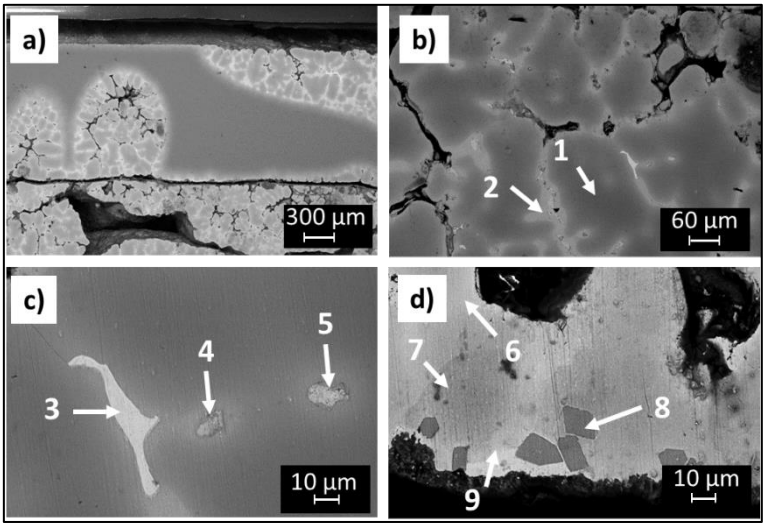

Figure 3-14. SEM micro images SHT-2 Al-7046/Al-foam joint interface using Zn2Al alloy as joining material.

It can be assumed that the solution heat treatment of AFS specimens have both positive and negative effect on the mechanical properties of the AFS sandwich panel. The Al-facing skins properties are recovered to a certain extent but the

agglomeration of secondary phase particles in the Al-foam most probably affect the mechanical properties of the AFS specimen. The chemical composition of the regions identified in Figure 3-14 are reported in Table 3-8.

Table 3-8 Electron Dispersion X-Ray (EDX) spectroscopy analysis of BHT-2 AFS-E interface and SHT-2 AFS F interface.

b	**Composition (wt.%)**	**c**	**Composition (wt.%)**	**d**	**Composition (wt.%)**
1	69.26 % Al - 30.74 % Zn	**3**	2.90 % Al – 97.10 % Zn	**6**	48.20 % Al – 51.80 % Zn
2	0.59 % Mg - 32.82% Al - 66.59% Zn	**4**	10.28 % Mg - 21.52 % Al – 0.62 % Fe -67.58 % Zn	**7**	53.25 % Al – 46.75 % Zn
		5	12.72 % O – 9.31 % Mg - 10.68 % Al - 67.29 % Zn	**8**	3.31 % Mg – 67.98 % Al – 0.83 % Si – 27.88 Zn
				9	35.06 % Al – 64.94 % Zn

The slow cooling after the brazing/soldering thermal treatment led to a random distribution of precipitates. A.A 7046 with higher Mg, Cu and zinc content, has more Al_2CuMg to be dissolved at the solutionizing temperature compared to other dilute Al-alloys which can rapidly dissolve all of the zinc-rich phases. The overheating of 7xxx Al-alloys results in the segregated regions with unusual concentrations of AI_2CuMg. Rosettes may appear if alloys contain Al_2CuMg phase are subjected to very high heating rates due to inadequate time for diffusion and particle dissolution before exceeding the nonequilibrium eutectic temperature [166].

3.5.2 Micro Hardness Analysis

3.5.2.1 AFS Specimens

Polished cross-sections of the AFS specimens were subjected to microhardness test to analyse the effect of soldering/brazing process on the hardness of the base components. Vickers hardness values were obtained in the Al-sheet, joint seam (diffusion zone) and Al-foam area. The average Vickers hardness values of the base components before and after the joining thermal treatment are plotted, Figure 3-15.

The average microhardness of the Al-alloys, Al-6016 and Al-7046 was found almost similar. The as-received Al-foam displayed around 48 % lower microhardness with respect to the as-received massive Al-sheets. It was observed that brazing in the range of 580 ^{o}C – 610 ^{o}C, adopted for AFS-C and AFS-D, affected the microhardness of Al-6016 plates by around 37 %, while the Al-foam

somehow showed a little improvement in the microhardness after brazing treatment. The microhardness observed near the joining seam in AFS-C and AFS-D was around 23% higher with respect to Al-6016 after the brazing process.

After brazing, the Al-7046 sheets in AFS-E and AFS-F displayed around 27 % lower hardness compared to the as received while the micro-hardness of Al-foam showed improvement by 23 %. The microhardness observed in the diffusion zone of AFS-E and AFS-F specimens at the interface were around 32 % higher with respect to Al-7046 after brazing.

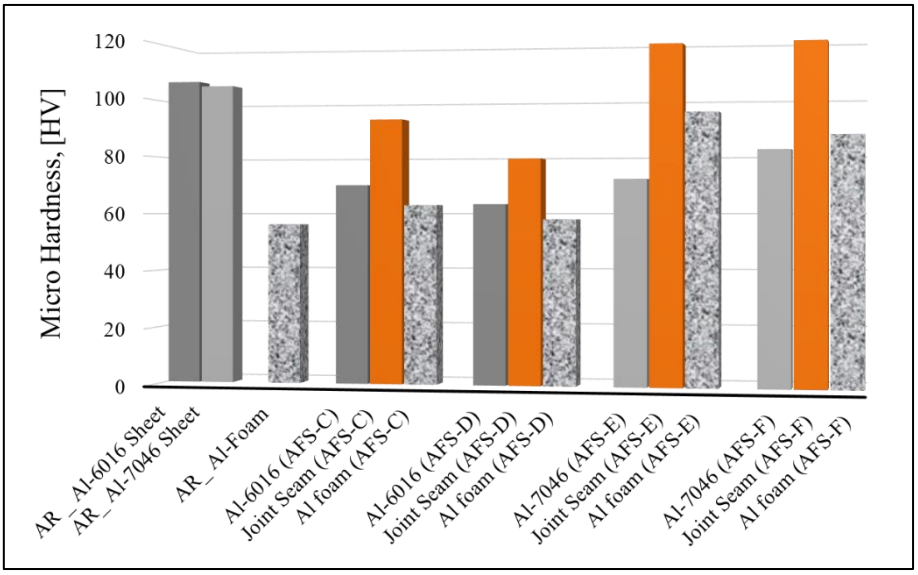

Figure 3-15 Microhardness test average results for base materials before and after soldering/brazing.

As a whole, a decrease in the microhardness of Al-sheets was observed after the brazing process due to the precipitation of strengthening elements. Higher microhardness values observed in the diffusion zones are due to the formation of secondary hard phases. The brazing process apparently did not affect the hardness properties of Al-foam and a slight improvement in hardness was observed. As discussed in earlier sections, it is because the Al-foam was produced by solidification from a liquid state (> 700 ^{o}C) and will require higher temperature or prolonged thermal exposure to affect the micro-structure. Relatively noticeable diffusion of agglomerated precipitates occurred during the high-temperature brazing process (AFS-E and AFS-F) resulted in the increase of microhardness values of the Al-foam, most probably due to the redistribution of agglomerated secondary phases.

3.5.2.2 Effect on Micro Hardness by Post Brazing Heat Treatment

Figure 3-16 represents the average microhardness values recorded for as the received and the heat-treated Al-7046 specimens. Around 27 % decrease in the hardness of Al-7046 alloy was observed after the BHT-1 heat treatment. The SHT-

1 heat treatment leads to the recovery of around 21 % hardness of the Al-7046 alloy sheet.

The BHT-2 heat treatment caused around 34 % decrease in the hardness of Al-7046 alloy sheet. But when the BHT-2 heat treated Al-7046 sheet was further subjected to the SHT-2 heat treatment around 17 % hardness of the Al-7046 alloy sheet was recovered. At higher temperatures, the precipitation kinetics are faster, but the hardening is less effective because of non-homogenous nucleation and the over ageing starts before the peak is reached. Moreover, the Vacancy Rich Clusters (VRC) are not retained at higher temperatures, therefore, the density of hardening precipitates will be low. This behaviour could be due to Al_3Zr compounds that don't dissolve at a high-temperature treatment and act as nucleation sites for hardening precipitate η' phase [45-49].

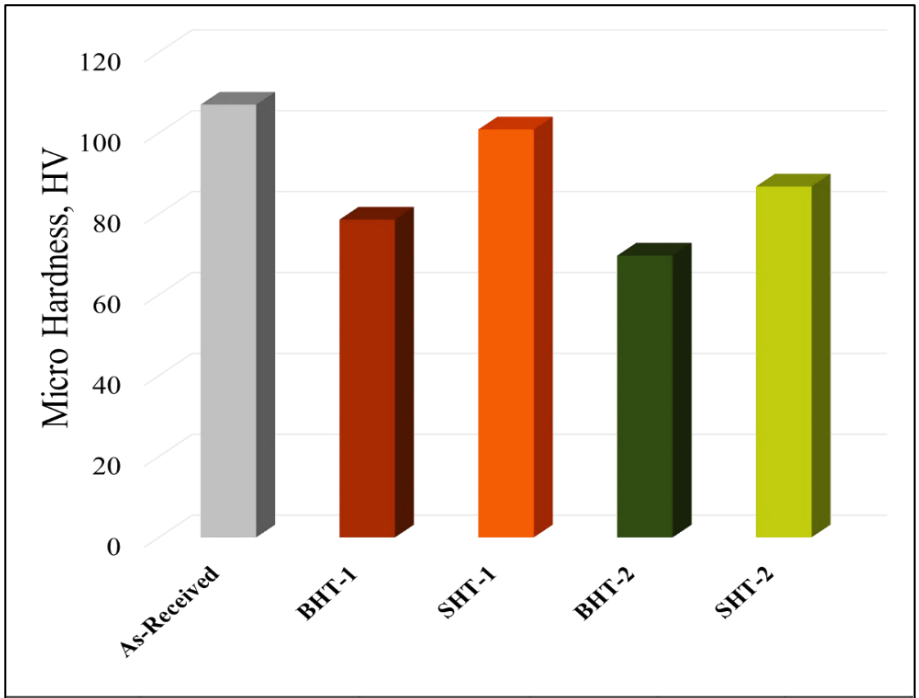

Specimen	As Received	BHT-1	SHT-1	BHT-2	SHT-2
HV (Average)	107	78.57	100.85	69.67	86.76
S.D	14,4	13,64	11,01	12.6	9.6

Figure 3-16 Micro hardness analysis of as received and thermally treated Al-7046 alloy.

When the Al-7046 alloy was subjected to BHT heat treatment, in both the experiments (1 and 2), a clear grain boundary appeared, and the precipitates of the alloying element were observed agglomerated. The agglomeration of alloying elements decreases the mechanical properties of the Al matrix and hence affects its hardness and overall performance. However, during brazing, it is difficult to avoid such occurrences, therefore a solution heat treatment was proposed which showed a successful redistribution of the agglomerated precipitates into the matrix and

recovered the microstructure of the BHT heat treated Al-7046 alloys to a certain extent.

The microhardness of the Al-7046 skin/Al-foam interface was determined in three distinct sections as identified in Figure 3-17.

The microhardness of the Al-skin, where there was no diffusion, increased by around 12 % for AFS-E and around 15 % for AFS-F after the solution heat treatment (SHT-2). The SHT-2 showed a pronounced effect on the microhardness of the diffusion zone. Around 30 % and 32 % improved in the microhardness of the diffusion zone at the joining interface of AFS-E and AFS-F was observed respectively. However, the micro-hardness of the Al-foam was not observed affected after the SHT-2 compared to the brazed specimens.

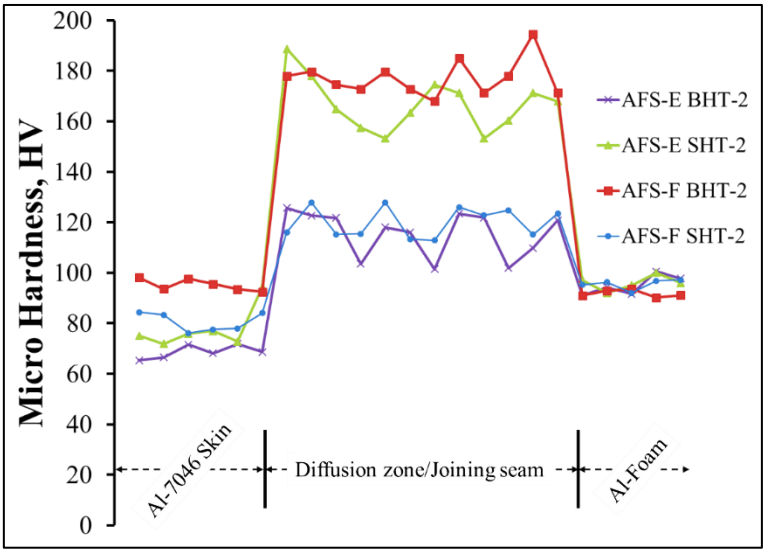

Figure 3-17. Microhardness analysis of the Al-skin/Al-foam interface in AFS-E and AFS-F specimens before and after the solution heat treatment (SHT-2).

The phenomenon behind the recovery of mechanical strength and the hardness of Al alloy of 7000 series lies in the redistribution of the precipitates in its microstructure. The alloying elements are basically added to the Al matrix to enhance its mechanical properties and hardness. These elements make different phases distributed throughout the matrix of the parent material. The increase in the microhardness values is attributed to the formation of GP-zones during ageing [166].

3.5.3 Flexural Properties

3.5.3.1 Flexural Behaviour of AFS Base components (Al-Sheets and Al-foam)

The results reported in Figure 3-18 (a) and (b) shows the behaviour of the Al-6016, Al-7046 sheets and Al-foam plate subjected to three-point bending test. The curves of load-cross head displacement for Al-sheets almost overlap while those

for Al-foam display a scattered behaviour due to the non-homogeneity of the pore size and distribution. The curve for Al-sheets, evidence improvement in ductility and decrease in stiffness after the heat treatment (simulated brazing conditions).

In the initial part of the bending curve, the AFS base materials display elastic behaviour until the maximum bending strength. Beyond the maximum bending load value, the specimens started to deform plastically but with a different behaviour. The Al-sheets display strain hardening behaviour at increased deformation until the loading was stopped. The Al-foam showed strain hardening behaviour until 50 N and 1.5 mm of displacement, when it needed the maximum load required for deformation followed by local plastic deformation in the foam cell walls at the load contact point, which resulted in the reduction of bending strength to around 30 N. After the displacement of 7 mm, bulking effect was observed where the porous material starts behaving like a massive material.

A decrease of ~60% in bending load was observed for the Al-6016 sheets after the thermal treatment similar to the soldering conditions adopted for AFS-A and B joining and around 70 % decrease in the bending strength was observed for Al-7046 sheets after subjecting to the brazing thermal treatment adopted to braze the AFS-E and D.

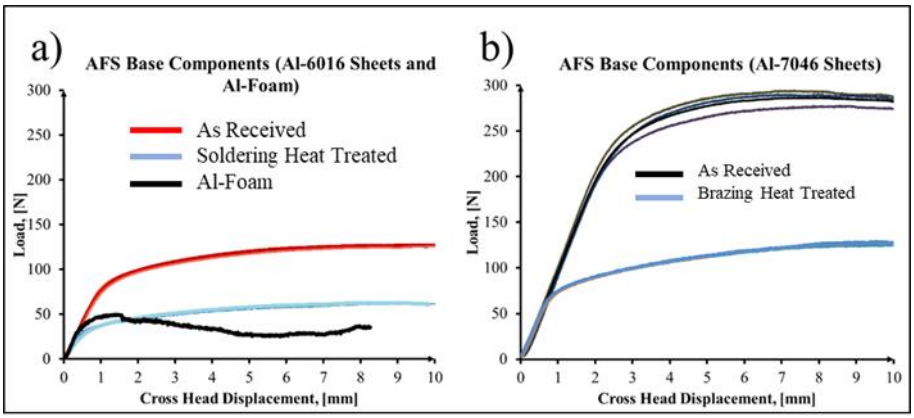

Figure 3-18 Behaviour of AFS base components before and after the soldering/brazing treatment subjected to the static three-point bending test.

The Al-foam, which is basically obtained by the solidification of liquid Al-melt having air/gas bubbles was observed unaffected and showed no prominent effect on mechanical properties in post heat treatment samples when subjected to the three-point bending test. The bending stiffness of Al-foam cannot be compared to Al-sheets due to the difference in the thickness of corresponding test specimens. The decrease in bending strength of Al-sheets is related to over ageing phenomenon. Average three-point bending results of AFS base components are reported in Table 3-9.

The deformation response of the only Al-foam can be divided mainly into three progressive stages. The first stage involves the localized plastic straining at cell nodes; the second stage involves plastic buckling, elastically constrained by surrounding cells [170] and the third one involves the consequent plastic collapse of cells with the increase of strain.

3.5.3.2 Flexural behaviour of AFS specimens

Figure 3-19 represents the behaviour of the AFS-A, AFS-B, AFS-C, AFS-D and AFS-F composite specimens subjected to a flexural load. Average three-point bending results are reported in Table 3-9.

The scattering observed in the load curves, presented in Figure 3-19, was mainly due to the non-homogenous distribution of pores in the Al-foam core. The AFS specimens showed an initial elastic behaviour which reaches the maximum bending strength value. After the maximum bending strength, the elastic behaviour was followed by a plateau region representing the energy absorbing behaviour of AFS mainly due to the porous core material. Longer plateau region with constant or slightly increasing/decreasing trend for an extended crosshead displacement was corresponing to the energy absorbing capacity of each AFS specimen.

The AFS components produced using Zn2Al as a joining material showed slightly higher bending strength compared to AFS components produced using pure Zn foil. The AFS specimens produced at a lower temperature using Zn based joining alloy showed improved joining properties, responded with higher bending strength values and displayed improved energy absorbance capacity for extended displacement before failure compared to AFS specimens produced at a higher temperature with the Al-based amorphous joining alloys.

The lower mechanical properties of AFS-C and AFS-D are due to the development of brittle intermetallic compounds [159], observed in the brazed joining microstructure, which can be, however, avoided by controlling the extent of oxidation by further optimization of the brazing process and the joining materials.

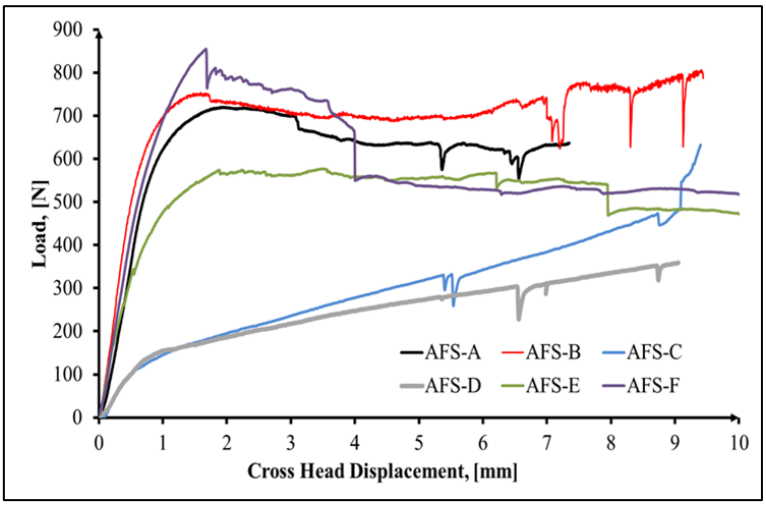

Figure 3-19 Comparison of the flexural response of the AFS composite panels

Figure 3-20 represents the post flexural test images of the AFS specimens. The failure modes of the AFS specimens were investigated during the three-point bending tests with the help of a digital camera to record the step-by-step deformation.

The AFS specimens displayed a multi-stage collapse behaviour during the flexural test. After the maximum bending strength, the deformation in the sandwich specimens with a localized deformation of the skin initially at a load contact point. During the plateau regime, Al-foam compression right beneath the central head cylinder was observed, which was followed by shear displacement until the cracks appeared, mainly in the core along an approximate centre line of the core material.

A sharp drop in the load curve corresponds to the failure of a joining point at the Al-foam/Al-skin interface, partial or complete delamination. It was observed that AFS-A and AFS B did not show delamination and the failure was mainly due to the collapse of core material due to excessive after the extended plateau region as the progressive collapse of the foam cells was followed shear stress along the Al-sheet/Al-foam interfaces.

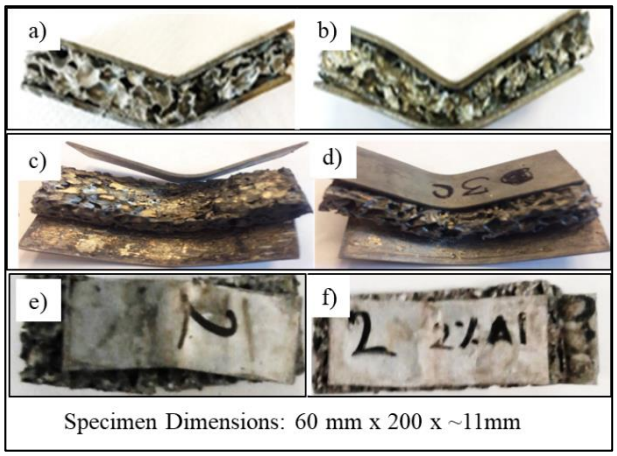

Figure 3-20 Post three-point bending test - representative AFS specimens: a) AFS-A, b) AFS-B, c) AFS-C, d) AFS-D, e) AFS-E, f) AFS-F

If the induced shear stresses along the joining interfaces are higher than the Al-sheet/Al-foam joint strength face skin, the delamination occurs otherwise failure occurs due cracks produced by shear stresses in the core, along with the midline of Al-foam [169,171]. AFS-C and AFS-D specimens were observed completely delaminated due to lower Al-Skin/Al/Foam joint strength. The AFS-E the AFS-F specimens did not display a complete delamination even when the cross-head displacement reached 10 mm, where all the three-point bending test events were put to stop.

The decreasing trend in flexural load after each big sharp drop shows a potential loss in flexural strength of the AFS composite panels. The collapse behaviour of AFS components involves localized indentation at the loading point, core compression, core shear and sometimes cracks in the Al-foam, along with face skin buckling (top skin) or face skin delamination (top or bottom skin) after a certain amount of deflection, as also reported in [126,172].

Table 3-9. Average results of three-point bending test.

Base Material	Joining Parameters	Joining Material	Specimen Dimensions, [mm^3] *	Approx. Service Temperature	Bending Strength, [N]
AL-Foam (Post heat treatment)	-	-	60x20x9		40±10
Al-6016 (As received)	-	-	60x20x1.2		80±3

Al-6016 (Post heat treatment)	-	-	60x 20x1.2		35±3
Al-7046 (As received)	-	-	60x 20x1.3		251±10
Al-6016 (Post heat treatment)	-	-	60x 20x1.3		75±3
AFS-A: Al-6016/Al-foam	1 min @ 420 ºC	Pure Zn foils	60x20x11.4	**380 ºC**	711±50
AFS-B: Al-6016/Al-foam	5 min @ 430 ºC	Zn2Al alloy strips	60x20x11.4	**380 ºC**	751±60
AFS-C: Al-6016/Al-foam	10 min @ 580 ºC	Al-Cu-Mg amorphous alloy	60x20x11.4	**520 ºC**	126±20
AFS-D: Al-6016/Al-foam	10 min @ 590 ºC	Al-Si-Mg-Ti amorphous alloy	60x20x11.4	**520 ºC**	155±20
AFS-E: Al-7046/Al-foam	5 min @ 490 ºC	Pure Zn foils	60x20x11.6	**450 ºC**	566±20
AFS-F: Al-7046/Al-foam	5 min @ 510 ºC	Zn2Al alloy strips	60x20x11.6	**470 ºC**	854±20
Al-1100/Al-Foam [173]	60 min @ 180 **ºC, 100 kPa**	Epoxy	150x35x12	**~100 ºC**	450
Al 3104-H19/Al-foam [173]	Adhesive	Epoxy	150x35x12	**~100 ºC**	650
Al-5056/Al-foam [133]	2 min @ 450 ºC, 2-3 kPa	Zn6.2Al4.3Cu1.2Mg0.8Mn0.5Ag alloy	60x15x17.4	**350 ºC**	930

**Specimen Dimension: Length(l) x Width(b) x Thickness (t).*

The results of current work are compared to the results reported by other researchers in the recent past in Table 3-9. Since the adoption of different test parameters such as span length [102,104], cross-head velocity [103,174], core and skin thickness [173], during the analysis of flexural properties of AFS components results in dissimilar values, the comparison of results may be inappropriate and difficult [126].

The AFS composites panels produced by soldering or brazing (in this research work) and by other researchers in the recent past [49,133,173] showed higher mechanical properties, Table 3-9, compared to AFS-C and AFS-D. However, the applications of the former are limited to service temperature below ~380 ^{o}C. The AFS-C and AFS-D composites offer service temperature up to ~520 ^{o}C for applications where low mechanical strength and high thermal stability is a requirement.

3.5.3.3 Effect of post-brazing thermal treatment on flexural behaviour of Al-skin

Figure 3-21 shows the average behaviour of AR and thermally treated Al-7046 alloy specimens subjected to a flexural load. It was noticed that after the thermal treatment (similar to brazing parameter adopted in this study) the bending strength of Al-7046 alloy was severely affected. When subjected to a flexural load, besides the decrease in bending, the deformation in heat treated specimens initiated at lower cross head displacement compared to as received specimens.

The results obtained in experiment 1 show around 35 % decrease in the bending strength of the Al-7046 alloy sheet after the thermal treatment at 450 ^{o}C for 10 min. Around 10% bending strength was recovered after the solution heat treatment (370 ^{o}C for 600 min followed by water quenching) of these specimens. This improvement in bending is attributed to the redistribution of fine precipitates, mainly of the metastable η’ phase $MgZn_2$, which is possible by artificial ageing from a supersaturated solid solution [175,176].

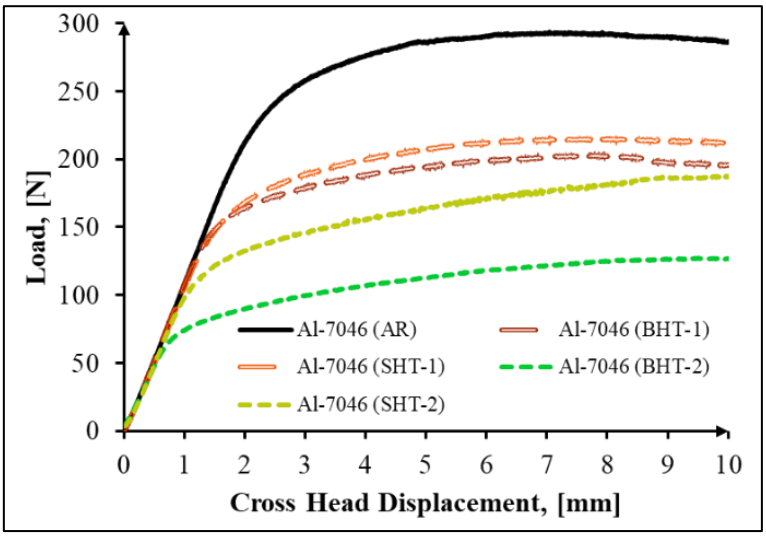

Figure 3-21. Comparison of bending behaviour of as received, and thermally treated Al-7046 alloy subjected to a transverse load.

In experiment 2 when the Al-7046 alloy sheet specimens were subjected to thermal treatment at 500 ^{o}C for 5 min, around 70 % decrease in the bending strength was observed compared to the as-received specimen. However, when these heat-treated specimens were subjected to solution heat treatment (370 ^{o}C for 180 min followed by water quenching), around 20 % of the lost bending strength was recovered.

It can be, therefore, assumed that the deterioration in the mechanical properties of 7000 Al alloys remarkably increases with the increase in brazing temperatures. The solution heat treatment temperature was set around 10 degrees below the eutectic temperature of Al. The dwell time was decreased because it was noticed that with shorter dwell time the similar amount of recovery in microstructure can be achieved [177]. The proposed solution heat treatment can be further optimized to achieve more stable microstructure and recover the lost mechanical properties, which will be focused in future.

3.5.3.4 Effect of post-brazing thermal treatment on flexural behaviour of AFS specimens

Figure 3-22 represents the average flexural behaviour of brazed and post-brazing solution heat treated AFS-E and AFS-F composite specimens subjected to a transverse load. All the specimens displayed initial elastic behaviour till the maximum bending load followed by a slightly decreasing plateau region. The average bending strength values obtained in experiment 3 are reported in Table 3-10.

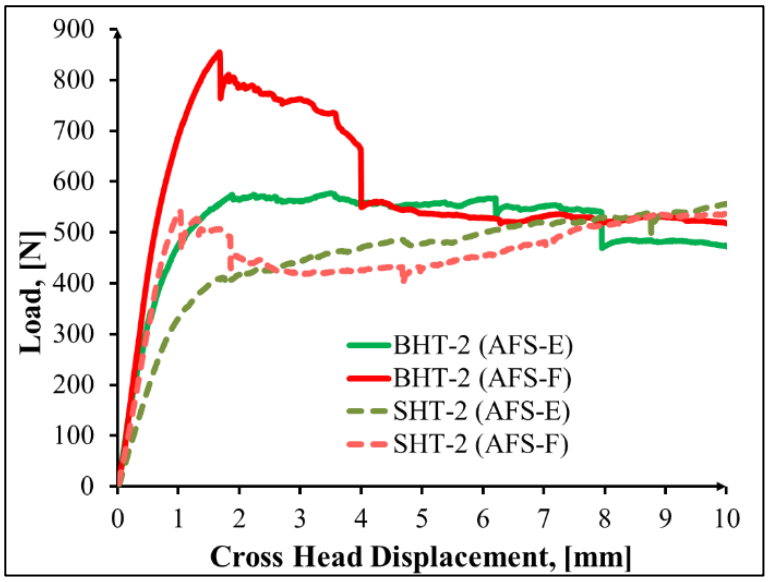

Figure 3-22. Comparison of the flexural behaviour of the AFS-E and AFS-F specimens before and after the solution heat treatment.

Unlike Al-7046 alloy sheet specimens, the AFS composite specimens is a rather complex structure and responded differently to the solution heat treatment. Around 27 % - 35 % decrease in the mechanical properties of the AFS composite specimens was observed when the brazed specimens were subjected solution heat treatment (370 ^{o}C for 180 min followed by water shower quenching).

The early failure and complete delamination of solution heat treated specimens, shown in Figure 3-23, are mainly due to lower joint strength. The reasons for the decrease in the flexural properties of AFS was the lower joining strength at the Al-7046/Al-foam interface. The interface strength was deteriorated during the solution heat treatment process where during the shower quenching, the facing skins were rapidly cooled compared to Al-foam. The resultant contraction of Al-skin upon cooling compared Al-foam affected the joining seam properties.

Figure 3-23 Solution heat treated a) AFS-E and b) AFS-F specimens before and after the three-point bending test.

In general, the Al-foams are produced at temperature ~ 700 ^{o}C [120]. The soldering/brazing heat treatment, for the AFS production, which was carried out for short period of time (~ 5 – 30 min) do not affect the properties of Al-foam. However, when the AFS were subjected to 3 hrs long solution heat treatment at 370 ^{o}C, the aggregation of alloying elements rich precipitates were observed in the aluminium foam cell walls microstructure which resulted in the formation soft matrix patches.

Adopting different test parameters such as span length, cross-head velocity, core and skin thickness, to analyse the mechanical properties of AFS components, results in dissimilar values, which makes the comparison of results very difficult [49]. However, the joining technique and test parameters used in [133,173] are comparable to those used in the current study and the maximum bending loads observed for the AFS produced are compared in Table 3-10.

Table 3-10. Average three-point bending results as received and heat-treated Al-7046 sheets and the AFS-E and AFS-F before and after the solution heat treatment.

Specimen	Heat treatment	Joining Material	Specimen Dimensions, [mm^3] *	Bending Load, [N]
AL-Foam	5 min @ 400 ^{o}C	-	60x20x9	40±10
Al-7046	(As received)	-	60x 20x1.3	251±10
Al-7046	BHT-1	-	60x 20x1.3	171±3
Al-7046	SHT-1	-	60x 20x1.3	185±3
Al-7046	BHT-2	-	60x 20x1.3	77±3
Al-7046	SHT-2	-	60x 20x1.3	127±3
AFS-E: Al-7046/Al-foam	5 min @ 490 ^{o}C	Pure Zn foils	60x20x11.6	566±20
AFS-E: Al-7046/Al-foam	SHT-2	Pure Zn foils	60x20x11.6	410.56±20
AFS-F: Al-7046/Al-foam	5 min @ 510 ^{o}C	Zn2Al alloy strips	60x20x11.6	854±20
AFS-F: Al-7046/Al-foam	SHT-2	Zn2Al alloy strips	60x20x11.6	542±20

Al-1100/Al-Foam [173]	60 min @ 180 **ºC, 100 kPa**	Epoxy	150x35x12	**~100 ºC**
Al 3104-H19/Al-foam [173]	Adhesive	Epoxy	150x35x12	**~100 ºC**
Al-5056/Al-foam [133]	2 min @ 450 ºC, 2-3 kPa	Zn6.2Al4.3Cu1.2Mg0.8Mn0.5Ag alloy	60x15x17.4	**350 ºC**

Microstructural analysis of the solution heat treated AFS specimens revealed the redistribution of fine precipitates in Al-7046 alloy skins and the precipitates agglomeration in the microstate of Al-foam cell walls. Lower hardness values after solution heat treatment also support this argument, hence it was assumed that the decrease in the elasticity of the Al-foam is one of the reasons for lower flexural properties AFS panels.

3.5.4 Finite Element Analysis

Preliminary work on finite element analysis of the above-discussed AFS composites subjected to three-point bending test was conducted using Abaqus software. This work was carried out in collaboration with the Department of Mechanical and Aerospace Engineering, Politecnico di Torino as a final year project of a Master degree student (Mr. Payam Zahidi) under the supervision of Prof. Graziano Ubertalli, DISAT, Politecnico di Torino.

Figure 3-24 concludes the results of finite element analysis of AFS specimen subjected to a flexural load. The details of this work are reported in a separate thesis (available in DISAT library, Politecnico di Torino) under the title “Finite Element Analysis of Al-Foam Sandwich Subjected to Three-Point Bending Test “.

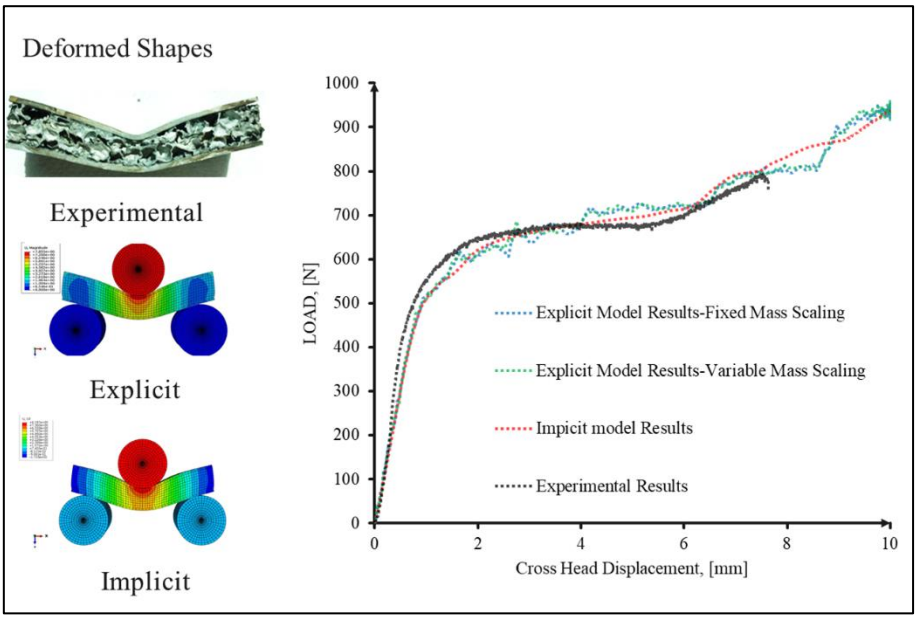

Figure 3-24 Results of finite element analysis of Al-foam sandwich subjected to the three-point bending test.

The preliminary finite element analysis work was concluded with the following two observations:

- DESHPANDE-FLECK Model can be adopted for load-deformation Prediction. Compared to the implicit-static method,
- The explicit-dynamic method can be preferable in 3-point bending test as stability time and Energy values are well controlled.

3.6 Conclusion

Five joining solutions are proposed to join Al-6016 and Al-7046 facing skins to Al-Foam to produce AFS composites using Zn based alloys and Al-based amorphous alloys as joining materials for higher temperature applications.

In the Al-6016/Al-foam and Al-7046/Al-foam joint, the presence of Al-rich and Zn rich dendritic segregation confirms the diffusion of the Zn based joining alloy into the joining substrates.

AFS specimens produced with Zn2Al alloy as a joining material displayed higher flexural properties with respect to AFS components produced with other joining alloys used in this study.

The selection of Al-based amorphous alloys was based on the precursor materials used for Al-foam production. Higher diffusion of Al-Cu-Mg amorphous brazing alloy was observed into the joining substrates with respect to Al-Si-Mg-Ti amorphous alloy.

AFS produced with amorphous alloys as a joining alloy showed lower bending strength before failure compared to AFS produced with Zn based joining alloys due to the formation of hard and brittle intermetallic phases in the joining seam.

The extended plateau region at around constant load for extending cross head displacement in the flexural load curves shows the energy absorbance capacity of the produced AFS composites. Core shear failure was dominating failure mode in AFS-B and AFS-F specimens. AFS-A and AFS-E specimens displayed mixed, core shear and/or partial delamination failure while AFS-C and AFS-D responded with complete delamination.

AFS produced in this study can sustain the operational temperatures from 380 °C to 500 °C. In the current research work, AFS composite panels were produced in a batch furnace, but the joining solutions proposed, favoured by diffusion, can easily be automated in a continuous furnace which can ensure the mass productivity, reproducibility, and lower production costs.

4. Development and Characterisation of Hybrid Dynamic Epoxy/PU Composites for Enhanced Impact Resistance

4.1 Abstract

Despite the several advantages of the Fibre Reinforced Polymer (FRP) thermoset composites over the metallic materials such as high strength-light weight, the former is more susceptible to mechanical damages especially when subjected to impact loads. Moreover, the thermosets are non-repairable and non-recyclable due to non-reversible cross-links in polymer networks.

The introduction of reversible/dynamic chemical bonds into thermoset polymer networks can possibly be a way of overcoming such limitations which can extend the reliability and life expectancy while expanding the usage of thermoset FRPs in structural applications.

In this study, utilizing the dynamic polymer systems, a new approach to enhance the impact resistance of thermoset composites is adopted. Separate CFRP laminates produced with dynamic epoxy and dynamic PU resin systems were joined in three different configurations to obtain hybrid dynamic composites with repairable, recyclable, self-healing and enhanced impact resistance properties. The hybrid dynamic composites were characterised for structural, thermal, flexural and impact properties in comparison to a reference non-hybrid dynamic epoxy composite.

Keywords: Hybrid Composite, Dynamic Thermosets, DMA, Impact resistance, Flexural strength, ILSS.

Graphical Abstract

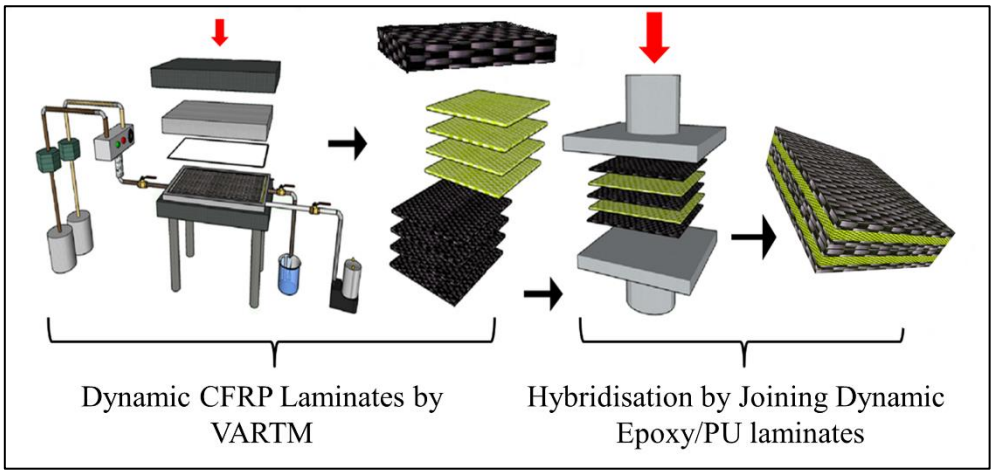

4.2 Introduction

Hybridisation is a successful strategy in the development of new structural materials. Nature shows one of the best examples of the hybridisation potential with the shells of molluscs. The shells are basically composed of one or more ceramic phases and a minimal amount (0.1 to 5%) of proteins. These ceramic phases, such as calcium carbonate ($CaCO_3$) are brittle in nature and wouldn't serve as armour. However, when they are combined with proteins to form a complex layered structure, the resulting bio-composite have exceptional mechanical properties. The fracture toughness and tensile strength of monolithic $CaCO_3$ are 20-30 times lower than the bio-composites of shells [178].

Carbon Fibre Reinforced Polymers (CFRPs) are materials with higher specific strength and stiffness properties for structural applications in automotive and aerospace industries. Despite the several advantages of the FRP composites over the metallic materials, the FRPs show inferior resistance to mechanical damages, even to a low velocity to impact loads. Several efforts are made to improve the mechanical performance of the FRPs but the impact performance of components made of FRPs is still one of the main challenge [179].

4.2.1 Methods to Improve Impact Resistance

Since 70's, the addition of liquid rubbers or rubber particles remained among the most common methods to toughen the thermosets [180,181], however, the melt blending or solvent blending of thermoplastic additives to resin lead to premature curing of the epoxy resin and increase in viscosity [182]. Increase in resin viscosity is a problem related to such approaches. Alternatively, the toughening components can be incorporated into the preforms or at interlayers such as thermoplastic veils, electro-spun nanofibers or thermoplastic fibres woven (Cycom's PRIFORM® system) etc. [183].

Reinforcement hybridisation is another promising strategy to toughen composite materials [184]. The combination of two or more fibre types in a

composite material offer improved balance in mechanical properties [185,186]. Multi-layered structures consisting of stacked metal sheets and FRP thin plates, Fibre metal laminates (FMLs), with high stiffness and strength properties offer excellent fatigue and impact resistance at a cost of higher density [187].

The modification in the chemistry of resin polymers allows vast opportunities to improve the toughness of the matrix material in the FRPs.

The thermoplastics are solid below a given temperature and becomes liquid when heated above. Thermosets offer superior mechanical and thermal properties for permanent parts. Unlike thermoplastics, the thermosets once cured undergo irreversible chemical crosslinking and hence, cannot be repaired, reshaped and recycled. This has recently been made possible by the introduction of reversible/dynamic chemical bonds in polymer networks.

4.2.2 Reversible/Dynamic Thermosets

A reversible bond is a covalent/non-covalent bond that can break and reform under equilibrium conditions [188]. Outstanding improvement in properties is reported with the introduction of covalent adaptable networks (CANs) [189] and vitrimers [190]. The CANs display a drastic drop in viscosity beyond the critic temperature. The vitrimers retains a fixed crosslinking density during the thermal processing and show a restrained drop in viscosity. Therefore, vitrimers are generally characterised by second critic temperature at which the shift from viscoelastic solid to viscoelastic liquid occurs and is defined as topology freezing temperature (Tv). Below Tv, these polymer networks show typical properties of thermosets, but above it, the material display functionalities similar to thermoplastics [189,190].

An alternative approach to preparing dynamic polymer networks based on disulfide bridges in polymer systems is reported in ref [191]. The two most important sulfur-based chemistries introduced in this regard are a thiol-disulfide exchange and the disulfide exchange. In the thiol-disulfide exchange mechanism, the nucleophilic displacement of a thiolate anion from the disulfide occurs through an attack by another thiolate anion [192].

The disulfide exchange is generally stimulated by catalysts, moderate temperature or UV radiation at room-temperature [193]. Itxaso et al. [193] introduced aromatic disulfide cross-links in polyurethanes, poly(urea- urethanes), polyimides and epoxy resins concluding that a radical-mediated [2 + 1] reaction mechanism is responsible for the dynamic behaviour of these materials. Martin et al. [194] demonstrated the reprocessable, repairable and recyclable behaviour of dynamic polymer systems in fibre-reinforced thermoset epoxy composites.

4.2.3 Proposed Solution

Introduction of dynamic functionalities into the thermoset resins open tremendous opportunities for material processing. In this study, utilizing the dynamic polymer systems, a new approach to enhance the impact resistance of thermoset composites is adopted. Individual CFRP laminates using dynamic epoxy and dynamic PU resin systems were produced separately. Hybrid composites were produced by combining/joining the dynamic epoxy and the dynamic PU laminates in different configurations to obtain unique properties of reprocess-ability, self-healing and recyclability with enhanced impact resistance in the composites structure.

The hybrid composites were then characterised for structural, thermal, flexural and impact properties and the results were compared to a reference non-hybrid dynamic epoxy composite.

4.3 Experimental Work

The experimental work was mainly carried out in IK4-CIDETEC, San Sebastián, Spain under a KMM-VIN joint research project.

4.3.1 Materials

Commercial high-strength plain-woven (warp at 0° and fill at 90°) carbon fabric (43199 Hexcell, 200 GSM), supplied by Hexcel Parla Madrid, Spain, was used as reinforcement. Materials used during the VARTM fabrication of FRP laminates such as release film and breather cloth were purchased from Gazechim and the Frekote 770-NC release agent was purchased from Loctite. Modified epoxy resin system was used to produce the dynamic rigid CFR laminates and modified PU resin system was used to produce the dynamic tough laminates.

Polyurethane resin (PU 4000/2000) was synthesised by adopting aromatic disulfide metathesis. Trifunctional poly (propylene glycol) (PPG) (Mn 4000) was purchased from Bayer Materials Science. Isophorone diisocyanate (IPDI, 98 %), dibutyltin dilaurate (DBTDL, 95 %), were purchased from Sigma-Aldrich and were used without further purification.

A commercial bisphenol A (DGEBA, 1) based epoxy resin (Araldite LY1564, density 1.2 g/cm^3, Supplied by Huntsman Advanced Materials, Switzerland) with 4-aminophenyl disulfide (AFD) was used as a dynamic hardener. DMF > 99%, 2-mercaptoethanol 99% and AFD 98% were purchased from Sigma-Aldrich and were used as received.

4.3.2 Synthesis of Dynamic PU

The detailed synthesis of dynamic PU elastomer reversibly crosslinked with aromatic disulfide bridges adopted in this study is discussed by Martin et al. [194].

Tris-isocyanate terminated prepolymer (PU4000) was prepared by feeding trifunctional PPG (Mn 4000) 1 (900 g, 718 mmol) and IPDI (167.430 g, 740 mmol) into a 1 L steel reactor equipped with a mechanical stirrer and a vacuum inlet. The molar ratio between isocyanate and hydroxyl groups was set to 2.1/1.0. The reaction was catalysed with 100 ppm of DBTDL and carried out at 70 °C for 30 minutes under vacuum and high shear mechanical stirring (1200 rpm). The reaction was monitored by FTIR spectroscopy, [194].

The tris-isocyanate terminated prepolymer PU4000 was obtained in the form of a colourless liquid and stored in a tightly closed glass bottle. The NCO content of the prepolymer was determined by FTIR monitored titration with n-butylamine, following the disappearance of the NCO signal at 2264 cm^{-1}. The measured NCO content (2.90 wt. %) was observed in good agreement with theoretical value (2.92 wt. %).

4.3.3 Synthesis of Dynamic Epoxy

Luzuriaga et al. [195] reported the detailed synthesis of epoxy resin with exchangeable disulfide crosslinks, which was followed in this study.

The DGBA resin (100 g) was mixed with bulk AFD (43 g) instead of a classical diamine hardener (DETDA) at 80 ºC. The mix was cured in oven at 120 ºC for 2.5 h followed by post-curing for 2 h at 150 ºC. The FTIR analysis of the cured dynamic epoxy confirmed the complete curing with the disappearance of epoxide bands [195].

4.3.4 Hybrid Composites Fabrication

The hybrid composites were produced in two stages using dynamic epoxy and dynamic PU, as shown in Figure 4-1. In Stage 1, VARTM fabrication of dynamic FRP-Epoxy and FRP-PU laminates was performed using an Isojet DPE COMPACT injection machine. In the second step, the dynamic FRP-Epoxy and FRP-PU laminates were joined face to face in a hot press to produce a hybrid composite.

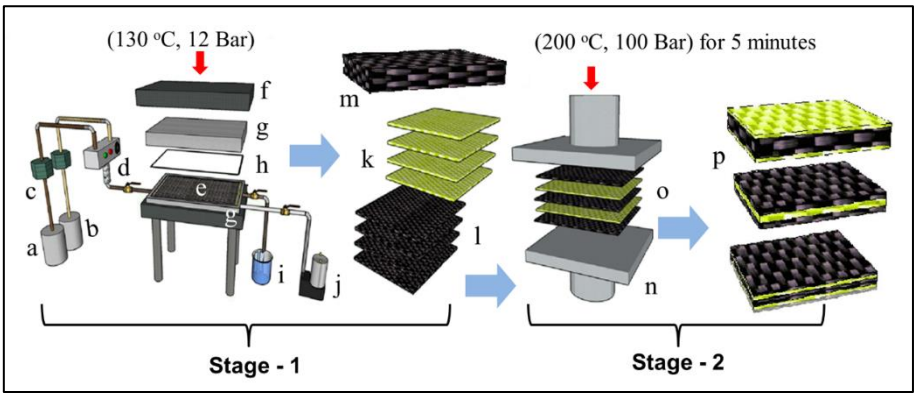

Figure 4-1 Hybrid composite Fabrication. Stage 1: Individual CFR laminates fabrication by VARTM method. Stage 2: Hybridisation of composites by joining multiple laminates in a hot press. a) Resin, b) Hardener, c) Pumps, d) Mixer, e) Preform, f) Hot Press, g) 2-Piece Al Mould, h) Metal frame, i) Excess resin, j) Vacuum Pump, k) PU laminates, l) Epoxy laminates m) Pure epoxy (ref) laminate, n) Hot-press, o) Stacked laminates, p) Hybrid composite.

During the FRP (epoxy or PU) laminate fabrication step, a sealant tape was placed on a 400 × 350 mm rectangular aluminium mould and a releasing agent (Frekote 770-NC) was sprayed evenly onto its surface. The carbon preform plies were placed in a mould according to the desired laminate thickness (4 plies/1 mm thickness). The thickness of laminate was ensured by placing a metal frame (spacer) between two pieces of mould. A release film was placed onto the reinforcement and then a layer of flow mesh and breather cloth was placed to soak up excess resin and ensure an adequate path for the dynamic resin and the vacuum pressure. The mould was vacuumed, heated (130 ^{o}C) and pressurised (up to 12 bars) to avoid leakages, void formation, cooling of resin and to ensure the compaction.

The resins and the hardener were degassed separately for 30 minutes prior to mixing and injection to remove the bubbles. Preheated (epoxy or PU) resin (resin tank at 60 ^{o}C, hardener tank at 100 ^{o}C) was injected into the pressurized mould (2.5 Bar) and was left to cure for 1 hour at 130 ^{o}C and for 24 hrs at Room Temperature (RT) at the same pressure. The resin/hardener mix ratio was kept 100:40 and 100:10 parts by weight for dynamic epoxy and PU resins respectively. Multiple Individual dynamic epoxy and PU laminates (width (b) = 250 mm, length (l) = 300 mm) of thicknesses 0.5 mm, 1 mm, 2 mm were produced separately.

A 3 mm thick dynamic epoxy composite panel (l = 350 mm, b = 250 mm), was produced in a single step by VARTM as a reference non-hybrid dynamic epoxy composite to establish a comparison during characterisation.

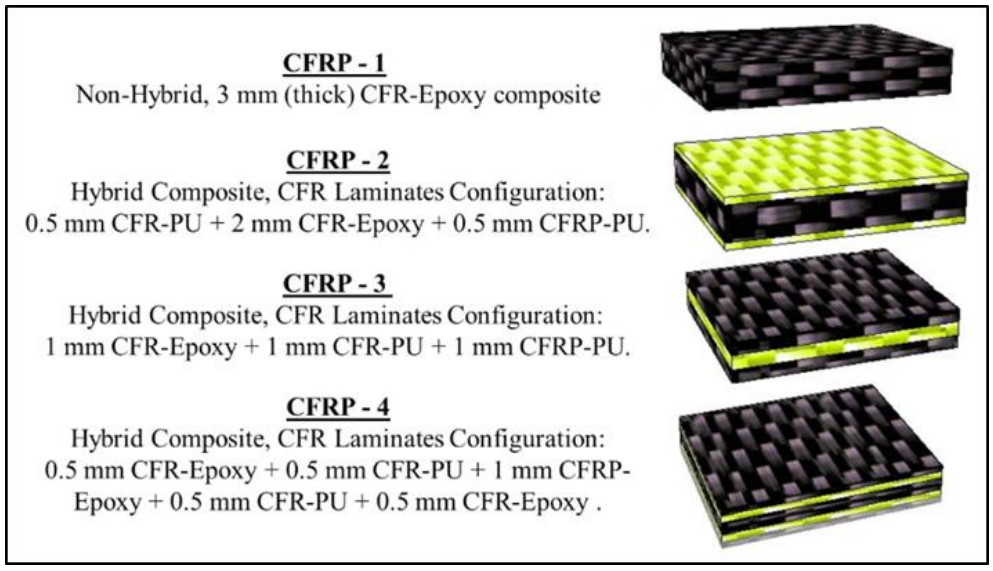

Figure 4-2 CFRP laminates stacking plan and nomenclature adopted for composites.

In general, the joining of thermoset laminates is carried out with glues or adhesives. However, the dynamic thermosets offer a new paradigm towards laminate joining. The aromatic disulfide containing elastomers have been shown to have self-healing ability at room temperature and displayed around 97% dynamic crosslinking efficiency [196]. However, in the dynamic epoxy and dynamic PU systems used in this study, the reshuffling of disulfide crosslinks is frozen due to their high Tg [197]. Therefore, the joining in the dynamic epoxy and dynamic PU systems require heat (above Tg) to trigger the reshuffling of disulfide crosslinks

In the hybridisation stage, 50 mm × 60 mm dynamic CFR-epoxy and CFRP-PU laminates of different thicknesses were staked in three different configurations, as shown in Figure 4-2.

As the dynamic polymer network system can be easily reprocessed at temperatures above Tg. Thus, each pile of stacked dynamic epoxy/PU laminates was subjected to hot press at 200 ºC and 100 bars for 5 minutes and were cooled down below Tg and demoulded. A compact multi-laminate hybrid dynamic composite was obtained.

In total 4 carbon fabric layers impregnated with dynamic PU, which makes 33.33% of the total composite thickness were incorporated into hybrid configurations while its distribution through thickness was varied. It was made sure that each of the composites receives 12 layers of carbon preform layers and an average thickness of 3 mm.

4.3.4.1 Structural Properties

Three specimens of each dynamic composite (Dimensions: *b = 10mm, l = 20 mm*) were obtained to analyse the density, Fibre Volume Fraction (FVF) and void content. Air-water method (ASTM D792-08) was adopted to measure the density of the dynamic composite specimens. ISO EN 2564-1998 and ASTM D2734-09 standard procedures were followed to determine the fibre volume fraction and the void content respectively. Optical Microscope (OM) and Scanning Electron Microscope (SEM) images of the polished cross-sections of the individual CFR-epoxy and CFR-PU laminates, and the hybrid composites produced to analyse the 2D geometric arrangement of the fibres within the laminates and through the composite thickness. using a Scanning Electron Microscope (SEM) and an optical microscope.

4.3.4.2 Dynamic Mechanical Analysis (DMA)

The capacity to store and the dissipated energy by imposing deformation as a function of temperature was measured using DMA-Q 800 equipment. Three samples (Dimensions: b=12mm, l= 35mm) of each of the composite were analysed in a three-point bending mode with a double cantilevers strain ramp at an oscillation frequency of 1 Hz under controlled amplitude (30 N/m^2). A ramp of 3 ^oC/min was set to reach 220 ^oC.

4.3.4.3 Interlaminar Shear Strength

Short beam three-point bending test was carried out to evaluate the apparent Inter-Laminar Shear Strength (ILSS) of each composite and the ISO-14130 standard procedure [198] was followed. Five rectangular specimens (*b=12.5mm, l= 25mm*), of each composite, were subjected to a transverse load at a loading speed of 1 mm/min and a span length of 12 mm on INSTRON 5985 equipped with a 5kN load cell, at 23 ^oC and 50% humidity. ILSS parameter was computed from the maximum load observed during the test using the Eq. 1.

$$\mathrm{ILSS} = 0.75 * \mathrm{Fmax}/\mathrm{bt} \qquad \text{Eq. 1}$$

Where b and t are the width and thickness of the rectangular specimens respectively.

4.3.4.4 Flexural Strength

A long span three-point bending test was carried out to evaluate the flexural strength of the composites and the ISO-14125 standard procedure was followed. During the transverse loading, compressive stresses are produced at the concave while the tensile stresses are produced on the convex surface resulting in an area of shear stress along the midline. Five specimens (*b=15mm, l= 125mm*) of each composite were subjected to long span three-point bending keeping a total span length of 100 mm using INSTRON 5985 equipped with a 5kN load cell, at 23 ^oC

and 50% humidity. The flexural strength, σ_f (MPa), was calculated according to the following formulae:

$$\sigma f = 3FL/2bt^2 \qquad \text{Eq. 2}$$

Where F (N) is applied load and L is total span length (mm).

4.3.4.5 Impact Test

Circular specimens of 60 mm diameter, of each composite type were subjected to impacts at multiple energy levels in supercritical energy range i.e. 3J – 50J. Impact tests were conducted to evaluate the energy required to initiate a fracture and/or perforation.

The contact force and energy curves were recorded via 5kN load cell attached to a striker, the impactor. The diameter of hemispherical (striker) impactor head was 20 mm. The impact energy was modified by varying velocity form 0.98 m/s to 4.43 m/s. During the test, the specimen was supported on an annular ring within and out the diameter of 40 and 60 mm respectively. Fractovis-Plus drop weight equipment by Ceast assisted with D8EXTWIN software was used for impact tests and all the tests were carried out at room temperature (23 ^oC) and 50% humidity.

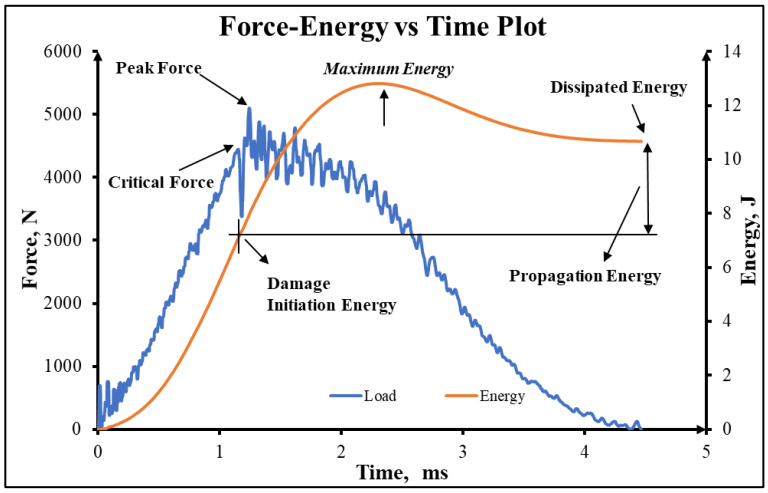

Figure 4-3 Demonstration of terminologies used to explain load-energy and time relations.

Some important terminologies that are commonly used in impact analysis [199,200], shown in a (representative) Force-Energy-time plot Figure 4-3 are interpreted as;

Impact energy - The maximum kinetic energy of impactor.

Critical force – The force value related to the first change in out of the plane.

Critical energy - The energy value corresponding to critical force.

Peak force – The maximum force value observed in a force curve.

Maximum energy - The maximum energy value observed in a force curve.

Dissipated energy – The amount of energy dissipated in damage initiation.

Propagation Energy- The energy utilised in the propagation of damage in the composite specimen.

Elastic energy - The difference between maximum energy and dissipated energy.

4.4 Results and Discussion

4.4.1 Structural properties

Figure 4-4 shows the SEM images of a cross-section of the individual dynamic epoxy and PU laminates produced in a single step. It was observed that a very uniform impregnation was achieved in the laminates due to the pressurized resin injection. The small un-impregnated spots in the dynamic PU laminate which are contributing to the overall void content of the composites, visible in Figure 4-4 (b), are due to the relatively higher viscosity of the dynamic PU compared to Dynamic epoxy. This higher viscosity resulted in poor impregnation of around the kinks in carbon rovings induced by weaving process.

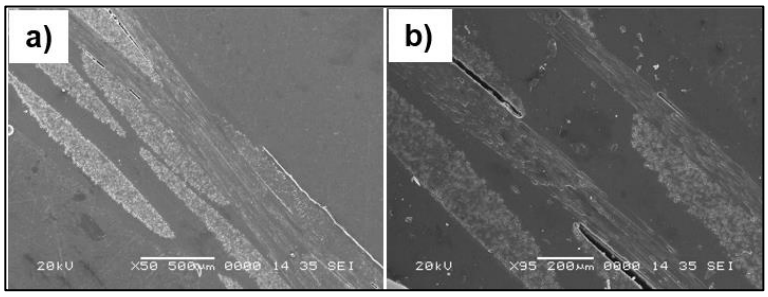

Figure 4-4 SEM images a) Dynamic CFR-epoxy laminate, b) Dynamic CFR-PU laminate

Figure 4-5 represents the OM images of the cross-section of the dynamic CFRP composites. The average values obtained for density, FVF and void content of the reference composite and the three hybrid composites are reported Table 4-1. It was observed that the additional step involved in the production of hybrid structures (VARTM + Hot Press) resulted in extra voids at the interlaminate interfaces/joints, indicated in Figure 4-5 (b) (c) and (d). The voids at the interlaminate joining seams are the reason for increased void content in the hybrid composites.

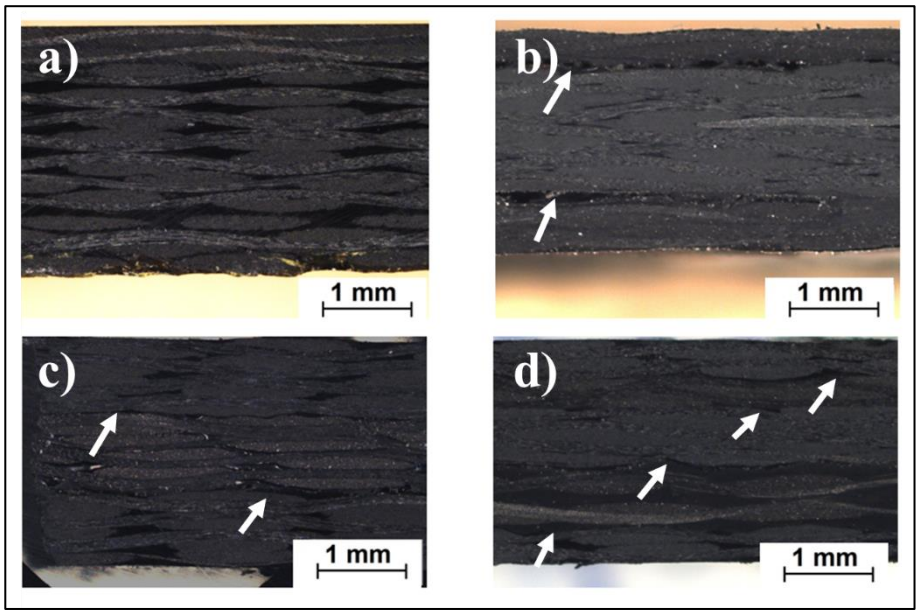

Figure 4-5 Cross Section of CFRP composites, a) CFRP-1, b) CFRP-2, c) CFRP-3, d) CFRP-4 after hybridisation in hot press.

The reference composite contains only the intra-laminate voids while the hybrid composites have both, the inter-laminate and the intra-laminate voids. Inter-laminate voids are quite evident in the cross-section and around 50% to 80% of void content in the hybrid composites were assumed to be concentrated at the inter-laminate interfaces.

The hybrid composites, when subjected to pressure (100 Bar) in a hot press, their overall thickness decreased by around 10% compared to the reference composite thickness. The decrease in the thickness of hybrid composites contributed towards the increase in FVF by an average of around 22% in the hybrid composites compared to the reference composite, Table 4-1.

Table 4-1 Average results obtained for structural properties of a reference non-hybrid and hybrid composites.

Composite	Thickness, t (mm)	Density, g/cm^3	FVF, %	Void Content %
CFRP-1	2.85 ± 0.05	1.44 ± 0.005	43.36	2.18
CFRP-2	2.6 ± 0.01	1.43 ± 0.005	51	4.66
CFRP-3	2.75 ± 0.06	1.40 ± 0.005	58.4	11.09
CFRP-4	2.6 ± 0.08	1.44 ± 0.005	54.52	8.01

Voids, in general, are considered as the critical imperfections and have detrimental effects on the performance of fibre reinforced composite materials. They mainly affect the matrix-dominated properties, such as interlaminar shear (ILS), flexural, compressive, fatigue and fracture toughness properties [201]. However, increase in the FVF improves the ILS and flexural strength properties of

a composite [202]. Suhat et al. [203] reported that a 2% increase in void content reduces the flexural strength of a composite material by 12.7%. the variation in thickness of the composite panel influence the flexural properties. Rathnakar et al. [204] observed 14% increase in flexural strength when the thickness of composite was increased from 2 mm to 3 mm.

4.4.2 Dynamic Mechanical Analysis

The glass transition temperature, Storage and Loss moduli were measured to determine the viscoelastic properties of the hybrid composites in comparison to reference non-hybrid composite.

Figure 4-6 represents the DMA results for all the four dynamic composites. Storage modulus is a measure of the stiffness or elastic response of a material [205]. As the stiffness is mainly attributed to the epoxy component, a noticeable decrease in the stiffness of the hybrid composites was observed in the hybrid composites where the dynamic PU laminates were incorporated into the composite structure. The different hybrid configurations responded with a degree of decrease in rigidity ranging from 32% to 75% at room temperature, Figure 4-6 (a). The hybrid configuration with relatively thicker individual dynamic epoxy laminates in it displayed higher stiffness.

All the composite configurations sustained their respective stiffness property with a slight decrease with the increase in temperature till around 120 ^{o}C or when the resin started softening. After the softening point, a noticeable decrease in the stiffness was observed. It was noticed that the thicker individual dynamic epoxy laminates in the hybrid composites configuration responds with higher stiffness values before the softening point and also show a higher loss in stiffness of the composite after softening temperature.

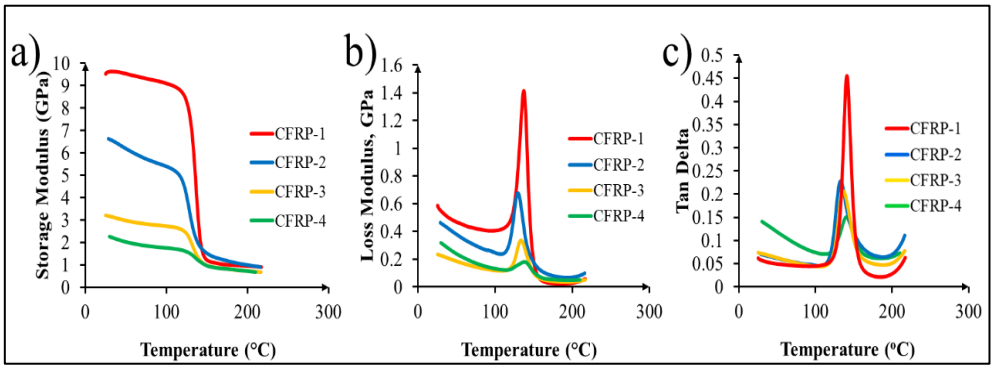

Figure 4-6 Dynamic Mechanical Analysis Results. (a) Storage Modulus, (b) Loss Modulus, (c) Tan Delta.

Loss modulus corresponds to the viscous response of the materials and is measured as energy loss as heat per cycle under a stress or deformation [206]. Loss modulus curves, presented in Figure 4-6 (b), confirms the higher viscoelastic

properties of hybrid composite structures in comparison to the non-hybrid one. Improved viscoelastic behaviour was displayed by CFRP-4 where the individual dynamic epoxy laminates with relatively less thickness were incorporated. Reduction in peak height of the curve for hybrid composites is mainly due to the two-phase (Epoxy-PU) similar trends and agreements are reported by other researchers for two-phase systems [207].

For all three hybrids and a non-hybrid dynamic composite tan delta as a function of temperature is presented in Figure 4-6 (c). Tan delta is the measure of damping property of a material and it also specifies the elastic or viscous properties of a system. For viscoelastic materials, the energy stored during stress at a loading frequency is out-of-phase with the strain by angle φ, (where $0 < \varphi < \pi/2$) [207,208]. The lower values of corresponding φ evidence the higher energy storage capacity of the dynamic composites compared to the non-hybrid where the improved damping properties are displayed. The sharp narrow peak of CFRP-1 corresponds to lower amorphous content which is obvious due to its pure dynamic epoxy content and lower void content in the structure.

In the hybrid configurations where dynamic PU laminates were distributed more evenly throughout the thickness (CFRP-4) responded with viscoelastic dominated properties as compared to a hybrid configuration where the epoxy content is relatively concentrated such as CFRP-2.

4.4.3 Inter Laminate Shear strength

The dynamic composite specimens were subjected to a transverse load in a short span three-point bending assembly to analyse the interlaminar and shear strength. For each of the four configurations tested, a load–cross head displacement curve which best represents the average of five separate specimens of each hybrid and a reference non-hybrid composite are presented in Figure 4-7.

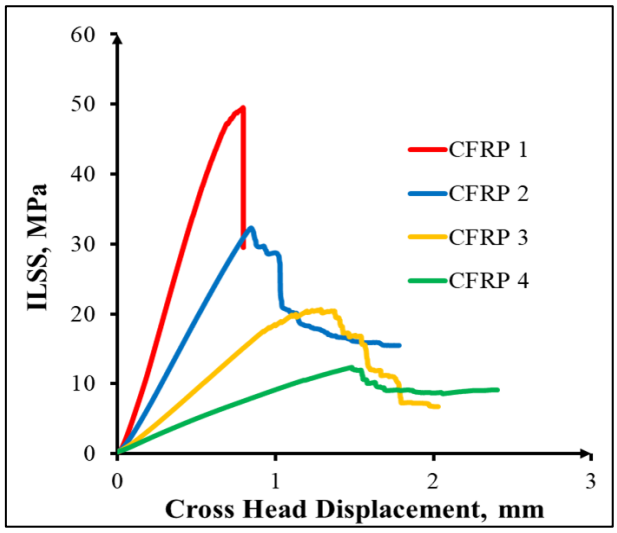

Figure 4-7 Average behaviour of the hybrid composites specimens compared to reference non-hybrid composite specimens subjected to short span 3-point bending test.

The reference composite displayed no interlaminar shear failure and a brittle fracture was observed at the point of loading when the cross-head displacement reached around 0.8 mm. The hybrid structures showed resistance to inter-laminar shear failure for extended displacement followed by interlaminate shear failure. It is due to the fact that the interlaminar bonding, produced during curing, were stronger and more coherent compared the interlaminate interface bonding. The interlaminate bonding which relies on exchangeable bonds in a polymer network which was rearranged thermally in polymer networks during the hybridisation (hot press) step. The observations reported by Selmyet et al. [209] supports the detrimental effect of poor adjacent layers interface bonding on the ILS results.

Average apparent ILSS values and the corresponding failure modes recorded for each dynamic hybrid and a non-hybrid composite are reported in Table 4-2. A pattern of decrease in ILSS values with the increase in the number of interlaminate interfaces in the hybrid configurations is evident.

Table 4-2 Average results obtained for short and long span three-point bending test.

Configuration	**Flexural Strength, σ (MPa)**	**Flexural Strain, (%)**	**Flexural modulus, (GPa)**	**Failure Mode (Long span)**	**ILSS (MPa)**	**Failure Mode (Short span)**
CFRP-1	818 ± 64.82	1.9	51.8 ± 3.2	Tensile fracture of fibres	53,2 ± 1.32	Brittle fracture at loading point

CFRP-2	386 ± 9.39	3.2	19 ± 1.6	Compressive fracture	32.2 ± 1.45	Shear and brittle failure
CFRP-3	147 ± 47.97	2.5	19.9 ± 7.5	Interlaminate shear	20.3 ± 0.086	Multiple shear
CFRP-4	147 ± 29.2	2.3	11 ± 15.8	Interlaminate shear	13.5 ± 3.06	Delamination

The fracture analysis of the dynamic hybrid composite specimens after the ILSS test display dominant intra-laminate shear failure, Figure 4-8. Cracks were observed were only in the 2 mm thick rigid epoxy layer of CFRP-2 specimens. However, no cracks were apparently observed in the hybrid configurations having the epoxy laminates of less than 2 mm thickness.

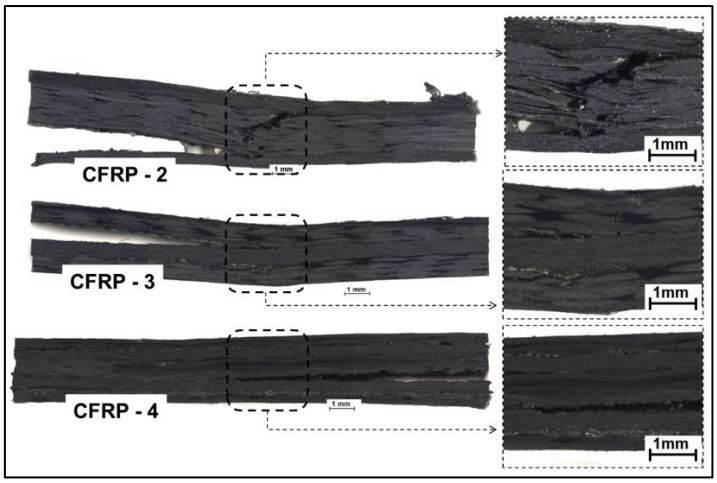

Figure 4-8 Inter-Laminar Shear (ILS) fracture analysis.

Another reason for the interlaminate shear failure was the relatively higher void content at the interlaminate interfaces in the hybrid composites, Table 4-1. Zhu et al [210] reported that the voids content, the position and size of voids in the composite laminates defines the interlaminar and flexural properties of a composite. The voids in the hybrid structures were relatively concentrated at the interfaces between the laminates, therefore, the load applied was not transferred across the thickness and delaminated the composites at the weaker interlaminate interfaces.

4.4.4 Flexural Strength

Flexural properties of the three hybrids and non-hybrid CFRP composites were analysed using a long span three-point bending test assembly. The Average flexural strength, strain, modulus values and failure modes evaluated for five specimens of each configuration are reported in Table 4-2. Figure 4-9 represents the average behaviour of composites specimens subjected to a flexural load.

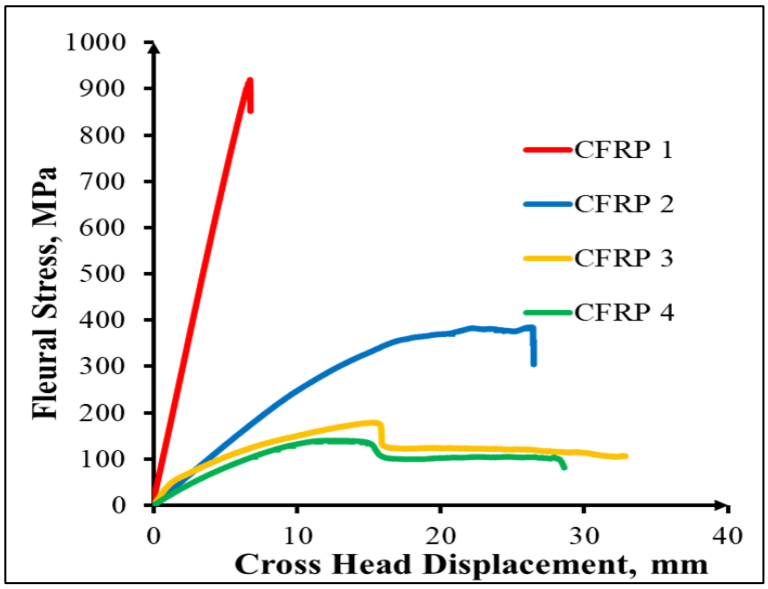

Figure 4-9 Average flexural behaviour of the hybrid composites specimens compared to reference non-hybrid composite specimens subjected to long span 3-point bending.

When subjected to a flexural load, the reference dynamic composite displayed initially an elasticity, comparatively higher than the hybrid composites, followed by brittle a failure. At a lower cross head displacement at a point of loading. The hybrid dynamic composites showed relatively lower rigidity due to PU content and responded with a ductile failure without any failure for an extended crosshead displacement. However, the CFRP-3 and CFRP-4 failed at lower load values due to delamination of bonded laminates, as can be seen in Figure 4-10.

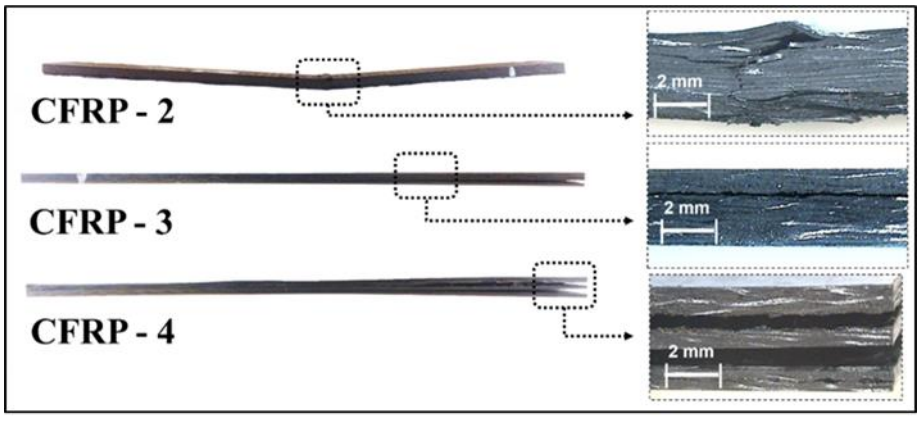

Figure 4-10 Fracture analysis of specimens subjected to a flexural load.

The flexural properties of hybrid configuration were found highly influenced by the distribution of dynamic epoxy and PU laminates in the composite thickness. The CFRP-2 hybrid composite exhibited the highest stiffness among the hybrid configurations due to a 2 mm thick epoxy laminate in its configuration. It displayed brittle failure mainly in the thick epoxy laminate at a point of loading but at a

displacement higher than the reference composite. The failure in the CFRP-3 and CFRP-4 was less catastrophic with respect to CFRP-1 and CFRP-2.

4.4.5 Impact Analysis

The plots of force and energy versus time of a dynamic non-hybrid composite (CFRP-1) are compared to three hybrid dynamic composites (CFRP-2, CFRP-3 and CFRP-4), shown in Figure 4-11 for impact events conducted in the ranger 5 – 50 J.

The specimens of a hybrid configuration practically responded with quite a different contact time duration (Tc) and peak force (Fp) compared to the non-hybrid configuration. The lower contact time at a similar energy level impact corresponds to higher stiffness and lower energy absorbance (Ea) of the reference composite compared to the hybrid composites. Similar behaviour was observed for all impact events at different energy levels, Figure 4-11.

The oscillations in the force curve appear due to the breakage of fibres/matric and/or delamination of the laminas facing the impact. Therefore, the first apparent oscillations in the force curve, indicated green in Figure 4-11, was interpreted as damage initiation in a composite specimen. The corresponding damage initiation energies which initiated the damage in the specimen are reported in Table 4-3. The damage initiation was observed at lower energy levels in the reference non-hybrid composite capered to the hybrid ones.

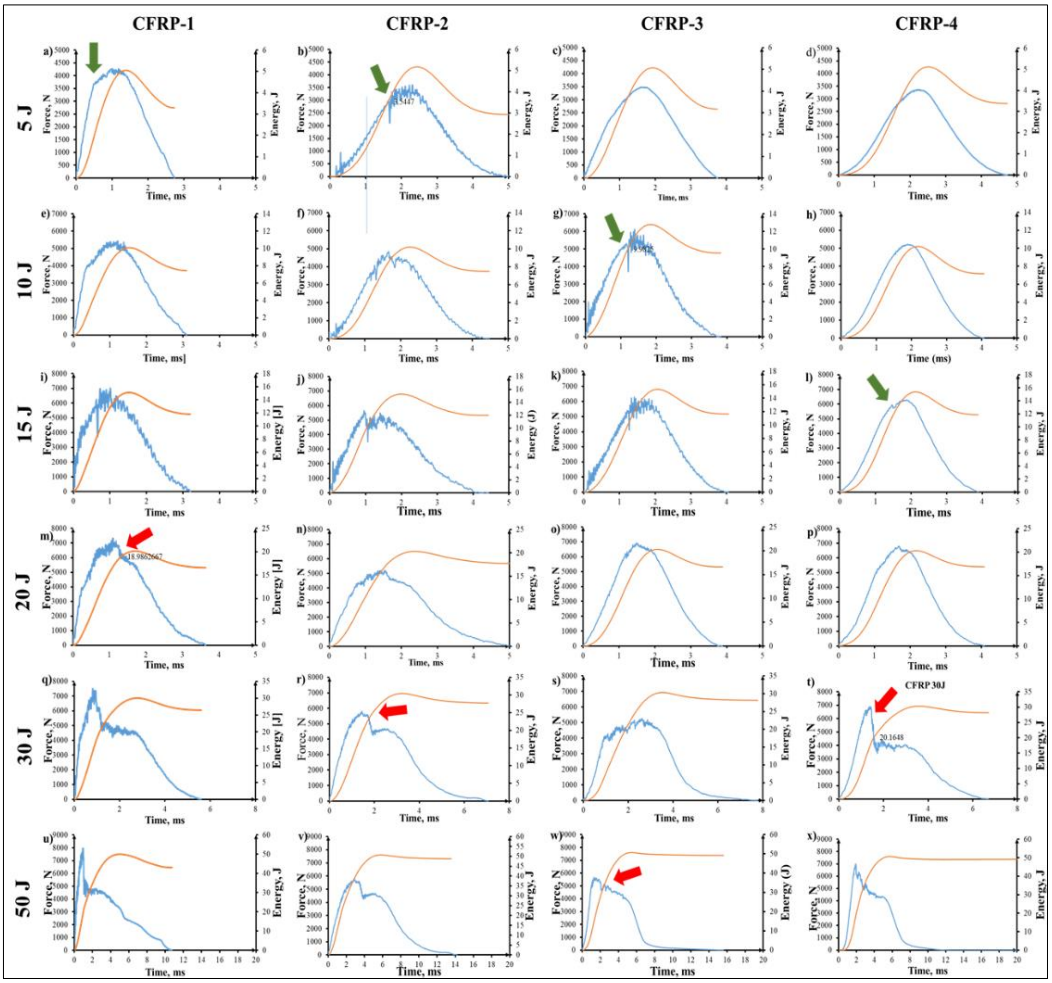

Figure 4-11 Response of dynamic composites to different impact energies. The green indicator shows damage initiation and the red indicator shows perforation initiation in the composite specimen.

At higher impact energies where a sudden drop in the force curve is followed by the peak forces indicate a drop in the transverse stiffness of the composite specimen. The drop is then followed by low amplitude and frequency load oscillations till it reaches to zero. The progressive drop corresponds to the damage propagation or sometimes partial or complete perforation. Therefore, the energy corresponding to the post-peak sudden drop in the force was considered as the perforation initiation energy or perforation threshold. The perforation energy values analysed for the four configurations of the dynamic composite are reported in Table 4-3.

Table 4-3 Analysed damage initiation and perforation energies corresponding to hybrid and non-hybrid composites.

Configuration	**Damage Initiation Energy, J**	**Perforation Energy Threshold, J**

CFRP 1	0.52	18.9
CFRP 2	3.55	23.19
CFRP 3	9.98	34.50
CFRP 4	12.42	20.17

The hybrid composites apparently displayed a noticeable improvement in the impact resistance compared to a non-hybrid reference composite. Due to the tuff dynamic PU content, sustained the lower impacts without any damage and resisted the perforation by absorbing higher impact energies compared to a rigid non-hybrid composite.

The impacted facings of the non-hybrid dynamic composite specimens are shown in Figure 4-12, in comparison to the hybrid dynamic composite specimens. After the complete perforation in hybrid specimens, the energy curve displays saturation because the specimens are unable to absorb more damage. However, the reference specimens displayed saturation at lower impact energies where complete perforation was not noticed even at 50 J impact due to the dissipation of partial impact energy in the propagation of damage across the specimen area.

It was noticed that, after the perforation energy level, in the hybrid specimens, the perforation together with the fibre pull out was extended to the back surface.

While in the of non-hybrid configuration, horizontally extended propagation of impact damage was noticed along the composite laminate plane.

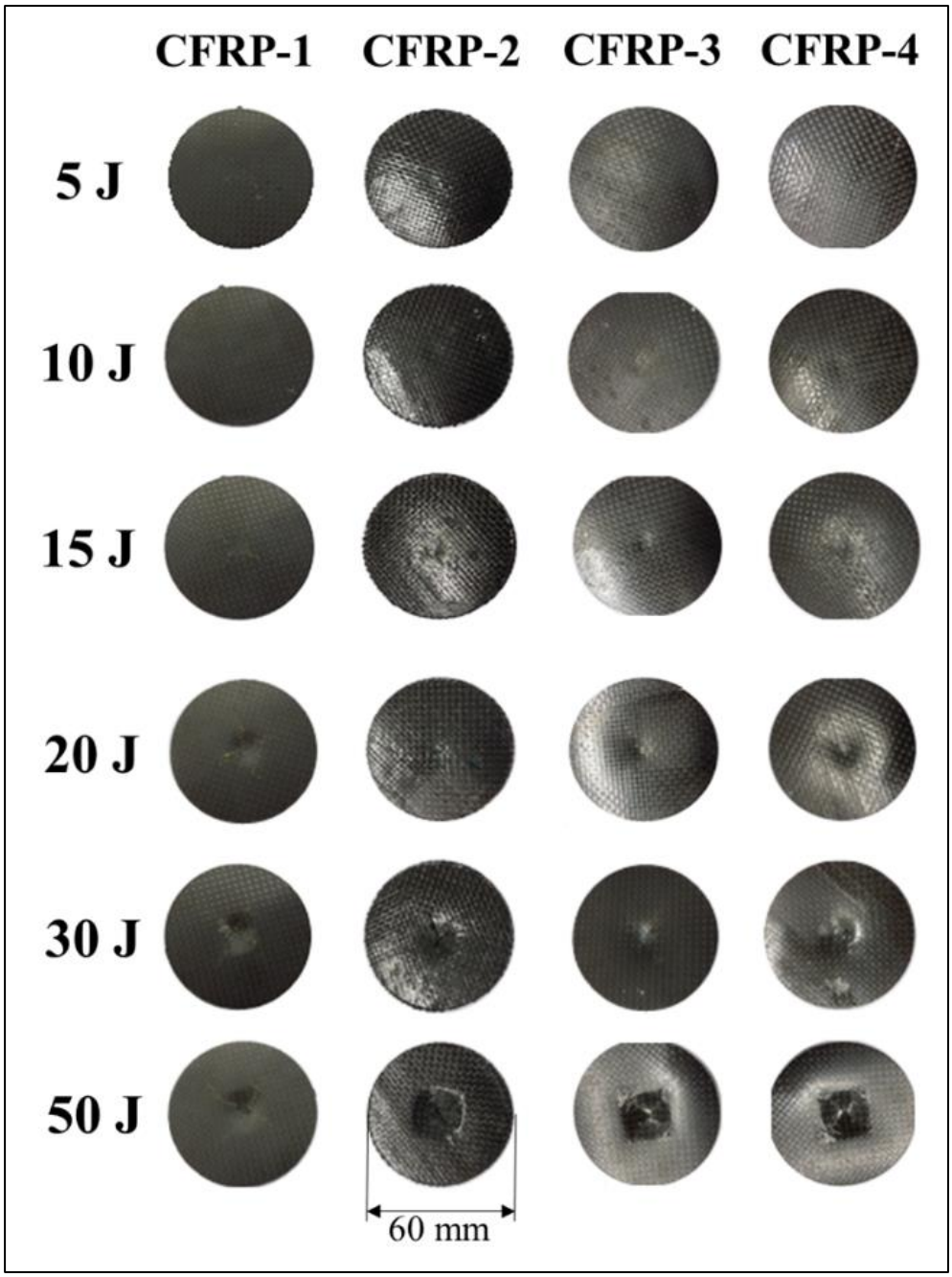

Figure 4-12 Images of the impacted face of the dynamic composite specimens.

The distribution of the dynamic CFR-PU laminates in the hybrid configurations highly influenced the response of hybrid specimens to an impact. The hybrid configurations with relatively thicker FRP-epoxy laminates responded with lower impact resistance and behaved more like a rigid laminate. However, the hybrid configurations with relatively thinner dynamic CFR-epoxy laminates and well

distributed PU laminates through the thickness (CFRP-4) responded with highest impact resistance.

On the basis of the experimental data, the impact resistance of the three hybrid dynamic composites is compared a non-hybrid dynamic epoxy composite utilizing the composite structure assessment procedure suggested by Paolo Feraboli et.al [211].

4.4.5.1 Force Plot

The peak force curves, presented in Figure 4-13, can be divided into the sub-critical and supercritical regimes. The sub-critical regime is the range of impact energy values below the damage threshold (energy level at which the damage initiates), while the Super-critical regime is the range of impact energy values above the damage threshold.

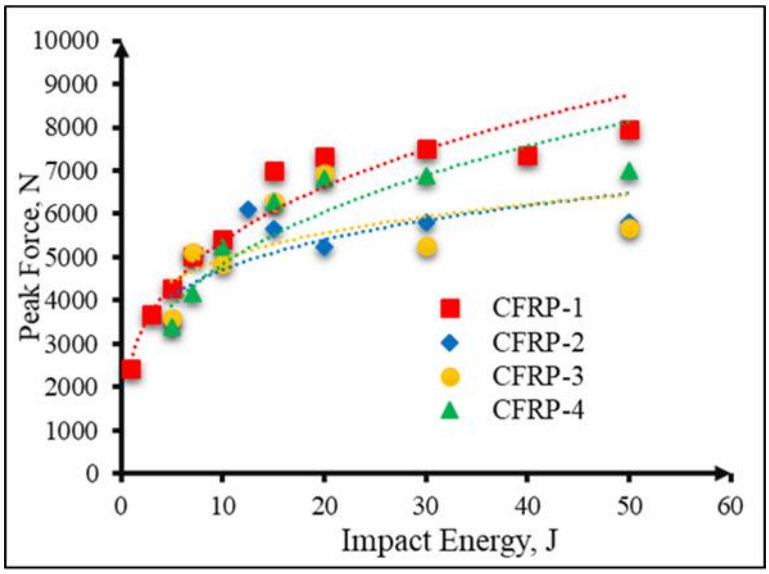

Figure 4-13 Force Plot.

The peak force increases follow a power law according to a simple spring-mass model below the damage threshold [211]. In the sub-critical regime, where the damage is not initiated, the peak and critical force values almost coincide. Therefore, at very low impact levels, critical energy is not relevant as failures do not occur and the peak force indicates the elastic response. However, in the supercritical regime, these values vary and separate values for critical and peak force can be recorded. After the damage threshold, which is independent of the impact energy, the curve deviates from theoretical power law prediction and achieve a so-called plateau which was noticed at 7500 ± 70 N, 5800 ± 120 N 6000 +100 N 7000 ± 80 for CFRP-1, CFRP-2, CFRP-3 and CFRP-4 respectively.

4.4.5.2 Energy Plot

The energy plot, presented in Figure 4-14, is comprised of dissipated energy curves and the 1:1 line of incident kinetic energy. In the recent past, researchers [211–213] suggest that the dissipated energy increases quadratically with the increasing impact energy while the critical energy is independent of the impact energy level at which the test is performed. The dissipated energy is directly related to the amount of damage in a specimen. Feraboli et al. [211] suggest that a perforation in specimens can be predicted by forecasting the point of intersection between the (quadratic) dissipated energy curve and the 1:1 incident energy line. According to that, hybrid dynamic composite displayed around 37 % higher penetration energy compared to non-dynamic CFRP-epoxy composites reported in [199].

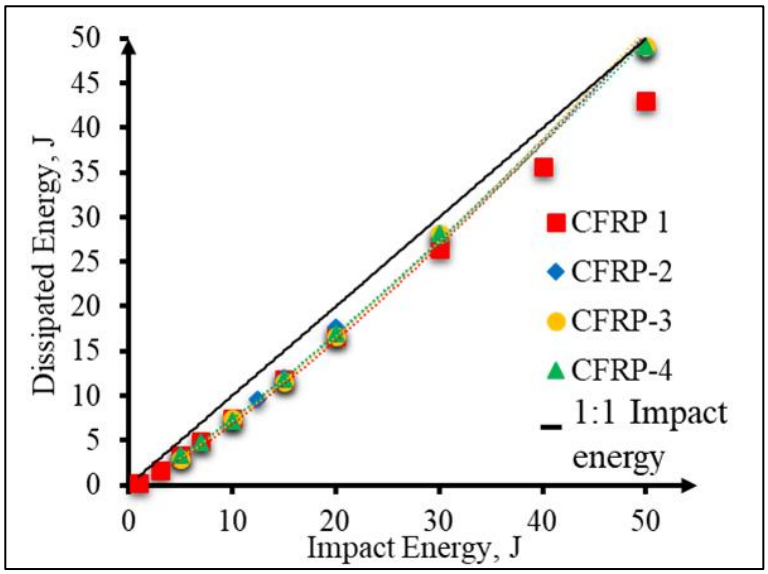

Figure 4-14 Energy Plot.

The dissipated energy curves for the hybrid composites, Figure 4-14, cross the incident energy line in the range 40 J-50 J. The visual investigation of the impacted specimens, Figure 4-12, also supports this argument as the complete perforation in the hybrid composites was observed in the similar impact energy range.

The quadratic dissipated energy curve of the reference dynamic composite specimens crossed the incident energy line at around 50 J as it displayed only partial perforation and the rest of the dissipated energy was utilised in the delamination of composite laminas. From a structural point of view such propagation of damage are more catastrophic than the localised perforation displayed by hybrid configuration specimens.

4.4.5.3 Coefficient of Restitution (COR) Plot

Figure 4-15 represents the COR values plotted against the impact energy. The COR values at impact energies below the damage threshold remain almost the same

due to no or a negligible amount of energy loss. Beyond the damage threshold, a sharp drop in COR values is the evidence of energy loss consumed in damage initiation and propagation.

The Coefficient of Restitution (COR) is a direct representation of failure mode estimation occurring in the specimen at different energy levels. For a stationary target, COR is the ratio of the exit velocity to the incident or the square root of the ratio of the exit energy to the incident. Eq. 3 [211].

$$COR = v_{out}/v_{in} = \sqrt{E_{out/E_{in}}} \qquad \text{Eq. 3}$$

The trend in COR values recorded for the reference non-hybrid dynamic composites specimens displays a sharp drop since the beginning which evidences that the damage was initiated at the very low energy level. However, for the hybrid configuration, the damage initiation was noticed at comparatively higher energies with respect to reference composite. Therefore, unlike the reference specimens, the COR values for the hybrid composites remain almost the same till their respective damage thresholds. Which is followed by a relatively sharp drop corresponding to a sudden increase in damage (after the perforation threshold). This shift in the slope also indicates the transition from the matrix to fibre dominated failure mechanism.

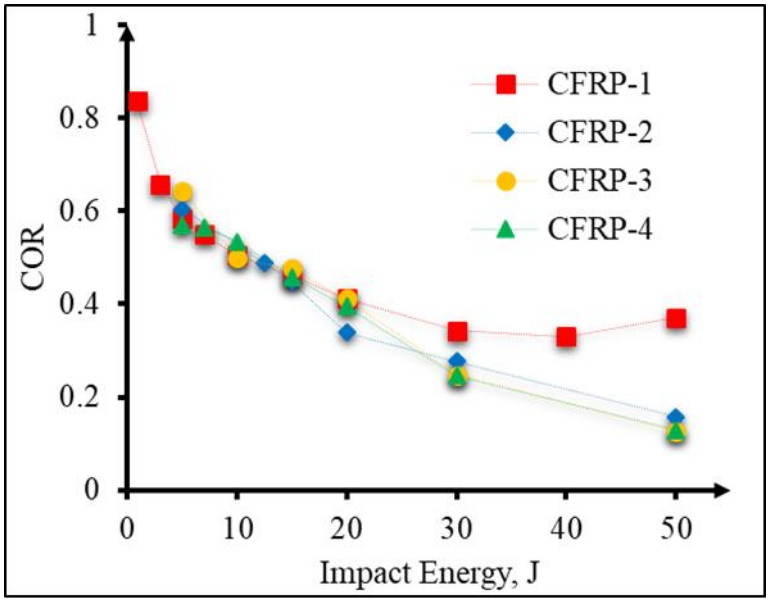

Figure 4-15 Coefficient of restitution plot.

The larger apertures noticed in the hybrid specimens compared to a non-hybrid, Figure 4-12, after the perforation threshold can be assumed as the result of higher contact duration.

The hybrid composites having 33.33% tough PU content in the structure absorbed more energy upon impact than a non-hybrid rigid having 100% pure

epoxy content in the matrix. For the same energy level, higher COR values for the non-hybrid composite are due to its higher stiffness and rigidity compared to the hybrid ones.

4.4.5.4 Contact Duration

Contact duration analysis is related to the instantaneous stiffness of material subjected to impact load and describes the damage state accurately. Higher contact time for an impact energy corresponds to higher energy absorption and lower stiffness property of a material. The contact duration values oscillate around the same mean before perforation threshold. However, it increases progressively after the onset of damage. The sharp increase in duration of contact at higher impact energies, in the plot presented in Figure 4-16, corresponds to progressive damage and ultimate perforation in a composite specimen. This also indications of the transition from the matrix to fibre dominated fractures and dissipation of energy within the composited.

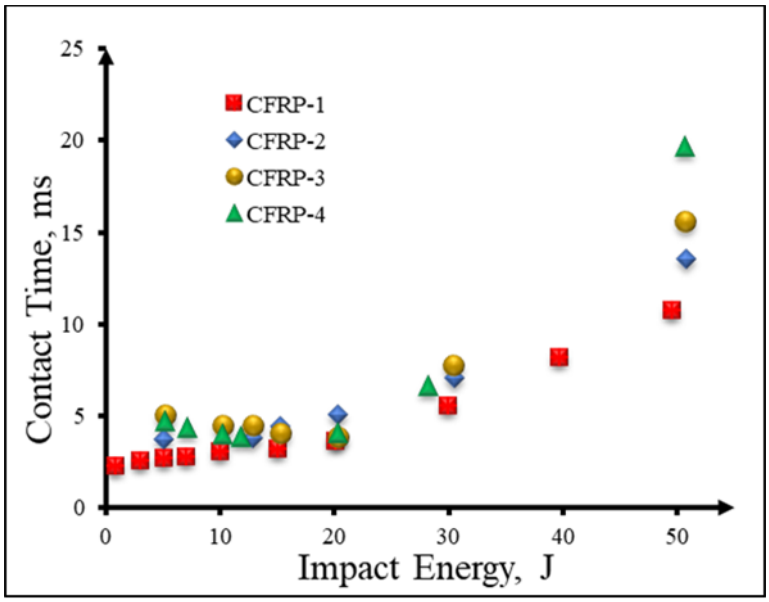

Figure 4-16 Contact duration plot.

The contact time is inversely proportional to the effective structural stiffness and depends on properties of impactor/target system. As the same impactor was used during all the impact tests in the current work, therefore it can be assumed that the variation in the contact durations was mainly due to the intrinsic properties and the configuration of the epoxy/PU laminates in the hybrid structures. The curves for hybrid configurations, in general, displayed 60-100% higher duration of contact throughout the entire range of impact energy values, due to the difference in effective structural stiffness, Figure 4-16.

Further investigation of the detailed mechanics involved in dynamic hybrid structures using finite element analysis and damage analysis using CT scan to better

predict the integrity of the dynamic epoxy/PU hybrid composites in complex structures are the focus of our Future work.

4.5 Conclusion

Hybrid dynamic epoxy/PU composites were successfully produced by a two-step, VARTM + hot press, manufacturing technique in three different configurations. The additional step in the manufacturing of hybrid composites, however, contributed to the added void content and increased FVF % and decrease in the relative thickness of the hybrid dynamic composites.

The hybrid dynamic composites displayed relatively lower stiffness due to PU content. Lower inter-laminate interfaces shear strength resulted in delamination of dynamic epoxy/PU which can be improved by further optimisation of the pressure and temperature parameters during the hybridisation step.

Impact damage initiation was observed at around 95% higher impact energy in the hybrid configuration, CFRP-4, compared to the non-hybrid configuration. The hybrid configuration, CFRP-3, displayed around 55% improved impact resistance compared the non-hybrid configuration.

Comparing the hybrid configurations, CFRP-2 responded with relatively higher stiffness and flexural properties, CFRP-3 displayed the highest perforation threshold and the CFRP-4 showed the uppermost resistance to damage initiation value.

The possible hybridisation of dynamic thermoset resins to allow the optimization of mechanical properties demonstrated in this study, will open new horizons for the engineering structure designers.

5. Surface Modification of Ti6Al4V by Micro-Electrical Discharge Machining to Improve Adhesive Joining

5.1 Abstract

Surface modification for adhesive joining improvement is widely utilized for various applications in modern automotive and aerospace industries. Finding more economically viable techniques to modify surfaces is becoming an important issue.

This chapter describes the preliminary work done on the effect of surface modification of titanium surfaces by means of a low cost, in-house developed Micro-Electrical Discharge Machining (Micro-EDM) and the design of micro-slot on the adhesion and strength of the adhesive joint. Three types of micro-slots: V, semi-circle and U-shaped micro-slots were produced on Ti6Al4V alloy sheet surface. Ti6Al4V specimens with and without micro-machined surfaces were bonded together using a commercial epoxy adhesive. Each set of bonded specimens, with and without micro-slots, were subjected to Single Lap Offset (SLO) shear test to observe the effect of micro-slots on the adhesion and joint strength.

Macro and micro-scale image was produced to analyse the joint fractures and to observe the failure modes. It was observed that the increase in the joined surface area may not necessarily increase the joint shear strength. The shape of micro-slots, alignment of micro-slots with respect to the direction of load and the alignment of micro-slots with respect to each other at the joining seam were observed as the influencing parameters.

5.2 Graphical Abstract

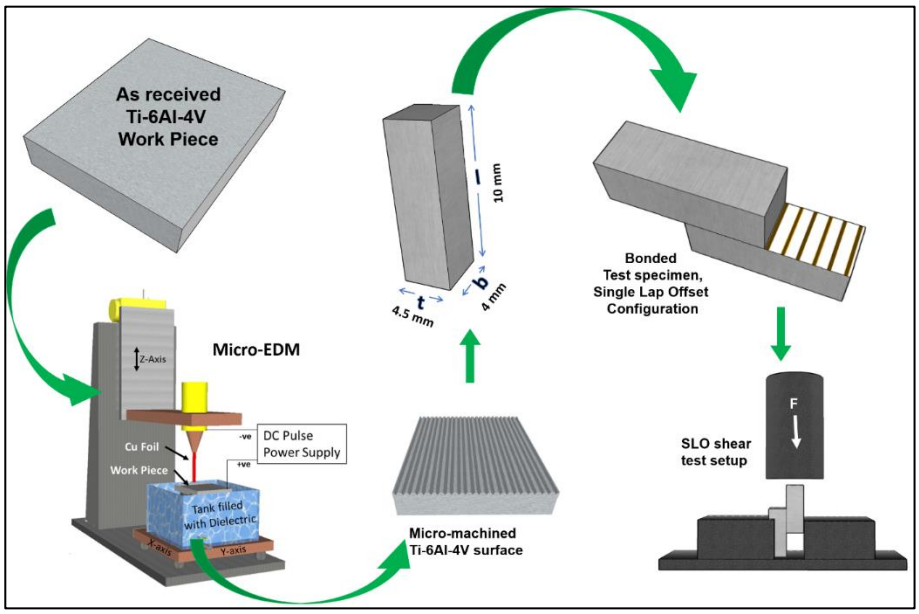

Keywords: Micro-EDM, Surface machining, Single lap offset shear test, Adhesive bonding.

5.3 Introduction

Today, there is a growing demand for highly reliable joints of Ti6Al4V alloys for structural applications in high-end automotive and aerospace industries [214]. Adhesives are widely used for joining metals to themselves or to dissimilar materials, both for structural and for non-structural applications [215].

Unlike polymeric materials, metals and metal oxides usually have higher surface free energies in the ultra-clean state, typically greater than 500 mJm^{-2}. In the ultra-clean state and controlled environment, metals are readily wetted by the organic adhesives having lower surface free energies [216]. The adhesion between the adherent and the adhesive influences the joining strength. The surface oxides or the rust hinder the adhesion which must be removed to achieve an optimum bonding [217].

Ti6Al4V alloy is an important structural material often used for manufacturing critical components of aerospace vehicles and high end automobiles due to its lower density combined with better high-temperature mechanical properties [218]. Compared to mechanical or chemical bonding, the adhesive joining of Ti6Al4V components is an efficient solution. However, the adhesive joining is still not reliable due to the unpredictable joint strengths caused by variability in surface preparation techniques and are therefore reinforced with mechanical fasteners for safety reasons [219,220]. Several attempts have been made in the past to improve the adhesive bonding of Ti6Al4V alloys [221–226].

Some of the well-known techniques to increasing the surface area of Ti6Al4V by surface machining to improve the adhesive bonding used in recent past are: electro-chemical machining [227,228], Jet-Electrochemical Micromachining (Jet-EMM) [229], laser ablation [19], laser-induced surface oxidation and roughening [230], elliptical vibration cutting [231], femtosecond laser micromachining [232], Electrical Discharge Machining (EDM) and Electrochemical Machining (ECM) [233].

The adhesive joint strength relies on the coherence of adhesive and adherence between adhesive and adherent. Several methods are proposed in the past to determine the adhesive joint strength properties [128,234–236].

The Lap shear test is one of the most commonly used method to determine the adhesive joint strength and offer results with low scattering in data [237,238]. However, in the case of lap joints, the failure does not occur simultaneously all over the joined area but results from the extension of cracks [239]. Although, the Lap tests do not provide a shear strength value suitable to be used for design purposes [240], but with the use of specimens of similar dimensions it can give a first approximation on the micro-machining effectiveness on the adhesion and joint strength.

Depending on the nature of joint fracture of the adhesive joint, three failure types are expected during the Ti6Al4V/Ti6Al4V adhesive joint failure: adhesive, cohesive or mixed failure. Siegmann [241] classified the adhesive joint failure into three main categories:

- Mode I - where adherence < coherence
- Mode II - adherence ≅ coherence and is also known as mixed mode failure.
- Mode III - where adherence > coherence

Micro-slots were produced on the Ti6Al4V surfaces using an in-house developed, low-cost, Micro Electrical Discharge Machining (Micro-EDM), developed by the Indian School of Mining (ISM), Indian Institute of Technology, Dhanbad, India under the supervision of Dr. Alok Kumar Das, Erasmus visiting Professor at Politecnico di Torino during this Thesis, with whom a collaboration on this subject was established and was used to produce micro-slots on Ti6Al4V alloy surface. It is an economic alternative to the earlier reported high-cost micro-machining operations. In this work, micro-slots of three different shapes were machined on the Ti6Al4V alloy sheet surface.

A commercial epoxy adhesive was used to join the metal substrates with and without surface modification to analyse the effectiveness of the micro-slots and its shape and size on the joint strength. Specimens with and without micro-slots were bonded in seven different micro-slots alignment and tested in Single Lap Offset

(SLO) configuration and characterized to determine the effect of micro-slots and their orientation on the adhesion and the adhesive joining strength.

5.4 Experimental Work

5.4.1 Materials

Ti6Al4V alloy sheets (10 mm x10 mm x 3 mm), supplied by M/s Aich Enterprise, Kolkata-6, India were used as a joining substrate and for surface modification.

A two-component thixotropic paste adhesive, Hysol EA 9321 AERO, supplied by Henkel Corporation, USA, was used as a joining material. Part A of the commercial adhesive was grey in colour with density 1.24 g/ml and viscosity 290 - 710 Pa·s at 25 ^{o}C while the Part B was off-white in colour with density 1.22 g/ml and viscosity 20 - 80 Pa·s at 25 ^{o}C. The two components of adhesive were mixed in a ratio of 100 (Part A) to 50 (Part B) by weight, at room temperature prior to application. The density of the mixture, grey in colour, was ~1.23 g/ml.

Lap shear strength of Hysol EA 9321 AERO adhesive is around 40 MPa at room temperature (25 ^{o}C) [242,243].

5.4.2 Ti6Al4V Surface Modification

The Ti6Al4V alloy surface was modified by micromachining three different shapes of micro-slots on separate specimens using In-house built Micro-EDM setup developed by the Indian School of Mining (ISM), Indian Institute of Technology, Dhanbad, India under the supervision of Dr. Alok Kumar Das, Erasmus visiting Professor at Politecnico di Torino during this Thesis, with whom a collaboration on this subject was established and was used to produce micro-slots on Ti6Al4V alloy surface.

5.4.2.1 Micro-EDM working

The model presented in Figure 5-1 shows the Micro-EDM setup. The Micro-EDM setup had a rotating spindle, and X-Y-Z CNC (Computer Numerical Control) stages. The spindle was mounted on the Z-stage while the workpiece was merged in a dielectric tank which was mounted on an X-Y stage. A 100 µm thick, copper foil, mounted on the spindle, was used as a machining tool.

Uniform micro-slots (parallel to each other) with a pitch of 11 micro-slots per centimetre were machined on the workpiece surface. The material removal in micro-EDM was done by the electrical sparks which were produced between the tool and the job merged in a dielectric liquid medium when a threshold electrical potential was applied to them.

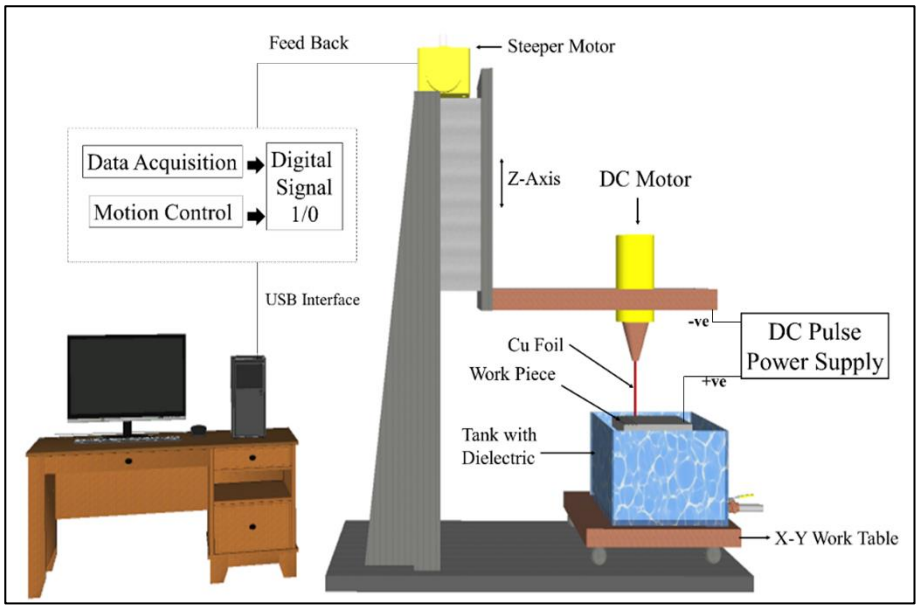

Figure 5-1 Model of Micro-EDM set-up used to micro-machine Ti6Al4V surface.

During the micro-machining process, when the applied voltage crosses the threshold potential, dielectric breakdown takes place and the spark is produced between the two closest points on the tool and the workpiece which offers the lowest resistance to the current flow. The temperature of the points reaches up to 10000 °C which melts the material at those points.

To control the spark energy, a pulsed DC power supply was used. During the pulse-on-time, spark is developed and during the pulse-off-time the molten material in the pole suddenly cools down which generates a high-pressure shock wave in the liquid dielectric medium and with that the material from the molten metal pole comes out into the dielectric medium in the form of debris leaving a micro-crater on both the tool and the workpiece surface.

Figure 5-2 (a) and (c) represents the macro images of a Ti-6Al-4V workpiece before and after the micro-machining.

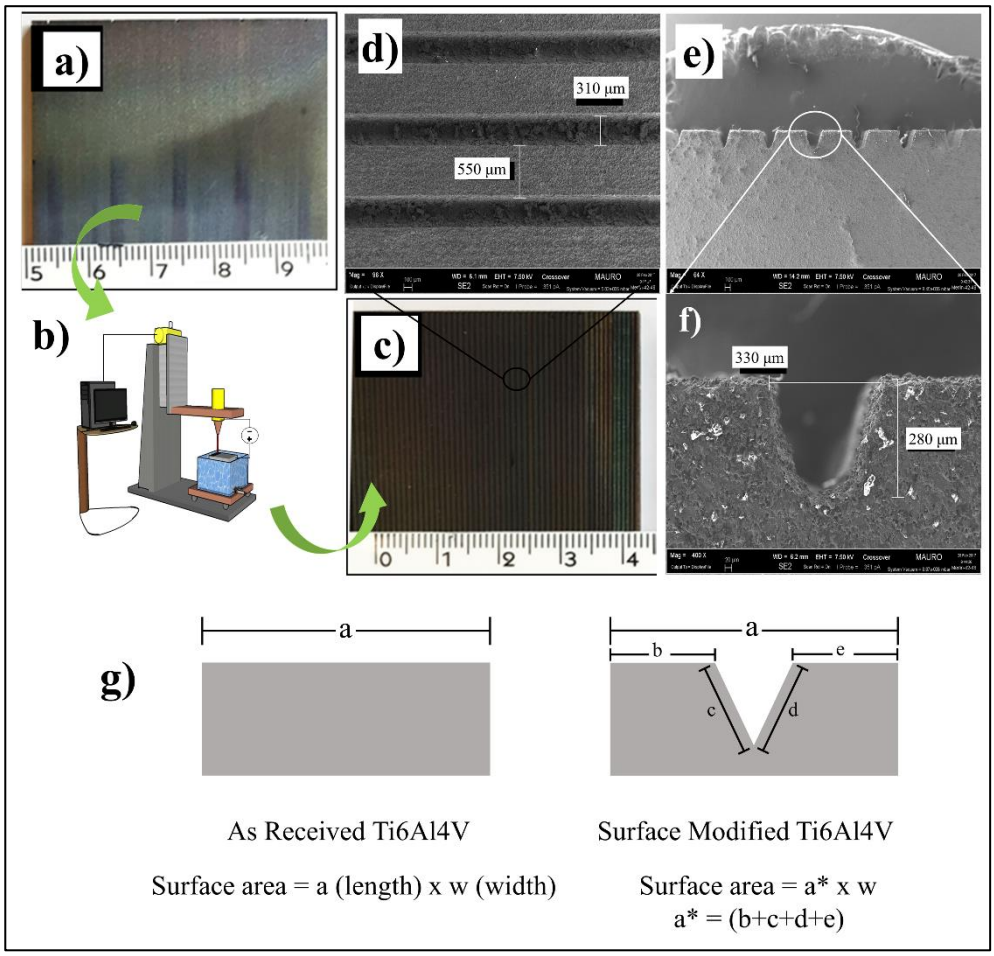

Figure 5-2 (a) As received Ti6Al4V surface, (b) Micro-EDM Set-up, (c) Micro-machined Ti6Al4V surface, (d), (e), (f) SEM images of micro-machined Ti6Al4V surface and cross-section, g) Surface area calculation.

The micro-machined Ti6Al4V surfaces were analysed to observe the effect of the micro-machining process. The accumulation of the craters on the workpiece shows the material removal from the substrate but the accumulation of crates on the tool surface indicates the tool erosion. The coloured surface of the machined workpiece shown in Figure 5-2 (c) indicates the material transfer from the cupper electrode to the work surface. Figure 5-2 (d), (e) and (f) shows the SEM micrographs of the micro-machined surface.

5.4.2.2 Configuration of Micro-Slots

The Micro-EDM machine was set to produce V-shaped, U-shaped and semi-circle micro-slots on the Ti6Al4V surface. Figure 5-3 shows the optical microscope images of the cross-sections of the as received and micro-machined surfaces produces by using in-house Micro-EDM on Ti6Al4V workpieces.

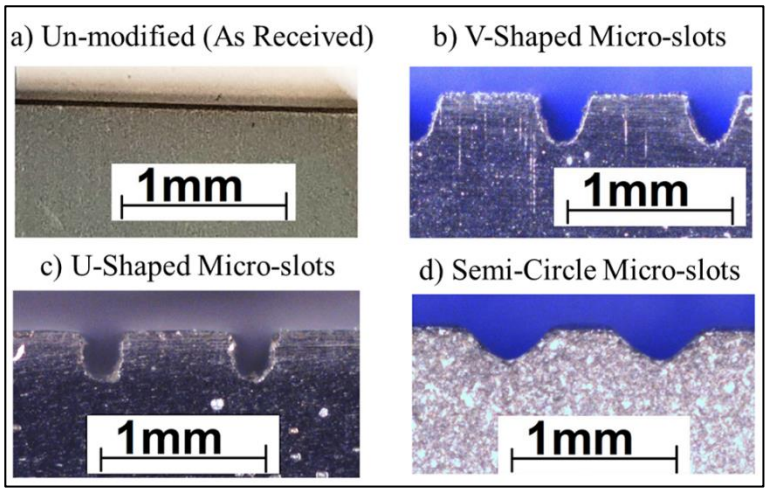

Figure 5-3 Macro images of a cross-sectional view of the un-modified micro-slots produced by in-house built Micro-EDM.

The specifications of the produced micro-slots are reported in Table 5-1. The average dimensions of the micro-slots were calculated by adopting a method shown in Figure 5-2 (g). The produced micro slots dimensions deviated around 5-10 % on average from the pre-set values fed to the machine. However, the reproducibility of the in-house built Micro-EDM is still under study for improvement.

Table 5-1. Average dimensions of micro-slots produced on Ti6Al4V surfaces.

Surface	width, µm	Depth, µm	Spacing, µm	Slots/cm	Surface area, cm^2	Joining configuration
As-Receive	-	-	-	-	1	Face-face
V-Shaped	330	280	550	11.36	+27%	Semi Overlapped *(Slots ⊥ to the load direction)*
						Semi Overlapped (*Slots ∥ to the load direction)*
U-Shaped	258	230	628	12.04	+38%	Semi Overlapped
						Overlapped
						Unaligned
Semi-Circle	500	197	345	11.83	+23%	Interlocked

⊥ = *Perpendicular,* ∥ = *Parallel*

The micro-machining helped increase in the surface area of Ti6Al4V alloy compared to the as received by around 30 % (on Average). The number of micro-slots achieved per centimetre and relative increase in the surface area for each shape of micro-slot is reported in Table 5-1. Figure 5-4 shows the SEM images of Ti6Al4V alloy the as received and the micro-machined surface (V-Shaped micro-slots).

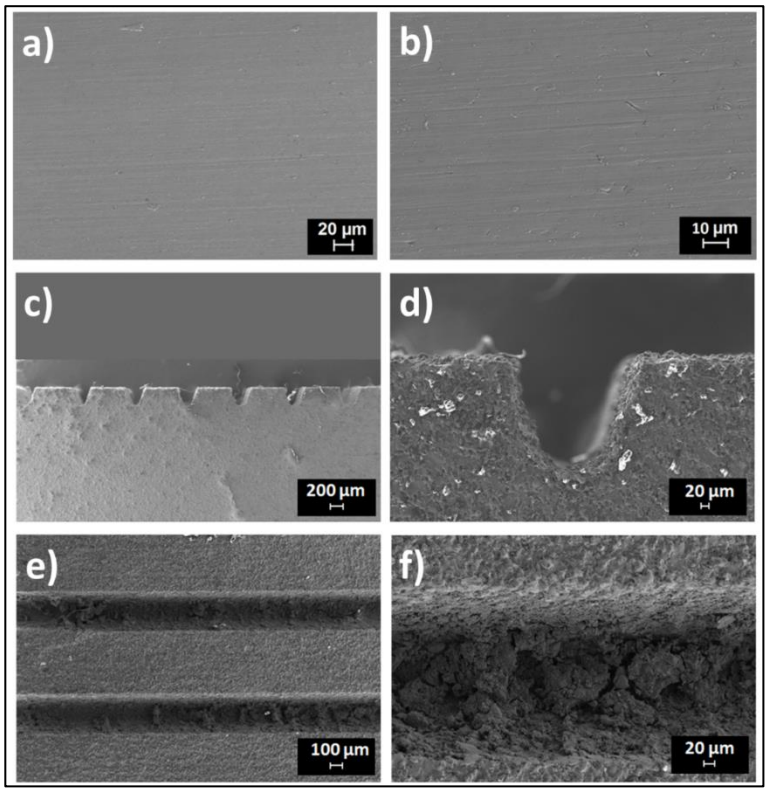

Figure 5-4 Micrographs of a representative micro-machined Ti6Al4V sample (V-Shaped micro-slots). (a) and (b) side view, (c) and (d) top view.

Micro-EDM process resulted in an uneven surface in the machined area. Figure 5-4 (e) and (f), reveals protruding nano-structured surface at a higher magnification which potentially can enhance the interlocking at the adhesive/metal joining interface.

5.4.3 Specimen Preparation

Ti6Al4V substrates, of dimension 10 mm x 4 mm x 3 mm, were cut off from the micro-machined and as received Ti6Al4V sheets using a ceramic blade. Prior to joining, the as-received Ti6Al4V substrates were polished with SiC-paper (P-600). The micro-machined surfaces were not abraded to maintain the dimensions of the micro-slots. Prior to joining, all Ti6Al4V joining substrates (with and without surface modification) were cleaned with alcohol in an ultrasonic bath for 10 min at 60 ^{o}C to de-grease the surface and remove the impurities.

The two parts of commercial epoxy adhesive were mixed, and the mixture was applied to the dried surfaces of the joining substrates. The joining substrates were then stacked in an offset configuration, as shown in Figure 5-5 (b).

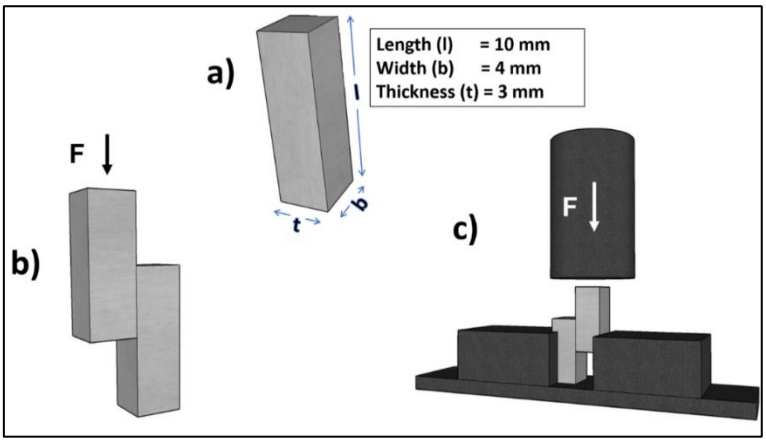

Figure 5-5. The Single Lap Offset (SLO) shear test specimen and test configuration. (a) Ti6Al4V substrate dimensions, (b) bonded sample configuration, (c) SLO test setup.

After applying the adhesive to the joining surfaces, each pair of joining substrates was shimmed together before subjecting to curing cycle to ensure that the adhesive fills the micro-slots. All the specimens were placed in an oven for curing 82 ^{o}C for 1 hour in the air without using any pressure.

Three pairs of bonded specimens with and with-out micro-machined surfaces were produced together for each configuration reported in Table 5-1. A set of three bonded specimens having V-shaped micro-machined surface was produced to analyse the effect micro slots on adhesion also when the micro-slots are oriented ‖ to the direction of load. In total, seven sets of specimens, each having three pairs of bonded substrates, were produced.

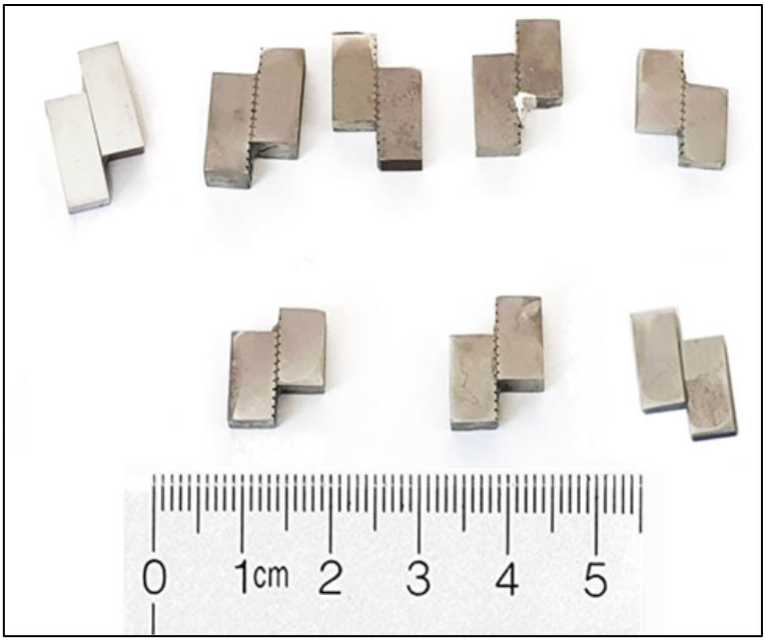

Figure 5-6. Macro-image of produced specimens for microscopic analysis and SLO test.

All the bonded pair of specimens were subjected to compression load in a Single Lap Offset (SLO) test configuration shown in Figure 5-5 (c). Single Lap Offset test procedure is derived from ASTM D905-03 and is described by Casalegno et.al [240]. Figure 5-6 shows the specimens prepared for SLO test in this study. The loading speed was set to 1 mm/min on a universal mechanical testing machine (SINTEC 10/D) equipped with a 5 kN load cell to determine the apparent joint shear strength of bonded samples. The loading was stopped when the joint failure occurred.

All the SLO tests were conducted at a room temperature (25 ^{o}C) and 65% relative humidity. Maximum load values at failure were recorded for each bonded specimen. Macro and micro images of tested specimens were obtained to analyse the joint failure mechanism. Lap shear strength for each specimen was calculated as maximum load divided by the total joined area.

5.5 Results and Discussion

5.5.1 Microscopic Analysis

Figure 5-7 (a) and (b) shows the cross-section of a bonded specimens with un-modified surfaces. The porosity observed in the joining seam is a defect and can influence the joint strength [32]: porosity is common when adhesives are used as joining material; during curing, the adhesive releases volatile gases which creates porosity in the joining seam. In this study, as all the joints were produced with similar adhesive and at same curing conditions, therefore, the effect of porosity was observed similar for all the joints.

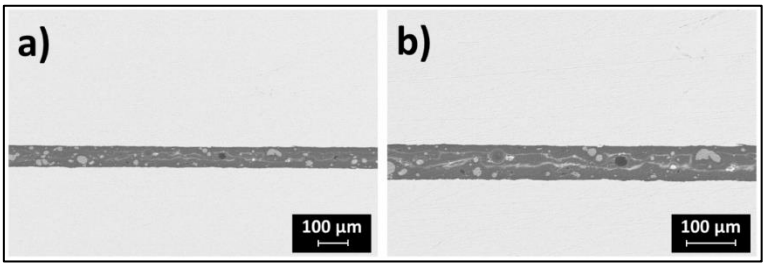

Figure 5-7. (a) and (b) Cross-section of the bonded specimen as received Ti6Al4V surface prepared for joining.

Figure 5-8 (a) and (b) show the cross section of bonded specimens with V-shaped micro slotted surfaces. The cross-section of the bonded specimen with V-shaped micro-machined surface displayed fully filled micro-slots with a semi-overlapped configuration.

The semi-circle micro-slots were produced with relatively curved edges to facilitate the interlocking at the joining interface as can be seen in Figure 5-8 (b)

and (d). The mechanical interlocking between the adhesive and the adherent surface in the micro-machined area are more evident for the semi-circle micro-slots.

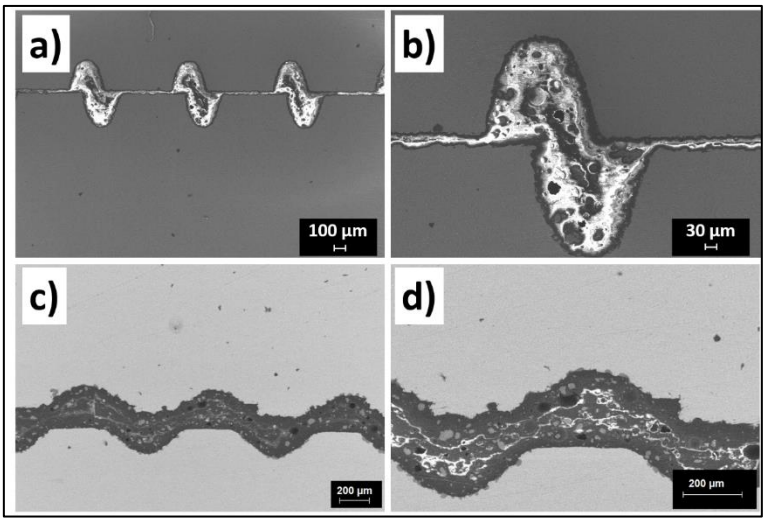

Figure 5-8. (a) and (b) Cross-section of the bonded specimen with V-shaped micro-machined with micro-slots semi aligned to each other (c) and (d) Cross-section of the bonded specimen with a semi-circle shaped micro-machined with interlocked misaligned micro-slots.

Substrates with U-shaped micro-machined surfaces were bonded in three different alignments as shown in Figure 5-9.

Practically it was quite difficult to perfectly align the micro-scale slots in the desired position, however, the best of the efforts were put to achieve the discussed alignments.

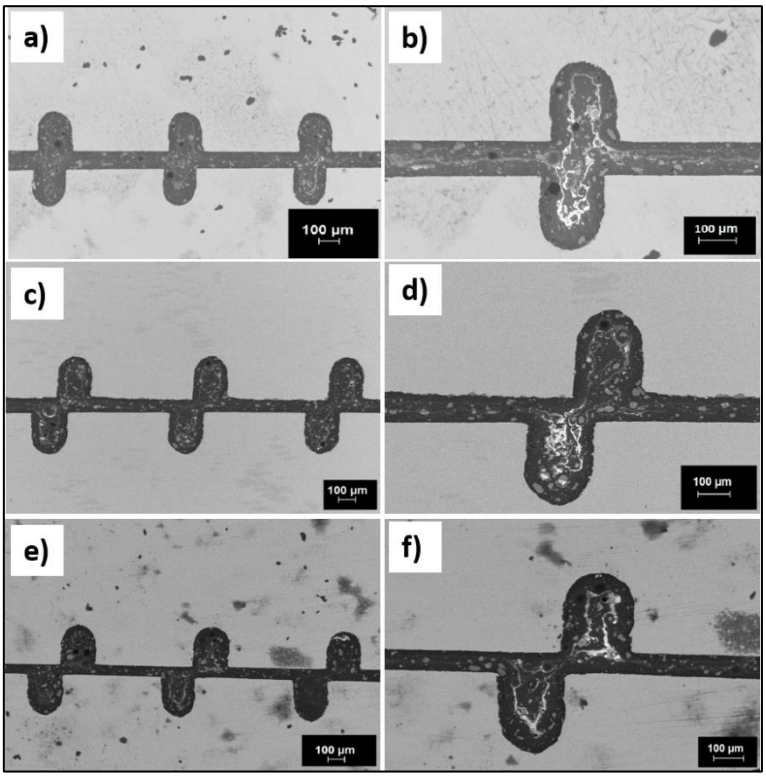

Figure 5-9. (a) and (b) Cross-section of bonded specimen with U-shaped micro-machined with micro-slots aligned to each other (c) and (d) Cross-section of bonded specimen with U-shaped micro-machined with partial misaligned micro-slots, (e) and (f) Cross-section of bonded specimen with U-shaped micro-machined with completely misaligned micro-slots.

The increase in surface area by surface modification increases the potential area for bonding. The micro slots were observed completely filled with the adhesive as is evidenced in Figure 5-7, Figure 5-8 and Figure 5-9.

Adhesive joint thickness is considered as an influencing factor in determining the joint strength of a bonded specimen [244]. The average thickness values

presented in Figure 5-10 are taken at the facing points where the surfaces were not modified.

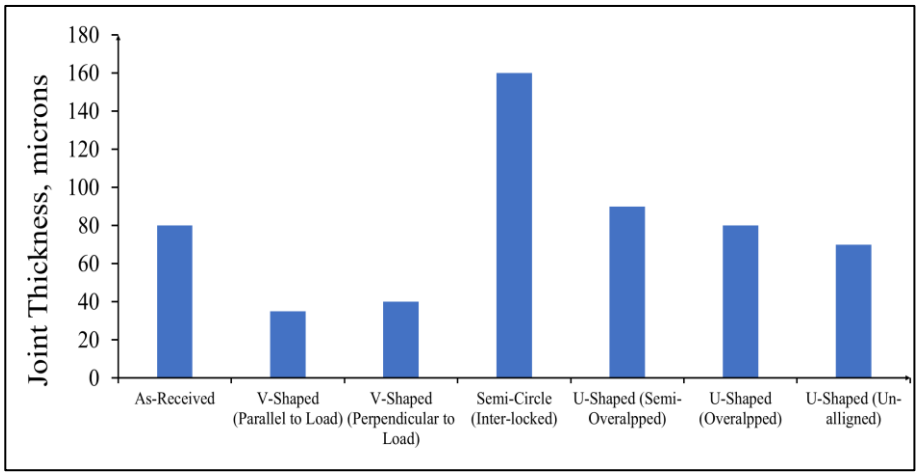

Figure 5-10. Average joint thickness recorded for each set of bonded specimens.

In a pressure less joining, it is generally not easy to maintain the joint thickness at a constant value because the volatile gases which releases during the curing can push out the joined substrates by creating porosity inside the joining seam. Techniques such as introducing glass beads in the adhesive joining seam are employed to control the joint thickness. As the glass beads not only control the thickness but also act as a particle reinforcement in the joining seam, therefore, were avoided.

During the preliminary experiments, around same quantity of joining material was used for all the specimens. Furthermore, the joining substrates were shimmed manually to ensure the filling of micro slots with adhesive which resulted in dissimilar joint thicknesses. However, instead of using glass beads, the use of particular fixtures to hold specimens and control joint thickness during curing cycles will be adopted in the future experiments.

5.5.2 Mechanical Characterization

The average single lap shear test values for each set of bonded specimens are reported in Figure 5-11. The surface machining by Micro-EDM technique showed a significant effect on the joint shear strength.

The orientation of the micro-slots with respect to the applied load was observed as a critical factor in the joining configuration. Compared to non-modified (as-received) surfaces joint, around 12% increase in the joint strength was observed when the samples with V-shaped micro-machined slots were subjected perpendicular ($\perp$) to the applied load while about 11% decrease in joint strength was noticed when the same were subjected parallel ($\parallel$) to the applied load.

The edges of the micro-slots when ⊥ to the applied load, play an important role in resisting the cracks and ultimate failure. While in the specimens where the micro-slots were ‖ to the applied load, the resistance by edges was missing. Moreover, it was assumed that the propagation of fracture is relatively swift when micro-channels were ‖ to the applied load compared to the microchannels oriented ⊥ to the load.

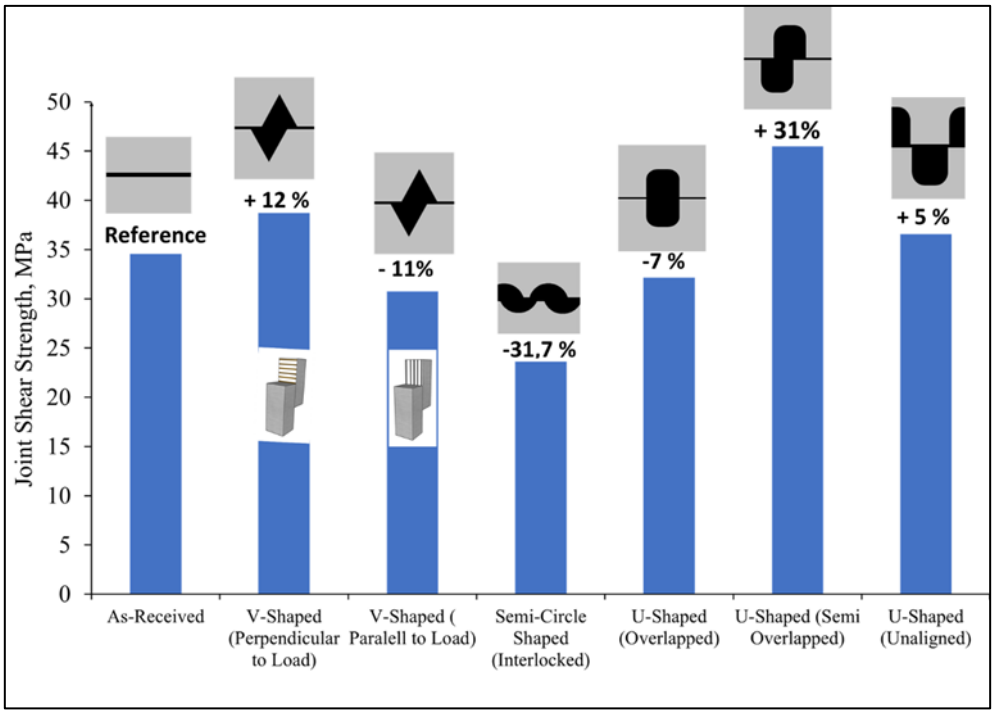

Figure 5-11. Average joint shear strength calculated for each set of bonded specimens.

The specimens with semi-circle micro-slots on the surface displayed around 31 % decrease in the joint shear strength compared to specimens with unmodified surfaces. The round edges of the semi-circle micro-slots were designed to avoid stress concentration points at the micro-slot edge where a crack can be initiated. Another advantage of this design is to achieve physical interlocking between the adherents. However, due to the relatively higher joint thickness of these specimens, the physical interlocking of the micro-slots was not satisfactorily achieved.

The micro-slots alignment with respect each other in the joining seam was also found an influencing factor while determining the joint shear strength of a bonded specimen. It was observed that the U-shaped micro slots when overlapped show decrease in the joint shear strength compared to non-overlapped (misaligned) configurations, which displayed around 5 % increase in the joining strength compared to the as-received specimens. However, when the U-shaped micro-slots were bonded together in semi-overlap configuration, a remarkable increase in the joint strength, around 31 % compare to as received surfaces, was observed. The

micro-slots alignment in an adhesive joint influence the mechanics of load distribution and the resistance to crack propagation during loading.

According to fracture mechanics principles there are two failure criterions: the stress intensity factor criterion and the energetic concepts. A stress intensity failure in adhesive joints is assumed to initiate from local sites of initial imperfection such as pores, cracks or unbonded points along the interface. An imperfectly bonded interface initiates sudden and adhesive failures leading to delamination the bonded substrates at interface and the cohesive fracture initiate from a pre-existing crack in the adhesive layer. While the energetic criteria rely on the supposition that the propagation of an internal defect [245].

The results presented in Figure 5-11 confirms that the alignment of micro-slots with respect to each other and the shape and depths of micro-slots in a joint seam influences the distribution of loads and the propagation of cracks. The variation in the shape and design of micro-slot allowed variable distribution of load and propagation of fracturs which resulted in different joint strength.

When the micro-slots are parallel to the applied load, the mechanical interlocking do not apparently establish due to the orientation of micro-slots and the transition of pure adhesive failure mode into mixed adhesive/cohesive mode is mainly due to the improved adhesion bonding at metal/adhesive interface. Furthermore, the parallel orientation favored the fracture propagation along the load direction resulting in the lower joint strength due to the sliding of the bonded substrates at adhesive/metal interface. De Silva et al. [246] also reported around 6 % decrease in joint strength when the micro slots in bonded area were oriented parallel to the applied load.

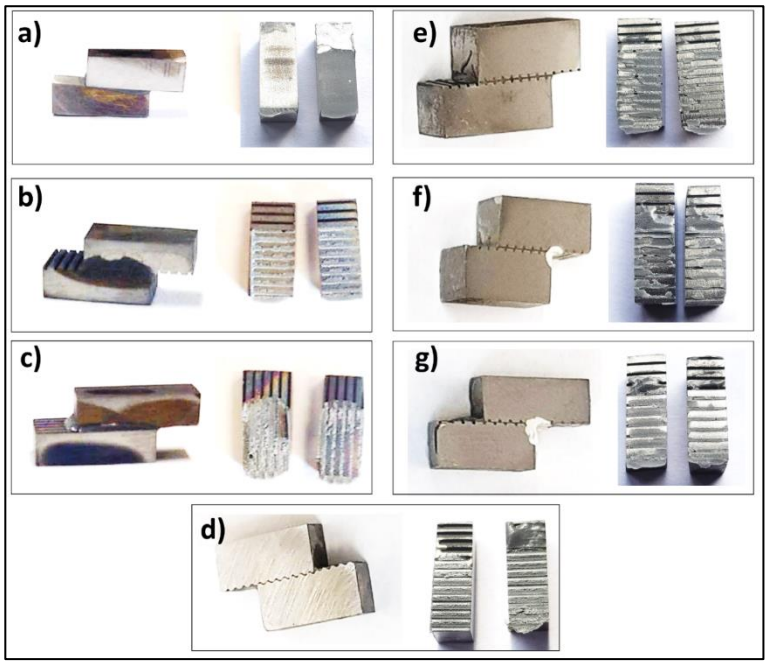

Figure 5-12. Macrographs of post SLO test bonded substrates surfaces. (a) As received Ti6Al4V joint, (b) Micro-machined surfaces joint with V-slots ⊥ to the load, (c) Micro-machined surfaces joint with V-slots ‖ to the load, (d) Micro-machined surfaces with Semi circle-slots, (e) Micro-machined surfaces joint with U-slots in overlapped alignment, (f) Micro-machined surfaces joint with U-slots in semi overlapped alignment, (g) Micro-machined surfaces joint with misaligned U-slots.

Figure 5-12 shows the representative, post SLO test fractured joint surface for each set of bonded specimens. A complete adhesive failure was observed in the specimens with un-modified surfaces, Figure 5-12 (a), which shows a poor adhesion of the surface. Decreases in apparent shear strength correlate well with increases in adhesive failure mode, as anticipated. Surface modification appears to play a key role in maintaining an adhesive bond and driving the specimen to a cohesive failure mode. The rough surface in the micro-machined area has protruding nanostructures which give interlocking effect at the adhesive/Ti6Al4V interface and improves the adhesion [247].

The pitch of micro slots, which also influences the adhesive joint strength properties [19], was kept constant in this study. However, unlike the machined area, the spacings between two micro-slots displayed typical adhesive behaviour like as-received un-modified specimens. The joint failure in the micro-machined specimens can be, therefore, termed as a mixed failure due to the combination of both adhesive and cohesive failure in the joined area.

The increase in the surface area increased the number of adhesives bonds and along with physical interlocking of adhesive with the nano-structured protruding surface in the machined area overcame the adhesive forces leading to cohesive

dominated failures. The shift from complete adhesive failure to a mixed failure evidences the improvement in adhesion by the surface modification of Ti6Al4V alloy. Similar failure modes are reported by other researchers [19,226,248] in the recent past while studying the improvement in adhesion by the surface modification of Ti6Al4V alloy.

Table 5-2 Comparison of in-house developed Micro-EDM micro-machining effect on joining strength with established techniques.

Reference	**Joints Specifications**	**Type of lap shear test**	**Effect of micromachining on joint strength**
Current study	(As received) Ti-6Al-4V/Ti-6Al-4V (Reference samples)	Single Lap-Offset shear (derived from ASTM D905-03)	Reference Value
	V-Slots (Micro-slots Perpendicular to Load)		**12.00%**
	V-Slots (Micro-slots parallel to load)		-11.00%
	Wavy-Interlocked		-31.70%
	U-slots overlapped		-7.00%
	U-Slots semi overlapped		31.00%
	U-Slots misaligned		5.00%
[249]		lap-shear	Reference Value

	Ti (99.6%)/Ti (99.6%) (As received), (epoxy adhesive) *	(ASTM E8/E8M-11)	
	Ti (99.6%)Pre-treated with Plasma Electrolytic Oxidation (PEO) in aluminate-phosphate electrolyte, (epoxy adhesive)	lap-shear	1.65%
		(ASTM E8/E8M-11)	
	Ti (99.6%) Pre-treated with PEO in silicate-phosphate electrolyte, (epoxy adhesive)	lap-shear	-18.62%
		(ASTM E8/E8M-11)	
[19]	Ti-6Al-4V/ Ti-6Al-4V (As received), (PETI-5 adhesive) **	Single lap-shear	Reference Value
		(ASTM D1002-05)	
	Ti-6Al-4V surfaces modified using laser ablation (at 25.4 ablation pattern pitch), (PETI-5 adhesive)	Single lap-shear	15.30%
		(ASTM D1002-05)	
	Ti-6Al-4V surfaces modified using laser ablation (at 12.7 ablation pattern pitch), (PETI-5 adhesive)	Single lap-shear	15.30%
		(ASTM D1002-05)	

Yukimoto et al [250] reported interfacial failure along the step-shaped micro slots, followed by cohesive failure of the CFRP micro slots and epoxy adhesive while only interfacial failure was observed in unmodified bonded surfaces. They further propose that with the increase in the aspect ratio of the micro slots, the

fracture transition to cohesive failure occurs. Vorobyev et al. [247] also reported the improvement in adhesive bonding performance due to improved interlocking within the micro-slots area after Micro-EDM treatment.

The micro-machining increased the surface area available for adhesive bonding compared to as-received surface and has a direct relation with joint strength [19,226]. The effect of Micro-EDM micro machining on the adhesion and joint strength is compared to other currently established surface modification techniques in Table 5-2. However, the preliminary experimental results, presented in Figure 5-11, reveals that the alignment of micro-slots with respect to the direction of load and the alignment of micro-slots with respect to each other in the joint are influencing parameters and governs the load carrying capacity of the adhesive joints.

Considering the variation in the adhesive joint thickness, the preliminary results will be reproduced to obtain a comparable data (experimental is in progress). To understand the effect of micro-machined area, shape and size on the mechanics of crack propagation will be studied in detail according to the principles of fracture mechanics. The load distribution in the joint area of with and without surface modified specimens will be studied using the finite element analysis which is proposed as a future work.

5.6 Conclusion

Ti6Al4V/Ti6Al4V bonded specimens with and without surface modification were produced to analyse the effect of microgeometry of micro-slots on adhesion and the adhesive joint shear strength. V, U and semi-circle shaped micro-slots were successfully produced on Ti6Al4V surfaces using an in-house developed Micro-EDM setup (in Indian School of Mines, India).

Preliminary results show that the bonded specimens with U-shaped micro-slots on the joining surface aligned in semi-overlap configuration exhibit around 30 % improvement in the joint shear strength compared to the specimens with unmodified surfaces.

When the V-shaped micro-slots in a perpendicular ($\perp$) orientation in the bonded specimens were subjected to the applied load, displayed around 23% higher joining strength compared to when the micro-slots were oriented parallel ($\parallel$) to the applied load.

Around 31% decrease in joint strength compared to reference un-modified specimens was noticed when the specimens with a semi-circle shaped micro-slots in interlocking configuration were tested.

Following three factors were observed that apparently influenced the joint shear strength of the adhesive bonded micro-machined specimens:

- The shape/design of micro-slots.
- The alignment of micro-slots with respect to the direction of load.
- The alignment of micro-slots with respect to each other at the joining interface.

The joint fracture analysis confirmed the improvement in adhesion with the increase in bonded surface area and cohesive fractures dominated failure was observed for bonded specimens with micro-machined surfaces compared to the as received.

Authors confidently put forward that further improvement to the in-house built Micro-EDM micromachining setup can emerge as a cost-effective and alternative solution to industries, where surface machining is employed.

The preliminary results obtained during this research activity will help in the selection of micro-slots designing and their configuration at the joint interface for the future work.

6. Joining of SiC-SiC and C/SiC Ceramic Matrix Composites (CMC) To Ti6Al4V Alloy

6.1 Abstract

The aim of this chapter is to review SiC-based Ceramic Matrix Composites (CMC)/Ti6Al4V joining techniques and to discuss the new joining solutions proposed in the current study, such as SiC/SiC and C/SiC composites joined to Ti6Al4V by using active brazing alloy (Cusil-ABA) and Zr-based brazing alloy (TiB590) and the joint strength improvement by surface modification Ti6Al4V alloy.

The microstructure of the joining seams and the elemental compositions of the diffusion zones are investigated using Optical Microscope (OM), Scanning Electron Microscope (SEM) and Electron Dispersion Spectroscopy (EDS) analysis. The joint shear strength values are evaluated using Single Lap (SL) and/or Single Lap Offset (SLO) mechanical tests and the fractured surfaces are analysed to determine the failure modes.

6.2 Graphical Abstract

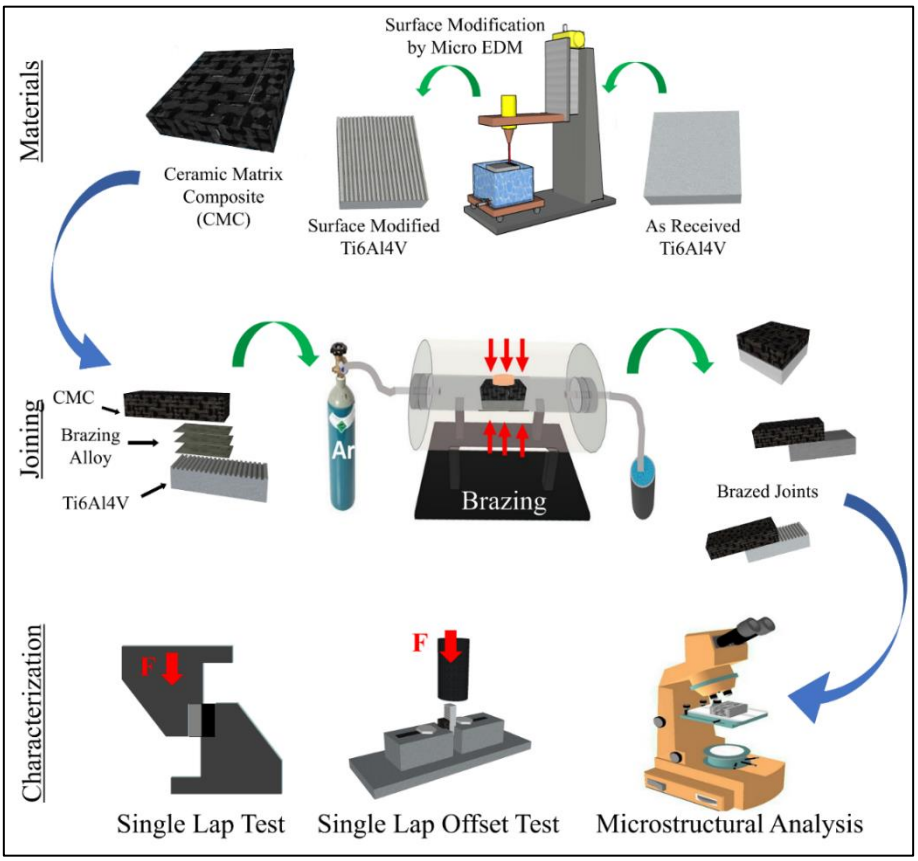

6.3 Introduction

The CMC considered in this study consist of carbon or SiC ceramic fibres embedded in a SiC matrix. They have recently found applications in the fields of advanced aerospace vehicles and energy production.

Ti6Al4V is one of the most commonly used titanium alloys, accounting for more than 50% of total titanium usage. It is an alpha beta ($\alpha + \beta$) alloy i.e. heat treatable to achieve moderate increases in strength. The Ti6Al4V alloys show higher specific strength with good corrosion and oxidation resistance and can retain strength at higher temperatures [8].

Ti6Al4V alloy has found extensive applications in aircraft, automotive and aerospace industries such as aircraft turbine engine components, aircraft structural components, aerospace fasteners; high-performance automotive parts, marine applications, medical devices, and sports equipment [251].

6.3.1 Joining of CMC-Ti6Al4V

Due to the brittle nature and complex production processes of CMC materials, it is difficult to manufacture large and complex structures. For a complex structure,

the smaller parts of CMC are, therefore, joined to itself or to metals, especially Ti alloy.

The development of appropriate joining processes and joining materials is crucial for expanding the structural applications of CMC and Ti6Al4V alloy-based components. Table 6-1 summarises the joining techniques and materials used to join CMC to Ti6Al4V in the recent past.

Heat treatment of α + β titanium alloys above the β transus temperature (935 ^{o}C) affects its mechanical properties due to change in microstructure [252]. However, by adopting an appropriate post-brazing heat treatment, the loss of strength or ductility Ti6Al4V can be recovered [253].

Table 6-1 CMC-Ti6Al4V joining solution proposed in the recent past.

Ref	Joining Substrates	Joining Material, (wt. %)	Joining Method	Joint Strength, [MPa]	Phases at the joining interface
[254]	C/SiC-Ti6Al4V	94 (72Ag–28Cu)–6Ti (wt.%) alloy powder	Vacuum Brazing 890–950◦C for 1–35 min	at 20 ^{o}C =102 at 500 ^{o}C=51	TiC, Ti_3SiC_2, Ti_5Si_3, Ag, TiCu, Ti_3Cu_4, Ti_2Cu, Ti_2Cu+Ti
[222]	C/SiC-Ti6Al4V	Ag-26.7Cu-4.5Ti	Vacuum Brazing 935 ^{o}C for 10 min	with modified C/SiC surface = 10 Otherwise = 3	TiC, $TiSi_2$, TiCu, TiCuSi, Ag, Ti_3Cu
[255]	C/SiC-Nb	Ti-39.4Ni-21.2-Nb	Vacuum Brazing 1160–1260 ^{o}C for 10 min	at 20 ^{o}C = 149 at 600 ^{o}C = 120 at 800 ^{o}C = 73	(Ti,Nb)C, Nb_5Si_3, $(Ti,Nb)_2Ni$ and Ti_5Si_3
[256]	C/C-Ti6Al4V	Graphene nanotubes (GNPs)/Ag-26.7Cu-4.5Ti composite	Vacuum Brazing 750 ^{o}C for 10 min + 880 ^{o}C for 10 min	23.3	Ti_2Cu, TiCu, Ti_3Cu_4, $TiCu_4$/Ag (s,s), Ti_3Cu_4, $TiCu_4$, TiCu/TiC/C/C
[257]	C/C-Ti6Al4V	Ag-26.7Cu-4.6Ti	Vacuum Brazing 910 °C for 10 min	With 15 Vol% SiC particles = 29 Otherwise = 22	TiCu, TiC, TiSiC, Ti_2Cu and Ti_2Cu+Ti (s.s)

[258]	C/C and C/SiC-Ti6Al4V	Metal Glasses 1. MBF-20 (Ni–6.48Cr–3.13Fe–4.38Si–3.13B–0.06C–0.07Co–0.01Al) 2. MBF-30 (Ni-4.61Si–2.8B–0.02Fe–0.02Co–0.01(Al, P, Ti, Zr))	Vacuum Brazing MBF-20 = 1040 °C for 4 min MBF-30 = 1070 °C for 4 min	1. 42 MPa 2. 73 MPa-	C–C/MBF-20 = Single phase enriched in Ti C–C/MBF-30 = Two phase, Ti and light Ni-rich phase TiC, NiCoCr, Cr3B4, Cr3B5, (CrFeMo)xBy,
[259]	C/C-Ti6Al4V	GNPs/Ti-23Cu-11Zr-9Ni powder	Vacuum Brazing 940 °C for 10 min	With 1 wt. % GNPs = 43.7 Otherwise = 22	TiC, $(Ti, Zr)_2(Cu, Ni)$, (Ti, Zr) (Cu, Ni), Ti (s.s) $+Ti_2Cu$
[260]	Cr coated C/C-Ti6Al4V	1.Ti–23Cu–11Zr–9Ni (wt%) 2.Ti–23Cu–11Zr–9Ni (wt%) + pure Cu (40 µm) layer	Vacuum Brazing 960 °C for 15 min	TiCuZrNi = 11.7 TiCuZrNi+ Cu = 39	CrxCy/TiC/β-(Ti,Cr) + $(Ti,Zr)_2Cu$ + (Ti, Zr)Cu + TiC particles/Ti(s.s) + Ti2Cu

6.3.2 Joining Materials for CMC-Ti6Al4V joining

In the C/SiC-Ti6Al4V joint system, silver and aluminium based brazing fillers are generally used as a joining material to achieve a uniform and cracks free joining seam. However, they also have some serious disadvantages such as lower corrosion resistance, lower joint shear strength and are restricted to relatively low service temperature [13]. Joints produce with Ag based fillers are suitable for services temperature up to 400 °C while the joints produce using Al-based joining alloys are restricted to service temperatures below 250 °C [261].

Metallic glass brazes provide high strength, leak tight, corrosion, and fatigue resistant joints [262]. The liquidus temperature of such joining alloys is higher than the beta transus of the Ti6Al4V alloys, however, they display excellent surface wetting properties and are used to join steels, superalloys, and cemented carbides [258]. Zr based fillers were proposed as an alternative to join the Ti alloys and display higher joint shear strength, improved corrosion resistance and can sustain higher working temperatures i.e. ~600 °C [263].

Most of the Zr-based brazing alloys adopted to join ceramic composites to Ti6Al4V alloy contains Cu as an alloying element to relax the stress concentrations and to enhance the ductility of the joint. However, it results in the formation of brittle intermetallic phases (such as $TiCu_2$, $TiAl_3$, $TiNi_2$, Ti_3Cu_4, $(Ti, Zr)_2Cu$, etc.) practically in all titanium brazed joints which are the primary cause of fracture in the joints [259,260,263,264].

Most recently, Shapiro et al. used (Zr-Ti-Ni-Hf) fillers to join Ti6Al4V to itself to avoid the brittle intermetallics produced with quaternary near-eutectic filler metals of the Ti-Zr-Cu-Ni family [263,264].

Besides the selection of a suitable joining process and joining material, the strength of a CMC-metal joint system can also be improved by the modification of joining surfaces.

6.3.3 Surface Modification

Due to extreme hardness and relatively low ductility of CMC parts, they are difficult to machine. On the contrary, metals are ductile and can be machined easily.

Micro Electrical Discharge Machining (Micro-EDM) is an economic and a versatile process for machining different micro-texturing features that can be modelled to optimize effectiveness, for both conductive and non-conductive materials [265]. The details of surface modification of Ti6Al4V surfaces using Micro-EDM technique is discussed in Chapter 5.

6.4 Experimental Work

In this research activity, the brazing of CMCs (C/SiC and SiC/SiC) to Ti6Al4V using Active brazing alloy (CusilABA) foils and Zr-based braze (TiB590) foils as joining materials was carried out utilizing a pressure-less brazing technique in an argon atmosphere. Further improvement in the joint strength is experimented by adopting surface modified Ti6Al4V substrates.

The joining interfaces of the brazed specimens were investigated, and the joint shear strength was determined.

6.4.1 Materials

The CMC used were SiC/SiC and C/SiC composites, shown in Figure 6-1. The SiC/SiC (density = 2.3-2.4 g/cm^3) composites were supplied by MT Aerospace, Augsburg, Germany.

The C/SiC composites (density=1.8 g/cm^3), were supplied by Airbus Defence and Space GmbH, Germany: SiC/SiC was reinforced with 0/90 woven SiC fabric and the C/SiC was reinforced with layers of unidirectional long carbon fibres stacked in 0/90 nonwoven configuration.

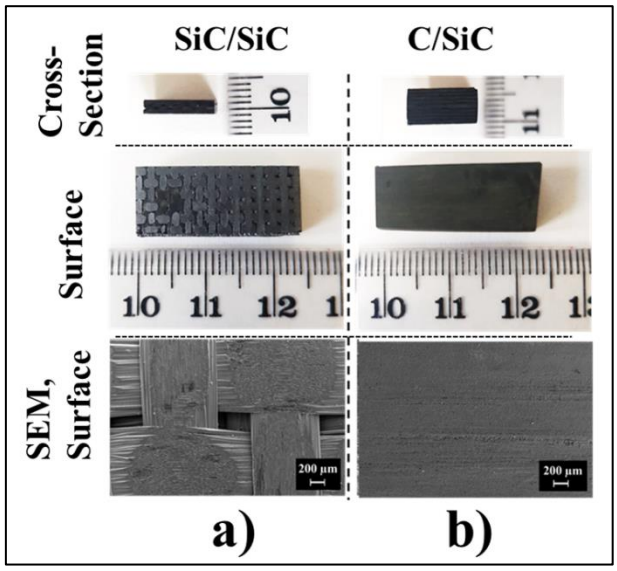

Figure 6-1 Morphology of SiC-based CMC used in this work a) SiC/SiC, b) C/SiC

The active brazing alloy foils, (Cusil ABA, 50 µm thick), were supplied by Wesgo-Metal, USA. Zr-based filler foils, 50 µm thick, (TiBraze® 590), were supplied by Titanium Brazing, Inc. Columbus, Ohio, USA. The properties of materials (joining substrates and joining materials) discussed in this chapter are reported in

Table 6-2.

Table 6-2. Properties of material used in this chapter.

Material	**Physical Form**	**Composition, (wt.%)**	**Solidus, °C**	**Liquidus, °C**	**CTE** (10^{-6} K^{-1})
SiC/SiC	coupon	Reinforcement: SiC fibres, Matrix: SiC	-	-	4
C/SiC	coupon	Reinforcement: Carbon fibres, Matrix: SiC	-	-	$\parallel$=2, $\perp$ = 5
Ti Alloy	Sheet	Ti-6Al-4V	1604	1660	8.7-9.1
Cusil-ABA	Foil	63.0 Ag-35.3 Cu-1.8 Ti	780	815	18.5
TiB590	Foil	61.7Zr-17.3Ti-20Ni-1Hf	796	813	8.8

Ti6Al4V alloy sheets having a thickness of 1.5 mm and 4.5 mm were supplied by MTA, Aerospace Germany and M/s Aich Enterprise, Kolkata-6, India respectively.

6.4.2 Ti6Al4V Surface Modification

The Ti-6Al-4V surface was modified by using an in-house built Micro-EDM setup in the Indian School of Mining (Indian Institute of Technology (ISM), Dhanbad, India). The Micro-EDM working is discussed in Chapter 5 section 5.4.2.

Ti6Al4V with V-shaped micro-slots on the surface were brazed to C/SiC composites. Using a digital interface, the Micro-EDM was set to produce 300 μm wide and 200 μm deep V-shaped micro-slots at a distance of 500 μm from each other on the surface of a 4.5 mm thick Ti6Al4V alloy sheet. The average width of the V-shaped micro-slot was calculated around 330±10 μm, the average depth was 280±20 μm and the average distance between the slots were found 550±30 μm, Table 5-1.

The micro-machining process resulted in around 30% increase (measured by the method shown in Figure 5-2 (g)) in the surface area of the Ti6Al4V surface. In the machined area, surface with protruding nano-structures was observed which can further enhance the interlocking at the joining seam/metal substrate interface.

6.4.3 Joined Specimen Preparation

The CMC-Ti6Al4V joints were produced mainly in two different configurations: Single lap and single lap offset configurations. Ti6Al4V sheets were cut using a ceramic blade and the CMC composite sheets were cut using a diamond blade to the desired size using a precision cutting machine.

The joining surfaces were abraded with SiC paper (no. 360) and were cleaned with alcohol in an ultrasonic bath for 10 minutes at 60 ^{o}C to remove the surface impurities prior to brazing.

All the joining components (CMC, joining materials and Ti6Al4V) were then stacked in a configuration shown in Figure 6-2 (a), (b) and (c). The CMC composites adopted in this study were relatively porous, therefore, during the brazing process, they were placed in the top position to avoid excessive infiltration of brazing alloy.

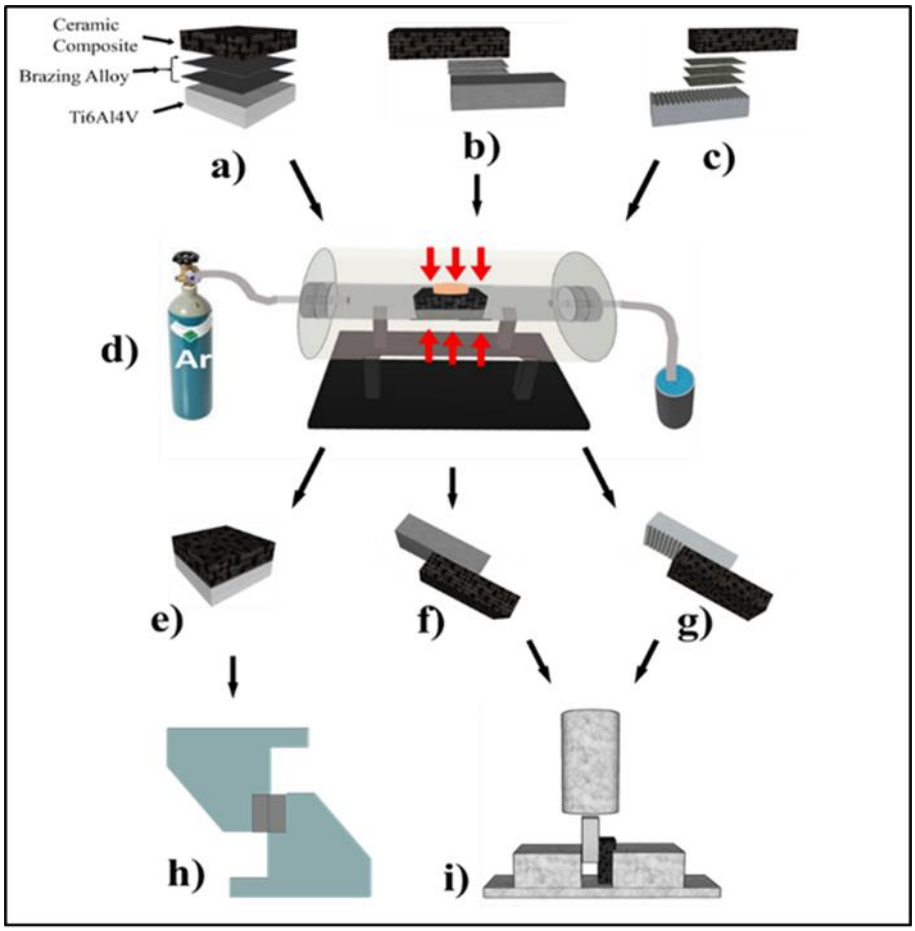

Figure 6-2. Specimen preparation and brazing, (a), (b) and (c) Joining components stacking configuration, (d) Brazing in a tubular furnace equipped with Argon Supply, (e), (f) and (g) Brazed Joints, (h) Single Lap (SL) test, (i) Single Lap Offset (SLO) test

A small weight (15 g) was placed on the stacked configuration to ensure the stacking alignment during the brazing experiments. All the brazing experiments were carried out in a Carbolite® tube furnace equipped with Argon (Ar) gas supply and a digital control panel. A model of brazing setup is shown in Figure 6-2 (d).

Several sets of brazing parameters (time, temperature, heating rate (H/R) and amount of joining material based on the literature review and phase diagram studies were tried to achieve a uniform joining seam with the adequate diffusion of the joining material into the joining substrates (CMC-Metal) along the interface. The optimised brazing parameters were decided when the surface wettability, adequate diffusion and non-porous uniform joining seam was achieved. Moreover, to avoid the effect of higher temperature on Ti6Al4V microstructure, a set of lower temperature and higher dwell were preferred over higher temperature and lower dwell time. The sets of optimized joining conditions at which sound joining was observed are reported in Table 6-3.

At the optimum brazing conditions, three SL specimens of dimension 10 mm (l) x 10 mm (w) were produced while 10 mm (l) x 4 mm (w) x 4.5 mm (t) joining substrates (CMC and Ti6Al4V) were brazed together with a 6 mm offset for SLO test configuration.

Table 6-3 Set of optimised brazing parameter

#	Joining Configuration	No. of Brazing Foils	Joining parameters		
			Temperature, ^{o}C	Dwell Time, min	Heating Rate, ^{o}C/hr.
1	SiC/SiC-CusilABA-Ti6Al4V	2	900	15	2000
2	C/SiC-CusilABA-**Surface Modified Ti6Al4V**	4	900	15	2000
3	C/SiC-TiB590-Ti6Al4V	2	920	10	1000
4	C/SiC-TiB590-**Surface modified Ti6Al4V**	4	940	15	1000

The joining interfaces were analysed using Optical Microscope (OM) and Scanning Electron Microscope SEM equipped before and after the mechanical test. The compositions of the multiple phases across the joints were investigated using the Electron Dispersion Spectroscopy (EDS).

The joint shear strength of the brazed joints was determined using a universal mechanical testing machine (SINTEC D/10) equipped with a 5 kN load cell at a room temperature and 65% relative humidity. Single lap (SL) shear test method [266], adapted from ASTM D1002-05, and Single Lap Offset (SLO) shear test method (as discussed in Chapter 5).

Before the mechanical test, the SL test specimens were glued to aluminium fixtures (Figure 6-2 (h)) using Scotch-Weld DP 490 epoxy and the curing was carried out for 45 minutes at 90 ^{o}C in Heraeus™ oven while the SLO test samples were carefully placed (not glued) in a steel fixture, (Figure 6-2 (i)), before subjecting to load without gluing. All the test samples were subjected to a compression load at a speed of 1 mm/min. The loading was stopped when the joint failure was ensured. Maximum load values at failure were recorded for each sample and macro images of the joint fracture were obtained to analyse the failure modes.

Joint shear strengths values were calculated by dividing maximum load over the joined area.

6.5 Results and Discussion

6.5.1 SiC/SiC-CusilABA-Ti6Al4V Joint

Figure 6-3 (a) and (b) represents the optical microscope images of the SiC/SiC-Ti6Al4V joint cross-section produced using a single (50 microns thick) CusilABA foil. During the brazing process, some of the joining melt infiltrated into the pores of the ceramic substrate, therefore a single CusilABA foil was observed not enough to produce a continuous joint. A uniform and around 40-45 microns thick continuous joining seam was achieved, Figure 6-3 (c) and (d), when two foils of CusilABA were used as a joining material.

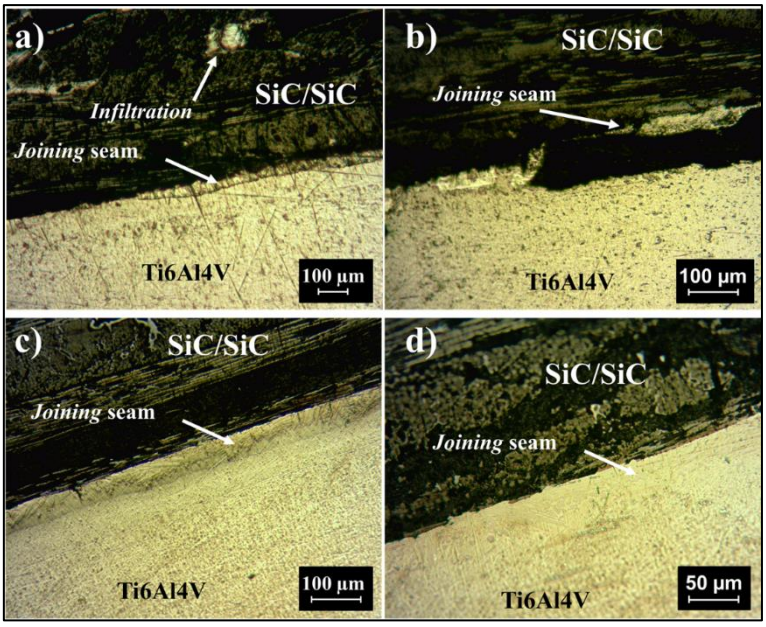

Figure 6-3. OM images of the (a) and (b) SiC/SiC-Ti6Al4V joint produced using one CusilABA foil, (c) and (d) SiC/SiC-Ti6Al4V joint produced using two CusilABA foils.

Figure 6-4 presents the SEM micro images and the EDS analysis carried out at the SiC/SiC-CusilABA (2-foils)-Ti6Al4V joint interface. At the brazing temperature, Ti from the joining melt migrated to the ceramic surface to form a non-continuous TiC and TiSi reaction layer. The EDS analysis shows Si, Ti and C enrichment at or near the SiC/SiC-CusilABA joint interface which is due to the high chemical affinity of Ti towards C and Si. The affinity of Ti towards C, in particular, is beneficial because it promotes surface wetting but the formation of Brittle TiC layer is detrimental to the joint strength [258]. Singh et al. [267] reported that the formation of titanium carbide and titanium silicides at this point is

thermodynamically possible as ΔG<0 while analysing the reaction between SiC fibre-bonded ceramics brazed with Ag-Cu-Ti alloy.

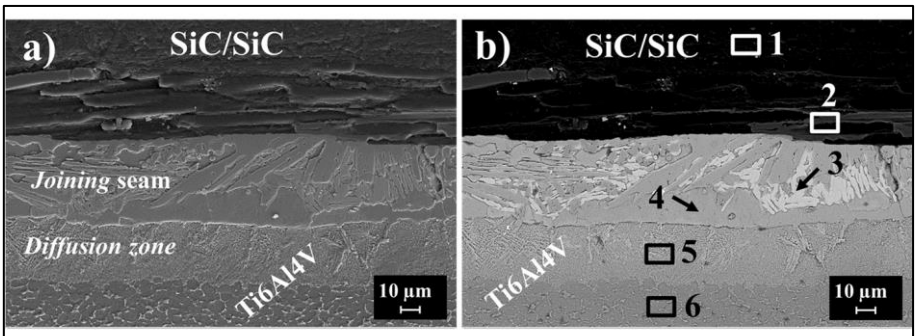

	EDS/Elements	Ag	Cu	V	Ti	Al	C	Si	O
c)	1	-	-	-	-	-	56.59	43.41	-
	2	12.01	22.36	-	57.73	5.79	4.70	1.09	-
	3	94.51	4.31	-	0.77	0.41	-	-	-
	4	11.12	36.50	-	32.68	6.88	12.81	-	-
	5	9.93	20.45	3.12	57.30	4.21	-	-	4.99
	6	-	-	3.61	89.55	6.85	-	-	-

Figure 6-4 (a) In-lens SEM, (b) Bask scattered SEM image and (c) EDS analysis of the SiC/SiC-CusilABA-Ti6Al4V joint interface.

The presence of Si evidenced at the SiC/SiC-Cusil ABA interface favours the formation of titanium silicides besides the TiC_x compounds [268]. During the brazing of C/SiC and Ti6Al4V using Ag-Cu-Ti ABA, Xiong et al. [254] observed that Ti reaction with SiC matrix is more evident than with carbon. The Ti-Si compounds forms during the solidification where SiC dissolves in brazing melt. Lui et.al [269] and Asthana et.al [270] also reported the formation of Ti_5Si_3 and TiC compounds in the reaction layers during self-joining of SiC ceramics using Ag-Cu-Ti alloys as a joining material.

The solidified braze matrix in the joining seam displays a two-phase eutectic microstructure with the Ag-rich light grey areas, Figure 6-4 (b) EDS 3, and the Cu-Ti rich dark grey, Figure 6-4 (b) EDS 4. Literature study summarised in Table 6-1 suggests the possible formation of Ag, TiCu, Ti_3Cu_4, Ti_2Cu, phases in this zone [254].

The grey zone appeared in the Ti6Al4V component at the Ti6Al4V-Joining seam interface is due to the diffusion of Ti and Al diffusion from Ti6Al4V alloy towards the joining seam and the diffusion of Ag and Cu from the joining melt towards the Ti6Al4V surface, Figure 6-4, EDS 5.

Three brazed specimens of dimension 10 mm x 10 mm were subjected to compression load in an SL test to analyse the joint shear strength of the SiC/SiC-

Ti6Al4V joints produced using two foils of Cusil ABA as a joining material. Figure 6-5 (a) and (b) represents the macro images of the SL test specimens before and after the mechanical test.

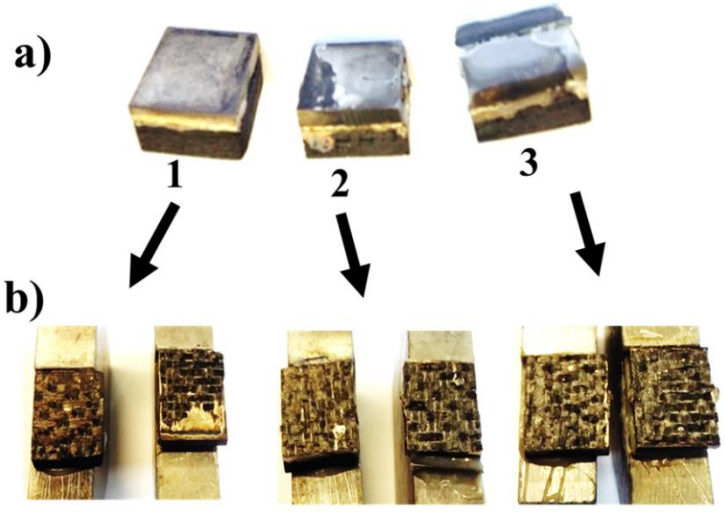

c)

Specimens No.	Maximum Load, [N]	Joining Area, [mm2]	Joint Shear Strength, [MPa]
1	285	108.6	2.37
2	101	105	0.96
3	68	116.6	0.58

Figure 6-5. (a) SiC/SiC-Ti6Al4V brazed SL test specimens, (b) post SL test joint surfaces top view, (c) SL test results

During the mechanical test, it was observed that all the specimens failed due to the *delamination of the SiC/SiC composite and no failure was observed at the joining seam*. It is evidenced in Figure 6-5(b) that delaminated SiC/SiC layer is still attached to the Ti6Al4V component while the joint is still in place. The interlaminar shear strength of the SiC/SiC composites is around 2-3 MPa. Around the same was observed during the SL test, reported in a table shown in Figure 6-5 (c).

Although the SL test results do not represent the true value of the C/SiC-CusilABA-Ti6Al4V joint strength, however, it confirms that the apparent joint strength is higher than the interlaminar strength of the SiC/SiC component.

6.5.2 C/SiC-TiB590-Ti6Al4V Joint

At the brazing conditions, reported in Table 6-3, satisfactory spreading of TiB-590 foils on the C/SIC and Ti6Al4V surfaces was observed. C/SiC composite

substrates were brazed to Ti6Al4V (un-modified surface) using two, 50-micron thick, TiB590 foils in an argon atmosphere.

Figure 6-6 represents the SEM images of the C/SiC-TiB590-Ti6Al4V joining seam using as received and surface modified Ti6Al4V substrates. At the optimised brazing conditions, a uniform, crack-free and void-free joining interface was observed.

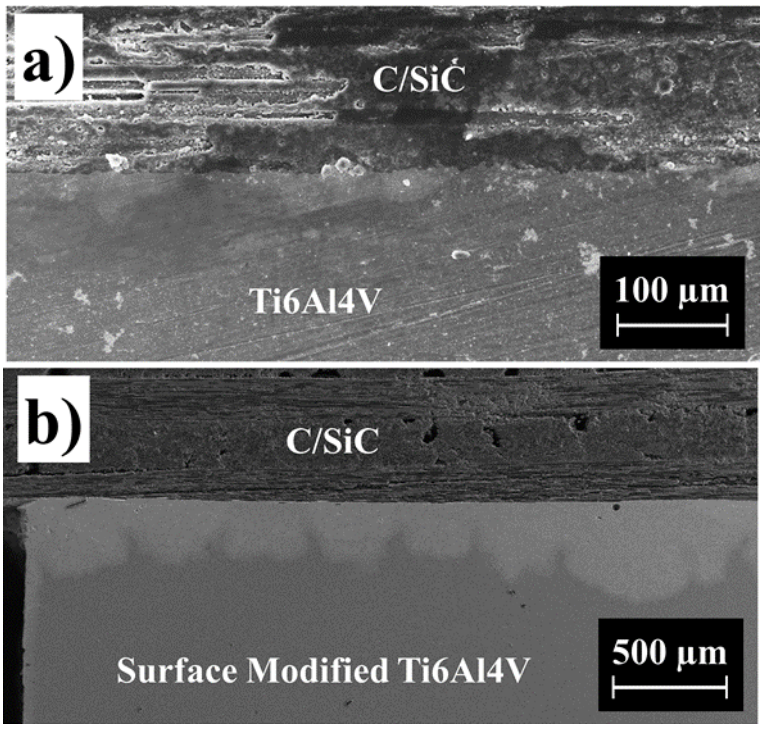

Figure 6-6 SEM images of the C/SiC-TiB590-Ti6Al4V joining seam using a) unmodified and b) surface modified Ti6Al4V substrates.

Almost half of the micro-slots on Ti6Al4V substrate surface were filled when two foils of TiB590 alloy were used as a joining material and without modifying the brazing parameters. The complete filling of micro-slots was achieved when the brazing temperature and number of brazing foils was increased as reported in Table 6-3.

The TiB590 fillers contain active Ti and Zr elements with good metal-glass forming ability. At the brazing temperature, these active elements supposedly diffuse and forms a diffusion layer at the substrates surfaces near the joining interface.

According to the supporting literature, the joining interface layer adjacent to C/SiC is possibly composed of $HfSi_2$ [271] and C (Ti, Zr) [272], the interlayer Ti_2Zr, Ti_3Si, Zr (s.s), $HfSi_2$ and Al_3NiZr_6 compounds, while the diffusion area adjacent to Ti6AlV is possibly composed of $AlNi_3$, $AlZr_4$ Al(Ni, Zr) and Ti(Al, V) compounds.

The metal carbides (ZrC and TiC) formed in the joining seam are relatively brittle in nature, however, compared to SiC matrix, the ZrC and TiC exhibit larger bulk modulus, smaller changes in the Young's and shear moduli, as well as better ductility [272,273].

Hf and Si react at temperature 600 ^{o}C to form HfSi and at 765 ^{o}C to form $HfSi_2$ [274]. Hafnium di Silicide ($HfSi_2$) is high-oxidation resistant compound and is commonly used as high-temperature oxidation resistant coating in high temperature structural materials and aviation and spaceflight etc [271].

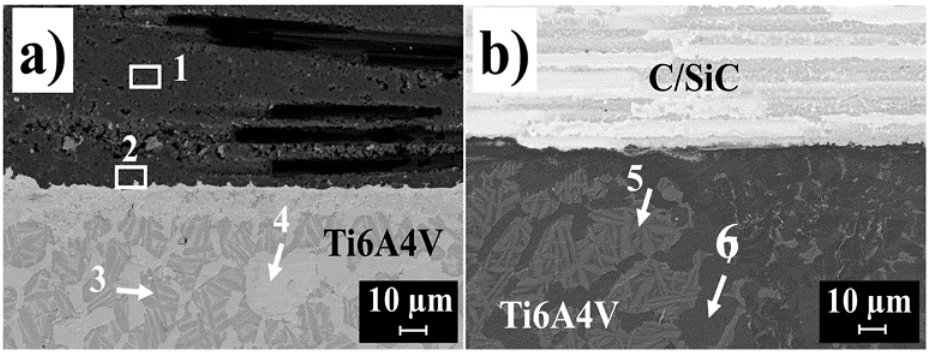

C)

EDS/Elements	Composition, wt. %								
	Zr	Ni	V	Ti	Si	Al	C	Hf	O
1	-	-	-	-	55.54	-	31.94	-	12.52
2	35.58	12.03	-	27.61	5.9	1.4	6.92	0.68	9.88
3	49.77	20.58	1.59	27.2	-	0.86	-	-	-
4	37.82	13.4	-	17.65	-	1.39	18.85	-	8.35
5	41.83	14.43	0.91	27.4	3.15	1.33	10	0.95	-
6	26.59	12.73	1.59	56.75	-	2.34	-	-	-

Figure 6-7. a) and b) SEM images of the C/SiC-Ti6Al4V joint interface, c) EDS analysis of C/SiC-Ti6Al4V interface

A strong attraction between Ti-Al and Ti-Si as well to form intermetallic compounds have been reported by Vahlus et al. [275] and the thermodynamic assessment shows the formation of Ti_3Si+TiAl compounds at ~1049 ^{o}C [275,276]. However, the ductile to the brittle transition temperature of the TiAl and Ti_3Al intermetallics is above 800 ^{o}C and have coarse-grained lamellar or equiaxed structures [277].

In the diffusion layer adjacent to Ti6Al4V, a two-phase microstructure was observed. The grains of Zr rich dark phase (Figure 6-7, EDS-3) distributed through the matrix were composed of ~50Zr-27Ti-21Ni-1.6Al-0.8V wt.% alloy (with traces of Hf). The matrix phase (Figure 6-7, EDS-4) is represented by large islands of ~37Zr-17Ti-13Ni-1.4Al wt.% alloy (with traces of V and Hf) where the V and Al

are diffused from base Ti6Al4V alloy due to the diffusion driving force caused by the concentration gradients. The obtained results are supported by observations reported in [253,263].

Ti-Zr compounds observed at the joining interface generally display low structural stress concentrations, therefore the Ti6Al4V-Joining seam interface is potentially resistant to dynamic loading [278]. According to phase diagram, the dark phase grains constitute Zr-Ti α solid solution system which has solidification temperature ~1600 ºC [279]. The crystals within are solidified first, most probably at the brazing temperature, and left all the nickel in the ternary eutectic Zr-Ti-Ni liquid, which solidifies only below 820 ºC during cooling after brazing. Shapiro et al. observed similar behaviour while brazing Ti alloys using TiBraze foils [263].

6.5.2.1 C/SiC-TiB590-Ti6Al4V Joint Shear Strength analysis

Three C/SiC-TiB590-Ti6Al4V brazed specimens (with un-modified Ti6Al4V surfaces) of dimension 10 mm x 10 mm were produced and subjected to compression load in an SL test configuration to evaluate the joint shear strength. Figure 6-8 represents the macro images of the SL test specimens after the mechanical test and the average SL test results.

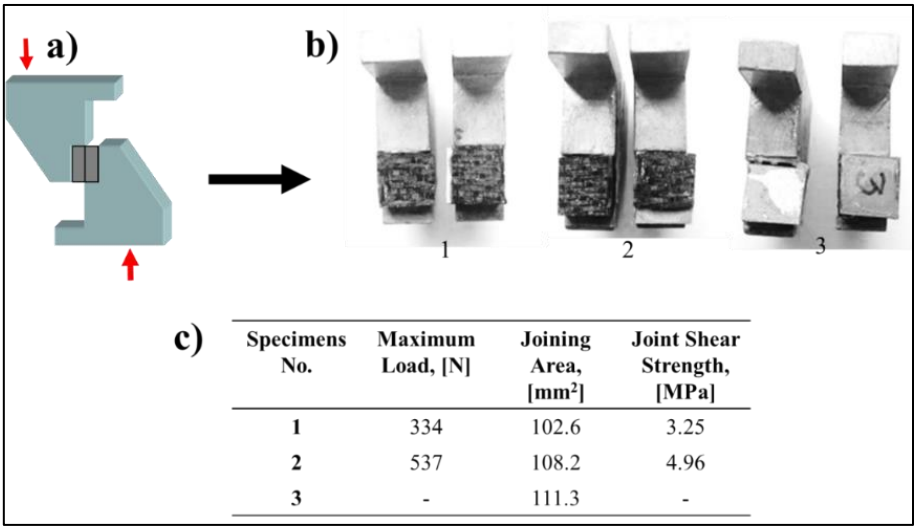

Specimens No.	Maximum Load, [N]	Joining Area, [mm²]	Joint Shear Strength, [MPa]
1	334	102.6	3.25
2	537	108.2	4.96
3	-	111.3	-

Figure 6-8 (a) Single Lap (SL) configuration, (b) Macro images of post SL test fractured surface of C/SiC-TiB590-Ti6Al4V, (c) SL test results.

During the SL test, the specimen 1 and 2 failed due to the delamination of the C/SiC composites while the specimen 3 was discarded because the epoxy glue with which the specimen was bonded to the aluminium fixture failed. The delaminated layer of the C/SiC composite attached to Ti6Al4V component after the failure is shown in Figure 6-8 (b) while the C/SiC-Ti6Al4V joint remained intact. The interlaminar shear strength of the uncoated C/SiC composites used in this work was around 4 MPa. The results displayed in Figure 6-8 (c) shows that the specimen failure occurred in the range of 3-5 MPa, therefore it was assumed that the C/SiC-

Ti6Al4V joint produced with Zr-based alloy is higher than the interlaminar shear strength of the C/SiC composites.

As discussed earlier, SL test configuration was adopted to evaluate the joint shear strength of the CMC/Ti6Al4V joints, but all the specimens failed due to low interlaminar delamination of the ceramic composites. Therefore, Single Lap Offset (SLO) test configuration was adopted for further joint shear strength analysis to avoid delamination of the ceramic specimen during the test and ensure the failure in the joining seam.

C/SiC-Ti6Al4V SLO test specimens were produced with as received and surface modified Ti6Al4V substrates using Zr-based filler (TiB590) fillers as a joining material. To establish a comparison, another set of C/SiC-Ti6Al4V SLO specimens was produced using CusilABA as a joining material. The interface properties of C/SiC-CusilABA-Ti6Al4V joints are discussed in section 6.5.1. As CusilABA is a conventional alloy used to join SiC based CMCs to Ti6Al4V and Itself, therefore, is also reported by several researchers [268,280] in the recent past.

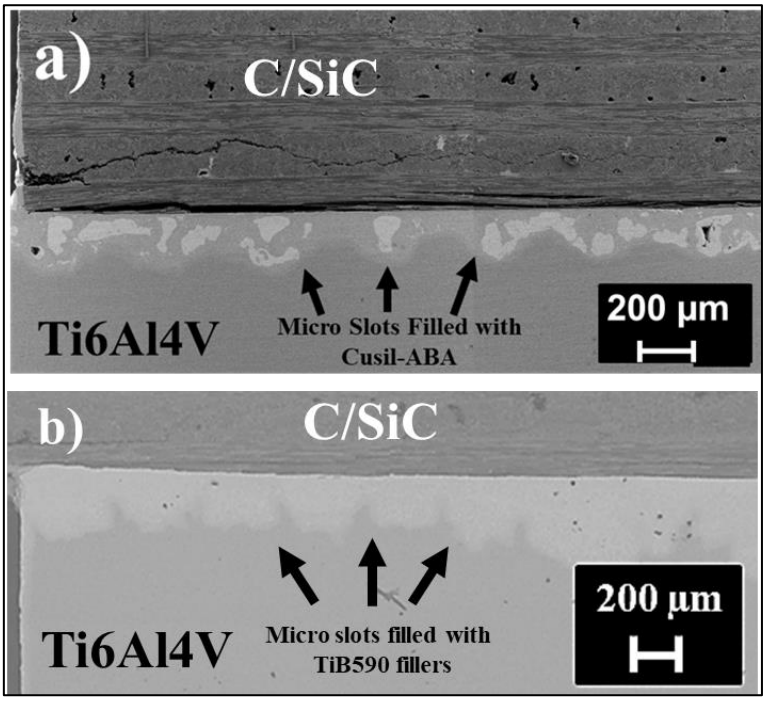

Figure 6-9. Polished cross section of (a) C/SiC/Cusil-ABA/Surface modified Ti6Al4V joining seam, (b) C/SiC/TiB590/Surface modified Ti6Al4V joining seam.

Figure 6-9 (a) and (b) represents the polished cross-section of the C/SiC-Surface modified Ti6Al4V joining seams using CusilABA and TiB590 as a joining material respectively. In the C/SiC-surface modified Ti6Al4V joint, the micro slots were observed filled, when four foils of CusilABA were used as joining material. The visible cracks in C/SiC part (Figure 6-9 (a)) appeared during polishing of the brazed specimen.

Table 6-4 Single Lap Offset (SLO) mechanical test results.

No.	Joint Configuration	Joint Shear Strength, [MPa]	Failure Mode
1	C/SiC-TiB590-Ti6Al4V	43 ± 3	Mixed Mode
3	C/SiC-TiB590-Ti6Al4V *	*6.33 ± 2*	C/SiC delamination
4	C/SiC/Cusil-ABA/ Ti6Al4V	18 ± 3	Mixed Mode
5	C/SiC-CusilABA-Ti6Al4V *	7.9 ± 3	C/SiC delamination

*Surface modified Ti6Al4V substrate

A set of three C/SiC-Ti6Al4V SLO specimens, for each for each of the four joint configurations, reported in Table 6-4 were subjected to compression load using SLO test configuration as shown in Figure 6-2 (i).

It was observed that C/SiC-Ti6Al4V joints produced with Zr based fillers display around **40 % higher joint shear strength** compared to conventional Ag-based (CusilABA) fillers, Table 6-4 (1) and (4). All the brazed specimens produced with unmodified Ti6Al4V surfaces failed at the joining interface.

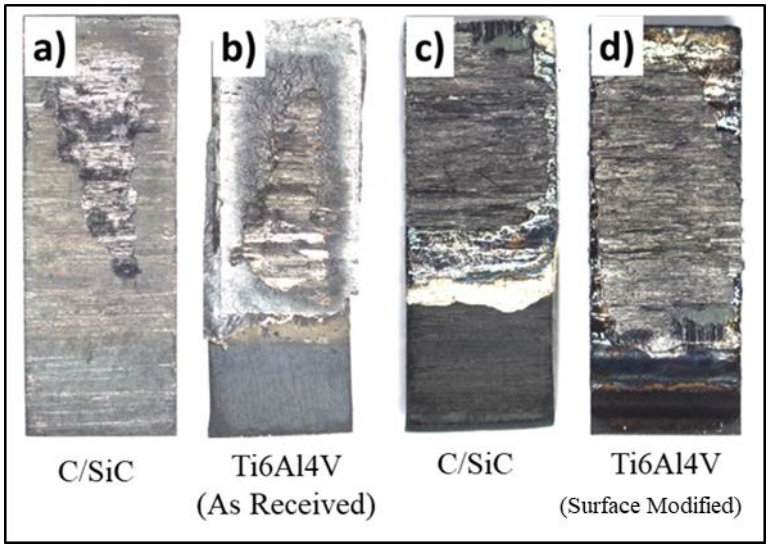

Figure 6-10 Macrographs of post SLO fracture surfaces of (a) and (b) C/SiC-CusilABA-Ti6Al4V and (c) and (d) C/SiC-CusilABA-Surface modified Ti6Al4V bonded specimens.

The brazed joints having a surface modified Ti6Al4V substrates, however, did not fail at the joining interface and the failure observed was mainly due to the delamination of the ceramic composite substrate. Figure 6-10 and Figure 6-11

represents the stitched OM images of the fractured surfaces of the tested SLO specimens.

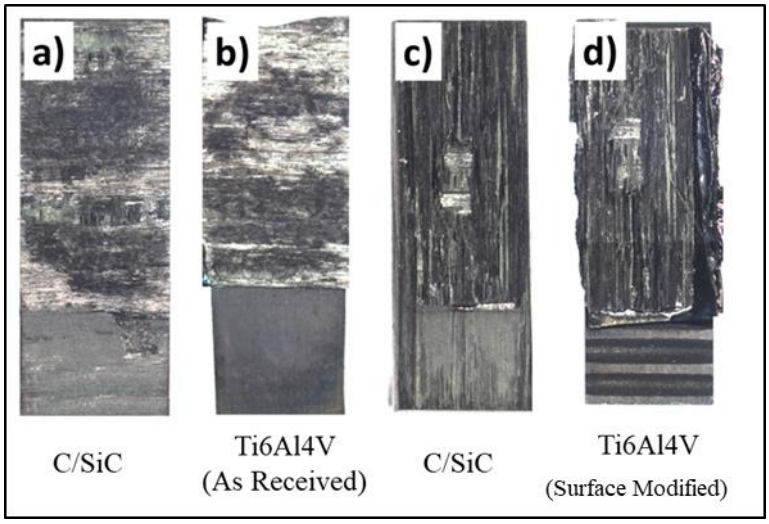

Figure 6-11 Macrographs of Post SLO fracture surfaces of (a) and (b) C/SiC-TiB590-Ti6Al4V and (c) and (d) C/SiC-TiB590-Surface modified Ti6Al4V bonded specimens.

The joints obtained with modified Ti6Al4V surfaces were observed intact after the SLO test which apparently evidences the improvement in the joining seam. The results (2) and (4) in Table 6-4 do not represent the true values of the C/SiC-Surface-modified Ti6Al4V joints strength, however, it gives an indication of improvement in joint strength as the joining interface was not failed for both the joining materials.

6.6 Other CMC-Ti6Al4V Joining trials

During this part of research work, several other attempts were made to join CMC to Ti6Al4V but were discontinued due to scientific reasons. The summary of some of those attempts is discussed in the following sections.

6.6.1 CVD C/SiC-TiNi based powders-Ti6Al4V Joint

The joining of CVD (Chemical Vapour Deposition) SiC coated C/SiC to Ti6Al4V was carried out using TiNi (70:30 wt. %, mesh size 325) alloy powder 950 ^{o}C for 30 min with a heating rate of around 16 ^{o}C/min in Argon atmosphere in a Carbolite tube furnace. A porous and discontinuous joining seam was observed with no apparent diffusion of joining material into the joining substrates (CVD SiC coated C/SiC and Ti6Al4V).

This process was improved with the addition of 20 wt. % Cu powder of mesh size 325 to the TiNi alloy powder. Using TiNi-20Cu (wt. %) as a joining material the brazing of the CVD SiC coated C/SiC to Ti6Al4V was carried out at 930 ^{o}C for

20 minutes in an argon atmosphere and heating rate 16 ^{o}C/min. The diffusion of joining material into the joining substrates was achieved, however, the infiltration of the joining material into the porous C-SiC substrate was observed.

A sputtering technique was employed to avoid this problem. A Ti layer of around 700 nm – 900 nm was sputtered on the surface of porous the CVD SiC coated C/SiC composites to avoid the infiltration of joining material during the brazing process. The sputtering helped to avoid the infiltration of joining melt into the joined substrates, but the porosity in the joining seam still remained a challenge. For this reason, working with powder alloys was not continued further.

6.6.2 CVD SiC Coated C/SiC-Metal Glass Brazing Foils (MBF)-Ti6Al4V joint system

Two Ni-based Metal Glass Foils: MBF-50 (50Ni-19Cr-7.3Si-0.08C-1.5B) and MBF-80 (80Ni-15Cr-0.06C-4B) (both 40 microns thick) were used to join CVD SiC coated C/SiC composites to Ti6Al4V alloys substrates.

Using 2 foils of MBF-50 CVD SiC coated C/SiC components were brazed to Ti6Al4V components. The optimised joining was achieved by brazing at 1200 ^{o}C for 5 min in an argon atmosphere. The heating rate adopted was 16 ^{o}C/min and the specimens were slow cooled (10 ^{o}C/min) after brazing to avoid residual stresses.

In another brazing attempt, for a similar pair of joining substrates, MBF-50 amorphous foils were replaced with MBF-80 amorphous foils and the brazing was carried out at 1120 ^{o}C for 5 min in argon (heating rate = 16 ^{o}C/min, and cooling rate = 10 ^{o}C/min).

Joining interface analysis revealed a uniform and continuous joining seam with the diffusion of both the Ni-based amorphous joining alloys into the joining substrates. However, this approach to join the CMC to Ti6Al4V was not further followed due to the high-temperature parameters during brazing (beyond the beta transus temperature of Ti6Al4V), which results in the deterioration of mechanical properties of the Ti6Al4V alloy.

6.7 Conclusion

Uniform, void and crack free SiC/SiC-Ti64, C/SiC-Ti64 joints with and without surface modification were demonstrated utilizing a pressure less brazing technique in an argon atmosphere.

Around 40% increase in joining strength was recorded when the conventional active brazing alloy was replaced with an Zr-based brazing alloy as a joining material.

Ti6Al4V surfaces with V-Shaped micro-slots were employed to analyse the effect of micro-machining on C/SiC-Ti6Al4V joint strength. Brazed joints

produced with surface modified Ti6Al4V displayed prominent improvement in the joining strength.

To further understand the interfacial reactions and phased formed at C/SiC-TiB590-Ti6Al4V joining interface, XRD analysis will be carried out and the results analysis will be updated.

Ti6Al4V specimens with different micro-slots shape and size will be experimented to analyse the effect of micro-slot configuration on the joint shear strength of brazed CMC-Ti6Al4V specimens.

7. Thesis Conclusion

Reliable joining techniques are necessary to integrate the lightweight, dissimilar materials for structural and functional applications. Despite its technological advances, the joining of dissimilar materials is not problem free and still poses challenges.

The aim of this research work is to produce alternative and efficient joining solutions for automotive and aerospace applications. Experiments were performed to improve the joining processes by optimising the current joining techniques, to introduce new joining solutions and to develop non-conventional light-weight composite materials with improved properties.

The potential replacement of expensive honeycomb material with low-cost Al-foam in a sandwich structure is experimented for automotive, marine and civil applications. The Al-foam and Al-honeycomb core materials are joined to the Glass and Carbon Fibre Reinforced Polymer (FRP) facing skins by in-situ fabrication of sandwich panels method. The experimental results show that, compared to honeycomb sandwich panels, the Al-foam sandwich panels display ~25 % and ~65 % higher flexural properties in a long and short span three-point bending test respectively. Furthermore, the addition of MWCNTs to the CFRP skins improved the stiffness properties of the facing skins and hence the flexural behaviour of the sandwich structure. The flexural behaviour of sandwich structure is observed highly influenced by the type of core material, facing skins properties and the span length adopted during the flexural test.

Five soldering/brazing solutions are proposed to join Al-6016 and Al-7046 facing skins to Al-Foam to produce AFS composites of complete metallic character using Zn based alloys and Al-based amorphous alloys as joining materials for higher temperature applications. The experimental results show that, AFS specimens produced with Zn2Al alloy as joining material displayed higher flexural properties with no delamination at the Al-foam/Al-skin interface when compared to AFS components produced with other joining alloys used in this study. The types of AFS produced in this study can sustain operational temperatures from 380 °C to 500 °C. Although, the AFS composite panels were produced in a batch furnace; however, the joining solutions proposed in this study, favoured by diffusion, can easily be automated in a continuous furnace which can ensure the mass productivity, reproducibility, and lower production costs.

A unique class of dynamic composites with improved impact resistance properties are produced by joining epoxy and polyurethane laminates reinforced with carbon fabric. The joining was achieved by utilising the reversible crosslinking chemistry of the modified epoxy and PU resins. The thermal, flexural and impact response of the multilayer epoxy/PU laminates produced in three different combinations are compared with a pure epoxy composite laminate. The Epoxy/PU configurations displayed ~95% higher damage initiation threshold (CFRP-4) and ~55% higher perforation threshold energy (CFRP-3) when compared to the pure epoxy composite. Unlike the conventional thermosets, the dynamic thermoset composites, due to the reversible crosslinking chemistry of resins, are recyclable, repairable and reshape able. The dynamic composites have great potential to replace the conventional thermoset composite used for body and interior parts in automobiles and aeroplanes.

To analyse the effect of shape and orientation of a micro-slots in a joint on the adhesion and joint strength, V, semi-circle and U-shaped micro-slots were produced on Ti6Al4V sheet surface by using an in-house developed Micro-Electro-Discharge Machining (Micro-EDM) setup. The preliminary Single Lap Offset (SLO) joint shear test results show that the micro-slots oriented perpendicular to the applied load displayed around 23 % higher joint strength when compared to parallel orientation. The U-shaped micro-slots configuration displayed around 30 % improvement in the joint shear strength compared to the reference plain surface bonded specimens. The variation in the shape and design of micro-slot allowed variable distribution of load and propagation of fractures which resulted in increase/decrease of the joint strength values. The shape, alignment of micro-slots with respect to the direction of load and the alignment of micro-slots with respect to each other at the joining interface are found as the main parameters influencing the adhesive joint strength.

The joining of CMCs (C/SiC and SiC/SiC) to Ti6Al4V alloy is experimented to produce a high strength and corrosion resistant joining seam by replacing the conventional active brazing alloy(Cusil-ABA) with a Zr-based brazing alloy (TiB590) in a pressure-less argon atmosphere. Around 40% higher joining strength was recorded when the Zr-based brazing alloy was used as a joining material compared Cusil-ABA. Further improvement in the joining strength was noticed when the Ti6Al4V surface was modified by Micro-EDM technique prior to joining.

The best of efforts is put to develop the missing knowledge to fill in the highlighted gaps and transfer it to industry. However, there are still some improvements, verifications of the results and most importantly integration of the proposed joining solutions into the relative engineering structures, which will be the focus of future research work preferably in collaboration with industries.

References

[1] Messler RW. Joining of materials and structures : from pragmatic process to enabling technology. Elsevier; 2004.

[2] Campbell, Flake C. ed. Joining: Understanding the Basics. ASM International; 2011.

[3] Savage W. Joining of Advanced Materials. Elsevier Science; 2013.

[4] K Srivastava A, Sharma A. Advances in Joining and Welding Technologies for Automotive and Electronic Applications. Am J Mater Eng Technol 2017;5:7–13. doi:10.12691/materials-5-1-2.

[5] Ford S, Despeisse M. Additive manufacturing and sustainability: an exploratory study of the advantages and challenges. J Clean Prod 2016;137:1573–87. doi:10.1016/j.jclepro.2016.04.150.

[6] Hu SJ. Assembly. In: Laperrière L, Reinhart G, editors. CIRP Encycl. Prod. Eng., Berlin, Heidelberg: Springer Berlin Heidelberg; 2014, p. 50–2. doi:10.1007/978-3-642-20617-7_6616.

[7] Zhang SH, Wang ZR, Wang ZT, Xu Y, Chen KB. Some new features in the development of metal forming technology. J Mater Process Technol 2004;151:39–47. doi:10.1016/j.jmatprotec.2004.04.098.

[8] Lino Alves FJ, Baptista AM, Marques AT. Metal and ceramic matrix composites in aerospace engineering. Elsevier Ltd; 2016. doi:10.1016/B978-0-08-100037-3.00003-1.

[9] Martinsen K, Hu SJ, Carlson BE. Joining of dissimilar materials. CIRP Ann - Manuf Technol 2015;64:679–99. doi:10.1016/j.cirp.2015.05.006.

[10] Al Hajri M, Malik AU, Meroufel A, Al-Muaili F. Premature failure of dissimilar metal weld joint at intermediate temperature superheater tube. Case Stud Eng Fail Anal 2015;3:96–103. doi:10.1016/j.csefa.2015.03.006.

[11] Kah P, Suoranta R, Martikainen J, Magnus C. Techniques for joining dissimilar materials: Metals and polymers. Rev Adv Mater Sci 2014;36:152–64.

[12] Ucsnik S, Stelzer S, Sieglhuber G. Composite To Composite Joint With Lightweight Metal. ECCM16 - 16TH Eur. Conf. Compos. Mater. Seville, Spain, 2014, p. 22–6.

[13] Reisgen U, Olschok S, Longerich S. Laser Beam Welding of Open-Porous Metallic Foams for Application in Cooling Structures of Combined Cycle Power Plants. J Eng Gas Turbines Power 2010;132:54502. doi:10.1115/1.3204512.

[14] Kellar EJC. 12 - Joining similar and dissimilar materials. In: Adams RD, editor. Adhes. Bond., Woodhead Publishing; 2005, p. 257–78. doi:https://doi.org/10.1533/9781845690755.3.257.

[15] Al Hajri M, Malik AU, Meroufel A, Al-Muaili F. Premature failure of dissimilar metal weld joint at intermediate temperature superheater tube. Case Stud Eng Fail Anal 2015;3:96–103. doi:10.1016/j.csefa.2015.03.006.

[16] Gerhard T, Friedrich C. Mechanical fastening of carbon composite tubes, numerical calculation of axial loading capacity and experimental verification. Compos Part B Eng 2014;67:391–9. doi:10.1016/j.compositesb.2014.07.024.

[17] Spišák E, Kaščák Ľ. Alternative Joining Methods in Car Body Production. Int J Eng Sci 2016;5:42–6. doi:10.9790/1813-0511024246.

[18] Robert W. Messler Jr. Joining Composite Materials and Structures: Some Thought-provoking Possibilities. J Thermoplast Compos Mater 2004;17:51–75. doi:10.1177/0892705704033336.

[19] Palmieri FL, Watson KA, Morales G, Williams T, Hicks R, Wohl CJ, et al. Laser ablative surface treatment for enhanced bonding of Ti-6Al-4V alloy. ACS Appl Mater Interfaces 2013;5:1254–61. doi:10.1021/am302293m.

[20] Doshi SJ, V Gohil A, Mehta N, Vaghasiya S. Challenges in Fusion Welding of Al alloy for Body in White. Mater Today Proc 2018;5:6370–5. doi:10.1016/j.matpr.2017.12.247.

[21] Vara Prasad V, Madhu Babu C, Ajay P. A Review on Rotating Arc Welding Process. Mater Today Proc 2018;5:3551–5. doi:10.1016/j.matpr.2017.11.603.

[22] Mikno Z, Pilarczyk A, Korzeniowski M, Kustroń P, Ambroziak A. Analysis of resistance welding processes and expulsion of liquid metal from the weld nugget. Arch Civ Mech Eng 2018;18:522–31. doi:10.1016/j.acme.2017.08.003.

[23] Kirk S, Suder W, Keogh K, Tremethick T, Loving A. Laser welding of fusion relevant steels for the European DEMO. Fusion Eng Des 2018:0–1. doi:10.1016/j.fusengdes.2018.03.039.

[24] Węglowski MS, Błacha S, Phillips A. Electron beam welding - Techniques and trends - Review. Vacuum 2016;130:72–92. doi:10.1016/j.vacuum.2016.05.004.

[25] Choudhury B, Chandrasekaran M. Investigation on welding characteristics

of aerospace materials - A review. Mater Today Proc 2017;4:7519–26. doi:10.1016/j.matpr.2017.07.083.

[26] Surya N, Rao PK, G.Umesh. COMPARISION OF SOLID STATE AND FUSION WELDING PROCESS. Int J Curr Eng Sci Res 2018;5:430–3.

[27] Akca E, Gürsel A. Solid State Welding and Application in Aeronautical Industry. Period Eng Nat Sci 2016;4. doi:10.21533/pen.v4i1.46.

[28] Vianco PT. Fundamentals of soldering technologies. Solder. Handb., vol. 3, 2013, p. 3–5.

[29] AWS C3 Committee on Brazing and Soldering. Brazing Handbook. 2006.

[30] David M. Jacobson GH. Diffusion Brazing. Princ. brazing, Ohio: ASM International; 2005, p. 207–16.

[31] Walker CA, Hodges VC, Method P. Comparing metal-ceramic brazing methods. Weld J 2008;10:43–50.

[32] Fernandez G, Vandepitte D, Usabiaga H, Debruyne S. Static and cyclic strength properties of brittle adhesives with porosity. Procedia Struct Integr 2017;7:291–8. doi:10.1016/j.prostr.2017.11.091.

[33] European Aluminium Association. Joining dissimilar materials. EAA Alum. Automot. Man. – Join., 2015. doi:10.1016/S0921-5093(03)00469-6.

[34] Malfait WJ, Klemenčič R, Lang B, Rist T, Klučka M, Zajacz Z, et al. Optimized solder alloy for glass-to-metal joints by simultaneous soldering and anodic bonding. J Mater Process Technol 2016;236:176–82. doi:10.1016/j.jmatprotec.2016.05.017.

[35] Koleňák R, Kostolný I, Kusý M. Characterization of soldering alloy type Zn-In-Mg and the study of direct soldering of silicon and copper. Mater Sci Eng A 2018;712:302–12. doi:10.1016/j.msea.2017.11.120.

[36] Koleňák R, Kostolný I. Study of Direct Bonding Ceramics with Metal Using Sn2La Solder. Adv Mater Sci Eng 2015;2015:4–7. doi:10.1155/2015/269167.

[37] Provaznik M. A Study of the Interface of Soldered Joints of SnInAgTi Active Solder with Ito Ceramics. Acta Polytech 2010;50:70–3.

[38] Budhe S, Banea MD, de Barros S, da Silva LFM. An updated review of adhesively bonded joints in composite materials. Int J Adhes Adhes 2017;72:30–42. doi:10.1016/j.ijadhadh.2016.10.010.

[39] Soldering F, Vol T, Edition UW. Soldering is now possible even on glass and ceramic materials with " Ultrasonic Wave Soldering ." Fundam Solder Technol 2013;3:3–5.

[40] Omura S, Kawazoe Y, Uemura D. Development of a novel adhesive composed of all-natural components. Int J Adhes Adhes 2017;74:35–9.

doi:10.1016/j.ijadhadh.2016.12.009.

[41] Jang Y, Li K. An All-Natural Adhesive for Bonding Wood. J Am Oil Chem Soc 2015;92:431–8. doi:10.1007/s11746-015-2610-y.

[42] Jin FL, Li X, Park SJ. Synthesis and application of epoxy resins: A review. J Ind Eng Chem 2015;29:1–11. doi:10.1016/j.jiec.2015.03.026.

[43] Duarte AP, Coelho JF, Bordado JC, Cidade MT, Gil MH. Surgical adhesives: Systematic review of the main types and development forecast. Prog Polym Sci 2012;37:1031–50. doi:10.1016/j.progpolymsci.2011.12.003.

[44] Deng S, Djukic L, Paton R, Ye L. Thermoplastic-epoxy interactions and their potential applications in joining composite structures - A review. Compos Part A Appl Sci Manuf 2015;68:121–32. doi:10.1016/j.compositesa.2014.09.027.

[45] Engels T. Chapter 10 - Thermoset adhesives. In: Guo Q, editor. Thermosets (Second Ed. Second Edi, Elsevier; 2018, p. 341–68. doi:https://doi.org/10.1016/B978-0-08-101021-1.00010-1.

[46] Fink JK. 4 - Phenol/Formaldehyde Resins. In: Fink JK, editor. React. Polym. Fundam. Appl. (Third Ed. Third edit, William Andrew Publishing; 2018, p. 225–53. doi:https://doi.org/10.1016/B978-0-12-814509-8.00004-X.

[47] Gibson G. Chapter 27 - Epoxy Resins. In: Gilbert M, editor. Brydson's Plast. Mater. (Eighth Ed. Eighth Edi, Butterworth-Heinemann; 2017, p. 773–97. doi:https://doi.org/10.1016/B978-0-323-35824-8.00027-X.

[48] Nash NH, Young TM, McGrail PT, Stanley WF. Inclusion of a thermoplastic phase to improve impact and post-impact performances of carbon fibre reinforced thermosetting composites - A review. Mater Des 2015;85:582–97. doi:10.1016/j.matdes.2015.07.001.

[49] Ubertalli G, Ferraris M, Bangash MK. Joining of AL-6016 to Al-foam using Zn-based joining materials. Compos Part A Appl Sci Manuf 2017;96:122–8. doi:10.1016/j.compositesa.2017.02.019.

[50] Birman V, Kardomateas GA. Review of current trends in research and applications of sandwich structures. Compos Part B Eng 2018;142:221–40. doi:10.1016/j.compositesb.2018.01.027.

[51] Banhart J. Aluminium foams for lighter vehicles. Int J Veh Des 2005;37:114. doi:10.1504/IJVD.2005.006640.

[52] Surace R, Filippis LACD. Investigation and Comparison of Aluminium Foams Manufactured by Different Techniques. In: Fuerstner I, editor. Adv. Knowl. Appl. Pract., Sciyo; 2010, p. 378.

[53] Ding X, Liu Y, Chen X, Zhang H, Li Y. Optimization of cellular structure of aluminum foams produced by powder metallurgy method. Mater Lett 2018;216:38–41. doi:10.1016/j.matlet.2017.12.144.

[54] Chen S, Bourham M, Rabiei A. Applications of Open-cell and Closed-cell Metal Foams for Radiation Shielding. Procedia Mater Sci 2014;4:293–8. doi:10.1016/j.mspro.2014.07.560.

[55] Rupani S V. Design , Modelling and Manufacturing aspects of Honeycomb Sandwich Structures : A Review. Int J Sci Dev Res 2017;2:526–32. doi:10.1712/ijsdr.17013.

[56] Al Antali A, Umer R, Zhou J, Cantwell WJ. The energy-absorbing properties of composite tube-reinforced aluminum honeycomb. Compos Struct 2017;176:630–9. doi:10.1016/j.compstruct.2017.05.063.

[57] Kumre A, Rana RS, Purohit R. A Review on mechanical property of sisal glass fibre reinforced polymer composites. Mater Today Proc 2017;4:3466–76. doi:10.1016/j.matpr.2017.02.236.

[58] Karataş MA, Gökkaya H. A review on machinability of carbon fibre reinforced polymer (CFRP) and glass fibre reinforced polymer (GFRP) composite materials. Def Technol 2018. doi:10.1016/j.dt.2018.02.001.

[59] Agirregomezkorta A, Sánchez-Soto M, Aretxaga G, Sarrionandia M, Aurrekoetxea J. Effects of vacuum infusion processing parameters on the impact behavior of carbon fibre reinforced cyclic butylene terephthalate composites. J Compos Mater 2014;48:333–44. doi:10.1177/0021998312472218.

[60] MEDVED V, CIFREK M. Fibre reinforced polymers - The technology applied for concerete repair. Introd. to fibre-reinforced Polym. - Polym. Compos. Concepts, Prop. Process., 2012, p. 135–52. doi:10.5772/67458.

[61] Newcomb BA. Processing, structure, and properties of carbon fibres. Compos Part A Appl Sci Manuf 2016;91:262–82. doi:10.1016/j.compositesa.2016.10.018.

[62] Huang X. Fabrication and properties of carbon fibres. Materials (Basel) 2009;2:2369–403. doi:10.3390/ma2042369.

[63] Punchaipetch P, D'Souza NA, Brostow W, Smith JT. Mechanical properties of glass fibre composites with an epoxy resin modified by a liquid crystalline epoxy. Polym Compos 2002;23:564–73. doi:10.1002/pc.10457.

[64] Shirvanimoghaddam K, Hamim SU, Karbalaei Akbari M, Fakhrhoseini SM, Khayyam H, Pakseresht AH, et al. Carbon fibre reinforced metal matrix composites: Fabrication processes and properties. Compos Part A Appl Sci Manuf 2017;92:70–96. doi:10.1016/j.compositesa.2016.10.032.

[65] Naslain R. Design, preparation and properties of non-oxide CMCs for application in engines and nuclear reactors: An overview. Compos Sci Technol 2004;64:155–70. doi:10.1016/S0266-3538(03)00230-6.

[66] Ezugwu EO, Wang ZM. Materials Titanium alloys and their machinability-a review. J Mater Process Technol 1997;68:262–74.

[67] Pederson R. Microstructure and Phase Transformation of Ti-6Al-4V. Luleå University of Technology, 2002. doi:ISSN: 1402 - 1757.

[68] Lütjering, Gerd, Williams J. titanium. Springer Berlin Heidelberg; 2007. doi:10.1007/978-3-540-73036-1.

[69] Sankaran KK, Mishra RS. Chapter 4 - Aluminum Alloys. In: Sankaran KK, Mishra RS, editors. Metall. Des. Alloy. with Hierarchical Microstruct., Elsevier; 2017, p. 57–176. doi:https://doi.org/10.1016/B978-0-12-812068-2.00004-7.

[70] Banhart J. Aluminium Foam Sandwich Panels : Manufacture , Metallurgy and Applications. Adv Eng Mater 2008;10:793–802. doi:10.1002/adem.200800091.

[71] Arbaoui J, Schmitt Y, Pierrot J-L, Royer F-X. Experimental Bending Behaviour Of Multi-Layer Sandwich Structures. Arch Metall Mater 2009;54.

[72] Stickel JM, Nagarajan M. Glass Fibre-Reinforced Composites: From Formulation to Application. Int J Appl Glas Sci 2012;3:122–36. doi:10.1111/j.2041-1294.2012.00090.x.

[73] Li J, Zhang YF. The tensile properties of short carbon fibre reinforced ABS and ABS/PA6 composites. J Reinf Plast Compos 2010;29:1727–33. doi:10.1177/0731684409337551.

[74] Naslain RR. SiC-Matrix Composites : Nonbrittle Ceramics for Thermo-Structural Application. Int J Appl Ceram Technol 2005;2:75–84. doi:10.1111/j.1744-7402.2005.02009.x.

[75] Nozawa T, Hinoki T, Hasegawa A, Kohyama A, Katoh Y, Snead LL, et al. Recent advances and issues in development of silicon carbide composites for fusion applications. J Nucl Mater 2009;386–388:622–7. doi:10.1016/j.jnucmat.2008.12.305.

[76] Gorjan L, Boretius M, Blugan G, Gili F, Mangherini D, Lizarralde X, et al. Ceramic protection plates brazed to aluminum brake discs. Ceram Int 2016;42:15739–46.

[77] Inagaki I, Tsutomu T, Yoshihisa S, Nozomu A. Application and Features of Titanium for the Aerospace Industry. Nippon Steel Sumitomo Met Tech Rep 2014:22–7.

[78] Gurrappa I. Characterization of titanium alloy Ti-6Al-4V for chemical, marine and industrial applications. Mater Charact 2003;51:131–9. doi:10.1016/j.matchar.2003.10.006.

[79] Matalkah F, Bharadwaj H, Soroushian P, Wu W, Almalkawi A, Balachandra AM, et al. Development of sandwich composites for building construction with locally available materials. Constr Build Mater 2017;147:380–7. doi:10.1016/j.conbuildmat.2017.04.113.

[80] Holmes M. Aerospace looks to composites for solutions. Reinf Plast 2017;0:1–5. doi:10.1016/j.repl.2017.06.079.

[81] Teng JG, Xiao QG, Yu T, Lam L. Three-dimensional finite element analysis of reinforced concrete columns with FRP and / or steel confinement. Eng Struct 2015;97:15–28. doi:10.1016/j.engstruct.2015.03.030.

[82] Kootsookos A, Burchill PJ. The effect of the degree of cure on the corrosion resistance of vinyl ester / glass fibre composites. Compos Part A Appl Sci Manuf 2004;35:501–8. doi:10.1016/j.compositesa.2003.08.010.

[83] Holmes M. High volume composites for the automotive challenge. Reinf Plast 2017;0:1–5. doi:10.1016/j.repl.2017.03.005.

[84] Azmi MA, Abdullah HZ, Idris MI. Properties of polyurethane foam/coconut coir fibre as a core material and as a sandwich composites component. IOP Conf Ser Mater Sci Eng 2013;50:12067. doi:10.1088/1757-899X/50/1/012067.

[85] Kaboglu C, Pimenta S, Morris A, Dear JP. The Effect Of Different Types Of Core Material On The Flexural Behavior Of Sandwich Composites For Wind Turbine Blades. J Therm Eng 2017;3:1102–9.

[86] Gibson L.J AM. Cellular solids, structure and properties. 2nd ed. Cambridge: Cambridge University Press; 1997. doi:10.1002/adv.1989.060090207.

[87] Evans AG, Hutchinson JW, Fleck NA. The topological design of multifunctional cellular metals. Prog Mater Sci 2001;46:309–27. doi:10.1016/S0079-6425(00)00016-5.

[88] Nunes JP, Silva JF. 5 - Sandwiched composites in aerospace engineering. Elsevier Ltd; 2016. doi:10.1016/B978-0-08-100037-3.00005-5.

[89] Xia X, Zhang Z, Zhao W, Li C, Ding J, Liu C, et al. Acoustic properties of closed-cell aluminum foams with different macrostructures. J Mater Sci Technol 2017. doi:10.1016/j.jmst.2017.07.012.

[90] Geramipour T, Oveisi H. Effects of foaming parameters on microstructure and compressive properties of aluminum foams produced by powder metallurgy method. Trans Nonferrous Met Soc China 2017;27:1569–79. doi:10.1016/S1003-6326(17)60178-X.

[91] Wang H, Zhou X, Long B, Yang J, Liu H. Thermal properties of closed-cell aluminum foams prepared by melt foaming technology. Trans Nonferrous Met Soc China 2016;26:3147–53. doi:10.1016/S1003-6326(16)64446-1.

[92] Zhu X, Ai S, Lu X, Cheng K, Ling X, Zhu L, et al. Collapse models of aluminum foam sandwiches under static three-point bending based on 3D geometrical reconstruction. Comput Mater Sci 2014;85:38–45. doi:10.1016/j.commatsci.2013.12.055.

[93] Kim P, Shi L, Majumdar A, Mceuen PL. Thermal Transport Measurements of Individual Multiwalled Nanotubes. Phys Rev Lett 2001;87:19–22.

doi:10.1103/PhysRevLett.87.215502.

[94] Qian D, Dickey EC, Andrews R, Rantell T. Load transfer and deformation mechanisms in carbon nanotube- polystyrene composites. Appl Phys Lett 2013;2868:14–7. doi:10.1063/1.126500.

[95] https://www.cheaptubes.com/product-tag/mwcnts/. Cheap Tubes Inc, USA 2017.

[96] Sharma SP, Lakkad SC. Composites : Part A Impact behavior and fractographic study of carbon nanotubes grafted carbon fibre-reinforced epoxy matrix multi-scale hybrid composites. Compos PART A 2015;69:124–31. doi:10.1016/j.compositesa.2014.11.005.

[97] Fares MM, Al-rub FAA. Lightweight MWCNTs-g-PAN Carbon Fibre Precursors. Sensitive High Absorptivity and Novel Wide-Bandgap Conjugated Polymers. Ind Eng Chem Res 2015. doi:10.1021/acs.iecr.5b01992.

[98] Crupi V, Montanini R. Aluminium foam sandwiches collapse modes under static and dynamic three-point bending. Int J Impact Eng 2007;34:509–21. doi:10.1016/j.ijimpeng.2005.10.001.

[99] Crupi V, Epasto G, Guglielmino E. Collapse modes in aluminium honeycomb sandwich panels under bending and impact loading. Int J Impact Eng 2012;43:6–15. doi:10.1016/j.ijimpeng.2011.12.002.

[100] Petras A, Sutcliffe MPF. Failure mode maps for honeycomb sandwich panels. Compos Struct 1999;44:237–52. doi:10.1016/S0263-8223(98)00123-8.

[101] Mohr D, Doyoyo M. Deformation-induced folding systems in thin-walled monolithic hexagonal metallic honeycomb. Int J Solids Struct 2004;41:3353–77. doi:10.1016/j.ijsolstr.2004.01.014.

[102] Styles M, Compston P, Kalyanasundaram S. The effect of core thickness on the flexural behaviour of aluminium foam sandwich structures. Compos Struct 2007;80:532–8. doi:10.1016/j.compstruct.2006.07.002.

[103] Duarte I, Teixeira-Dias F, Graça A, Ferreira AJM. Failure Modes and Influence of the Quasi-static Deformation Rate on the Mechanical Behavior of Sandwich Panels with Aluminum Foam Cores. Mech Adv Mater Struct 2010;17:335–42. doi:10.1080/15376494.2010.488563.

[104] Yu JL, Wang E, Li J, Zheng Z. Static and low-velocity impact behavior of sandwich beams with closed-cell aluminum-foam core in three-point bending. Int J Impact Eng 2008;35:885–94. doi:10.1016/j.ijimpeng.2008.01.006.

[105] Abbadi A, Koutsawa Y, Carmasol A, Belouettar S, Azari Z. Experimental and numerical characterization of honeycomb sandwich composite panels.

Simul. Model. Pract. Theory. 17th ed., 2009, p. 1533–47.

[106] Nikhil Gupta. Characterization of Flexural Properties of Syntactic Foam Core Sandwich Composites and Effect of Density Variation. J Compos Mater 2004;39:2197–212. doi:10.1177/0021998305052037.

[107] Duratek. Epoxy Based Fibre Lamination - Duratek 1000 Resin System. 2015.

[108] ASTM C365/C365M-11a. Standard test method for flatwise compressive properties of sandwich cores. American society for testing and materials. Annual Book for ASTM Standarts. 2011.

[109] ASTM international. C 393: Standard Test Method for Flexural Properties of Sandwich Constructions. Annu B ASTM Stand 2000:1–4. doi:ASTM C393.

[110] Zhao Z, Teng K, Li N, Li X, Xu Z, Chen L, et al. Mechanical , thermal and interfacial performances of carbon fibre reinforced composites flavored by carbon nanotube in matrix / interface. Compos Struct 2017;159:761–72. doi:10.1016/j.compstruct.2016.10.022.

[111] Mcdaniel G, Design R, Administrator S, Knight C. Fibre Reinforced Polymer (FRP) Composites. Des Train Expo 2014.

[112] Shen J, Lu G, Ruan D. Compressive behaviour of closed-cell aluminium foams at high strain rates. Compos Part B Eng 2010;41:678–85. doi:10.1016/j.compositesb.2010.07.005.

[113] Hasan R, Mines RAW, Shen E, Tsopanos S, Cantwell W. Comparison on Compressive Behaviour of Aluminium Honeycomb and Titanium Alloy Micro Lattice Blocks. Key Eng Mater 2011;462–463:213–8. doi:10.4028/www.scientific.net/KEM.462-463.213.

[114] Prakash MDAA, Guptha VLJ, Sharma RS. Influence of Cell Size on the Core Shear Properties of FRP Honeycomb Sandwich Panels Influence of Cell Size on the Core Shear Properties of FRP Honeycomb Sandwich Panels. Mater Manuf Process 2012;6914:1532–2475. doi:10.1080/10426914.2011.560227.

[115] Yan C, Song X, Zhu H, Jing C, Feng S. Flexural response of carbon fibre reinforced aluminum foam sandwich. J Compos Mater 2017. doi:10.1177/0021998317735166.

[116] Sadeghian P, Hristozov D, Woblewski L. Flexural Behavior of Sandwich Panels Made of Frp Composites: Synthetic and Natural Fibres. Resilient Infrastruct 2016:1–10.

[117] Kong CW, Nam GW, Jang YS, Yi YM. Experimental strength of composite sandwich panels with cores made of aluminum honeycomb and foam. Adv Compos Mater 2014;23:43–52. doi:10.1080/09243046.2013.862386.

[118] Lehmhus D, Hehl A von, Kayvantash K, Gradinger R, Becker T, Schimanski K, et al. Taking a downward turn on the weight spiral – Lightweight

materials in transport applications. Mater Des J 2015;66:385–9. doi:10.1016/j.matdes.2014.10.001.

[119] Fridlyander IN, Sister VG, Grushko OE, Berstenev V V., Sheveleva LM, Ivanova LA. Aluminum alloys: Promising materials in the automotive industry. Met Sci Heat Treat 2002;44:365–70. doi:10.1023/A:1021901715578.

[120] Duarte I, Oliveira M. Aluminium Alloy Foams: Production and Properties. Powder Metall., 2012, p. 47–72. doi:10.5772/1922.

[121] Güner A, Arıkan M, Nebioglu M. New Approaches to Aluminum Integral Foam Production with Casting Methods. Metals (Basel) 2015;5:1553–65. doi:10.3390/met5031553.

[122] Huang Z, Qin Z, Chu F. Damping Mechanism of Elastic-Viscoelastic-Elastic Sandwich Structures. Compos Struct 2016. doi:10.1016/j.compstruct.2016.05.105.

[123] Yu GC, Feng LJ, Wu LZ. Thermal and mechanical properties of a multifunctional composite square honeycomb sandwich structure. Mater Des 2016;102:238–46. doi:10.1016/j.matdes.2016.04.050.

[124] Biancolini ME. Evaluation of equivalent stiffness properties of corrugated board. Compos Struct 2005;69:322–8. doi:10.1016/j.compstruct.2004.07.014.

[125] Herrmann AS, Zahlen PC, Zuardy I. Sandwich Structures Technology in Commerical Aviation: Present Applications and Future Trends. Sandw Struct Adv with Sandw Struct Mater 2005;7:13–26. doi:10.1007/1-4020-3848-8_2.

[126] Li Z, Zheng Z, Yu J, Qian C, Lu F. Deformation and failure mechanisms of sandwich beams under three-point bending at elevated temperatures. Compos Struct 2014;111:285–90. doi:10.1016/j.compstruct.2014.01.005.

[127] Hexcel. Bonding technique. J Chem Inf Model 2013;53:1689–99. doi:10.1017/CBO9781107415324.004.

[128] Pantelakis S, Tserpes KI. Adhesive bonding of composite aircraft structures: Challenges and recent developments. Sci China Physics, Mech Astron 2014;57:2–11. doi:10.1007/s11433-013-5274-3.

[129] Banhart J, Seeliger H. Recent Trends in Aluminium Foam Sandwich Technology Industrial Implementation of AFS Technology. Adv Eng Mater Montpellier 2011:1–13. doi:10.1002/adem.201100333.

[130] Vicario I, Crespo I, Plaza LM, Caballero P, Idoiaga IK. Aluminium foam and magnesium compound casting produced by high-pressure die casting. Metals (Basel) 2016;6. doi:10.3390/met6010024.

[131] Nannan C, Yi F, Jie C, Bin L, Fanyan C, Jingsong Z. Vacuum Brazing

Processes of Aluminum Foam. Rare Met Mater Eng 2013;42:1118–22. doi:10.1016/S1875-5372(13)60072-7.

[132] Matsumoto R, Tsuruoka H, Otsu M, Utsunomiya H. Fabrication of skin layer on aluminum foam surface by friction stir incremental forming and its mechanical properties. J Mater Process Technol 2015;218:23–31. doi:10.1016/j.jmatprotec.2014.11.030.

[133] Wan L, Huang Y, Lv S, Feng J. Fabrication and interfacial characterization of aluminum foam sandwich via fluxless soldering with surface abrasion. Compos Struct 2015;123:366–73. doi:10.1016/j.compstruct.2014.12.055.

[134] Huang Y, Gong J, Lv S, Leng J, Li Y. Fluxless soldering with surface abrasion for joining metal foams. Mater Sci Eng A 2012;552:283–7. doi:10.1016/j.msea.2012.05.041.

[135] Campana G, Ascari A, Fortunato A. Laser foaming for joining aluminum foam cores inside a hollow profile. Opt Laser Technol 2013;48:331–6. doi:10.1016/j.optlastec.2012.11.005.

[136] Qingxian H, Sawei Q, Yuebo H. Development on Preparation Technology of Aluminum Foam Sandwich Panels. Rare Met Mater Eng 2015;44:548–52. doi:10.1016/S1875-5372(15)30036-9.

[137] Schwingel D, Seeliger HW, Vecchionacci C, Alwes D, Dittrich J. Aluminium foam sandwich structures for space applications. Acta Astronaut 2007;61:326–30. doi:10.1016/j.actaastro.2007.01.022.

[138] A. E. Gickler, F. H. LePrevost J. Tips for Soldering Aluminum. https://app.aws.org/wj/2004/02/046/ 2017:25-11–2017.

[139] Zhu YH. General Rule of Phase Decomposition in Zn-Al Based Alloys (II)-On Effects of External Stresses on Phase Transformation-. Mater Trans 2004;45:3083–97. doi:10.2320/matertrans.45.3083.

[140] Skoko Ž, Popović S, Štefanić G. Microstructure of Al-Zn and Zn-Al Alloys. Croat Chem Acta 2009;82:405–20.

[141] Hamoudi M. Discontinuous Precipitation and Dissolution under the Influence of the Plastic Strain and Temperature in Al-15 at.%Zn and Al-30 at.%Zn Alloys. Mater Sci Appl 2012;3:433–41. doi:10.4236/msa.2012.37061.

[142] Fleming KM, Zhu A, Scully JR. Corrosion of AA6061 brazed with an Al-Si alloy: Effects of Si on metallurgical and corrosion behavior. Corrosion 2012;68:1126–45. doi:10.5006/0677.

[143] Han Y, Ma K, Li L, Chen W, Nagaumi H. Study on microstructure and mechanical properties of Al-Mg-Si-Cu alloy with high manganese content. Mater Des 2012;39:418–24. doi:10.1016/j.matdes.2012.01.034.

[144] P. Weigand. Untersuchung der Einflussfaktoren auf die pulvermetallurgische Herstellung von Aluminiumschaum. RWTH Aachen,

Aachen, Germany, 1999., 1999.

[145] Banhart J, Baurneister J, Weber M. Damping properties of aluminium foams 1996;5093. doi:10.1016/0921-5093(95)09973-5.

[146] Polmear I. Light Alloys-From Traditional Alloys to Nanocrystals. 4th ed. New York, USA: An Imprint of Elsevier Publications; 2006.

[147] Luo YJ-G, Acoff VL. Interfacial Reactions of Titanium and Aluminum during Diffusion Welding (Supplement to Welding Journal). Weld Res 2000:239–43.

[148] Wang P, Gao Z, Niu J. Micro–nano filler metal foil on vacuum brazing of SiCp/Al composites. Appl Phys A Mater Sci Process 2016;122:1–11. doi:10.1007/s00339-016-0110-z.

[149] Shabestari SG, Wanderka N, Seeliger W, Banhart J. Optimisation of the Strength of Aluminium Foam Sandwich (AFS) Panels by Different Heat Treatments. Mater Sci Forum 2006;521:1221–6.

[150] Holmen JK, Frodal BH, Hopperstad OS, Børvik T. Strength differential effect in age hardened aluminum alloys. Int J Plast 2017;99:144–61. doi:10.1016/j.ijplas.2017.09.004.

[151] Alexopoulos ND, Velonaki Z, Stergiou CI, Kourkoulis SK. Effect of ageing on precipitation kinetics, tensile and work hardening behavior of Al-Cu-Mg (2024) alloy. Mater Sci Eng A 2017;700:457–67. doi:10.1016/j.msea.2017.05.090.

[152] Helwig H, Banhart J. A study of Mg and Cu additions on the foaming behaviour of Al-Si alloys ∗ 2011:1–32.

[153] Ponweiser N, Lengauer CL, Richter KW. Re-investigation of phase equilibria in the system Al-Cu and structural analysis of the high-temperature phase η1-Al 1-δCu. Intermetallics 2011;19:1737–46. doi:10.1016/j.intermet.2011.07.007.

[154] Orman L, Swidersky HW, Lauzon D. Brazing of Aluminum alloys with higher magnesium content using non-corrosive fluxes. Keikinzoku Yosetsu/Journal Light Met Weld Constr 2014;52:24–9.

[155] Moller C, Grann J. Aluminum Brazing – What Matters Most: Fundamentals and Case Studies. 5th Int. Brazing Solder. Conf., 2012.

[156] Swidersky HW. Aluminium Brazing with Non-corrosive Fluxes State of the Art and Trends in NOCOLOK ® Flux Technology. 6th Int Conf Brazing, High Temp Brazing Diffus Bond 2001.

[157] Feuerbacher em et. al M. The Samson phase, β-Mg2Al3, revisited. Z Krist 2007;222:259. doi:10.1524/zkri.2007.222.6.259.

[158] Zhong Y, Yang M, Liu ZK. Contribution of first-principles energetics to Al-

Mg thermodynamic modeling. Calphad Comput Coupling Phase Diagrams Thermochem 2005;29:303–11. doi:10.1016/j.calphad.2005.08.004.

[159] American Society for Metals and Davis JR. ASM handbook. 2. Properties and selection: nonferrous alloys and special-purpose materials. ASM International; 2009.

[160] Vušanovic I, Voronjec D, Krane MJM. Microsegregation Phenomena in Al-Cu-Mg Alloy with Considering of Diffusion Phenomena in Primary Phase. Facta Univ - Ser Mech Eng 2001;1:965–80.

[161] M.M. Makhlouf HVG. The aluminum–silicon eutectic reaction: mechanisms and crystallography. J Light Mater 2002;7.

[162] Liss K-D, Funakoshi K-I, Dippenaar R, Higo Y, Shiro A, Reid M, et al. Hydrostatic Compression Behavior and High-Pressure Stabilized β-Phase in γ-Based Titanium Aluminide Intermetallics. Metals (Basel) 2016;6:165. doi:10.3390/met6070165.

[163] Kumar PV, Reddy GM, Rao KS. Microstructure, mechanical and corrosion behavior of high strength AA7075 aluminium alloy friction stir welds – Effect of post weld heat treatment. Def Technol 2015;11:362–9. doi:10.1016/j.dt.2015.04.003.

[164] Takahashi T, Minamino Y, Yamane T. Quaternary Diffusion in 7000 Aluminum Alloys. Mater Trans 2002;43:232–8. doi:10.2320/matertrans.43.232.

[165] Gupta R, Chaudhari GP, Daniel BSS. Effect of in-situ formed Al3Ti particles on the microstructure and mechanical properties of 6061 Al alloy. IOP Conf Ser Mater Sci Eng 2018;330:0–6. doi:10.1088/1757-899X/330/1/012012.

[166] E J, Hatch. MICROSTRUCTURE OF ALLOYS Chapter 3. Alum Prop Phys Metall 1984:58–104. doi:10.1361/appm1984p058.

[167] Alisibramulisi A, Myhr OR, Lademo O, Larsen PK. An Experimental Investigation of the Heat Affected Zone (HAZ) Properties of AA6060 and AA7046 Following Different Heat Treatment Schedules. Proc. 12th Int. Conf. Alum. Alloy. Sept. 5-9, 2010, Yokohama, Japan Alum. Alloy. Sept. 5-9, 2010, Yokohama, Japan ©2010 Japan Inst. Light., 2010, p. 994–9.

[168] Lamb J. Decomposition and Its Effects on Mechanical Properties in Al-Zn-Mg-Cu Alloys. A Thesis Present to Acad Fac 2016.

[169] Wan L, Huang Y, Huang T, Lv S, Feng J. Novel method of fluxless soldering with self-abrasion for fabricating aluminum foam sandwich. J Alloys Compd 2015;640:1–7. doi:10.1016/j.jallcom.2015.04.005.

[170] Borovinšek M, Mathier V, Fiedler T. Mechanics of Materials Dynamic compression of aluminium foam derived from infiltration casting of salt dough 2016;93:96–108. doi:10.1016/j.mechmat.2015.10.012.

[171] Zu G, Song B, Zhong Z, Li X, Mu Y, Yao G. Static three-point bending

behavior of aluminum foam sandwich. J Alloys Compd 2012;540:275–8. doi:10.1016/j.jallcom.2012.06.079.

[172] Bastawros A. Experimental analysis of deformation mechanisms in a closed-cell aluminum alloy foam. J Mech Phys Solids 2000;48:301–22. doi:10.1016/S0022-5096(99)00035-6.

[173] Kabir K, Vodenitcharova T, Hoffman M. Response of aluminium foam-cored sandwich panels to bending load. Compos Part B Eng 2014;64:24–32. doi:10.1016/j.compositesb.2014.04.003.

[174] Rabiei A, Garcia-avila M. Materials Science & Engineering A Effect of various parameters on properties of composite steel foams under variety of loading rates. Mater Sci Eng A 2013;564:539–47. doi:10.1016/j.msea.2012.11.108.

[175] Engdahl T, Hansen V, Warren PJ, Stiller K. Investigation of fine scale precipitates in Al-Zn-Mg alloys after various heat treatments. Mater Sci Eng A 2002;327:59–64. doi:10.1016/S0921-5093(01)01876-7.

[176] Leo P, Cerri E. Pure 7000 Alloys : Microstructure , Heat Treatments and Hot Working. Alum. Alloy. - New Trends Fabr. Appl., InTech; 2013, p. 255–73. doi:10.5772/51489.

[177] Pinlung SB. Scholarship at UWindsor 7xxx Aluminum Sheets for Automotive Applications. 2015.

[178] Meyers MA, Chen P-Y, Lin AY-M, Seki Y. Biological materials: Structure and mechanical properties. Prog Mater Sci 2008;53:1–206. doi:10.1016/j.pmatsci.2007.05.002.

[179] Stelldinger E, Kühhorn A, Kober M. Experimental evaluation of the low-velocity impact damage resistance of CFRP tubes with integrated rubber layer. Compos Struct 2015. doi:10.1016/j.compstruct.2015.11.069.

[180] Bagheri R, Marouf BT, Pearson RA. Rubber-Toughened Epoxies: A Critical Review. Polym Rev 2009;49:201–25. doi:10.1080/15583720903048227.

[181] Abadyan M, Khademi V, Bagheri R, Haddadpour H, Kouchakzadeh MA, Farsadi M. Use of rubber modification technique to improve fracture-resistance of hoop wound composites. Mater Des 2009;30:1976–84. doi:10.1016/j.matdes.2008.09.001.

[182] Wong DWY, Lin L, McGrail PT, Peijs T, Hogg PJ. Improved fracture toughness of carbon fibre/epoxy composite laminates using dissolvable thermoplastic fibres. Compos Part A Appl Sci Manuf 2010;41:759–67. doi:10.1016/j.compositesa.2010.02.008.

[183] Nash NH, Young TM, McGrail PT, Stanley WF. Inclusion of a thermoplastic phase to improve impact and post-impact performances of carbon fibre reinforced thermosetting composites - A review. Mater Des 2015;85:582–

97. doi:10.1016/j.matdes.2015.07.001.

[184] Swolfs Y, Gorbatikh L, Verpoest I. Fibre hybridisation in polymer composites: A review. Compos Part A Appl Sci Manuf 2014;67:181–200. doi:10.1016/j.compositesa.2014.08.027.

[185] Enfedaque A, Molina-Aldareguia JM, Galvez F, Gonzalez C, LLorca J. Effect of Glass Fibre Hybridization on the Behavior Under Impact of Woven Carbon Fibre/Epoxy Laminates. J Compos Mater 2010;44:3051–68. doi:10.1177/0021998310369602.

[186] Swolfs Y, Crauwels L, Breda E Van, Gorbatikh L, Hine P, Ward I, et al. Tensile behaviour of intralayer hybrid composites of carbon fibre and self-reinforced polypropylene. Compos Part A Appl Sci Manuf 2014;59:78–84. doi:10.1016/j.compositesa.2014.01.001.

[187] Múgica JI, Aretxabaleta L, Ulacia I, Aurrekoetxea J. Impact characterization of thermoformable fibre metal laminates of 2024-T3 aluminium and AZ31B-H24 magnesium based on self-reinforced polypropylene. Compos Part A Appl Sci Manuf 2014;61:67–75. doi:10.1016/j.compositesa.2014.02.011.

[188] Rowan SJ, Cantrill SJ, Cousins GRL, Sanders JKM, Stoddart JF. Dynamic Covalent Chemistry. vol. 41. 2002. doi:10.1002/1521-3773(20020315)41:6<898::AID-ANIE898>3.0.CO;2-E.

[189] JM L. Dynamers: From Supramolecular Polymers to Adaptive Dynamic Polymers. Hierarchical Macromol. Struct. 60 Years after Staudinger Nobel Prize, Springer, Cham; 2013, p. 155–72. doi:10.1007/12_2013_267.

[190] Denissen W, Winne JM, Du Prez FE. Vitrimers: permanent organic networks with glass-like fluidity. Chem Sci 2016;7:30–8. doi:10.1039/C5SC02223A.

[191] Martin R, Rekondo A, De Luzuriaga AR, Casuso P, Dupin D, Cabañero G, et al. Dynamic sulfur chemistry as a key tool in the design of self-healing polymers. Smart Mater Struct 2016;25:1–8. doi:10.1088/0964-1726/25/8/084017.

[192] Fernandes PA, Ramos MJ. Theoretical Insights into the Mechanism for Thiol/Disulfide Exchange. Chem - A Eur J 2004;10:257–66. doi:10.1002/chem.200305343.

[193] Azcune I, Odriozola I. Aromatic disulfide crosslinks in polymer systems: Self-healing, reprocessability, recyclability and more. Eur Polym J 2016;84:147–60. doi:10.1016/j.eurpolymj.2016.09.023.

[194] Martin R, Rekondo A, Ruiz de Luzuriaga A, Cabañero G, Grande HJ, Odriozola I. The processability of a poly(urea-urethane) elastomer reversibly crosslinked with aromatic disulfide bridges. J Mater Chem A 2014;2:5710. doi:10.1039/c3ta14927g.

[195] Luzuriaga AR de, Martin R, Markaide N, Rekondo A, Cabañero G, Javier Rodríguez, et al. Electronic Supplementary “Information Epoxy Resin with Exchangeable Disulfide Crosslinks to Obtain Reprocessable, Repairable and

Recyclable Fibre-Reinforced Thermoset Composites." R Soc Chem 2016 2016:1–19.

[196] Rekondo A, Martin R, Ruiz de Luzuriaga A, Cabañero G, Grande HJ, Odriozola I. Catalyst-free room-temperature self-healing elastomers based on aromatic disulfide metathesis. Mater Horiz 2014;1:237–40. doi:10.1039/C3MH00061C.

[197] Horiz M, Ruiz de Luzuriaga A, Martin R, Markaide N, Rekondo A, Cabañ ero G, et al. Epoxy resin with exchangeable disulfide crosslinks to obtain reprocessable, repairable and recyclable fibre-reinforced thermoset composites 2016. doi:10.1039/c6mh00029k.

[198] Norm DE. Fibre-reinforced plastic composites Determination of apparent interlaminar shear strength by short-beam method (ISO 14130 : 1997). vol. 3, 1998, p. 1–9.

[199] Aurrekoetxea J, Agirregomezkorta a., Aretxaga G, Sarrionandia M. Impact behavior of carbon fibre/epoxy composite manufactured by vacuum-assisted compression resin transfer molding. J Compos Mater 2012;46:43–9. doi:10.1177/0021998311401938.

[200] Feraboli P, Ireland D, Kedward K. The Role of Force and Energy in Low Velocity Impact Events. 45th AIAA/ASME/ASCE/AHS/ASC Struct Struct Dyn & Mater Conf 2004. doi:10.2514/6.2004-1841.

[201] Dong C. Effects of Process-Induced Voids on the Properties of Fibre Reinforced Composites. J Mater Sci Technol 2016. doi:10.1016/j.jmst.2016.04.011.

[202] Siva I, Winowlin Jappes J T, Sankar i, Amico S C, D R. Effect of fibre volume fraction on the mechanical properties of coconut sheath/usp composite. Int J Res 2013;8:060–3.

[203] Suhot MA, Chambers AR. The Effects of Voids on the Flexural Properties and Failure Mechanisms of Carbon / Epoxy Composites. J Teknol (Sciences Eng 2014;2:151–7. doi:10.11113/jt.v71.3736.

[204] Rathnakar G, Shivanand HK. Effect of Thickness on Flexural Properties of Epoxy based Glass Fibre Reinforced Laminate 2012;2:409–12.

[205] Saba N, Jawaid M, Alothman OY, Paridah MT. A review on dynamic mechanical properties of natural fibre reinforced polymer composites. Constr Build Mater 2016;106:149–59. doi:10.1016/j.conbuildmat.2015.12.075.

[206] Abdul Khalil HPS, Jawaid M, Firoozian P, Zainudin ES, Paridah MT, Khalil HPSA. Dynamic Mechanical Properties of Activated Carbon–Filled Epoxy Nanocomposites. Int J Polym Anal Charact 2013;18:247–56. doi:10.1080/1023666X.2013.766553.

[207] Saba N, Paridah MT, Abdan K, Ibrahim NA. Dynamic mechanical properties of oil palm nano filler/kenaf/epoxy hybrid nanocomposites. Constr Build Mater 2016;124:133–8. doi:10.1016/j.conbuildmat.2016.07.059.

[208] Han SI, Lim JS, Kim DK, Kim MN, Im SS. In situ polymerized poly(butylene succinate)/silica nanocomposites: Physical properties and biodegradation. Polym Degrad Stab 2008;93:889–95. doi:10.1016/j.polymdegradstab.2008.02.007.

[209] Selmy AI, Elsesi AR, Azab NA, El-baky MAA. Composites : Part B Interlaminar shear behavior of unidirectional glass fibre (U)/ random glass fibre (R)/ epoxy hybrid and non-hybrid composite laminates. Compos Part B 2012;43:1714–9. doi:10.1016/j.compositesb.2012.01.031.

[210] ZHU Hong-yan, LI Di-hong, ZHANG Dong-xing, WU Bao-chang CY. Influence of voids on interlaminar shear strength of carbon / epoxy fabric laminates. Trans Nonferrous Met Soc China 2009;19:5–10. doi:10.1016/S1003-6326(10)60091-X.

[211] Feraboli P, Kedward KT. A new composite structure impact performance assessment program. Compos Sci Technol 2006;66:1336–47. doi:10.1016/j.compscitech.2005.09.009.

[212] Feraboli P, Kedward KT. Enhanced Evaluation of the Low-Velocity Impact Response of Composite Plates. AIAA J 2004;42:2143–52. doi:10.2514/1.4534.

[213] J T, K SR, G. A. Damage Resistance and Tolerance of Composite Sandwich Panels - Scaling Effects. 2004.

[214] Flegel PHA. The Future of Adhesive Bonding as a Joining Technique. Development 2002:64–7. doi:10.1007/BF03246730.

[215] Täljsten B. the Importance of Bonding - an Historic Overview and Future Possibilities. Proc Int Symp Bond Behav FRP Struct 2005:1–10.

[216] Baldan A. Adhesion phenomena in bonded joints. Int J Adhes Adhes 2012;38:95–116. doi:https://doi.org/10.1016/j.ijadhadh.2012.04.007.

[217] Takeda T, Yasuoka T, Hoshi H, Sugimoto S, Iwahori Y. Strength and bonding characteristics of adhesive joints with surface-treated titanium-alloy substrates. J Adhes Sci Technol 2018;32:553–71. doi:10.1080/01694243.2017.1371426.

[218] Fujii H, Takahashi K, Yamashita Y. Application of titanium and its alloys for automobile parts. Nippon Steel Tech Rep 2003:70–5.

[219] Corbett MC, Sharos PA, Hardiman M, McCarthy CT. Numerical design and multi-objective optimisation of novel adhesively bonded joints employing interlocking surface morphology. Int J Adhes Adhes 2017;78:111–20. doi:10.1016/j.ijadhadh.2017.06.002.

[220] Banea MD, da Silva LFM. Adhesively bonded joints in composite materials:

An overview. Proc Inst Mech Eng Part L J Mater Des Appl 2009;223:1–18. doi:10.1243/14644207JMDA219.

[221] Jojibabu P, Jagannatham M, Haridoss P, Janaki Ram GD, Deshpande AP, Bakshi SR. Effect of different carbon nano-fillers on rheological properties and lap shear strength of epoxy adhesive joints. Compos Part A Appl Sci Manuf 2016;82:53–64. doi:10.1016/j.compositesa.2015.12.003.

[222] Hernandez X, Jiménez C, Mergia K, Yialouris P, Messoloras S, Liedtke V, et al. An innovative joint structure for brazing Cf/SiC composite to titanium alloy. J Mater Eng Perform 2014;23:3069–76. doi:10.1007/s11665-014-1074-9.

[223] Demir AG, Maressa P, Previtali B. Fibre laser texturing for surface functionalization. Phys Procedia 2017;41:752–61. doi:10.1016/j.phpro.2013.03.145.

[224] Belcher MA, List MS, Wohl CJ, Ghose S, Watson KA, Hopkins JW, et al. Laser surface preparation for adhesive bonding of aerospace structural composites. Mater Manuf Process 2010:1–8.

[225] Liu X, Chu PK, Ding C. Surface modification of titanium, titanium alloys, and related materials for biomedical applications. Mater Sci Eng R Reports 2004;47:49–121. doi:10.1016/j.mser.2004.11.001.

[226] Aliasghari S, Němcová A, Skeldon P, Thompson GE. Influence of coating morphology on adhesive bonding of titanium pre-treated by plasma electrolytic oxidation. Surf Coat Technol 2016;289:101–9. doi:10.1016/j.surfcoat.2016.01.042.

[227] Li H, Gao C, Wang G, Qu N, Zhu D. OPEN A Study of Electrochemical Machining of Ti-6Al-4V in NaNO 3 solution. Nature 2016:1–11. doi:10.1038/srep35013.

[228] Sjöström T, Su B. Micropatterning of titanium surfaces using electrochemical micromachining with an ethylene glycol electrolyte. Mater Lett 2011;65:3489–92. doi:10.1016/j.matlet.2011.07.103.

[229] Lu X, Leng Y. Electrochemical micromachining of titanium surfaces for biomedical applications. J Mater Process Technol 2005;169:173–8. doi:10.1016/j.jmatprotec.2005.04.040.

[230] Zimmermann S, Specht U, Spieß L, Romanus H, Krischok S, Himmerlich M, et al. Improved adhesion at titanium surfaces via laser-induced surface oxidation and roughening. Mater Sci Eng A 2012;558:755–60. doi:10.1016/j.msea.2012.08.101.

[231] Kim GD, Loh BG. Machining of micro-channels and pyramid patterns using elliptical vibration cutting 2010:961–8. doi:10.1007/s00170-009-2451-7.

[232] Tanvir Ahmmed KM, Grambow C, Kietzig AM. Fabrication of micro/nano

structures on metals by femtosecond laser micromachining. Micromachines 2014;5:1219–53. doi:10.3390/mi5041219.

[233] Rajurkar KP, Sundaram MM, Malshe AP. Review of electrochemical and electrodischarge machining. Procedia CIRP 2013;6:13–26. doi:10.1016/j.procir.2013.03.002.

[234] O'Dwyer, D. J.O'Dwyer, D.J., O'Dowd, N.P., McCarthy CT. In-situ SEM mechanical testing of miniature bonded joints. Int J Adhes Adhes 2014;50:57–64. doi:10.1016/j.ijadhadh.2013.12.027.

[235] Ehrhart B, Valeske B, Muller C-E, Bockenheimer C. Methods for the Quality Assessment of Adhesive Bonded CFRP Structures - A Resumé. Proc Int 2010:1–9. doi:10.1109/TUFFC.924.

[236] Tavaloki SM, Pullen D a., Dunkerton SB. A review of adhesive bonding techniques for joining medical materials. Assem Autom 2005;25:100–5. doi:10.1108/01445150510700070.

[237] Grant LDR, Adams RD, da Silva LFM. Experimental and numerical analysis of single-lap joints for the automotive industry. Int J Adhes Adhes 2009;29:405–13. doi:10.1016/j.ijadhadh.2008.09.001.

[238] da Silva LFM, Campilho RDSG. Advances in Numerical Modeling of Adhesive Joints. Springer; 2012. doi:10.1007/978-3-642-23608-2.

[239] Malyshev BM, Salganik RL. The strength of adhesive joints using the theory of cracks. Int J Fract Mech 1965;1:114–28. doi:10.1007/BF00186749.

[240] Casalegno V, Chen Q, Chen Q, Salvo M, Smeacetto F, Ventrella A, et al. Joining of advanced ceramics, glasses and composites at Politecnico di Torino, Italy. Key Eng Mater 2010;434–435:197–201. doi:10.4028/www.scientific.net/KEM.434-435.197.

[241] Siegmann S, Dvorak M, Grützner H, Nassenstein K, Walter a. Shear testing for characterizing the adhesive and cohesive coating strength without the need of adhesives. Therm Spray 2005 Therm Spray Connect Explor Its Surf Potential! 2005;Basel, CH:823–9.

[242] Henkel Corporation Aerospace. LOCTITE EA 9396 QT AERO. Tech Data Sheet n.d. http://na.henkel-adhesives.com/product-search-1554.htm?nodeid=8797801152513.

[243] Goglio L, Peroni L, Peroni M, Rossetto M. High strain-rate compression and tension behaviour of an epoxy bi-component adhesive. Int J Adhes Adhes 2008;28:329–39. doi:10.1016/j.ijadhadh.2007.08.004.

[244] Yang S, Xu W, Liang L, Wang T, Wei Y. An experimental study on the dependence of the strength of adhesively bonded joints with thickness and mechanical properties of the adhesives. J Adhes Sci Technol 2014;28:1055–71. doi:10.1080/01694243.2014.884753.

[245] Filipe L, Dillard D. Fracture Mechanics Applied to the Design of Adhesively

Bonded Joints by Filipe José Palhares Chaves Supervisor : © Filipe José Palhares Chaves Departamento de Engenharia Mecânica Faculdade de Engenharia da Universidade do Porto. Univ Do Porto 2013.

[246] Da Silva LFM, Ferreira NMAJ, Richter-Trummer V, Marques EAS. Effect of grooves on the strength of adhesively bonded joints. Int J Adhes Adhes 2010;30:735–43. doi:10.1016/j.ijadhadh.2010.07.005.

[247] Vorobyev AY, Guo C. Femtosecond laser structuring of titanium implants. Appl Surf Sci 2007;253:7272–80. doi:10.1016/j.apsusc.2007.03.006.

[248] Zimmermann S, Specht U, Spieß L, Romanus H, Krischok S, Himmerlich M, et al. Improved adhesion at titanium surfaces via laser-induced surface oxidation and roughening. Mater Sci Eng A 2012;558:755–60. doi:10.1016/j.msea.2012.08.101.

[249] Aliasghari S, Němcová A, Skeldon P, Thompson GE. Influence of coating morphology on adhesive bonding of titanium pre-treated by plasma electrolytic oxidation. Surf Coatings Technol 2016;289:101–9. doi:10.1016/j.surfcoat.2016.01.042.

[250] Yukimoto Y, Matsuzaki R, Todoroki A. Composites : Part A Effects of mixed-mode ratio and step-shaped micro pattern surface on crack-propagation resistance of carbon-fibre-reinforced plastic / adhesive interface. Compos PART A 2015;69:139–49. doi:10.1016/j.compositesa.2014.11.014.

[251] Niknam SA, Khettabi R, Songmene V. Machinability and Machining of Titanium Alloys: A Review. In: Davim JP, editor. Mach. Titan. Alloy., Berlin, Heidelberg: Springer Berlin Heidelberg; 2014, p. 1–30. doi:10.1007/978-3-662-43902-9_1.

[252] Pederson R. Microstructure and Phase Transformation of Ti-6Al-4V. 2002. doi:LTU-LIC-0230-SE.

[253] Shapiro AE, Brazing T. Brazing of Conventional Titanium Alloys. In: D.L. Olson, T.A. Siewert, S. Liu and GRE, editor. ASM Handbook, Vol. 6, Welding, Brazing Solder., vol. 6, ASM International; 2016.

[254] Xiong JH, Huang JH, Zhang H, Zhao XK. Brazing of carbon fibre reinforced SiC composite and TC4 using Ag-Cu-Ti active brazing alloy. Mater Sci Eng A 2010;527:1096–101. doi:10.1016/j.msea.2009.09.024.

[255] Liu YZ, Zhang LX, Liu CB, Yang ZW, Li HW, Feng JC. Brazing C/SiC composites and Nb with TiNiNb active filler metal. Sci Technol Weld Join 2011;16:193–8. doi:10.1179/1362171810Y.0000000021.

[256] LIU D, SONG Y, ZHOU Y, SONG X, FU W, FENG J. Brazing of C/C composite and Ti-6Al-4V with graphene strengthened AgCuTi filler: Effects of graphene on wettability, microstructure and mechanical properties. Chinese J Aeronaut 2017:4–10. doi:10.1016/j.cja.2017.08.017.

[257] Qin Y, Yu Z. Joining of C/C composite to TC4 using SiC particle-reinforced brazing alloy. Mater Charact 2010;61:635–9. doi:10.1016/j.matchar.2010.03.008.

[258] Singh M, Asthana R, Shpargel TP. Brazing of ceramic-matrix composites to Ti and Hastealloy using Ni-base metallic glass interlayers. Mater Sci Eng A 2008;498:19–30. doi:10.1016/j.msea.2007.11.150.

[259] Song X rui, Li H jun, Zeng X, Zhang L. Brazing of C/C composites to Ti6Al4V using graphene nanoplatelets reinforced TiCuZrNi brazing alloy. Mater Lett 2016;183:232–5. doi:10.1016/j.matlet.2016.07.111.

[260] Song X, Li H, Casalegno V, Salvo M, Ferraris M, Zeng X. Microstructure and mechanical properties of C/C composite/Ti6Al4V joints with a Cu/TiCuZrNi composite brazing alloy. Ceram Int 2016;42:6347–54. doi:10.1016/j.ceramint.2016.01.026.

[261] Shapiro AE, Flom Y. Evaluation of Low-Temperature Amorphous Foils for Brazing Titanium and Ceramics. 6th Int. Brazing Solder. Conf., Long Beach, CA: American Welding Society; 2015, p. Paper 22.

[262] Hartmann T, Nuetzel D. Nickel-Chromium-Based Amorphous Brazing Foils for Continuous Furnace Brazing of Stainless Steel. Proc 9th Int Conf Brazing, High Temp Brazing Diffus Bond 2010.

[263] Shapiro AE. Brazing of Conventional Titanium Alloys. ASM Handbook, New Ed., vol. 6, 2016, p. 36–43.

[264] Eckardt, T., Hanhold, B., Petrasek, D., Sattler, S., Benatar, A., & Shapiro A. BRAZING & SOLDERING TODAY Evaluating Low-Temperature Brazing Filler Metals for BRAZING & SOLDERING TODAY. Weld J 2012;91:45–50.

[265] Sapkal SU, Jagtap PS. Optimization of Micro EDM Drilling Process Parameters for Titanium Alloy by Rotating Electrode. Procedia Manuf 2018;20:119–26. doi:10.1016/j.promfg.2018.02.017.

[266] Ferraris M, Salvo M, Isola C, Appendino Montorsi M, Kohyama a. Glass-ceramic joining and coating of SiC/SiC for fusion applications. J Nucl Mater 1998;258–263:1546–50. doi:10.1016/S0022-3115(98)00176-7.

[267] Singh M, Matsunaga T, Lin HT, Asthana R, Ishikawa T. Microstructure and mechanical properties of joints in sintered SiC fibre-bonded ceramics brazed with Ag-Cu-Ti alloy. Mater Sci Eng A 2012;557:69–76. doi:10.1016/j.msea.2012.05.110.

[268] Halbig MC, Coddington BP, Asthana R, Singh M. Characterization of silicon carbide joints fabricated using SiC particulate-reinforced Ag-Cu-Ti alloys. Ceram Int 2013;39:4151–62. doi:10.1016/j.ceramint.2012.10.271.

[269] Liu Y, Huang ZR, Liu XJ. Joining of sintered silicon carbide using ternary Ag-Cu-Ti active brazing alloy. Ceram Int 2009;35:3479–84. doi:10.1016/j.ceramint.2009.03.016.

[270] Asthana R, Singh M. 11 - Active metal brazing of advanced ceramic composites to metallic systems. Woodhead Publishing Limited; 2013. doi:http://dx.doi.org/10.1533/9780857096500.2.323.

[271] TSUNOURA1 T, OKUBO Y, YOSHIDA K, YANO T, AOKI T, OGASAWARA T. Oxidation behavior of monolithic HfSi2 and SiC fibre-reinforced composites fabricated by melt infiltration using Si-8.5 at%Hf alloy at 800-1200°C in dry air. J Ceram Soc Japan 2012;126:27–33. doi:10.1137/1.9780898717822.ch1.

[272] Ma Y, Li S, Li Q, Wang Z, Shi G, Wu C, et al. Fabrication of ZrC-SiC composites using zirconium salt as raw materials. J Asian Ceram Soc 2014;2:317–21. doi:10.1016/j.jascer.2014.07.002.

[273] Jiang M, Zheng JW, Xiao HY, Liu ZJ, Zu XT. A comparative study of the mechanical and thermal properties of defective ZrC, TiC and SiC. Sci Rep 2017;7:1–14. doi:10.1038/s41598-017-09562-x.

[274] Johnson-Steigelman HT, Brinck A V., Parihar SS, Lyman PF. Hafnium silicide formation on Si(001). Phys Rev B - Condens Matter Mater Phys 2004;69. doi:10.1103/PhysRevB.69.235322.

[275] Vahlas C, Chevalier PY, Blanquet E. A thermodynamic evaluation of four Si-M (M = Mo, Ta, Ti, W) binary systems. Calphad 1989;13:273–92. doi:10.1016/0364-5916(89)90007-2.

[276] Gupta SP. Intermetallic compounds in diffusion couples of Ti with an Al-Si eutectic alloy. Mater Charact 2003;49:321–30. doi:10.1016/S1044-5803(02)00342-X.

[277] Salishchev GA, Imayev RM, Senkov ON, Imayev VM, Gabdullin NK, Shagiev MR, et al. Formation of a submicrocrystalline structure in TiAl and Ti3Al intermetallics by hot working. Mater Sci Eng A 2000;286:236–43. doi:10.1016/S0921-5093(00)00806-6.

[278] Botstein 0., Schwarzman A, Rabinkinb A. Induction brazing of Ti-6Al-4V alloy with amorphous 25Ti-25Zr- 50Cu brazing filler metal. Mater Sci Eng 1996;206:14–23. doi:10.1016/0921-5093(95)09885-2.

[279] Predel B. Ti-Zr (Titanium-Zirconium). In: Madelung O, editor. Pu-Re -- Zn-Zr, Berlin, Heidelberg: Springer Berlin Heidelberg; 1998, p. 1–3. doi:10.1007/10551312_2847.

[280] Moszner F, Mata-Osoro G, Chiodi M, Janczak-Rusch J, Blugan G, Kuebler J. Mechanical behavior of SiC joints brazed using an active Ag-Cu-In-Ti braze at elevated temperatures. Int J Appl Ceram Technol 2017;14:703–11. doi:10.1111/ijac.12689.

Annex 1

List of Publications

Joining of Al-6016 to Al-Foam Using Zn-Based Joining Materials. Published in International Journal of Applied Science and Manufacturing: Composite Part A; 96:122–8. doi:10.1016/j.compositesa.2017.02.019, January, 2017.

Joining of Al-Sheet to Al-Foam Using Metal Glasses. Submitted to the Journal of Materials Processing Technology. Ref: PROTEC-D-18-01186, April 2018.

Development and Characterisation of Hybrid Dynamic Epoxy/PU Composites for Enhanced Impact Resistance. Ref: JCOMB_2018_1382. Reviewed, Journal of Applied Science and Manufacturing: Composite Part B, March 2018.

List of Conferences

Joining of C/SiC Ceramic Composites to themselves and to Ti-6Al-4V for aerospace applications. 23rd AIDAA Conference on Aeronautics and Astronautics, Turin Italy 17-19 November 2015.

Joining of Al-6016 To Al-foam Using Zn-based Alloys to Obtain Aluminium Foam Sandwich (AFS) For Aerospace Applications. 23rd AIDAA Conference on Aeronautics and Astronautics, Turin, Italy 17-19 November 2015.

Joining of C/SiC Ceramic Composite to Itself and TI64 For Aerospace Applications. 40th International Conference and Expo on Advanced Ceramics and Composites. Ref ID: 2349806, Daytona Beach, Florida, United States of America (USA) 24 – 29 January 2016.

Joining of C/SiC to Ti-6Al-4V by Zirconium-Based Brazing Alloys. 41st International Conference and Expo on Advanced Ceramics and Composites. Ref: 2586304, ICACC-S1-P082-2017, Daytona Beach, Florida, United States of America (USA) 22-27 January 2017.

Joint Strength Improvement of C-SiC/Ti6Al4V System by Surface Modification. 42nd International Conference and Exposition on Advanced Ceramics and Composites (ICACC 2018), Daytona Beach, Florida, Florida, United States of America (USA) January 21-26, 2018.

Development and Characterisation of Hybrid Epoxy/PU Dynamic Thermoset Composites with Enhanced Impact Resistance. European Congress

and Exhibition on Advance Materials and Processes (Ref: 1830 EUROMAT, 2017). Thessaloniki – Greece. 17-22 September 2017.

Joining of CFRP and low-CTE glass-ceramics for aerospace applications. European Congress and Exhibition on Advance Materials and Processes (EUROMAT, 2017). Thessaloniki – Greece (17-22 September 2017).

Brazing Joining Of C/SiC to Ti6Al4V and the Joint Strength Improvement by Surface Modification. Ref: CD: HP09. CIMTEC 2018, 14th Ceramics Congress (June 4-8, 2018) Perugia, Italy.

Effect and Comparison of MWCNTs on the Flexural Behaviour of Carbon Fibre Reinforced Polymer (CFRP)/Al-foam and Al-honeycomb Sandwich Composites. 18th world textile conference. Istanbul, Turkey. (20-22 June 2018).

A Comparison of Al-foam Core and Al-honeycomb Core Glass-fibre/Epoxy Sandwich Panels. ***(Accepted)*** 1st International Symposium on Mechanics, Glasgow, United Kingdom, 9-12 July 2018.

List of External Research Activities

Task: Development and Characterization of Fibre Reinforced Polymer / Al-foam and Al-Honey Comb Sandwich Panels. (Joint research activity of Politecnico di Torino and Istanbul Technical University). **Funding:** Higher Education Commission, Pakistan (HEC). **Host Institute:** Dept. of Textile Engineering, Design and Technology, Istanbul Technical University, Turkey. (September 2017-October 2017).

Task: Hybrid Epoxy / PU Dynamic Thermoset Composites with Enhanced Impact Resistance. **Funding:** 7th Call of KMM-VIN research fellowship**. Host Institute:** IK4-CIDETEC, San Sebastian, Spain. (September 2015-November 2015)

Awards

- HEC, Pakistan MS leading to PhD fellowship award (2012-2017).
- KMM-VIN Mobility Grant award, 2015.
- Glance Challenge Award, best project, selected by Brembo (http://www.brembo.com), 2018

Annex 2

Preparation and Investigation of AFS from Al-6013 and Al6Si Foams by Brazing Method

This project was started in collaboration with Institute of Metallurgy and Materials Science (Polish Academy of Sciences), Krakow, Poland under Erasmus staff mobility and training programme.

The joining of Al-6013 sheets to Al6Si foams (produced by Institute of Metallurgy and Materials Science, Poland) to obtain AFS composite panels. The joining substrates (Al-Sheets and Al-foams) were provided by the partner institute while the joining experiments were carried out in DISAT, Politecnico di Torino under the supervision of Prof. Graziano Ubertalli.

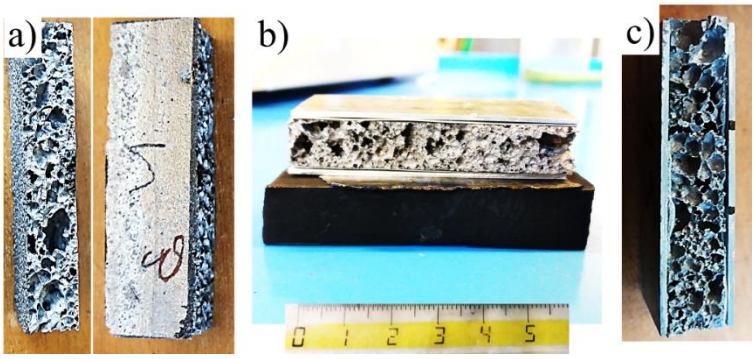

a) Al6Si Foam surface and cross-section, b) AFS base stacking for brazing, c) Transverse view of Al-6013/Al6Si AFS composite brazed specimen

The brazing parameters were optimised and AFS specimens were produced by joining un-treated and artificially aged Al-6013 sheets to Al6Si foams using Zn-based joining alloys.

The AFS cross-sections were investigated using OM, SEM and TEM. Rectangular specimens of dimension 60 mm (length) x 20 mm (width) x 11 mm (thick) were subjected to three-point bending test to analyse the flexural properties of the AFS composite panels.

The results are under analysis at this point. A joint research paper regarding this research activity will be published in near future.

Annex 3

Adhesive Joining and Disassembling of Alumina (Al_2O_3) – Steel

This research activity was conducted within J-TECH@POLITO, Advanced Joining Technologies inter-departmental research centre funded by Politecnico di Torino and under the supervision of Prof. Monica Ferraris. SASIL s.r.l. Italy is kindly acknowledged for having partially funded this experimental work.

Rollers are used to crush the waste glass in industry: since they are made of steel, it adds dark colour contamination to the crushed glass powder. Recently it was proposed to cover the steel roller surface with high wear resistant alumina ceramic inserts to avoid the problem of coloured contamination in the glass powder.

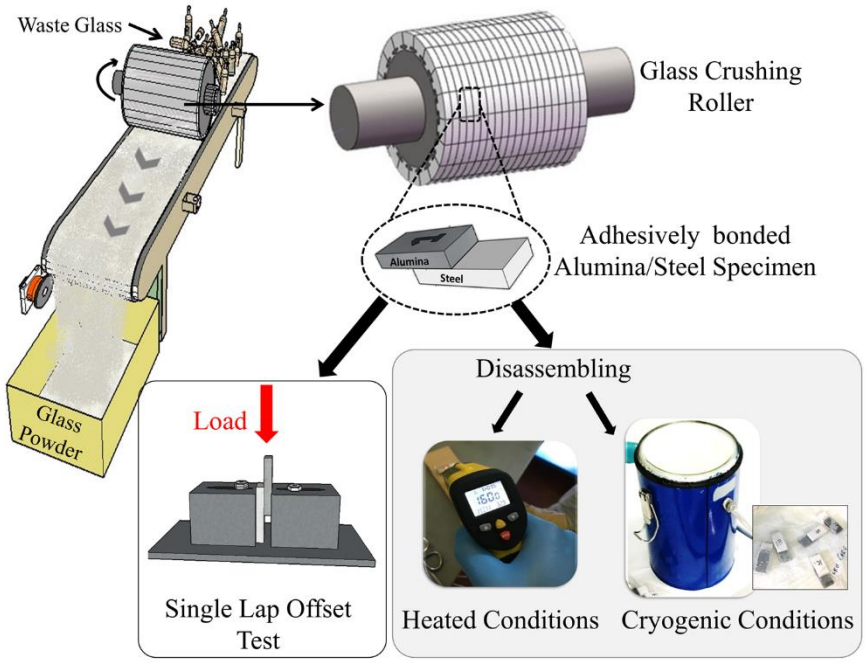

Adhesive joining and Disassembling of Alumina/Steel specimens

The aim of this research activity was to study the adhesive joining and disassembling of alumina inserts to C-45 steel. The joining was targeted to ensure that the alumina inserts remain intact to steel roller surface (minimum joint shear strength ≥10 MPa) during the operation. While the disassembling target was to ensure the easy replacement of individual alumina inserts broken/damaged during the operation.

Adhesive joints were produced using three types of commercial adhesives (Bondit: B-45TH, B-481 TH, and B-536 TH, supplied by RELTEK, USA). The bonded

substrates were subjected to single lap offset shear test to determine the joint shear strength.

The two adhesives, B-481 TH (~30 MPa) and B-536 TH (~18 MPa) displayed the joint shear strength well above the target i.e. 10 MPa and displayed mix adhesive-cohesive failure at the joining interface.

The disassembling tests were conducted at higher and at cryogenic temperatures. The alumina/steel substrates bonded with B-536 adhesive displayed easy disassembling when heated for 15 minutes at 160 ^{o}C. While the specimens bonded with B-481 TH and B-45 TH disassembled when heated for 25 minutes at 160 ^{o}C. The cryogenic disassembling test (using liquid nitrogen) apparently didn't work. Based on experimental results and observations, B-536 TH adhesive was found, the most suitable solution for this project due to adequate joint shear strength easy disassembling.

The lab-scale experimental work was successfully reproduced and upscaled for the industrial process in the partner company (SASIL s.r.l. Italy). A letter of appreciation issued by the SASIL s.r.l. Italy for the successful completion of research activity is attached.

Brusnengo, 19 febbraio 2018

Oggetto: PROVE SEMINDUSTRIALI SU DISTACCO ADESIVI

(Progetto "*Sviluppo di cilindraia innovativa con inserto di materiale ceramico per molino a rulli*")

Buongiorno Dott.ssa Ferraris,

con riferimento alla fase 2 della sperimentazione sul distacco Ferro-Allumina, in base alle indicazioni contenute sulla Vs relazione del 19/12/2016, sono lieto di comunicarle il buon esito della stessa.

Come anticipato per telefono, abbiamo provveduto a simulare un incollaggio tra Ferro e Allumina da voi consigliato seguendo la metodica da voi indicata, sia in fase di assemblaggio che di disassemblaggio.

Abbiamo anche simulato le stesse condizioni operative previste nel profilo industriale, quindi con lo stesso sviluppo di superficie di incollaggio.

Dopo un tempo di riscaldamento totale di 40 minuti, 20 minuti di rampa di salita e 20 minuti di stazionamento a 170°C, il distacco dell'allumina dal ferro è avvenuto molto facilmente lasciando la superficie di contatto senza incrostazioni, con un leggero velo di polvere biancastra rimovibile con semplici soffiaggi.

Pertanto ritengo che la fase 2 della ricerca possa considerarsi positiva.

Con l'occasione abbiamo preso contatto con la società Colorobbia, nelle persone dei Dott. Nannini e Dott. Macchi, per proporre una collaborazione nel senso di sviluppare un primo prototipo di rullo rivestito in allumina.

A questo proposito, visto che nel nostro accordo di confidenzialità del 9/12/2016, ai punti 13-14 (riservatezza e trattamento dati), si parla della modalità di condivisione dei risultati e di un accordo tra le parti per comunicazioni a terzi, chiedo in particolare all'Ing. Scattina e comunque al direttore del dipartimento che ha firmato l'accordo, Prof. Massimo Rossetto, l'autorizzazione a trasmettere alla Colorobbia la Vs relazione del 26/06/2017, dove appunto si illustrano i risultati da voi ottenuti sui vari adesivi ed in base ai quali abbiamo potuto dar corso positivamente alla sperimentazione semi-industriale.

La Colorobbia sarà nostro fornitore dei manufatti in allumina e quindi ha bisogno di studiare la compressibilità meccanica dell'adesivo scelto, in funzione di garantire la stabilità dell'incollaggio e la corretta trasmissione degli sforzi.

In attesa di una Vs comunicazione in merito alla diffusione dei dati porgo cordiali saluti.

Lodovico Ramon

Sasil S.r.l. Società con socio unico - AZIENDA CERTIFICATA NORMA UNI EN ISO 9001
Sede legale: Via Libertà, 8 - 13862 BRUSNENGO (BI) - Italia Tel: +39 015 985166 Fax: +39 015 985327
http://www.sasil-life.com e-mail: sasil@sasil-life.com pec: sasil@email-pec.it
Capitale Sociale € 5.000.000 i.v. - C.C.I.A.A. Biella: Registro Imprese n. 01232720027 REA n. 128218 C.F. e P. IVA 01232720027
Società soggetta all'attività di direzione e coordinamento di Minerali Industriali S.r.l. - Sito web: www.mineralindustriali.it

Stabilimento: Strada del Dosso 22-26 - 13862 BRUSNENGO (BI) - ItaliaTel: +39 015 985261 Fax: +39 015 985980

Corrispondenza: Sasil S.r.l. c/o Minerali Industriali S.r.l. - Piazza Martiri della Libertà, 4 - 28100 NOVARA (NO) – Italia Tel: +39 0321 377600 Fax: +39 0321 391874